THE (p,n) REACTION ON ^{9}Be AND ^{17}O AT 135 MeV

Billy Gene Pugh, Jr.
B.S. Baylor University
Waco, Texas
(1977)

Submitted to the department of physics in partial
fulfillment of the requirements
for the degree of

Doctor of Philosophy

at the
Massachusetts Institute of Technology
(August 1985)

Signature of Author_____
Department of Physics, August 1985

Certified by_____
William Bertozzi, Thesis Supervisor

Accepted by_____
George F. Koster, Chairman, Department Committee

THE (p,n) REACTION ON ^9Be AND ^{17}O AT 135 MeV

by

Billy Pugh

Submitted to the department of physics in August, 1985
in partial fulfillment of the requirements for the degree of
Doctor of Philosophy

Abstract

Differential cross sections and analyzing powers for the $^{17}O(p,n)^{17}F_{groundstate}$ reaction at 135 MeV have been measured from zero momentum transfer out to a center of mass momentum transfer of about 2.5 fm^{-1}. Cross sections have also been measured for states in ^{17}F at 4.84, 7.25, and 7.64 MeV for momentum transfers less than 0.5 fm^{-1}. The cross sections for transitions to the ground state of ^9B and its state at 2.36 MeV have been measured out to 2.2 fm^{-1}. The analyzing power of the (p,n) reaction to the ground state of ^9B has been partially measured out to 2.0 fm^{-1}.

The 0° $^{17}O(p,n)^{17}F_{g.s.}$ cross section is expected to be simply related to the β-decay rate of ^{17}F. The actual 0° $^{17}O(p,n)^{17}F_{g.s.}$ cross section is found to be consistent with the observed ^{17}F half-life against β-decay. Both quantities indicate a Gamow-Teller strength about 50% of the $\frac{5}{2}^+$ single particle value. This corroborates other evidence indicating a general deficiency of Gamow-Teller strength in nuclei.

In addition, the cross sections of several other states of ^9B and ^{17}F were measured over varying ranges of momentum transfer. Cross sections were measured at forward angles for Gamow-Teller states in ^{17}F at 4.8 MeV and 7.3 MeV. The measurement of a Gamow-Teller state at 4.8 MeV indicates an error in the currently accepted spin-parity assignment for this state. The cross sections of ^{17}F states at 9.3 MeV and 14.3 MeV were also measured at momentum transfers in the range 0.5 to 1.0 fm^{-1}. Integrating the 0° cross section for producing ^{17}F up to about 16 MeV of excitation yields only about 50 % of the strength expected on the basis of the Gamow-Teller sum rule. A similar result was obtained for $^9Be(p,n)^9B$.

Various sharp states in ^9B were seen from 11 to 18 MeV and their cross sections measured for varying ranges of momentum transfer. Some of these states are easily correlated with known states of ^9B. In addition a state in ^9B at 3.0 MeV, and with a FWHM of 3.2 MeV was seen to dominate the spectrum for momentum transfers less than 1 fm^{-1}. The angular distribution and transition strength for this state suggests that it may be the $p_{1/2}$ state of ^9B whose existence has been conjectured but not established by any other reaction. Evidently two sharper states at 2.7 MeV and 4.3 MeV were obscured by this 3.0 MeV state. Tentative cross sections for

these two states were extracted.

Preliminary distorted wave calculations are presented which attempt to describe the cross sections for the ground state analog transitions using wave functions which accurately describe magnetic elastic electron scattering from ^{9}Be and ^{17}O. These wave functions are found to be inadequate to account for the (p,n) cross sections. Partial *ad hoc* success is achieved by renormalizing the separate J-transfer cross sections and by judicious choice of radius parameters. The normalizations and parameters determined from the cross section data also describe the analyzing powers of the ground state analog transitions. This analysis indicates that the (p,n) reaction may reveal aspects of the structure of these nuclei not seen by electron scattering. A more consistent theoretical analysis of the data reported here seems justified in view of the possible sensitivity of this reaction to details of nuclear structure.

Thesis Supervisor: William Bertozzi

Title: Professor of Physics

CONTENTS

I. Introduction

Purpose of this Thesis

This thesis reports differential cross section measurements for the $^9Be(p,n)^9B$ and $^{17}O(p,n)^{17}F$ reactions at 135 MeV leaving the nuclei in various excited states. This thesis also reports the analyzing power of these reactions leaving the product nuclei in their ground states. These data are unique owing to their high resolution and their range of momentum transfer. The cross sections and analyzing powers for the transition to the ground state of ^{17}F have been measured out to about 2.5 fm^{-1}. The cross sections and analyzing powers for the transition to the ground state of ^9B have been measured out to 2.0 fm^{-1}. Several other excited states of ^9B and ^{17}F were resolved and the angular distribution of their cross sections measured. Altogether these data provide a wealth of information which should prove useful to those interested in these nuclei and to those investigating more general questions of nuclear degrees of freedom involved in the (p,n) process. The experimental results are compared to available DWIA calculations.

The Theory of Nuclear Reactions

The ultimate goal of a nuclear reaction study is to to gain an understanding of the nucleus itself. It is necessary therefore that the scattering event be well enough understood so that the results can be somehow interpreted. It is also desirable that the process be simple enough in its description that the human mind is offered a physical picture of the interpretation in addition to the technical mathematical aspects of the analysis. These requirements are fulfilled when the incident projectile interacts by a well understood force and when this interaction can largely be considered as perturbative in terms of the target system. Such experiments can be said to probe in a simple and direct manner the constitution of the target.

The earliest uses of hadronic reactions were confined to providing the energies of various nuclear stationary states. For low energy hadronic probes (less than a few MeV) Bohr introduced the idea of a compound nucleus formed by the probe and target nucleus. He did this in order to account for the various phenomena of neutron capture such as the sharpness of the gamma radiation which typically follows neutron capture at these energies [BOH36]. In this scheme, the probe and target collide to form a single intermediate nucleus which then disintegrates into a final nucleus and an outbound projectile. The intermediate compound nucleus is

supposed to disintegrate without regard to how it was formed. This model assumes that the incident projectile shares its energy or motion among the various target nucleons before any final projectile is sent forth. We may represent this sort of reaction symbolically,

$$A + a \rightarrow C \rightarrow B + b \qquad I-1$$

The mathematical description of this model employs Fermi's 1^{st} Golden Rule [FER50] which states that for a transition from an initial state A to a final state B via intermediate state C, the transition probability per unit time is given by

$$\frac{2\pi}{\hbar}\left|\frac{\mathcal{H}_{BC}\mathcal{H}_{CA}}{E_A - E_C}\right|^2 \times \begin{pmatrix}\text{energy}\\ \text{density of}\\ \text{states}\end{pmatrix} \qquad I-2$$

This model predicts sharp increases in cross section at those total energies corresponding to stationary states of the compound nucleus. This can be seen immediately in a qualitative sense from the denominator of equation IV-2. This formula is the second term of a perturbation expansion and is accurate only if there are no direct transitions from state A to state B. This application of dispersion theory to the compound nucleus reaction model was first introduced by Breit and Wigner [BRE36] and enjoyed success in describing the scattering and absorption of protons and neutrons from nuclei for reaction energies of less than one MeV.

At higher excitation energies, cross sections for nuclear reactions change character. They no longer display the sharp dependence on projectile energy since compound states of the target plus projectile system are broad in energy and short lived. Because of the decreased nucleon-nucleon cross section and high projectile speed, it becomes more difficult for the projectile to share its energy with the other particles and form an eigenstate of the compound nucleus system. This increase of the mean free path suggests that nuclear reactions at higher energies might be better described as a direct transition from state $A + a$ to state $B + b$ without the involvement of the intermediate state C.

The direct reaction model assumes that the transition from the initial to final state takes place without the formation of an intermediate stationary state. In reality, there are indeed compound nucleus resonances at these energies, but they are so broad (short lived) as to obscure any distinction amongst them. This feature in fact smoothes out the dependence of the cross section on energy so that observed cross sections do not exhibit sharp resonance behavior at these higher energies. As was first demonstrated by Feshbach, Porter, and Weisskopf [FES54], this effective averaging over resonances makes it possible to calculate the cross section for elastic scattering not involving the formation of a compound nucleus by describing the motion of the projectile in a single particle potential with an imaginary part to account for reactions. Since compound nucleus formation is negligible at these energies, this amounts to a description of elastic scattering. The single particle potential is called an *optical potential* and this simplified description is called the *optical model.* This model was originally motivated by the success of the shell model and may indeed be considered an independent particle model applied to positive

(continuum) energy states. The direct reaction theory of nuclear scattering is an application of the optical model.

This sort of motion is described by Fermi's 2^{nd} Golden Rule [FER50]. This rule states that for a direct transition from an initial state A to a final state B, the transition probability per unit time is given by

$$\frac{2\pi}{\hbar}|\mathcal{H}_{BA}|^2 \times \begin{pmatrix} \text{energy} \\ \text{density of} \\ \text{states} \end{pmatrix} \qquad I-3$$

The cross sections given by this formula do not exhibit sharp resonances at particular energies. If the states A and B are taken to be bound nuclear states plus a plane wave to represent the projectile we have the plane wave approximation. If an optical potential is used to generate the projectile wave function representing elastic scattering we have the distorted wave theory of nuclear reactions. A more exact scattering theory includes terms of higher order in the scattering Hamiltonian. The approximation of keeping only the first order term is commonly called the Born approximation [BORN26].

The Distorted Wave Born Approximation

In the distorted wave Born approximation, elastic scattering is described by an optical potential and inelastic scattering is considered a small effect in comparison. According the this approximation, the differential cross section for the reaction of expression $I-1$ can be obtained from

$$\sigma(\theta) = \frac{\mu_a \mu_b}{(2\pi\hbar^2)^2}\frac{k_b}{k_a}\frac{\sum|T|^2}{(2J_A+1)(2s_a+1)} \qquad I-4$$

μ_a and μ_b are the reduced energies of the respective particles in the center of mass frame. k_a and k_b refer to relative momenta in the center of mass frame. The target nucleus has spin J_A and in our case $s_a = \frac{1}{2}$ is the projectile's spin. The summation is over initial and final spin projections of the projectile and target.

The distorted wave Born approximation is based upon a transition amplitude of the form

$$T = J\int d\mathbf{r}_a \int d\mathbf{r}_b\, \chi_b^{(-)*}(\mathbf{k}_b,\mathbf{r}_b)\langle B,b|V|A,a\rangle\chi_a^{(+)}(\mathbf{k}_a,\mathbf{r}_a) \qquad I-5$$

χ_a and χ_b are the "distorted waves". They are elastic scattering wave functions which describe the relative motion of the pair a,A (asymptotically with relative momentum $\mathbf{k}_a$) before the collision, and of the pair b,B (with $\mathbf{k}_b$) after the collision. In the *optical model approximation*, the distorted waves are generated from a

Schrödinger equation. For example, nonrelativistically one would use

$$\left\{\nabla^2 + k^2 - \left(\frac{2\mu}{\hbar^2}\right)[U(r) + U_C(r)]\right\}\chi(\mathbf{k},\mathbf{r}) = 0 \qquad I-6$$

where U is the optical model potential and U_C the Coulomb potential. The optical model potential is usually chosen phenomenologically in order to reproduce elastic scattering.

The Role of (p,n) Reactions in Nuclear Physics

In the 1950's considerable progress was made in interpreting the data from hadron-nucleus reactions by assuming a one step, or direct reaction mechanism. Using this assumption it proved possible to obtain spectroscopic information useful in assigning spins and parities to various nuclear states [TOB61]. The (p,n) reaction was one of the many reactions employed.

In 1959 Bloom *et al* [BLO59] pointed out the unique potential of the (p,n) reaction in mirror nuclei as a probe of charge exchange in the effective proton-neutron force in nuclei. He argued that the common approximation in DWBA of neglecting the Pauli exchange integral, or knock-out integral, should be particularly valid for mirror nuclei because of the poor overlap of the bound and free wave functions and the good overlap of the extra-core nucleons in the initial and final target nucleus. Also, assuming the simple model of these nuclei as a closed inert core plus an orbiting nucleon, the projectile should not be able to significantly disturb the motion of the target nucleons prior to the interaction effecting the transition. Finally, the (p,n) reaction involves unambiguously a nucleon-nucleon interaction, whereas (p,p') might proceed by some sort of collective excitation. Thus, according to Bloom, using the (p,n) reaction eliminates many reaction uncertainties and leaves one free to study the effective nucleon-nucleon force itself. In particular, ^{17}O, ^{18}O, and ^{27}Al were used as targets in (p,n) studies at 7-14 MeV which demonstrated the existence of a sizable spin flip term in the effective two-body force [BLO65,AND69]. In addition, it was found that the inclusion of spin orbit distortions in DWBA calculations improved consistency with the data considerably.

In more recent years more hadronic scattering data has become available at higher energies which has proven amenable to direct reaction analysis [TELL79,TELL82]. At 100-200 MeV the nucleus has been found to become somewhat transparent to the projectile, making direct reaction theory even more valid than at lower energies . The investigation of [BLO65,AND69] concerning the ratio of the spin flip to non-spin flip isovector effective nucleon-nucleon force has been extended to these energies and generalized to several other nuclei [TAD81].

In addition it has become possible to make a quantitative connection between elastic nucleon-nucleus scattering and the nucleon-nucleon force. This connection

was first explored by Bethe [BET52]. Bethe's work was based on a phase shift description of the nucleon-nucleon force and has not been extended or elaborated in the following years. The well known work of Kerman, MacManus, and Thaler [KER59] used a potential description of the two body force in the context of a plane wave direct reaction theory. In order to make the connection to the phenomenological optical potentials typically used to introduce distortions it is necessary to consider the modification of the nucleon-nucleon force due to the presence of intervening nucleons. These effects are now treated by using the local density approximation which employs the nuclear matter effective interaction appropriate to the density in the vicinity of the interacting nucleons [BRI78,GER79]. In this way the optical potential is calculated on the basis of the nucleon-nucleon force. (p,n) reactions have not yet been described using the local density approximation. In this work distortion is computed using phenomenological optical potentials and the nucleon-nucleon potential is given no density dependence.

Electron scattering at energies above 100 MeV has long set the standard for the acquisition of precise knowledge of nuclear structure. The electron interacts with the nuclear constituents exclusively via the electromagnetic force (neglecting the weak interaction) which is not only well understood but is also very much smaller than the forces governing the nuclear dynamics. Thus perturbation theory can be applied to the scattering process and the reaction mechanism can be classified as predominately one-step or direct in character. The result is that the electromagnetic currents of the nucleons can be traced with confidence.

One important limitation of electron scattering is its relative insensitivity to neutrons. Generally electron scattering sees the magnetization of single particle neutron transitions and is insensitive to the bulk neutron distribution. Moreover, even the single particle magnetization of neutrons is easily confused by the magnetism due to any existing proton currents. This is because the electrons in general see all electromagnetic fields within the nucleus. Even for 180° scattering, where Coulombic scattering all but vanishes, the proton charges create magnetic fields by virtue of their motion as well as by their intrinsic magnetic dipoles. Thus, not only are neutrons masked, but it can be impossible to determine which aspect of proton magnetism is responsible for the observed scattering. The (p,n) reaction possibly offers a means of distinguishing these current and spin contributions.

At about 100-200 MeV the (p,n) reaction is dominated by the spin dependent part of the nuclear force [TAD81]. The tensor interaction and the spin-orbit interaction are small near zero momentum transfer. The (p,n) reaction at forward angles has then the property of exciting nuclear states by coupling to the spin of the nucleons. Electron scattering on the other hand has convective and spin-flip contributions even at small momentum transfer. If, with further developments of accurate reaction theory, it proves possible to quantitatively compare electron scattering and (p,n) reactions at small momentum transfer one may then obtain information regarding the orbital or current contributions to nuclear transitions [PET80]. This is one illustration of the possibilities in using hadronic reactions in combination with electromagnetic reactions to learn more about nuclear states.

Another important application of the results reported in this thesis has to do

with the isospin symmetry properties of the (p,n) reaction compared with those of β-decay. Goodman [GOOD80] has pointed out that the $0°(p,n)$ cross section provides a fairly direct measure of the so called Gamow-Teller matrix element for β decay [GOOD80]. This is because the (p,n) reaction selects the isovector parts of the effective nucleon-nucleon interaction and at small momentum transfer the central parts of the force dominate. This leaves only the isovector central and the isovector spin dependent forces which have the same isospin symmetry properties as the Fermi and Gamow-Teller matrix elements. The net result is that one expects a quantitative connection between the $0°(p,n)$ cross section and the corresponding β decay rate. In effect, nature calculates these two matrix elements in β decay and when these results are appropriately substituted in the DWBA formula for (p,n) scattering one expects agreement. In our case we expect to be able to use the β decay rate of ^{17}F to the ground state of ^{17}O to calculate the $^{17}O(p,n)^{17}F_{groundstate}$ cross section at 0°. There are other strongly excited states in the $^{17}O(p,n)^{17}F$ spectrum at 0°. These are expected also to be related to the Fermi and Gamow-Teller matrix elements. If one assumes the Fermi matrix element to be correctly given by some theoretical estimate, the (p,n) reaction at small momentum transfer can be used to measure the isovector spin-spin part of the nuclear force. In the case of mirror nuclei the Fermi matrix element is generally taken to be equal to unity. For virtually all nuclei tested this connection between β decay rates and the (p,n) reaction is found to be accurate to within 10% [GOOD80,TEL82]. This may be regarded as a partial test of the distorted wave direct reaction theory.

There is also in this connection a sum rule regarding the Gamow-Teller operator, the operator which describes both the isovector spin-spin part of the nuclear force and the spin flip part of β-decay (see equation $III-4$ in chapter III). The (p,n) reaction in this instance may be regarded as a device to count neutron excess in much the same way a X-ray scattering may be used to count the electrons of an atomic element. Any neutron of ^{17}O is a candidate for charge exchange (or a less likely knockout) unless this transition be Pauli blocked by a core proton of like motion. In all nuclei examined, this sum rule has been systematically violated by 30% to 50% . The experimentally observed sum is always less than that expected experimentally. The unexpected lack of participation of the projectile in these transitions could therefore very well indicate a very general misunderstanding of the nature of the nucleus itself. It has been suggested that the lack of Gamow-Teller strength is owing to the lack of neutrons, *i.e.* that nucleon motion in the nucleus is comprised partly of Δ degrees of freedom. Others feel that the missing strength is used to excite transitions into the continuum and into regions of excitation higher than experimentally used to determine the sum [OST82]. Whatever the solution proves to be, it is clear that accounting for this missing Gamow-Teller strength will reveal a very general feature of nuclear dynamics.

In the next chapter of this thesis the accelerator facility and other experimental apparatus will be described. Certain aspects of this particular experiment will be detailed and important operating principles of the equipment will be outlined as well. Important properties of the interaction of neutrons with matter are discussed in relation to detector efficiencies and atmospheric scattering.

Chapter III discusses the procedures used in data reduction and presents a representative sample of line fits. The 0° cross section for the $^{12}C(p,n)$ leading to the ground state of ^{12}N is related to previous measurements of this process in this energy region. This provides an important verification of the calculations of detector efficiencies. This chapter also presents graphs of all cross sections and analyzing powers measured. The chapter concludes with a report and discussion of the total Gamow-Teller strength measured for these nuclei.

In the final chapter, these experimental results are compared with available calculations made in the distorted wave Born approximation using the code DWBA70 to calculate the scattering potential in terms of simple nuclear models.

The appendix contains all measured cross sections and analyzing powers in tabular form.

II. Experimental Method

Synopsis of the Experimental Layout

These data were taken at the Indiana University Cyclotron Facility (IUCF) in Bloomington, Indiana. The unpolarized data run was during the winter of 1980. Polarized data were taken the summer of 1981. The machine at IUCF is a three-accelerator, three-beam line system employing an electrostatic accelerator feeding a tandem cyclotron arrangement. A diagram is shown in figure $II-1$.

This arrangement produced a source of 135 MeV protons which were made to strike a $Be^{17}O$ target. By means of two dipole magnets, described later as the beam swinger, the angle of the beam at the target could be varied as much as 26° from the beam line direction. Neutrons leaving the target were permitted to leave the facility through holes in the wall located at the angles 0°,24°, and 45° from the beam line direction. The beam swinger magnets permitted us to view scattering angles between these values. At roughly 100 meters from the target three huts containing the neutron detectors were placed to intercept the three neutron beams for time of flight measurements. This layout is shown schematically in figure $II-3$.

Beam Production

The beam source is a hydrogen gas. Polarized protons are produced by atomic beam methods [HAE67]. The protons are electrostatically accelerated through several hundred kilovolts before being handed off to the first cyclotron. It is here, before cyclotron injection, that the beam is given its waveform characteristics. The proton beam is initially a direct current. A beam chopper and buncher prepares a pulsed beam of 300 *ps* pulses separated by 130 *ns*. This pulsed beam must be injected into the first cyclotron properly phased so as to match the radio frequency of the dees in order to accomplish acceleration. This radio frequency varies from 24 to 36 MHz depending on the desired final projectile energy. In normal operation there are four to six bunches per orbit in the cyclotrons. In this experiment we chose to keep only one out of four bunches. This permitted sufficient temporal spacing between successive beam bursts for the long neutron flight paths used. The RF frequency is not modulated to accomodate relativistic kinematics. Instead, this is done geometrically by means of radial dependence of the static magnetic field which confines the charged particles. The beam is likewise handed off to another larger cyclotron for final acceleration and beam delivery. In between the cyclotrons

there is a Helium cell used for measuring the polarization in the case of a polarized beam. All these procedures are accomplished by the IUCF beam masters, whose heroic efforts produced for us polarized beam intensities from 50 nA to 200 nA.

The proton beam leaves the larger cyclotron and enters the beam swinger beam line shown in figure $II-2$. The beam is directed more than forty meters by six steering magnets and six quadrupoles before reaching the target area. The bunch width and separation is not significantly affected over this distance.[GOOD79]

In the target area, before reaching the scattering chamber, the beam is subjected to the actions of the beam swinger. The beam swinger consists of two dipole magnets whose design is to change the horizontal angle θ at which the beam enters the scattering chamber (see figure $II-3$). Any portion of the beam scattered an angle θ horizontally to the right will then proceed in direction parallel with the beam line. Thus the direction of 0° scattering has been moved to the left by an angle θ. We may in this fashion avoid moving detectors when measuring the intensities of particles scattered at different angles. Downstream of the scattering chamber a third magnet focuses and steers unscattered beam into a dump. The use of this third magnet allows the beam dump to remain in one location while θ is changed. The third magnet also facilitates the observation of neutrons produced at 0°.

The angle θ is determined primarily by the entrance dipole magnet as is shown in figure $II-3$. The second dipole magnet is used to effect the apex of an approximate isosceles triangle whose base is the line joining the entrance magnet and the target. Accomplishing 0° to 26° beam deflections required currents from 150 to 580 amperes in the entrance magnet and 220 to 340 ampere currents in the second magnet. The corresponding radii of curvature are shown in figure $II-4$.

The angle θ was measured by means of a movable auxiliary scintillating target which could be remotely erected in a position 18 inches upstream of the target. By using this target and another scintillating target on the target ladder to locate two points of the beam, the angle θ could be measured to within one-tenth of a degree.

The beam swinger operation was the only aspect of beam transport handled directly by the experimenters. All other beam handling was accomplished by the most excellent IUCF staff.

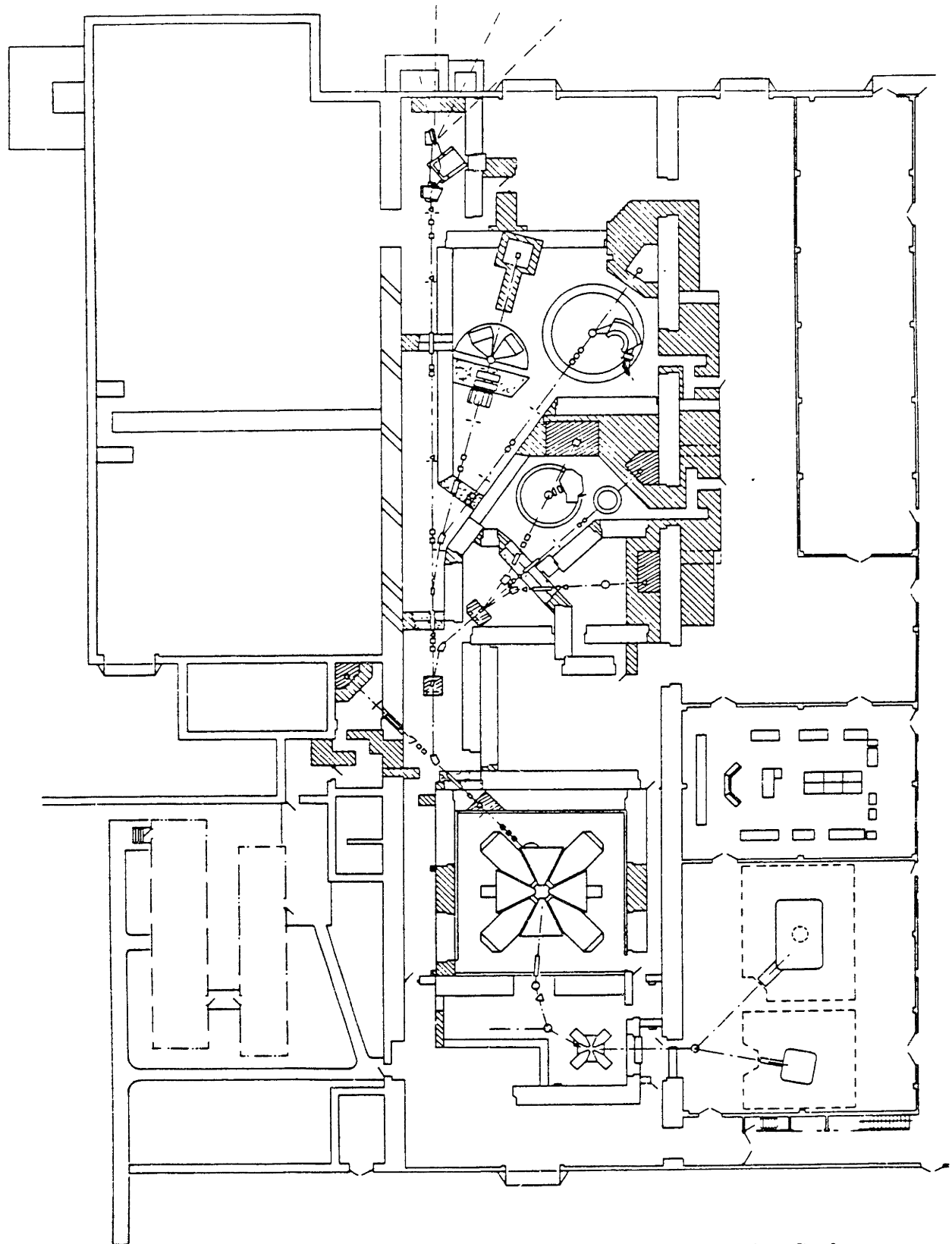

Figure $II-1$. A plan view of the Indiana University Cyclotron Facility.

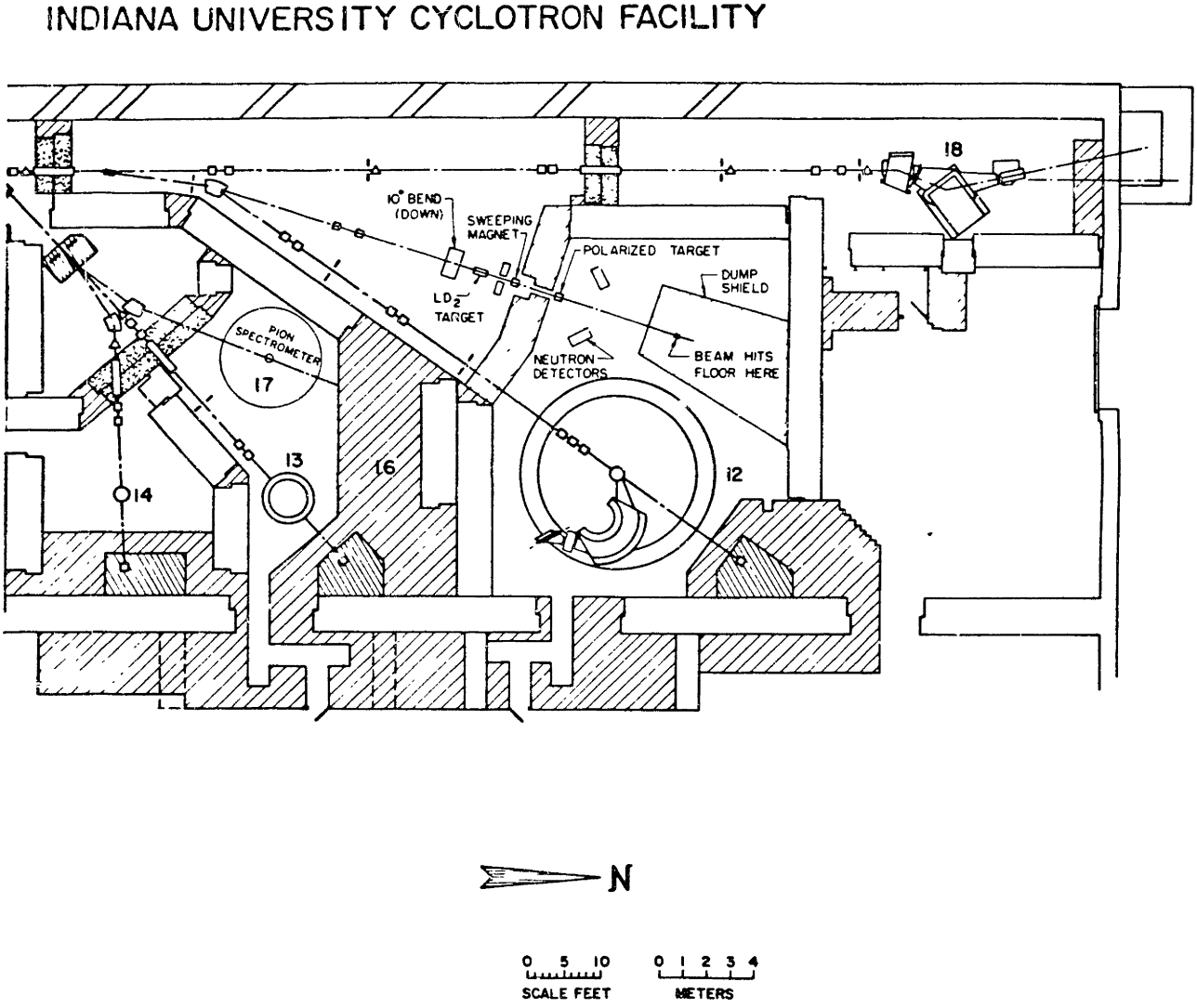

Figure II – 2. The beam swinger (labeled 18) and its beam line.

Figure II-3. Schematic of the beam swinger.

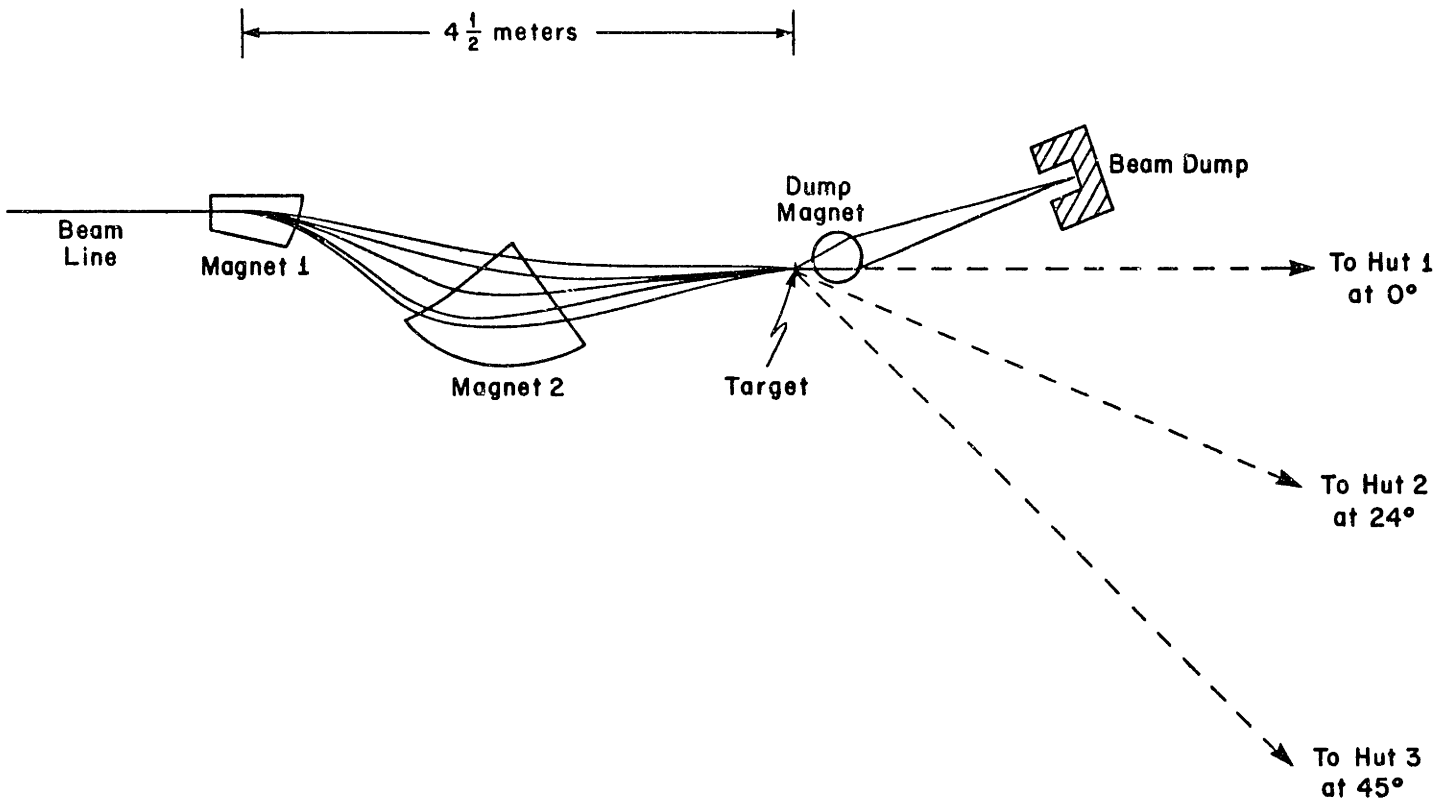

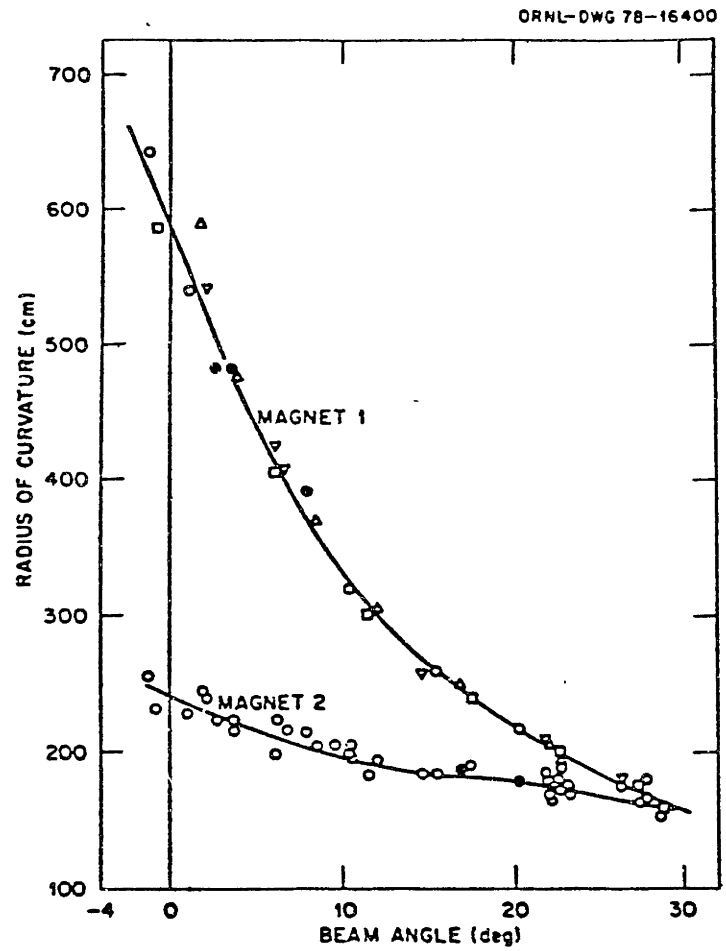

Figure $II - 4$. Operating characteristics of the beam swinger.

The Targets

The targets were housed within the beam pipe at a location just upstream of the dump magnet. The target angle was adjusted so that the proton beam was perpendicular to its surface whatever the beam swinger angle. The targets used are listed in table $II-1$. For the cross section measurements only the 29.1 mg/cm^2 $Be^{17}O$ target was used. During the polarized proton run both $Be^{17}O$ targets were placed in a single target frame to achieve a greater event rate. In addition to the beryllium oxide targets, a pure beryllium target of thickness 44.8 mg/cm^2 was used to measure the $^9Be(p,n)$ process and to provide background information. The thickness and isotopic abundance was known to within 1% for the beryllium target and to about 7% for each $Be^{17}O$ target. The cross section for $^9Be(p,n)^9B$ leading to the ground state of ^9B determined from the pure beryllium target agreed with the cross section for this process measured using the 29.1 mg/cm^2 beryllium oxide target to within 5%.

Table $II-1$. The beryllium oxide oxygen abundances.

thickness(mg/cm^2)	^{16}O	^{17}O	^{18}O
28.7	10.6%	85.3%	4.2%
29.1	11.6%	84.4%	4.0%

The Detection of Neutrons

The purpose of the experiment was to measure the neutron time-of-flight spectrum at various scattering angles. This allows the extraction of differential cross sections corresponding to the stationary states of the product target nucleus. Large rectangular plastic scintillators were housed in three huts at angles of 0°, 24°,and 45° relative to the beam line. The flight paths were generally 70 to 90 meters long. The neutron detecting scintillators were in all cases 4 inches thick to the beam but there were a variety of heights and widths. Each neutron detector was oriented with its face perpendicular to the neutron beam exposing each neutron to 4 inches of scintillator. Each neutron detector was a large rectangular piece of NE-102 plastic scintillator with plastic light guides affixed on opposite ends to facilitate the collection of light into two 5 inch diameter photomultiplier tubes. The entire assembly was wrapped first in paper and then several layers of black electrical tape to ensure an optically isolated environment for scintillation collection. The paper maximized

internal reflection by preventing optical contact between the black tape and the outer surface of the scintillator and light guides. Numerous $\frac{1}{2}$ inch thick NE-114 plastic scintillators were used to reject charged particle events due to protons from the target and cosmic rays. These charged particle detectors were two to three feet in length and width. The shortest edge was joined to a light pipe which guided light into a 2 inch diameter photomultiplier tube. The assembly was mummified in paper and tape in the same fashion as a neutron detector. During the unpolarized experiment the front and top of each neutron detector was guarded by these charged particle detectors. The back side was left open to allow the undetected passage of protons originating in the neutron detector itself. These protons were the result of neutron collisions with the hydrogen in the plastic. In order that these neutron events not be rejected, it is necessary to ensure that the associated protons not be detected. During the polarized experiment, the neutron detectors were completely surrounded by anticoincidence scintillators and recoil protons were stopped by 1 inch plexiglass before reaching the down stream scintillator.

Each hut housed two such neutron detecting scintillators, one stacked on top of the other. The particular dimensions of each neutron detecting scintillator is given in tables $II-2$ and $II-3$, along with associated flight paths.

Table $II-2$. The neutron detectors for the unpolarized experiment. Dimensions are given as height×width×thickness.

hut angle	flight path (*meters*)	top detector (*inches*)	bottom detector (*inches*)
0°	98.89	10x40x4	10x40x4
24°	90.80	20x40x4	20x40x4
45°	74.43	20x40x4	40x40x4

Table $II-3$. The neutron detectors for the polarized experiment. Dimensions are given as height×width×thickness.

hut angle	flight path (*meters*)	top detector (*inches*)	bottom detector (*inches*)
0°	71.04	20x40x4	20x40x4
24°	71.03	20x40x4	40x40x4
45°	37.34	30x60x4	30x60x4

The length of the flight paths was more or less fixed by energy resolution requirements. Time resolution was limited to 500 picoseconds. This limitation was due to the approximately equal effects of beam pulse width, target and detector thickness, and the multiple reflections of scintillated light in the detector before collection by the photomultiplier tubes.

Detector Logic

The mere physical detection of neutrons was not sufficient for our purpose. It was necessary to exclude events due to protons or cosmic rays and to measure for each neutron event an associated time interval which could be directly related to the time of flight of the neutron from production at the target to detection in the hut approximately 90 meters away. It was also necessary to measure the signal strength from the neutron detector photomultiplier tubes. This gave a measure of the total amount of light which resulted from the event. This is essential information in determining detector efficiency and in eliminating timing ambiguity associated with sucessive beam bursts.

We first describe the electronics associated directly with the neutron detectors and charged particle anticoincidence detectors in order to understand just what sort of information came from the huts to be processed. Figure $II - 5$ is a schematic of the electronics which gathered and disseminated information from the neutron detectors.

Figure II-5. Neutron detector electronics.

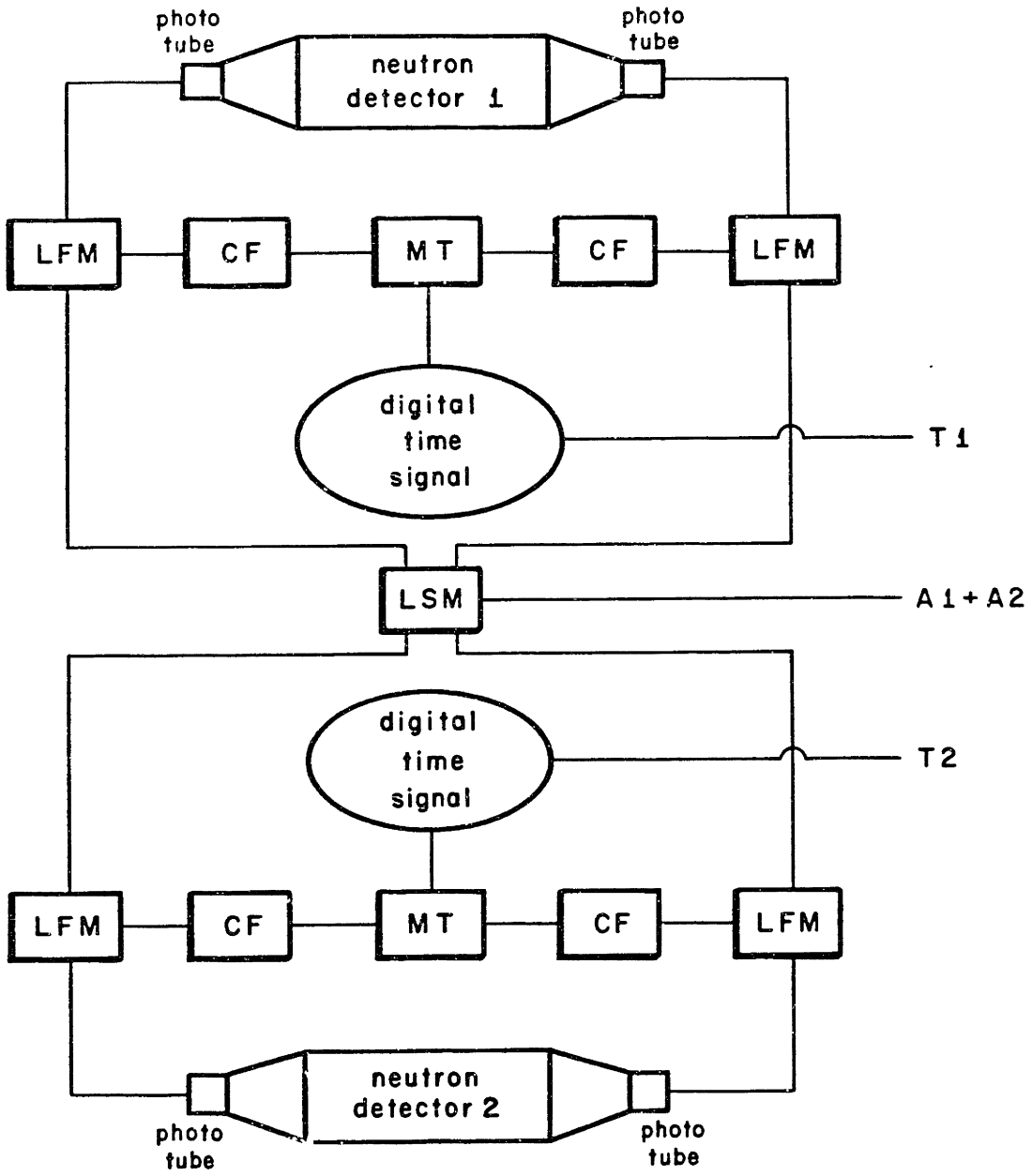

The anode signal from each photomultiplier tube was sent to a linear fanout module. A linear fanout module yields two signals, each equal in strength to the input. One of these output signals was used for timing and the other was used for measuring light intensity within the detector. The timing signal was directed to a constant fraction discriminator to produce a digital signal whose timing was independent of the signal strength. This digital signal was sent to the mean timer, the other input of which was the signal due to the other photomultiplier tube of the neutron detector. The mean timer produced from these two signals a digital pulse whose timing was independent of variations of the time between the two input signals. This property of the mean timer ensured a final timing signal which was not dependent on the location transverse to the beam of the ionizing event in the neutron detector. In this fashion each neutron detector was wired to produce a timing signal which is sent to the data taking PDP-11 computer.

The other signal from the linear fanout module was directed to a linear sum module. There was one such device in each hut. It accepted signals from both photomultiplier tubes of both neutron detectors in that hut. These signals were superimposed yielding a signal whose strength was very nearly proportional to the total light collected by the photomultiplier tubes. The calibration of this proportionality was accomplished using a source of natural gamma rays and will be described later. The summed anode signals left the linear sum module and were cabled to the data taking computer.

Also in the hut were the anticoincidence charged particle detectors. These were used to reject proton events. A typical deployment of these detectors is shown in figure $II-6$.

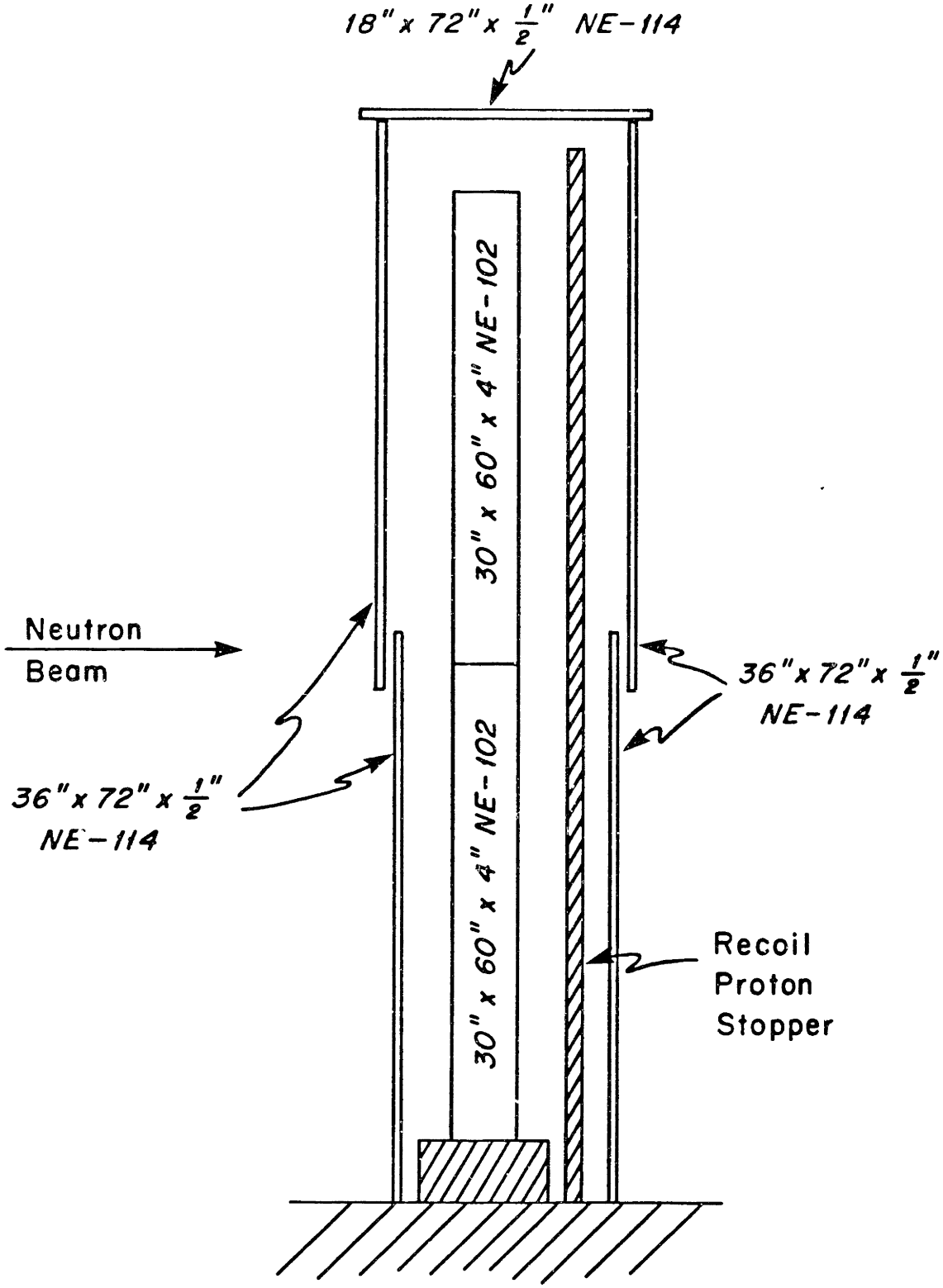

Figure II-6. Typical detector deployment.

The anode signal from each anticoincidence photomultiplier tube was sent to a constant fraction discriminator. The resulting logic signals were sent to an OR device which produced a logical signal if it received one or more signals. Outputs from this OR device left the hut for the data taking electronics located near the computer. Thus, a total of four data cables left each hut: a logic anticoincidence signal from the charged particle detectors, a summed analog signal from all neutron detector phototube anodes, and two timing logical signals, one from each neutron detector.

The Information Gathered

The objective was to get three pieces of information from each neutron event: which detector was involved, the anode signal strength, and a time of flight. This section describes how the information from each hut was used to achieve this. Figure $II-7$ is a schematic of the data taking electronics located near the computer.

Figure II-7. Data aquisition electronics.

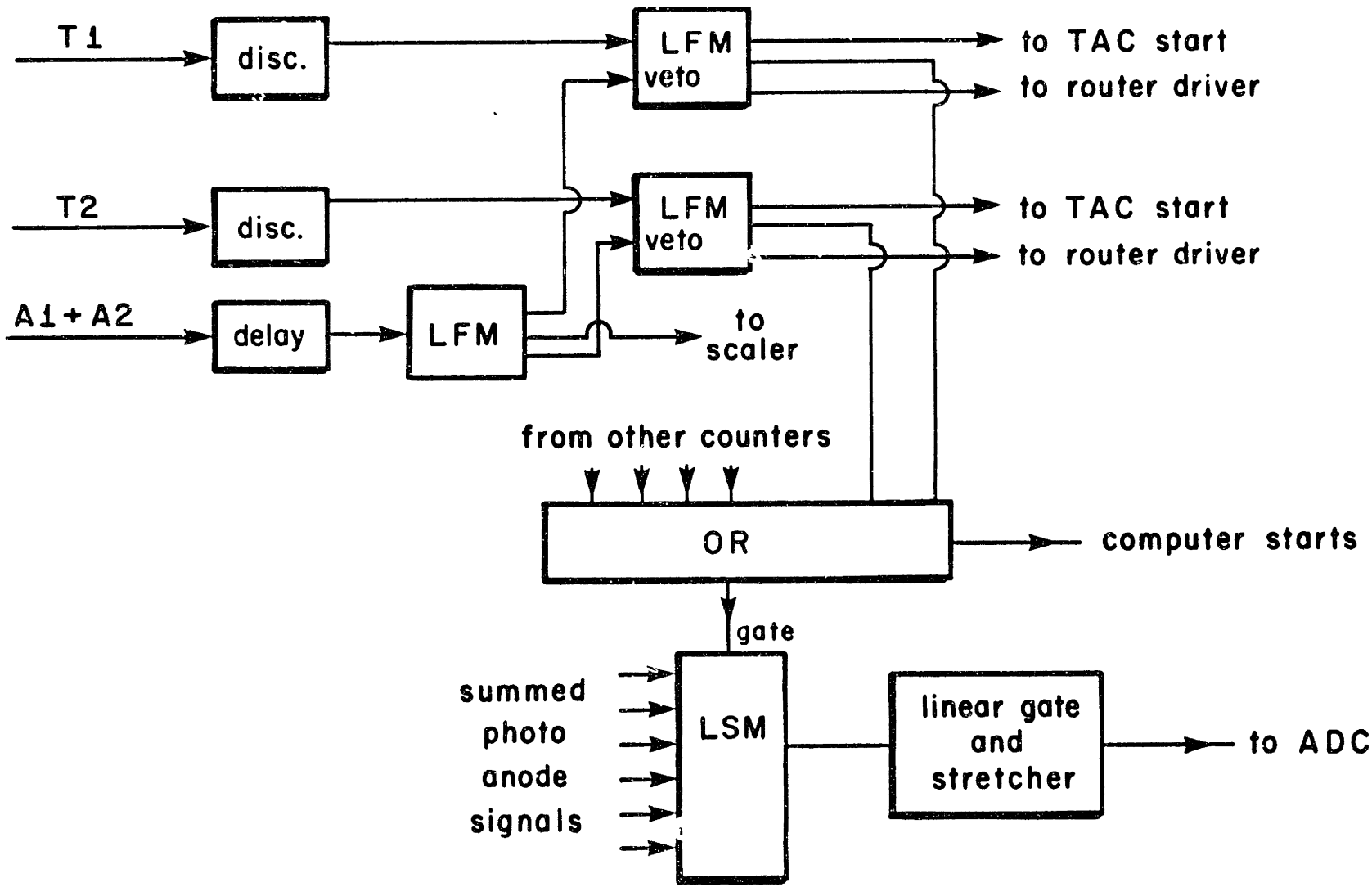

The logical signals from the anticoincidence charged particle detectors were used to veto timing signals. Each such veto was counted on a scalar. Unvetoed timing signals were split into three. One of these was used to start a time to analog converter. Another was sent to a particular module of the computer, the router driver. Depending on which input to the router driver received the signal, a particular number identifying the hut and counter was stored by the data acquisition system to be associated with the event. This number, a power of two, thus identified which detector saw the neutron. The third signal generated from the neutron detector timing signal was used to gate the linear gate and stretcher which integrated the summed anode pulses from the neutron detectors and also to start a time to analog converter. The TAC was stopped by the next signal from the phase compensation module. This module was part of a circuit which provided periodic timing signals based on the cyclotron radio frequency. The circuit essentially provided one timing signal per proton burst. Since there were many more bursts than neutron events, it was good to start the TAC with the neutron events rather than the periodic cyclotron based signal. This has no practical effect on data analysis, merely reversing the time of flight spectrum.

Thus it was arranged for the computer to recieve for every neutron event three pieces of information: 1) detector identification by means of the router driver. 2) the total anode pulse strength. 3) a particular time related linearly to the time of flight.

Phase compensation circuit

The timing signal used to stop the TAC as discussed above was based on the cyclotron radio frequency. In principle, a signal taken from each bunch by a loop just upstream of the target would be more relevant, however these signals would be weak and noisy. The problem with using the cyclotron frequency is that the transit time through the cyclotrons and to the target can drift by a few nanoseconds. The phase compensation circuit shown schematically in figure $II-8$ accounted for this drift allowing for a variable phase between the RF signal and the signal sent to stop the TAC.

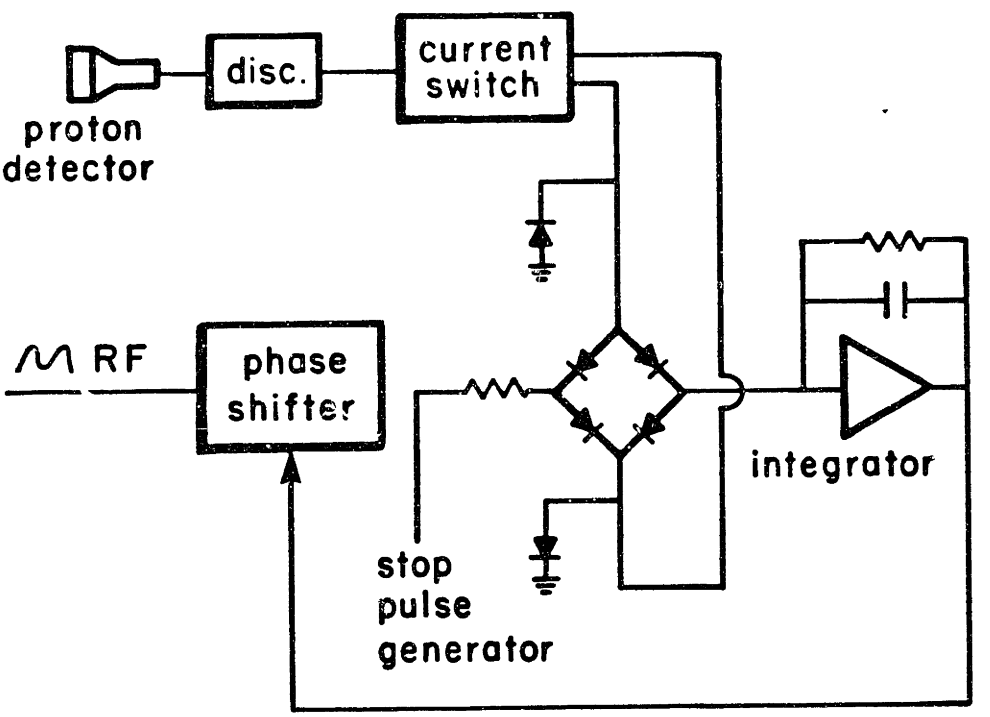

Figure II-8. Phase compensation circuit.

A small scintillator located near the target chamber monitored the actual arrival of beam bursts. Each signal from the associated discriminator opens a diode bridge current gate for a time about equal to one-half the RF period. All the while RF is entering the phase shifter and being sent therefrom to the stop pulse generator. Only when the gate is open is the diode bridge circuit effective in accumulating charge. The amount of charge accumulated depends on the phase between the RF and the period of the gate-open time. The operational amplifier integrates this with a time period containing many RF and beam burst cycles. This charge in turn effects a change of phase by means of the phase shifter. Thus gradual drifts in beam burst transit time are measured and corrections made.

Cross Sections

The general definition of the cross section for any outcome of a scattering experiment is given in terms of a single target nucleus, in this case an ^{17}O nucleus, bombarded for a period of time such that the target has been illuminated by a projectile beam of uniform areal intensity. Having counted the total number of events of the particular sort of interest and having integrated the projectile flux, the cross section for the event of interest is then given by

$$\frac{\#\ of\ events}{total\ \#\ of\ projectiles/unit\ area}$$

This definition ensures that the cross section characterizes only the reaction and is independent of beam intensity and size. The differential cross section is defined as the cross section for scattering into a particular solid angle divided by that solid angle measured in steradians. The solid angle is presumed small enough so that the cross section does not vary appreciably within that solid angle.

When using extended targets as is customary one measures the combined cross sections of every nucleus exposed to the beam. Let E be the number of events, ρ the number density of target species in the extended target, t the linear thickness of the extended target. Let Q be the total integrated beam charge of a beam of projectiles having an elementary charge e. Then the above definition of cross section is

$$\sigma = e \times \frac{E}{Q\rho t}$$

Using the symbol $\Delta\rho t$ to represent error in the knowledge of the target and like symbols for other errors, the error in the measurement of the cross section can be approximately calculated by

$$(\frac{\Delta\sigma}{\sigma})^2 = (\frac{\Delta E}{E})^2 + (\frac{\Delta Q}{Q})^2 + (\frac{\Delta\rho t}{\rho t})^2$$

The charge integration error was known from the experience of previous researchers to be less than 1%. The target thickness and abundance was known to an accuracy of 5-7%.[DEVLIN,HYN78] The rest of this chapter will detail what corrections to the raw data were necessary. These corrections included neutron attenuation, detector efficiency, and computer deadtime.

Neutron Attenuation

In this experiment the neutrons radiated from the target traversed a distance of nearly 100 meters before reaching the detectors. The distance of flights was fixed at about 100 meters due to requirements of time resolution. In order to maximize counting rate, the detectors were made as large as was possible to handle.

The neutrons were affected by material occupying the space between the target and the detector. These materials included a thin metal port of the scattering chamber, the atmosphere, divers wooden materials comprising the hut housing the detectors, and thicknesses of tape and paper covering the detectors. The scattering lengths of these various substances is given in table $II-4$ along with the percentage of neutrons which would be expected to interact with the substance in this experiment. The atmospheric effect is dominant.

Table $II-4$

material	estimated thickness present	collision length	percent interaction
aluminum	0.5 cm	22 cm	2.3%
wood	1.3 cm	97 cm	1.3%
air	90 m	447 m	20%

Unfortunately, this effect is most difficult to quantitatively understand, owing to the diversity of flight paths open to the neutron. Elastic scattering, for example, both depletes and augments the neutron beam intercepting the detector. The depletion is due to the scattering of neutrons whose undeflected path would intercept the detector. In most cases this results in the neutron missing the detector. In other cases atmospheric deflection augments the beam by causing certain neutrons, whose undeflected paths would miss the detector, to intercept the detector. Careful consideration shall show that both of these competing effects are significant. The

following discussion will describe how these and other effects were treated by means of Monte-Carlo simulation.

Atmospheric Scattering

The atmospheric disturbance of neutron flight may be considered to be entirely due to interactions with the atmospheric nuclei, neutron-electron interactions being relatively few in comparison with the nuclear interactions. For our purposes these nuclear interactions fall into the classes elastic or inelastic.

Inelastic scattering generally involves discrete energy loss readily sensible in this experiment. The smallest inelastic effect is due to nitrogen, its first excited state being at 2.3 MeV. A neutron which is detected after having been inelastically scattered will therefore have lost 2.3 MeV or more. Unless the neutron loses this energy close to the detector, the resulting loss of velocity will cause the neutron to fall outside the peak corresponding to its original energy. The energy resolution achieved was about one-half MeV. Assuming a hundred meter flight path this implies that unless the inelastic energy loss of 2.3 MeV occurs within 20 meters of the detector the neutron will fall outside its peak. Thus, roughly 80% of the neutrons exciting the 2.3 MeV state will be effectively removed from the spectrum. Only 20% will remain to be counted in the peak. Other inelastic processes may be expected to almost completely remove the neutron from the peak if not from the spectrum. From the $^{14}N(p,p')$ data of [MOA80] and [COM80] we may conclude that the 2.3 MeV state contributes less than 0.1% to the total inelastic cross section. Therefore all inelastic processes may be assumed to remove the neutron from its peak. That is, inelastic scattering may be treated as complete absorption. The mathematics of absorption is relatively simple to understand. If the average cross section, σ, for inelastic scattering by a single molecule of the atmosphere and the number density of the air, ρ, are known then one expects a fraction

$$exp(-\sigma\rho l) \qquad II-1$$

of the neutrons to travel a distance l without suffering inelastic collision.

Elastic scattering at these energies is dominated by forward scattering, decreasing the neutron's energy by no more than a few tenths of an MeV. This kinematic energy loss is not large compared to the system resolution and is of continuous distribution. It therefore does not in general prevent the neutron from showing up within a particular peak but rather redistributes it according to an energy loss no greater than the system resolution. The effect of elastic scattering is therefore of a different character than that of inelastic scattering and cannot be completely described by equation $II-1$. One could use equation $II-1$, substituting $\sigma = \sigma_{elastic}$ to determine what fraction of the neutrons escape elastic scattering. The ultimate

effect of an elastic scattering clearly depends on the particulars of the scattering event and the neutron's motion.

We may classify elastically scattered neutrons into four classes:

1) Those neutrons which were originally aimed at the detector but miss due to elastic deflection.

2) Those which were originally aimed at the detector and are elastically scattered and hit the detector.

3) Those which were not originally aimed at the detector but are elastically scattered so as to hit the detector.

4) Those which were not originally aimed at the detector and are elastically scattered and miss the detector.

The relative importance of these effects is evidently dependent on the angular distribution of elastic scattering, though we expect the second and third effects to be small unless the elastic scattering is extremely forward peaked.

It is therefore clear that in order to confidently apply a correction for atmospheric scattering, we must know the total inelastic integrated neutron cross sections, the total elastic integrated cross section, and the angular distribution for elastic scattering at forward angles. The detectors subtended less than 2° so it is certainly sufficient to accurately describe the elastic angular distribution out to 15°.

The elastic scattering was described by a single differential cross section assumed to be Gaussian with respect to the laboratory scattering angle. The width was chosen to represent the *forward angle* data at 136 MeV of van Zyl *et al* [ZYL56]. For example, the elastic differential cross section of nitrogen is well represented by

$$\sigma(\theta) = 1.7\ mb/sr\ exp\left(-\frac{1}{2}\left(\frac{\theta}{\sigma_\theta}\right)^2\right) \qquad II-2$$

with $\sigma_\theta = 8.1°$. The angular distribution for oxygen and nitrogen were not radically different so the two widths were averaged weighting each according to their normal atmospheric abundance in dry air. The effects of humidity are small. It is not necessary to describe large angle scattering accurately. Neutrons scattered into angles much greater than the angular size of the detector almost always miss the detector, independent of the details of their subsequent motion. The data of [ZYL56] at 136 MeV also indicates that the integrated elastic and inelastic cross sections for these nuclei are equal to within about 40% . This result is corroborated by other experiments [TAY53,MEA66,VOS56]. Since measurements of the total inelastic neutron cross sections of nitrogen and oxygen were unavailable, these inelastic cross sections were taken to be one-half of the total neutron cross sections reported for these elements in [MEA66]. The elastic differential cross sections given by equation $II-2$, which represents the nitrogen data of [ZYL56], when integrated over 4π gives an integrated cross section also equal to one-half the total cross section reported by [MEA66]. Therefore, it was assumed that elastic and inelastic cross sections were both equal to one-half of the total reaction cross section reported by [MEA66].

That paper reports the total cross section of various nuclei for neutrons in the energy range 80 to 150 MeV. The results relevant here are shown below.

Table $II-5$. Total neutron reaction cross sections.

Energy(MeV)	Nitrogen(mb)	Oxygen(mb)
140.9	407	451
129.4	437	497
119.6	471	537
110.0	508	581

These data were used to calculate the attenuation correction factor at the four neutron energies given. The air was assumed to consist of 78% nitrogen and 21% oxygen.

All elastic scattering was assumed to have an angular distribution proportional to the Gaussian form $exp(-\frac{1}{2}(\frac{\theta}{\sigma_\theta})^2)$ with $\sigma_\theta = 8.1°$.

The simulation makes no allowance for kinematic energy loss since the primary effect is to increase resolution. A neutron which is elastically scattered has sufficient energy remaining to place it in the same peak as a neutron which enjoyed uninhibited flight. Only in the event of repeated elastic scattering is a neutron's energy diminished sufficiently to remove it from a particular peak. In the case of 135 MeV neutrons traveling 100 meters, only about 2% are scattered more than once.

Using the code described in the next section, a multiplicative factor to correct for neutron attenuation due to atmospheric scattering was calculated. This was done at four neutron energies using the data of table II-5. The resulting attenuation correction factors were linear with respect to neutron energy. A least squares fit was performed on the results of the simulation code at these four energies to get the attenuation correction factor as a function of energy. The resulting attenuation correction factors for each hut in the cross section run are given in the formulae below.

$$\begin{aligned} factor\ for\ hut\ 1 &= 1.40 - 0.00163 \times T(MeV) \\ factor\ for\ hut\ 2 &= 1.43 - 0.00174 \times T(MeV) \\ factor\ for\ hut\ 3 &= 1.35 - 0.00138 \times T(MeV) \end{aligned} \qquad II-3$$

These formulas were used to describe the energy dependence of the neutron attenuation due to atmospheric scattering.

The algorithm described here is designed to account for these physical and geometrical effects by explicitly tracing the paths of numerous simulated neutrons generated by a random number generator. The algorithm calculates a multiplicative factor to correct for the net loss of particles due to the elastic and inelastic scattering of such radiated particles between a point source of these particles and a detector at some distance. The particle trajectories are collimated by a symmetrically placed rectangular hole a certain distance from the source and of given dimensions. The algorithm counts the number of particles whose initial trajectory would cause them to intercept a rectangular detector at some distance from the target or source.

The algorithm assumes the target, the center of the collimator, and the center of the detector to be collinear and that corresponding edges of the collimator and detector are parallel. The detector face is perpendicular to the undeflected beam. The algorithm describes the experimental geometry entirely in terms of the rectangular dimensions of the collimator and the detector and their respective distances from the target, which is assumed to be a point source of trajectories. The atmosphere is described as an ideal gas of identical scatterers.

The algorithm requires as input the detector and collimator dimensions and their distances from the hut along with the molar volume of the ideal gas. Also required are two integrated cross sections to characterize elastic and inelastic scattering along with the Gaussian width of the assumed elastic scattering distribution with respect to the laboratory scattering angle. Figure $II-9$ depicts the algorithm in schematic form.

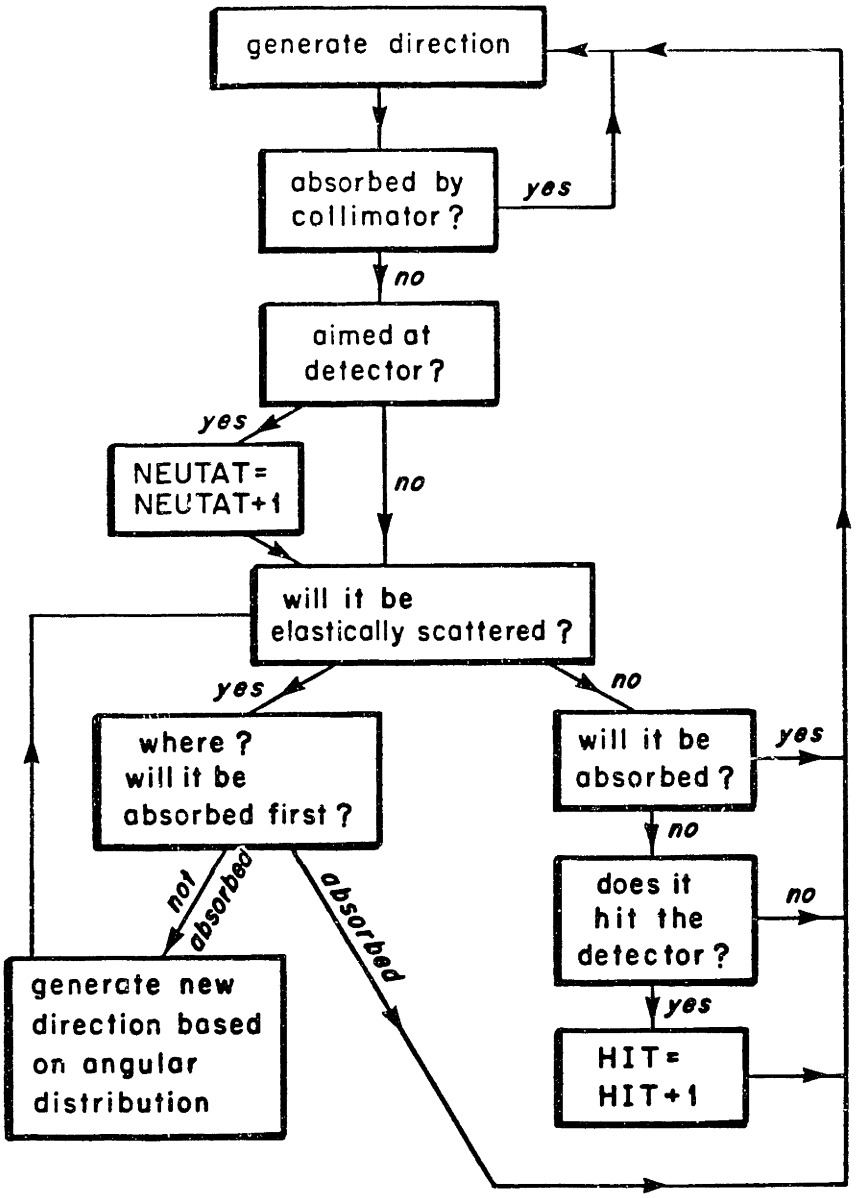

Figure II-9. The Simulation of Atmospheric Scattering.

The code picks two random numbers from zero to one and thereby determines an initial direction for the trajectory. The code produces in this way a cone of trajectories uniformly distributed in direction. This cone is chosen to be large enough to envelope the collimator completely. Most, but not all, particles generated this way pass through the collimator. For each trajectory that is not collimated, the code generates and details a complete history.

Assuming that a particle has been produced and has passed through the collimator, the code then determines whether or not its initial trajectory would cause it to intercept the detector. If so, a particular variable called NEUTAT, is incremented by one. Thus a running account is kept of those particles whose original unscattered flight would intercept the detector. The code in any case continues to detail a history for the particle *whether or not it is originally aimed at the detector.*

The code then calculates the distance to the detector *plane* and randomly determines whether or not the particle should be elastically scattered. This is done by using equation $II-1$ substituting the integrated *elastic* cross section for σ. The elastic cross section is derived from equations $II-3$. The distance to the detector plane replaces l. A random number is selected. If it happens to be greater than the value of equation $II-1$, then the neutron is to be elastically scattered. The point of elastic scattering is chosen by chosing another random number, r, and solving the equation

$$r = \frac{\sigma\rho l}{1-e^{-\sigma\rho l}} \int_0^x e^{-\sigma\rho x}\, dx \qquad II-4$$

for x, the distance traveled before scattering. It is possible that a particle might be inelastically scattered before reaching this point. Equation $II-1$ is therefore again used substituting the integrated *inelastic* cross section for σ and the path length from the target to the point of intended elastic scattering for l. A new random number is chosen and the particle's fate is determined. If it is inelastically scattered then the code begins all over again with a new particle.

If it is not to be inelastically scattered then the code generates a direction for elastic scattering using the Gaussian width given as input. A random number, r, is selected and a laboratory scattering angle, θ, is selected by solving the equation

$$r = \frac{1}{{\sigma_\theta}^2} \int_0^\theta e^{-\frac{1}{2}(\frac{\theta}{\sigma_\theta})^2} \theta\, d\theta \qquad II-5$$

for θ, where σ_θ is the Gaussian width of the forward angle elastic scattering. As mentioned earlier, this number is about 8° for 135 MeV neutrons. The approximation $sin(\theta) = \theta$ has been made. This fails only for angles larger than 30°. The Gaussian then dominates the expression so that very little error is made in assuming $sin(\theta) = \theta$ for all θ. The azimuthal direction of scattering is determined by an angle randomly selected between 0 and 2π. The new trajectory and its point of intersection with the detector plane is easily calculated by elementary vector methods. The procedure is then repeated for this new trajectory.

Thus the particle is repeatedly subjected to the possibility of elastic and inelastic scattering until finally it either passes the detector plane or is inelastically

scattered. Those particles which pass through the detector plane within the confines of the detector boundary are counted and the result stored in the variable called HIT. The ratio of NEUTAT to HIT is the desired correction factor. It permits us to simply use the solid angle subtended by the detector when calculating an experimental differential cross section.

Detector Efficiency

By far the largest correction necessary to the data was to account for detector efficiency. Not all neutrons passing through the four inch thick neutron detecting scintillators will interact with the plastic. Some which do interact will not leave sufficient light to exceed the discriminator threshold. It is also desirable to set a threshold even higher than that necessary for simple noise rejection. This is due to the fact the spectrum of neutrons from a given beam burst can be contaminated by very slow neutrons from previous beam bursts. These slower neutrons will tend to leave less light in the detector. It is therefore possible to preferentially reject these slower neutrons by increasing the anode pulse strength threshold for counting the event. Higher thresholds also mean that fewer neutrons from the immediate beam burst will be detected. Thus detector efficiency is a threshold dependent effect.

We used an efficiency code which is the result of years of experience and successive modifications. It is based on the code written by N. R. Stanton [STAN71], who based his work on a code written by Kurtz [KUR64]. The code was modified by M^{c}Naughton *et al*, [MCN74,MCN75], to obtain agreement with their own efficiency measurements. Del Guerra developed a code which included new cross sections for inelastic reactions on carbon based on his extensive compilation of those cross sections [DEL76]. Cecil *et al* added several improvements including use of relativistic kinematics and a more accurate description of light deposition by charged particles including the effects of charged particle escape [CEC79]. These improvements are described more completely in [AND79] and [CEC79].

For neutron energies below 30 MeV, the detection of neutrons is dominated by the scattering of neutrons off of atomic hydrogen in the scintillator. At higher energies the carbon (n,np) channel dominates. The energy dependence of this reaction is not well known above 50 MeV so it is parameterized to fit available efficiency measurements. The other neutron-carbon inelastic channels included are (n,2n), (n,γ), (n,3α), and (n,α).

This code incorporates the light response of the scintillator to the α rays and protons produced by the neutron interactions with the scintillator. The exact expressions used are published in [CEC79]. They are largely based on the proton measurements done by Madey *et al* [MAD78]. These authors used the T(d,n)α reaction to produce a monoenergetic neutron beam. The scintillator to be examined was placed in this beam and scattered neutrons were detected at various angles to

determine the recoil proton energy in the primary detector.

The code also includes effects due to charged particle escape from the scintillator as described in [WAT74]. All these effects are important in order to know the detector efficiency as a function of the threshold. It is also essential to know at what threshold the detectors are operating so that the results of the efficiency code can be related to their performance. This requires that the detectors be calibrated. We must know the correspondence between anode pulse strength in volts or ADC channels to the amount of light energy released in the scintillator. It is customary to express the scintillation energy deposited by a particular heavy particle in terms of MeVee, the MeV electron equivalent energy. This is the energy of a stopping electron yielding the same amount of light as the particular heavy particle of interest.

The 2.61 MeV γ rays from ThC'' were used to provide a known physical reference against which anode pulse strengths could be compared for calibration. At 2.61 MeV the dominant effect is that of Compton scattering. The electrons find it difficult to absorb so much energy, and though pair production is energetically possible, there isn't much phase space for it either. The kinematics of Compton scattering can be described by

$$1 - \cos\theta = \frac{m}{\omega_2} - \frac{m}{\omega_1} \qquad II-6$$

where θ is the scattering angle of the γ ray in the laboratory frame, m is the mass of the electron, and ω_1 and ω_2 are the initial and final energies of the γ rays in the laboratory frame. The cross section for compton scattering of a γ ray into a solid angle $d\Omega$ can be written

$$d\sigma = \frac{1}{2} r_e^2 \frac{\omega_2^2}{\omega_1^2} d\Omega \left[\frac{\omega_2}{\omega_1} + \frac{\omega_1}{\omega_2} - 2\left(\frac{m}{\omega_2} - \frac{m}{\omega_1}\right) + \left(\frac{m}{\omega_2} - \frac{m}{\omega_1}\right)^2 \right]$$

The kinematical relation $II-6$ can be used to convert this to the cross section for finding a γ having a final energy from ω_2 to $\omega_2 + d\omega_2$. This cross section is

$$d\sigma = \pi r_e^2 \frac{m}{{\omega_1}^2} d\omega_2 \left[\frac{\omega_2}{\omega_1} + \frac{\omega_1}{\omega_2} - 2\left(\frac{m}{\omega_2} - \frac{m}{\omega_1}\right) + \left(\frac{m}{\omega_2} - \frac{m}{\omega_1}\right)^2 \right] \qquad II-7$$

From energy conservation this is also evidently the cross section for finding the electron to have a kinetic energy in the range $\omega_1 - \omega_2$ to $\omega_1 - \omega_2 - d\omega_2$. Ideally this is the energy the photomultiplier anode sees. In reality there are some inefficiencies in the detection process. We estimated this effect at 5% following Knox *et al.* [KNO72]. These people investigated the position of the Compton elastic peak with respect to the pulse strength distribution from various γ ray energies including the 2.61 MeV γ from ThC''. They did this for two sizes of cylindrical hydrocarbon scintillators, the largest being 3'' in diameter and 3'' high. The Compton electrons travel no farther than about one-half an inch before stopping so there should be little effect due to electron loss. Knox *et al* indeed obtained almost the same result with a 2'' by 2'' scintillator.

In any case equation $II-7$ can be used to establish which energy of Compton electron would be most plentiful. Figure $II-10$ shows how the quantity $\frac{m}{r_e^2}\frac{d\sigma}{d\omega_2}$ depends on the final γ energy with an initial γ energy of 2.61 MeV. Clearly the γ rays of lowest energy are favored. These correspond to the highest energy electrons. This maximum electron kinetic energy is given by the kinematic expression

$$\frac{2\omega_1}{2+\frac{m}{\omega_1}}$$

This relation can be gotten from equation $II-6$ and energy conservation. In the case of the 2.61 MeV γ rays from ThC″ the maximum possible electron kinetic energy is 2.38 MeV. Since this is also the most plentiful of electron energies there will be a peak in the anode pulse height spectrum corresponding to this amount of light. Other calibration points were obtained simply amplifying the ThC″ signal. This method assumes that the detector response is linear with respect to electron energy [HOP51]. It is unfortunate that data replays must be done with thresholds corresponding to 40 or 50 MeVee in order to minimize overlap neutrons. Such a high threshold is far away from naturally available calibration γ rays and must be viewed warily when assigning probable errors to final results [WAT83].

After such a calibration is accomplished, one has some idea how much light must be created by charged particles in the scintillator in order to produce any particular anode pulse strength in terms of ADC channel number. Figure $II-11$ shows the calibration curve for one particular detector used in this experiment.

As mentioned earlier, the light response is measured here in terms of detector response to electrons of particular energies. Neutrons penetrating the detectors sometimes interacted with the hydrogen and carbon nuclei of the scintillator plastic to produce charged particles, mainly protons and α rays. It was the light produced by these protons and α rays which was detected. The conversion to electron equivalent energy using the methods mentioned above [CEC79] is done in the code and completes the calibration of the efficiency as a function of threshold.

Most data analysis was done using a threshold of 40 MeVee. For any threshold the efficiency is a function of neutron energy. Figure $II-12$ shows the efficiency for a particular detector as a function of neutron energy when the threshold is set at 40 MeVee. Cross sections quoted in this work incorporate the dependence of detector efficiency on neutron energy.

Figure II-10. Compton scattering energy distribution with respect to final γ energy as a function of final γ energy.
Initial γ energy = 2.61 MeV.

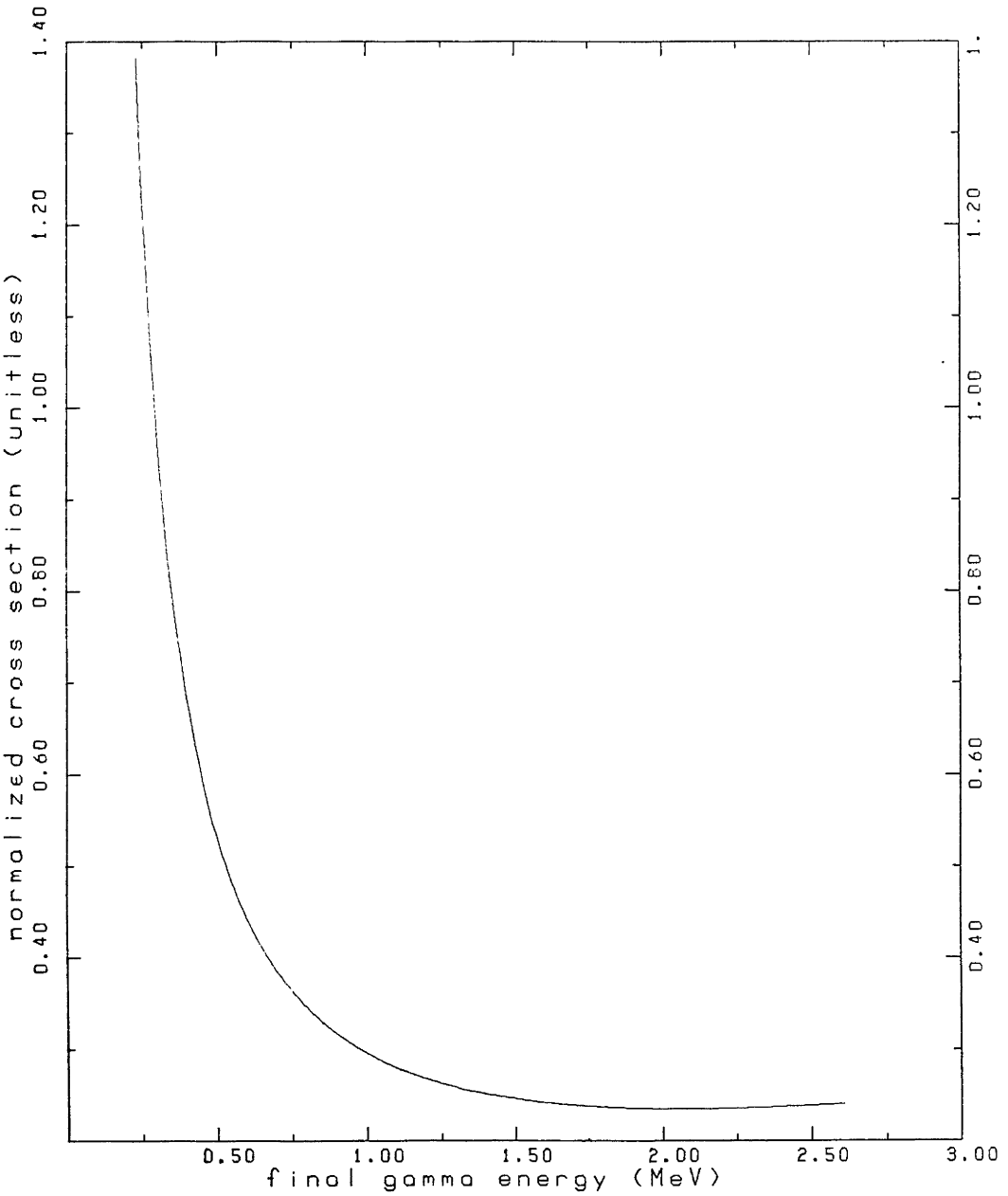

Figure II-11. Anode pulse strength calibration curve for a 10″x40″x4″ detector used in the cross section run.

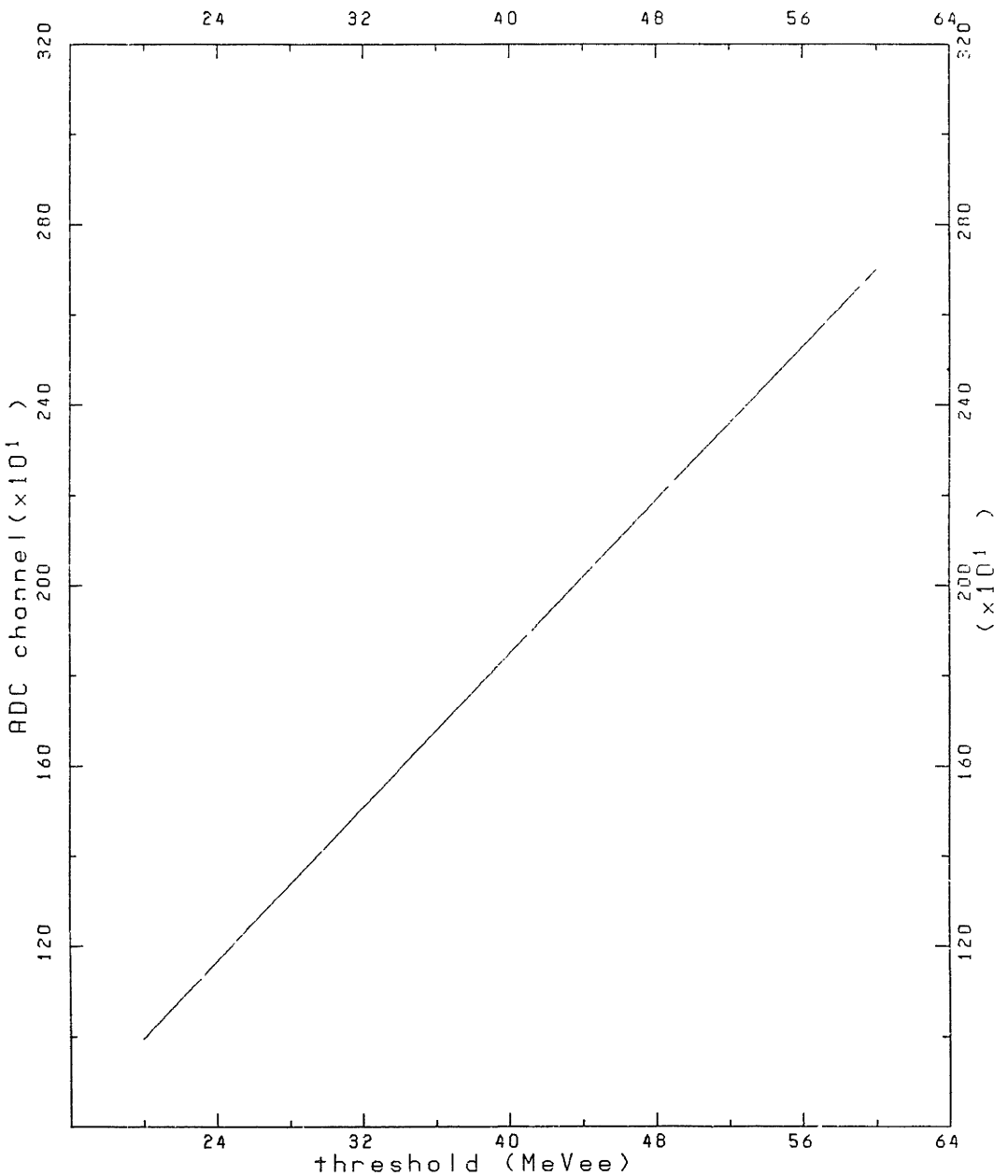

Figure II-12. Neutron detector efficiency as a function of neutron energy for a 10″ x 40″ x 4″ detector with a threshold of 40 MeVee.

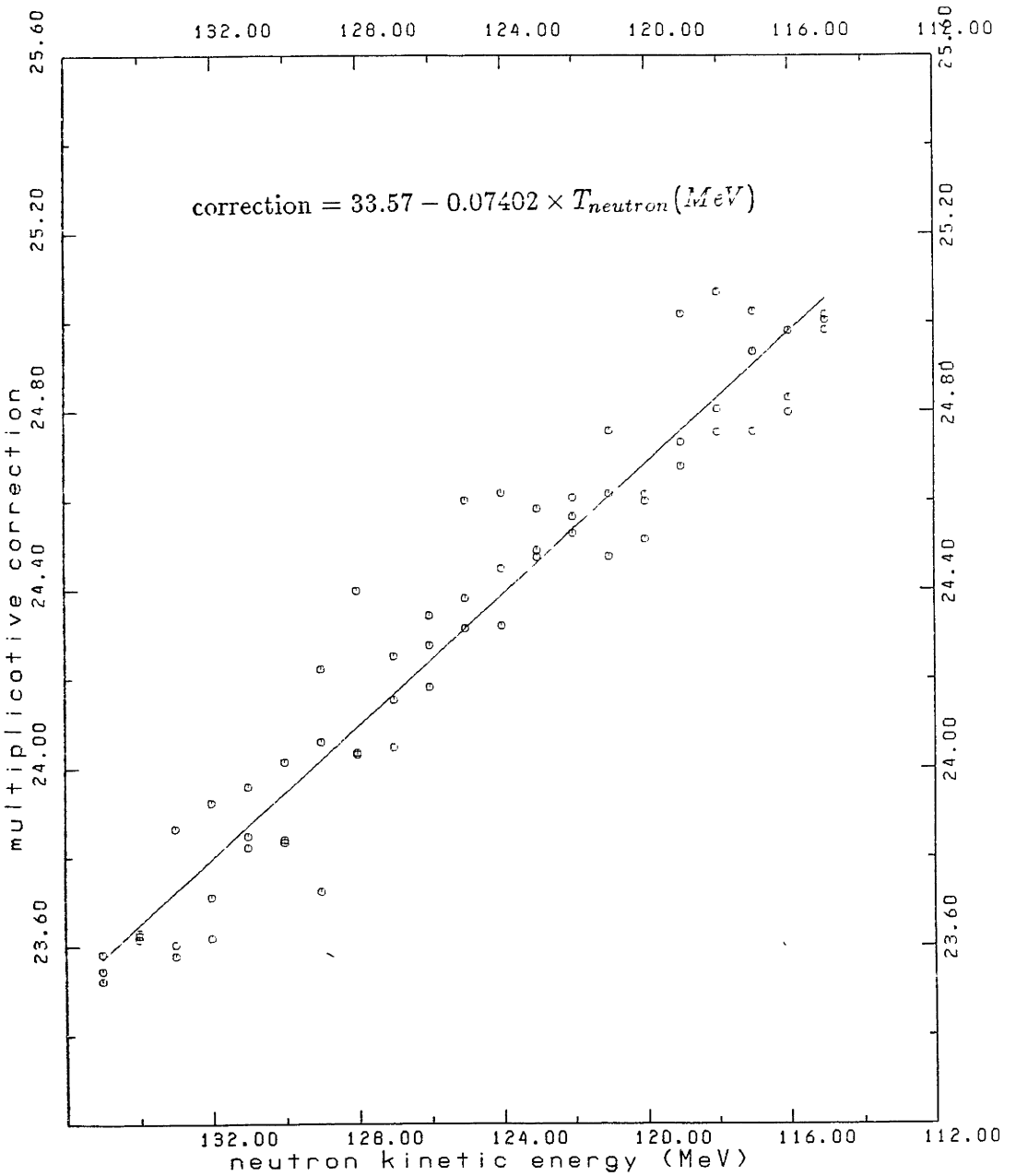

Computer Deadtime

Every time a neutron detector photomultiplier anode produced a signal exceeding the discriminator threshold and there was no veto from the charged particle detector this anode signal was sent to the data aquisition electronics located near the computer. Each such signal was counted on a scaler and also was sent to the linear gate and stretcher which enabled the ADCs to digitize the pulse amplitudes. If the computer was busy with an event then the signal was lost, lost but accounted for by the scalar. By comparing the number of events counted to the number analyzed and stored on tape (all of which were also counted) we can estimate the computer dead time.

$$\text{dead time} = \frac{\text{number of anode signals counted}}{\text{number of events stored on tape}}$$

There was also the case of overlapping events from different detectors which arrived too nearly at the same time to be distinguished by the electronics hardware. In these cases both events produced timing signals which entered the router driver and produced anode signals which were digitized as one pulse strength. These were recorded on the tape as events whose detector identifier was the sum of the two detectors involved. These identifier could not be confused with single neutron events and so there was no data contamination. These sort of events proved to be negligible in number.

Spectrum Analysis

The final result of an experimental run or data replay was a time of flight spectrum including all those events whose pulse strength met the particular threshold requirement in use. Figure $III-13$ shows the time of flight spectrum at 0° scattering angle for the (p,n) reaction on the $Be^{17}O$ target. In Figure $III-13$ channels are related to excitation energy assuming only the kinematics for A=17. As a result, the states of ^{9}B and ^{18}F are misplaced. The line shape analysis is properly carried out in the time of flight spectrum with the kinematics of each species that is in the target. Figure $III-14$ shows the neutron time of flight spectrum at 0° for the pure Beryllium target. The abscissa has been converted from time of flight channels to the excitation energy of Boron. The lineshapes were derived using the code ALLFIT developed by this group. The latest version compiled by James Kelly and Charles Hyde-Wright was used [HYD84]. This code has a plethora of lineshape features and calculational options, most of which were not used for this analysis.

The lineshape used for the narrow states in the spectrum depicted in figures

$III-13$ and $III-14$ is of the form

$$\begin{cases} f_L \cdot H \cdot e^{-\lambda_L \cdot \frac{(p-x-m_L)}{w_L})} & x < p - m_L \\ H \cdot e^{-\left|\frac{(p-x)}{\kappa_\gamma w_L}\right|^\gamma} & p - m_L < x < p \\ H \cdot e^{-\left|\frac{(x-p)}{\kappa_\gamma w_R}\right|^\gamma} & p < x < p + m_R \\ f_R \cdot H \cdot e^{-\lambda_R \cdot (\frac{x-p-m_R}{w_R})^\mu} & p + m_R < x \end{cases}$$

Where

$$\begin{aligned} w_L &= w(1-\alpha) \\ w_R &= w(1+\alpha) \\ \kappa_\gamma &= 0.5(\ln 2)^{-1/\gamma} \\ m_{R,L} &= \kappa_\gamma w_{R,L}(-\ln f_{R,L})^{1/\gamma} \end{aligned}$$

The external parameters used were

$$H, p, w, \alpha, \gamma, f_L, \lambda_L, f_R, \lambda_R, \mu$$

which have the meanings

$$\begin{aligned} H &= \text{peak height} \\ p &= \text{peak position} \\ w &= \text{peak full width at half maximum} \\ \lambda_L &= \text{left slope} \\ m_L &= \text{left match point} \\ f_L &= \text{left match fraction} \\ \lambda_R &= \text{right slope} \\ m_R &= \text{right match point} \\ f_R &= \text{right match fraction} \\ \alpha &= \text{asymmetry} \\ \gamma &= \text{exponent} \\ \mu &= \text{exponent} \end{aligned}$$

This lineshape function attempts to describe a peak as an asymmetric hypergaussian with variable exponent in the central region and with exponentially decaying tails in the low and high excitation (high and low neutron energy) regions. The widths of the line shape, given by w and α, and the peak position p and height H were generally varied in a fit. The tails describe the lineshape when the height of the lineshape on the left or right side of the peak falls respectively to the fraction f_L or f_R of the peak height H. The match point m_R or m_L denotes the distance from the peak position at which the peak falls to a fraction f_R or f_L of the peak

height H. The variable x and other kinematic scale parameters could be entered in terms of the Q value due to calibration schemes internal to ALLFIT.

The statistical errors in lineshape fitting are accurately handled by ALLFIT assuming Poisson distributions. Certain details of the linefitting procedures will be discussed in chapter *III*.

The Energy Scale

In order to identify the excited states it was necessary to interpret the time of flight spectra in terms of neutron velocity or energy. The time of flight channel number was provided by a TAC-ADC combination which was calibrated simply by timing signal propagation through cables of varying lengths of known impedance. As was discussed earlier, the time delay measured in the experiment was not equal to the actual time of flight but was linearly related. Since the inverse velocity (v^{-1}) of the neutron is linearly related to the actual time of flight, it follows that there is a linear correspondence between TAC-ADC channel number and inverse velocity of the neutron.

This correspondence was determined by two semi-independent methods. The lineshape code is designed to calculate this correspondence using the fact that the inverse velocity of the neutron is linearly related to the time of flight channel number. In addition to incident proton energy and neutron production angle, the fitting code is given the channel number of two known states. The inverse velocity is precisely calculated from kinematics and the linear relationship between time of flight channel number and inverse velocity is thereby determined. The ALLFIT results were compared to another kinematic calculation which made use of the TAC calibration and the flight paths. This method requires as input the proton energy, the neutron production angle, and the channel number of only one state in the spectrum. This information essentially determines the constant time offset between neutron detection and the TAC start. These two methods were found to agree to better than 0.1 MeV over a range of 18 MeV of neutron energies.

Finite Detector Effects

The theoretical quantity of interest is a cross section for scattering into an infinitesimal solid angle at various scattering angles, the so called differential cross section. Actually finite detectors must be used to achieve finite counting rates. This means that the quantity actually measured is an average of the differential cross

sections over all solid angles subtended by the detector. For scattering angles away from 0° the cross section is monotonically decreasing. The linear approximation is very good over the angular extension of any detector used in this experiment, so that the cross section at the center of the detector is very nearly equal to the average cross section measured by the detector.

For 0° scattering the measured result is smaller than the differential cross section at precisely 0°. This correction was done by using a DWBA calculation to estimate the angular dependence of the differential cross section for (p,n) scattering to the ground state of ^{17}O. The calculated cross sections at 0° and 3° were used to get a linear approximation which amounted to a differential cross section decrease of 0.22 mb/sr per degree of scattering angle away from zero degrees. This linear approximation has the effect of slightly over estimating the needed correction. Even so, the correction estimated in this way turns out to be an effect of less than 2% and was neglected.

Summary of corrections and uncertainties

This chapter has discussed the various manipulations and corrections necessary in order to convert the number of observed events as obtained from line shape analysis to an estimate of the actual number of events which occurred. These correction factors are summarized below along with a typical value for each. Each of these factors multiply the raw cross section derived from the peak areas obtained from line shape analysis.

Table $II-6$. Typical correction factors and their uncertainties.

physical effect	typical correction factor
air scattering	1.15 ± 0.01
detector efficiency	$25. \pm 2.5$
computer deadtime	1.1

The estimated uncertainty in the air scattering correction includes the possibility that the elastic and inelastic cross sections may differ by 40%. This possibility contributes less than $\pm$ 0.01 uncertainty. The neutron attenuation in air depends

mainly on the total cross section which is known to about 3%. Also included is a possible variation in atmospheric pressure of 1″ Hg. Uncertainties due to relative humidity are negligible.

The uncertainty in calculated detector efficiencies has been extensively studied by other workers who have compared the prediction of the efficiency code with experimentally determined neutron detector efficiencies [AND79,DEB79,CEC79]. These comparisons indicate agreement between measured and calculated efficiencies to within about 10% [WAT83]. The uncertainty in event correction is seen to be dominated by this uncertainty in determining the detector efficiency.

There are also other factors which go into producing a final cross section such as total integrated charge, the solid angle intercepted, and the target thickness and stoicheometry. The uncertainties associated with these various factors are listed below. The entry "event correction" refers to the total correction factor explained above and detailed in table III-1. The uncertainties represent percent uncertainties in final cross sections.

Table $II-7$. Cross section factors and their uncertainties.

multiplicative factor	typical estimated uncertainty
event correction	10%
target properties	5%
lineshape analysis	1-20%

The target uncertainty is based on the electron scattering work of Hynes [HYN78] and refers to variations in abundance over differing locations on the target.

As mentioned in the previous chapter, lineshape uncertainies were calculated by the fitting code and included both statistical uncertainty and uncertainty due to ignorance of the true lineshape.

All these uncertainties conspire to introduce about 11% uncertainty in final cross sections. In some cases the uncertainties are greater. This is due to the limitations of the lineshape analysis in certain spectra.

Comparison with previous results

Limited $^{12}C(p,n)$ data were taken which could be compared to previous measurements in this energy region in order to provide a check on the final results of the data analysis. This comparison provides a check on the overall data analysis including the rather sizable correction for detector efficiency.

Figure $III-1$ shows the $^{12}C(p,n)^{12}N_{g.s.}$ spectrum and fit at 0°. The ground state peak of ^{12}N is afflicted by a tail whose origin is not known. Since the ground state ^{9}B also has such a tail, discussed later, it was conjectured that the tail is general feature of kinematic origin. For example, the monotonically decreasing angular dependence of the neutron energy convolved over the finite solid angle of the detector might be expected to give such a tail. Quantative considerations rule this out. The detector at 0° subtended an angle of about 0.6°. The energy difference over this angle corresponds to less than one channel in the spectrum. It is possible that this tail is due to the reaction $^{12}C(p,pn)$. The particle threshold for proton emission from ^{12}N lies only 0.6 MeV above the ground state of ^{12}N which is just where the tail is. This idea could not be tested. Since the origin of this tail is not known, the area of the tail must be considered in assigning uncertainties to the cross section for this reaction. The area of this tail was estimated by fitting the ^{12}N ground state peak using a symmetric shape along with a peak to simulate the tail as shown in figure $III-1$. The area of the smaller peak shown in figure $III-1$ is 3% that of the main peak. Thus, the uncertainty in cross section is dominated by the 10% uncertainty in detector efficiency. We measured the $^{12}C(p,n)^{12}N_{g.s.}$ differential cross section at 0° to be 5.41 ± 0.6 mb/sr. Unlike the ^{9}B and ^{17}F cross section results quoted later, the uncertainty estimate here of ± 0.6 mb/sr includes the uncertainty associated with the detector efficiency in quadrature with other uncertainties.

Rapaport et al [RAP81] measured the $^{12}C(p,n)^{12}N_{g.s.}$ differential cross section at 120, 160, and 200 MeV. Their results at 0° are shown in figure $III-2$ along with the measurement reported here. The uncertainties in these results also include the uncertainty of detector efficiency. The detector efficiency was measured using the lithium activation method [SCH77,GOU79]. Interpolating their results, we expect a 0° differential cross section of about 6.6 ± 0.7 mb/sr, which is about 20% greater than our result. However, the result is consistent within the quoted errors of the measurement. This comparison is also in fair agreement with the conclusions of [WAT83] who find that the lithium activation method yields efficiencies for medium energy neutrons that are consistently smaller than efficiencies calculated by means of the efficiency code of [CEC79] employed in this thesis. Accordingly, the cross sections reported using the lithium activation method were found to be about 30%

greater than those measured in experiments using this efficiency code. The fact that the authors of [WAT83] report a 30% difference whereas we obtain only a 20% difference can be attributed to a difference in handling atmospheric effects. For their measurement of $^{12}C(p,n)^{12}N_{gs}$ at 135 MeV, the collaborators of [WAT83] used a factor of 1.1 to correct for loss of neutrons enroute to the detectors due to atmospheric scattering. We find, however, that for the experimental conditions which existed at that time a factor of 1.18 describes this neutron loss more closely. This factor of 1.18 was calculated using a Monte Carlo code described in chapter II.

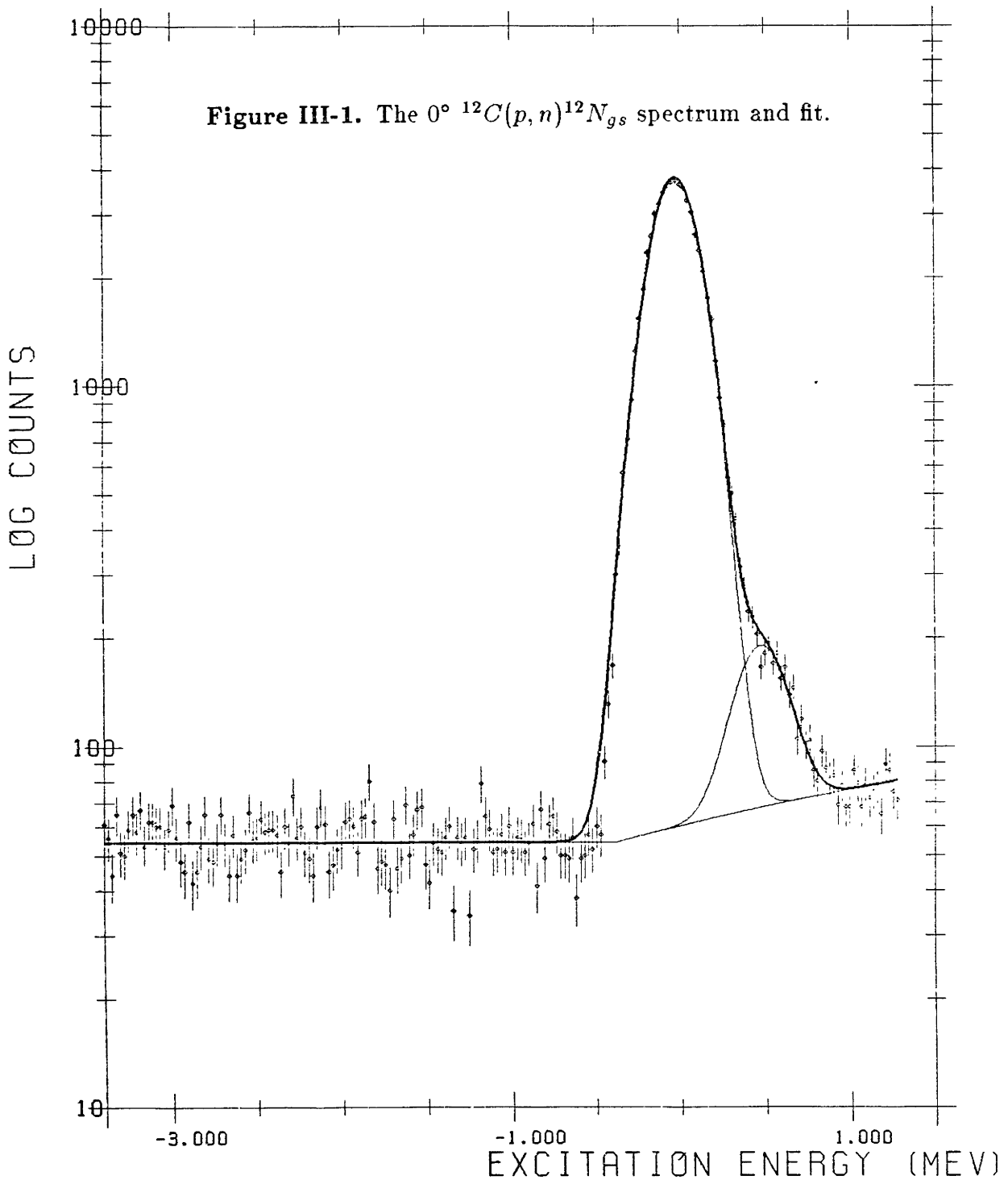

Figure III-1. The 0° $^{12}C(p,n)^{12}N_{gs}$ spectrum and fit.

Figure III-2. 0° differential cross section measurements of Rapaport *et al* for $^{12}C(p,n)^{12}N_{g.s.}$ at 120, 160, and 200 MeV. The result of this measurement is indicated by a triangle.

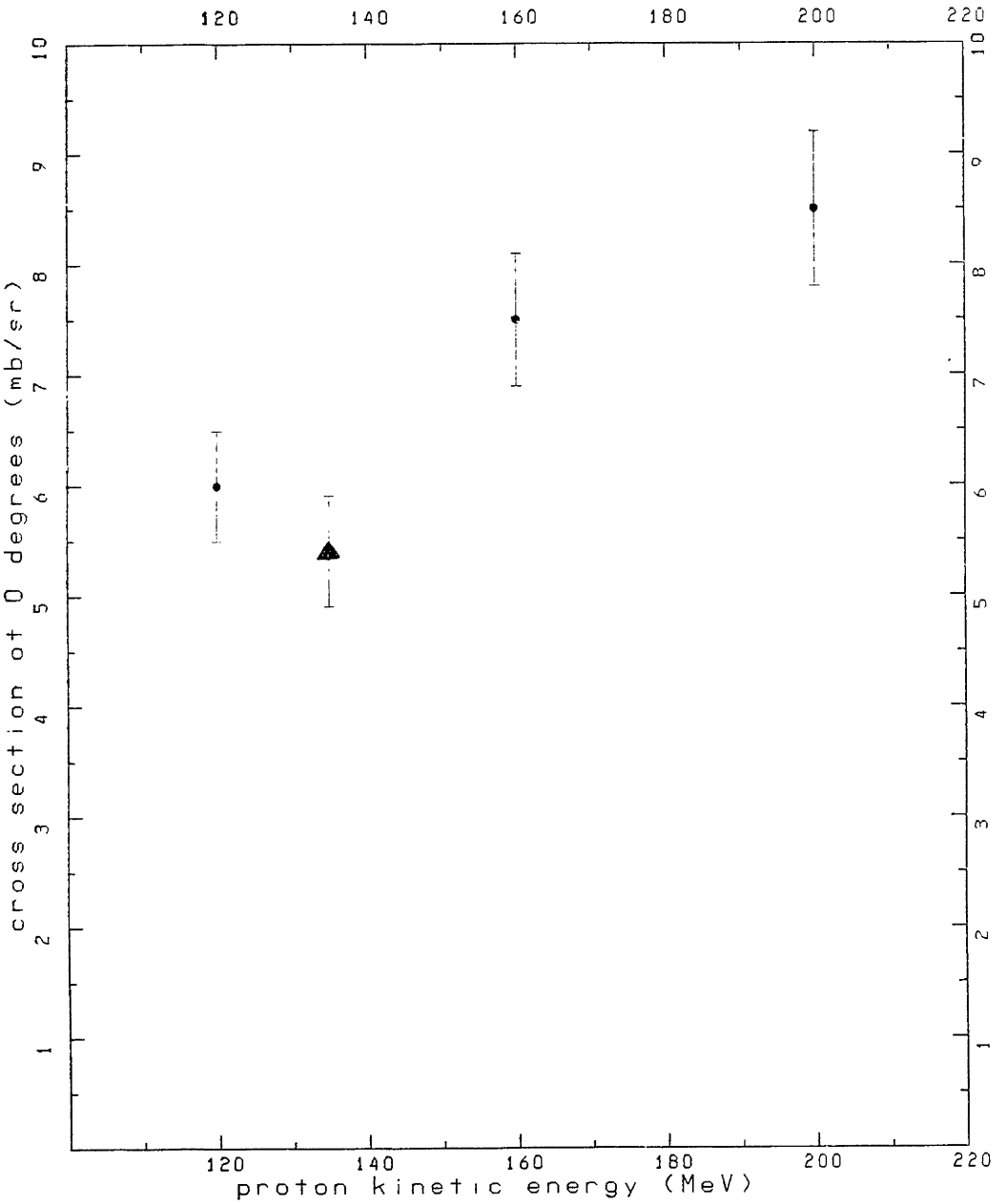

Also given in [WAT83] are the results of DWIA calculations for $^{12}C(p,n)^{12}N_{g.s.}$ including the 0° differential cross section at 135 MeV. Their calculation utilized the effective interaction of Love and Franey [LOV81], optical potentials from Comfort and Karp [COM80], and wave functions from Cohen and Kurath [COH67]. The resulting cross section was 5.2 mb/sr, 4% less than our measured value.

Rapaport et al [RAP81] also report a DWBA calculation that fits their data and the $^{12}C(p,p')^{12}C_{15.1}$ data of Comfort et al [COM80] out to 30°. If isospin is conserved, the differential cross section for $^{12}C(p,p')^{12}C$ leading to the $T=1$ state at 15.11 MeV is half of the $^{12}C(p,n)^{12}N_{g.s.}$ differential cross section. The DWBA calculation depicted graphically in [RAP81] is about 5.2 mb/sr at 0° for 120 MeV. Interpolating this result using figure $III-2$ one expects about 5.8 mb/sr for the 0° differential cross section at 135 MeV. This agrees with our result to within 7% .

It is also of interest to relate the 0° differential cross section for $^{17}O(p,n)^{17}F_{g.s.}$ reported in this thesis to the work of Goodman *et al* concerning the use of the (p,n) reaction in measuring Gamow-Teller strength [GOOD80]. In [GOOD80] Goodman pointed out that the $0°(p,n)$ cross section provides a fairly direct measure of the Gamow-Teller matrix element for β decay. This is because the (p,n) reaction selects the isovector parts of the effective nucleon-nucleon interaction and at small momentum transfer the central parts of the force dominate. This leaves only the isovector spin independent and the isovector spin dependent forces which have the same isospin symmetry properties as the Fermi and Gamow-Teller matrix elements respectively.

With these simplifications the 0° differential cross section for (p,n) reactions can be written [GOOD80,SAT64]

$$\sigma(\theta=0°)=\left(\frac{\mu}{\pi\hbar^2}\right)^2\frac{k_f}{k_i}\left[N_\tau^D|J_\tau M_F|^2+N_{\sigma\tau}^D|J_{\sigma\tau}M_{GT}|^2\right] \qquad III-1$$

where J_τ and $J_{\sigma\tau}$ are the magnitudes of the volume integrals of the $q=0$ components of the spin independent and effective spin dependent isovector central parts of the effective nucleon-nucleon interaction. μ is the reduced energy of the collision in the center of mass. In the case of $^{17}O(p,n)$ at 135 MeV μ =994.1 MeV. The factors N_τ^D and $N_{\sigma\tau}^D$ account for distortion and are generally calculated using an optical model. M_F and M_{GT} are the Fermi and Gamow-Teller matrix elements according to the convention of Bohr and Mottelson,

$$M_F=\left(\frac{1}{\sqrt{2J_i+1}}\right)\langle J_f \parallel T_- \parallel J_i\rangle$$

$$M_{GT}=\left(\frac{1}{\sqrt{2J_i+1}}\right)\langle J_f \parallel \sum_k t_-(k)\sigma(k) \parallel J_i\rangle$$

Using this convention the transition rate for allowed β decay is [GOOD80]

$$6200/ft=M_F^2+1.5M_{GT}^2 \qquad III-2$$

For the case of the $^{17}O(p,n)$ reaction leading to the ground state of ^{17}F these matrix elements are simply calculated according to the single particle picture to be

$$|M_F|^2 = |\langle \mathbf{1} \rangle|^2 = 1$$

$$|M_{GT}|^2 = \left(\frac{1}{2(2J_i+1)}\right) \sum_{\chi_i,\chi_f=\downarrow}^{\uparrow} \sum_{m_i=-\frac{5}{2}}^{\frac{5}{2}} \sum_{m_f=-\frac{5}{2}}^{\frac{5}{2}} |\langle \chi_f d_{\frac{5}{2}} m_f | \sigma_p \cdot \sigma_t | \chi_i d_{\frac{5}{2}} m_i \rangle|^2$$

$$= \frac{1}{12} \times \frac{84}{5} = \frac{7}{5} = 1.4 \qquad III-3$$

where χ_i and χ_f represent spin projections of the projectile. σ_p and σ_t operate on the projectile and target nucleons respectively. The matrix elements and summations were done explicitly by constructing normalized angular momentum states, a simple albeit tedious method.

The observed half life of ^{17}F against β decay to the ground state of ^{17}O is 64.49 ± 0.16 seconds [AJZ82] which corresponds to $\log ft = 3.488 \pm 0.001$. Using this information in equation $III-2$ indicates that both single particle matrix elements cannot correspond to the facts. If we adopt the assumption that the single particle Fermi matrix element is reliable then equation $III-2$ indicates that $|M_{GT}|^2 = 0.677$. This is about 50% smaller than the single particle prediction of equation $III-3$.

According to [GOOD80], the $0^\circ(p,n)$ cross sections at 120 MeV and β decay rates for several nuclei in the mass range $7 \leq A \leq 27$ can be best correlated by using the nuclear force volume integrals $J_\tau = 89 MeV fm^3$ and $J_{\sigma\tau} = 168 MeV fm^3$. In order to extrapolate this result to 135 MeV we may use the results of [TAD81] concerning the energy dependence of the ratio $J_{\sigma\tau}/J_\tau$. According to this work this ratio at 135 MeV has the value given by

$$\frac{J_{\sigma\tau}}{J_\tau} \times \sqrt{\frac{N^D_{\sigma\tau}}{N^D_\tau}} \approx 2.5$$

Since J_τ is almost constant at these energies, we use Goodman's value of J_τ to find $J_{\sigma\tau}$. The distortion factors N^D_τ and $N^D_{\sigma\tau}$ were calculated by comparing the results of a DWA and BA calculation of the cross section [PET85]. The distortion factors obtained agree with the eikonal motivated parameterization of [GOOD80] to within 10%. The result is $J_{\sigma\tau} = 194 Mevfm^3$.

Substituting $J_\tau = 89 MeV fm^3$ and $J_{\sigma\tau} = 194 Mevfm^3$ into equation $III-1$, we obtain

$$\sigma(\theta = 0°) = \left(\frac{\mu}{\pi\hbar^2}\right)^2 \frac{k_f}{k_i}\left[N_\tau^D |J_\tau \mathcal{M}_F|^2 + N_{\sigma\tau}^D |J_{\sigma\tau}\mathcal{M}_{GT}|^2\right]$$

$$= \left(\frac{994MeV}{\pi(197MeV\,fm)^2}\right)^2$$

$$\times \left[0.353 \times (89MeV\,fm^3)^2 + 0.463 \times (194MeV\,fm^3)^2 \times 0.677\right]$$

$$= 9.9mb/sr$$

This represents the predicted $^{17}O(p,n)^{17}F_{g.s.}$ differential cross section at 0° based on the parameterization of [GOOD80]. The fact that this result is 12% higher than the value measured in this experiment can be at least partially understood by considering that Goodman's measured cross sections were obtained using the lithium activation method and therefore are about 20% greater than those that would be measured using the detector efficiency code used in this experiment [WAT83]. Thus the nuclear volume integral J_τ would be correspondingly larger. We may correct for this by multiplying the above prediction by 0.8. The result is 7.9 mb/sr. The measured value is 8.4 mb/sr, which agrees within the 10% uncertainty in detector efficiency.

We may conclude that the measured 0° $^{17}O(p,n)^{17}F_{g.s.}$ cross section is consistent with the β decay rate of ^{17}F and provides a measure of the Gamow-Teller matrix element of a transition to within the experimental uncertainty.

The Observed ^9F States

The states seen in this measurement of the $^9Be(p,n)^9B$ reaction are listed in table $III-1$. A blank space in the width column means that the width of the state was too small to be discernible with our experimental resolution. System resolution was typically 300 to 400 keV. For comparision table $III-2$ lists the states of ^9B according to recent compilations [AJZ79,LED78]. Also included is a state at 4.1 MeV reported by [SAJ60,BAI64,SLO67] using the (p,n) reaction at energies of 20 MeV and less. The $^9Be(p,n)^9B$ cross section and analyzing power measurements reported here are shown graphically in figures $III-17$ to $III-33$. These results are tabulated numerically in the appendix. The appendix also details the correspondence between the scattering angle in the center of mass frame and momentum transfer.

The next few sections explain the manner in which peak areas were derived from the spectra by line shape analysis using the code ALLFIT described in chapter II. In most cases the uncertainties quoted for cross sections are those determined

by ALLFIT using the error matrix method described in [BEV69]. In a few cases special considerations were necessary in estimating uncertainties. These cases will be described below as they arise.

It should be emphasized that the cross section uncertainties quoted do not include the uncertainty in the detector efficiencies. As discussed in chapter II, this uncertainty is estimated to be 10% and applies systematically to all cross section data.

The ground state of ^9B

The cross section for the $^9Be(p,n)$ reaction leading to the ground state of ^9B is displayed in figure $III-17$. The spectrum and line fit at 0° is shown in figure $III-3$.

The ground state of ^9B seems to change its shape with angle. The high excitation energy side has a tail at forward angles which makes it asymmetric. This effect varies with angle. The most extreme case is at 9°, which corresponds to a momentum transfer $q = 0.413\ fm^{-1}$. This case is shown in figure $III-4$. While it is conceivable that this effect is due to a nearly degenerate state, this could not be determined from the data. A degenerate state is not expected from the structure of ^9Be, the analog nucleus. In all cases it was possible to fit the data with only one peak which had an exponential tail on the high excitation energy side. Another possibility is that this shape is due to influence of different reactions. The reaction $p + ^9Be \rightarrow n + ^9B$ has $Q = -1.851$ MeV. The reaction $p + ^9Be \rightarrow n + p + ^8Be$ has $Q = -1.665$ MeV. The reaction $p + ^9Be \rightarrow n + p + 2\alpha$ has $Q = -1.573$ MeV. Perhaps these other reactions contribute to the shape of the ^9B ground state.

In any case, the asymmetric tail of this peak remains a mystery and this must be considered in assigning uncertainties to the cross sections measured for this state. The area of this tail was estimated by fitting the ^9B ground state using a symmetric shape along with one or two peaks as necessary to simulate the asymmetry (figure $III-5$). The area of these additional peaks were taken to contribute to the uncertainty of the cross section of this state. The area of the tail determined in this way was generally less than 5% of the total peak area. However, at 9° it was about 20%.

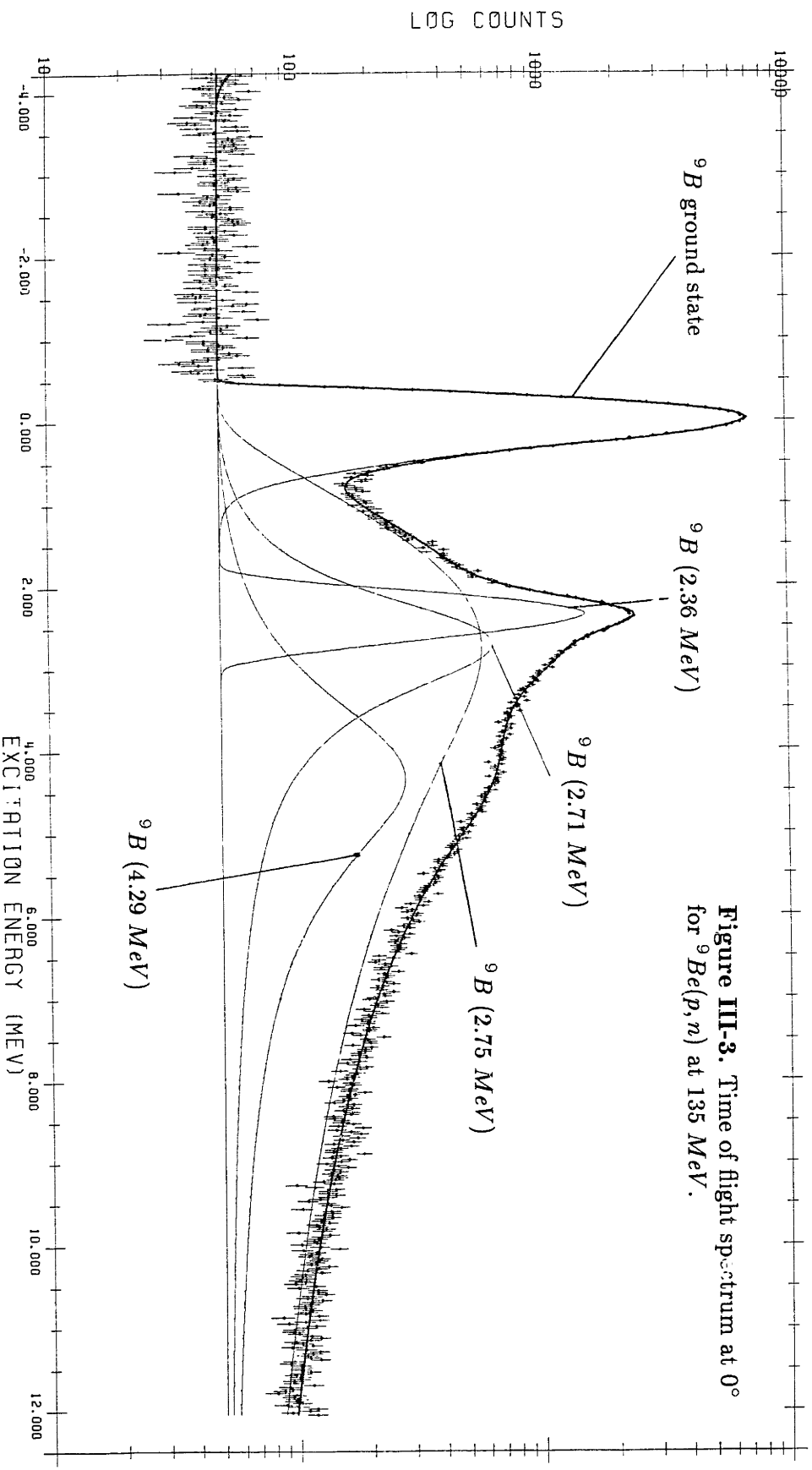

Figure III-3. Time of flight spectrum at 0° for $^9Be(p,n)$ at 135 MeV.

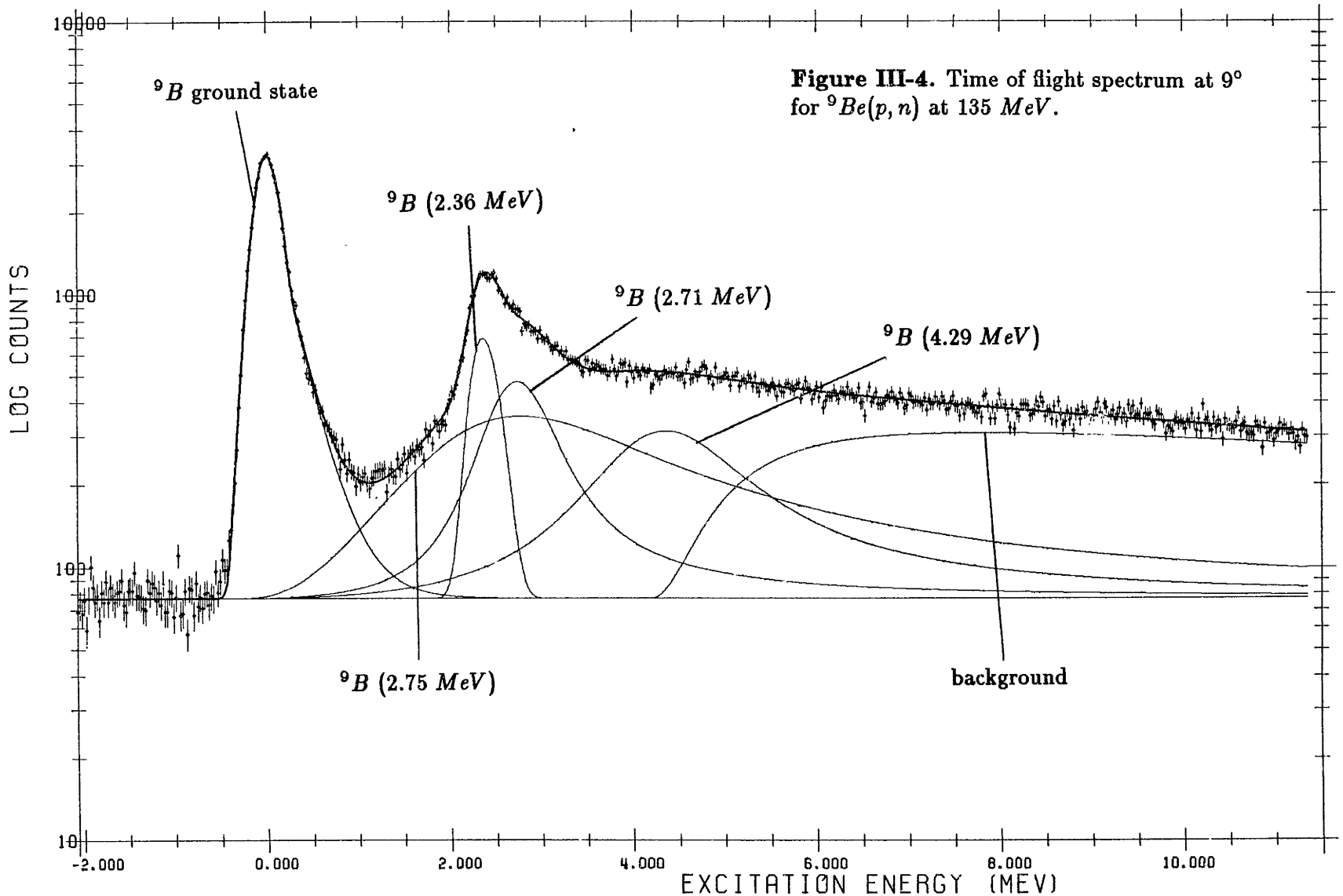

Figure III-4. Time of flight spectrum at 9° for $^9Be(p,n)$ at 135 MeV.

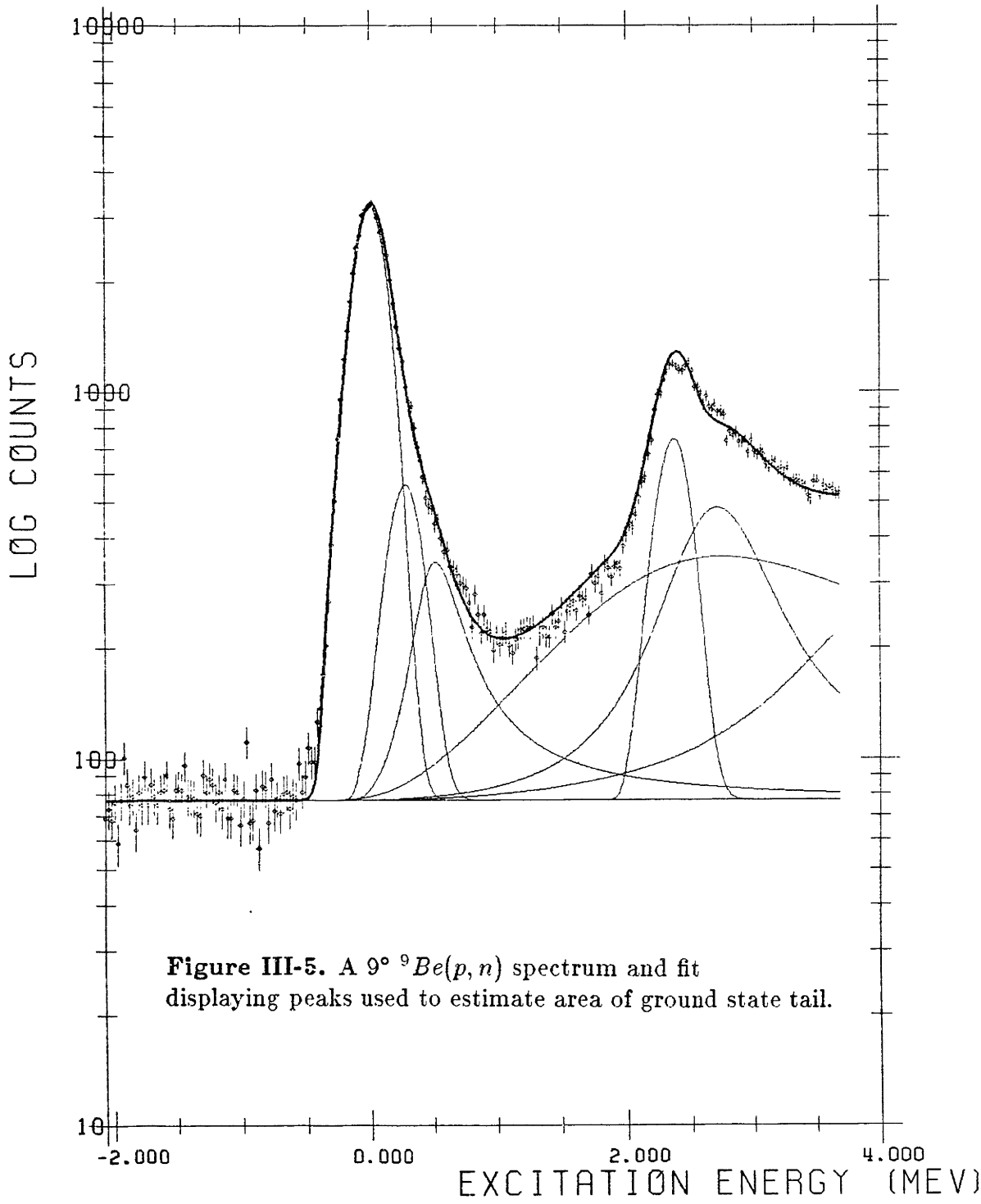

Figure III-5. A 9° $^{9}Be(p,n)$ spectrum and fit displaying peaks used to estimate area of ground state tail.

The ^9B state at 2.36 MeV

There is the possibility that this state shares the same shape as the ground state but this could not be determined owing to the obscuration of this peak's tails by the broad bump discussed below. This peak was assumed to be symmetric for the purposes of lineshape analysis. The uncertainties in cross section quoted for this state allow for the possibility that the peak may have the same shape as the ground state. The natural widths of both the ground state and the state at 2.36 MeV are small compared to system resolution and therefore their peak widths should be dominated by system resolution and hence have the same value. Fits were done forcing these two peak widths to be equal.

The ^9B bump at about 3 Mev

The ^9B spectra at forward angles are dominated by a broad bump at about 3 MeV and having a width of about 3 MeV. This bump has been seen previously by Goodman and others [TELL80]. It appears to be comprised of three states, though this cannot be unambiguously determined at forward angles. It appeared that this bump was dominated by a single broad peak. This was parameterized by a Lorentzian whose position and width were allowed to vary for the 0° fit. This fitting procedure characterized the broad Lorentzian by an excitation energy of 2.75 MeV and a width of 3.13 MeV. This parameterization of the 0° spectrum necessitated the presence of another peak at about 4.3 MeV. This peak was also given a Lorentzian shape. Its position and width were also allowed to vary for the 0° fit. This Lorentzian was characterized by an excitation energy of 4.3 MeV and a width of 1.7 MeV. At all other angles the position and width of these two peaks were fixed to the values determined by the 0° fit. After these peaks' positions and widths had been established, this author found references in the literature to a state with an excitation energy of about 4.1 MeV seen in $^9Be(p,n)^9B$ experiments at lower energies [SAJ60,BAI64,SLO67]. This may perhaps be viewed as a confirmation of the parameterization of the data chosen here.

The data also seem to indicate a more narrow peak at about 2.71 MeV. This state is clearly present at 12° and at several greater angles. This state also seems to be present at forward angles though the evidence is less conclusive. Figure $III-6$ shows the sort of fit obtainable at 0° omitting this state at 2.71 MeV. The fit includes the Lorentzian peaks at 2.75 and 4.3 MeV discussed above. Though the fit is clearly deficient just above the 2.36 MeV state, it seems possible that a different peak shape for the broad Lorentzian at 2.75 might provide a satisfactory fit. However, we were not able to determine such a shape.

For this measurement, the 2.71 MeV state was included at all angles. Figure

$III-3$ shows the same 0° spectrum fit including the peak at 2.7 MeV. The best fits were obtained with about a 700 keV width for this state. This agrees with the work of [WIL66] who determined an excitation energy of 2.71 ± 0.03 MeV and a width of 710 ± 60 keV. The position and width of this state were therefore fixed at 2.71 MeV and 710 keV. Figure $III-2$ shows the fit at 12° using these values for the excitation energy and width.

According to the compilation of [AJZ79], however, the position and width should be 2.788 ± 0.03 MeV and 550 ± 40 keV. The uncertainties ascribed therefore include the effects of changing the width, the minimum value being 590 keV. This is the maximum value allowed according to [AJZ79].

The cross section results for the states reported at 2.71, 2.75, and 4.3 MeV for momentum transfers of 0.5 fm^{-1} and less should be viewed with the difficulties in parameterizing the broad bump in mind. It is possible that a different parameterization of this broad state could eliminate the 2.71 MeV state at forward angles. Indeed, according to the positive parity assignment listed in [AJZ79], this state should not be seen at forward angles since a parity change implies a transfer of angular momentum. This transfer is unlikely at the small momentum transfer of forward angles. At 0° the momentum transfer for this state is $0.05 fm^{-1}$. The current parity assignment is tentative, however, and the data reported here seemed to prefer the presence of this state.

There is in any case an undeniable broad collection of strength at 0°. At all other angles it was necessary to supplement the above discussed three peak parameterization with a broad background. This background was characterized as a Lorentzian with a threshold corresponding to an excitation energy of about 4 MeV. It was possible to use various thresholds in the Lorentzian background ranging from 0 MeV to 4 MeV in excitation. Cross section uncertainties assigned to the states at 2.71, 2.75, and 4.3 MeV allow for these variations in the background threshold. This Lorentzian background is illustrated in figures $III-4$ and $III-7$. This background became stronger for increasing angles until about 18°. At angles greater than 18° this background diminished.

The presence of this background makes cross sections quoted for the broad 2.75 MeV Lorentzian especially ambiguous. Nevertheless, in order to provide some quantitative portrayal of the momentum transfer dependence of this state, the cross section of the 2.75 MeV Lorentzian was extracted at 0°, 3°, and 6°. Any cross sections in this work attributed to the 2.75 MeV state refer to these numbers. The uncertainty assigned is simply the ratio of the 2.71 MeV cross section to the 2.75 MeV cross section. This allows for the possibility of the nonexistence of the 2.71 MeV state at these angles. The resulting cross sections are consistent with zero angular momentum transfer for this excitation. Also, the cross section at 0° is 9.73 mb/sr, which is close to the value 9.52 mb/sr for the ground state analog transition to the ground state of ^9B. This broad 2.75 MeV state may well be identified with the transition to the $p_{\frac{1}{2}}$ state since it is expected to have a *log ft* value close to that of the ground state analog transition [COH65]. It is also expected to have an excitation energy close to that of the $\frac{5}{2}^-$ at 2.36 MeV.

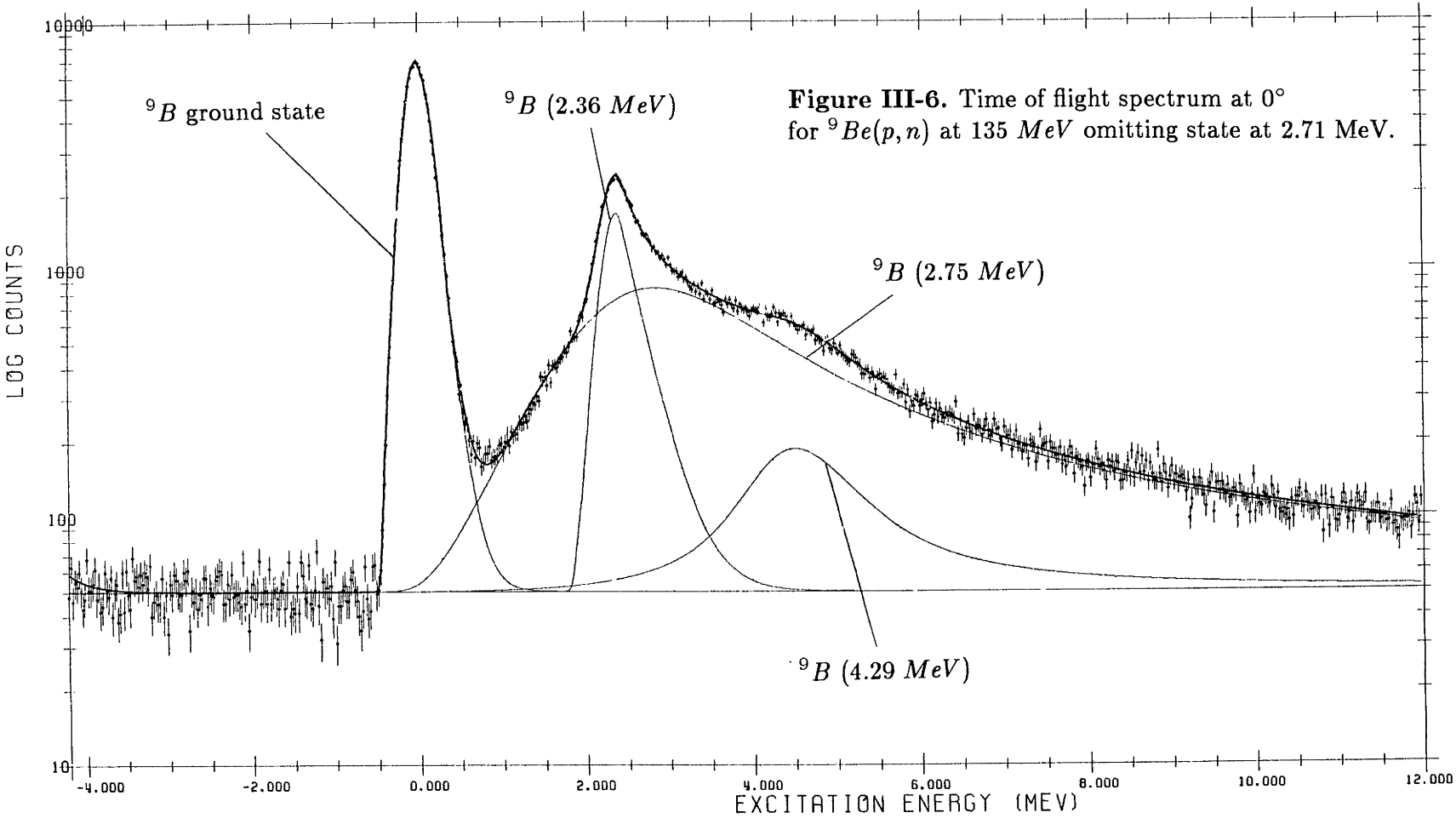

Figure III-6. Time of flight spectrum at 0° for $^9Be(p,n)$ at 135 MeV omitting state at 2.71 MeV.

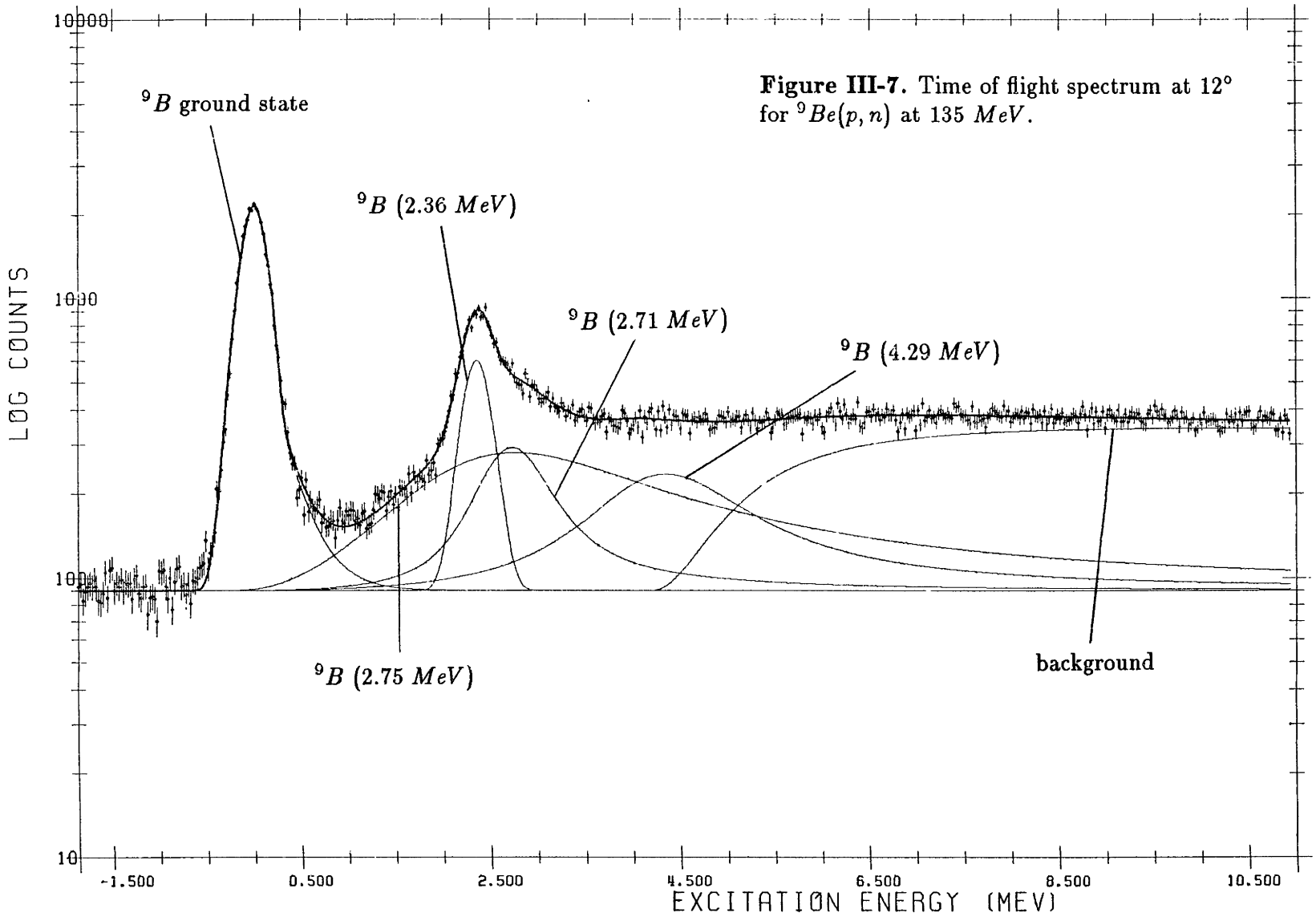

Figure III-7. Time of flight spectrum at 12° for $^9Be(p,n)$ at 135 MeV.

It proved possible to determine the cross sections of several other states in ^9B up to 17.5 MeV. The widths observed did not always agree well with the values compiled in [AJZ79]. The excitation energies generally agreed within the limits of experimental uncertainty. The quoted uncertainties in the cross sections include allowance for background uncertainty. In those cases where peak widths and positions were not well determined by the data, the quoted uncertainties reflect possible variations in these parameters.

Figure $III-8$ shows a fit at 27° fixing the excitation energy of a peak at 6.97 MeV and the width at 2.0 MeV. This state is almost certainly the $\frac{7}{2}^-$ state listed in [AJZ79]. The excitation energy and width were fixed at the reported values to determine cross sections for this state. The cross section uncertainties quoted include the variations in position and width allowed by the data and [AJZ79].

Figure $III-9$ shows a fit encompassing the 11.63 MeV and 12.23 MeV states at 18°. The primary uncertainty in this measurement is in the width and position of the 11.63 MeV state since the width of the state at 12.23 MeV was well determined at 0° as is shown in figure $III-6$. The 11.63 MeV state is not seen at 0° and therefore corresponds to a nonzero angular momentum transfer. Figure $III-10$ shows states at 12.23, 13.96, and 14.6 MeV. This fit at 0° determined the widths of these states for use at other angles. The widths for the 12.23 MeV and 14.6 MeV state determined in this way do not agree well with the values compiled for any nearby states as compiled by [AJZ79].

At certain angles there appeared another state at 14.6 MeV more narrow than the one discussed in the previous paragraph. Figure $III-11$ shows both of these states at 6° along with the states at 12.23 MeV and 13.96 MeV. At larger angles the broader 14.6 MeV state disappeared leaving the narrow state in an easily measurable situation. Two other states are shown which could not be identified at any angle other than 6°. They appeared at excitation energies of 15.15 and 15.44 MeV. Their cross sections are depicted in figures $III-28$ and $III-29$.

Finally, figure $III-12$ shows a spectrum at 6 ° which includes states at 15.86, 16.71, and 17.54 MeV. The state at 15.86 MeV could only be seen at one other angle. The other two were quite strong at several angles. The cross sections of these states appear in figures $III-30$ through $III-32$.

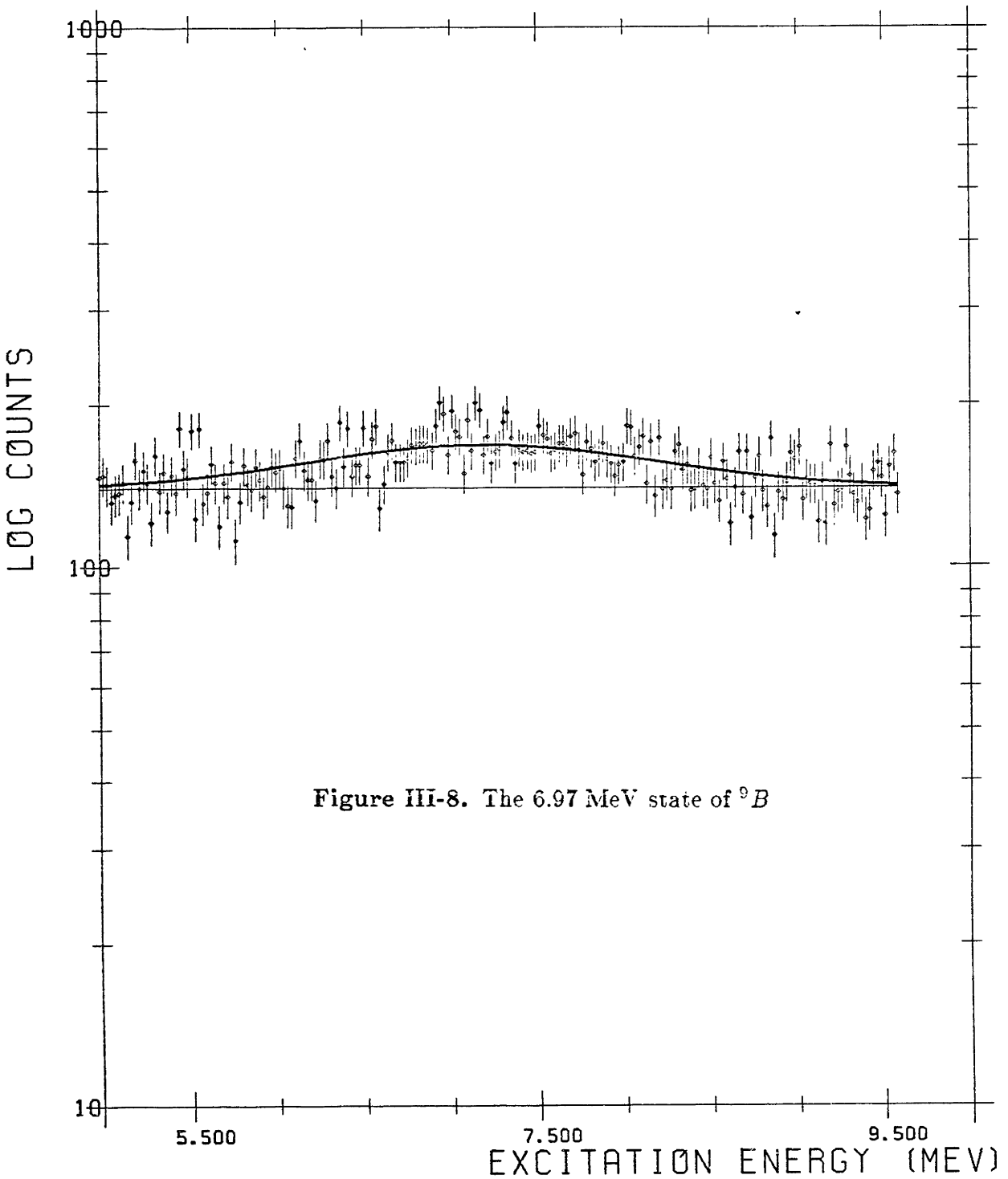

Figure III-8. The 6.97 MeV state of ^{9}B

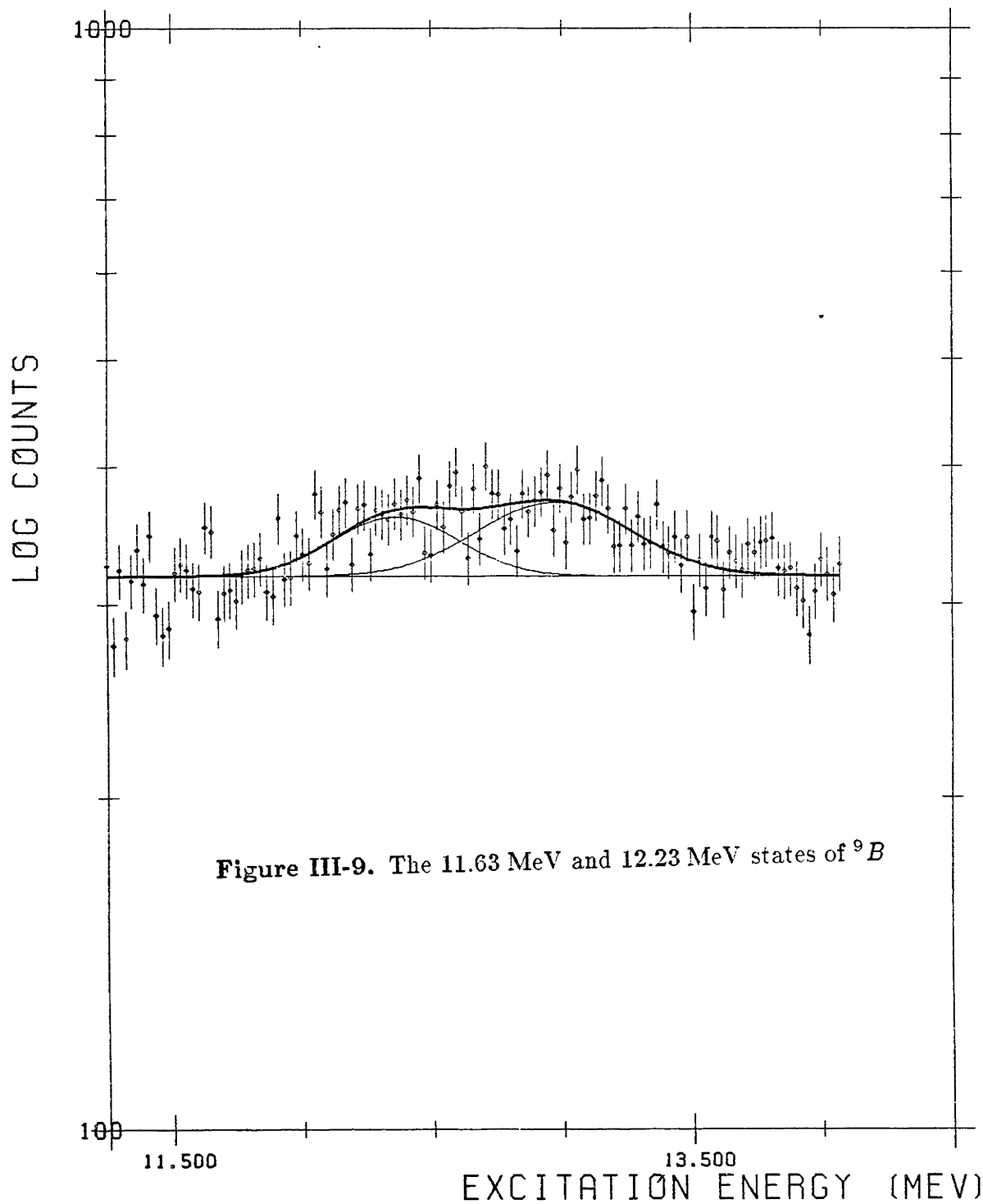

Figure III-9. The 11.63 MeV and 12.23 MeV states of ^{9}B

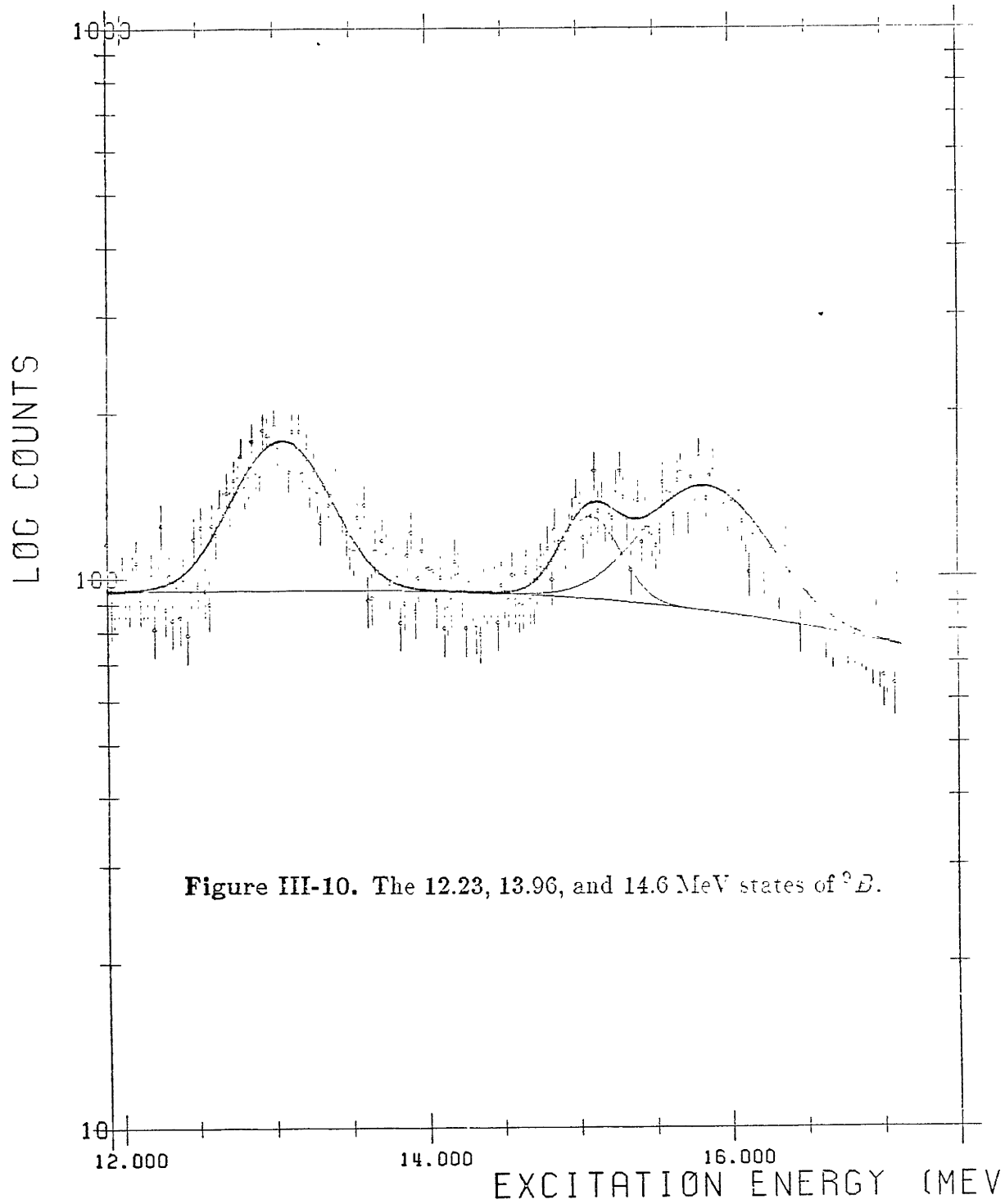

Figure III-10. The 12.23, 13.96, and 14.6 MeV states of ^9B.

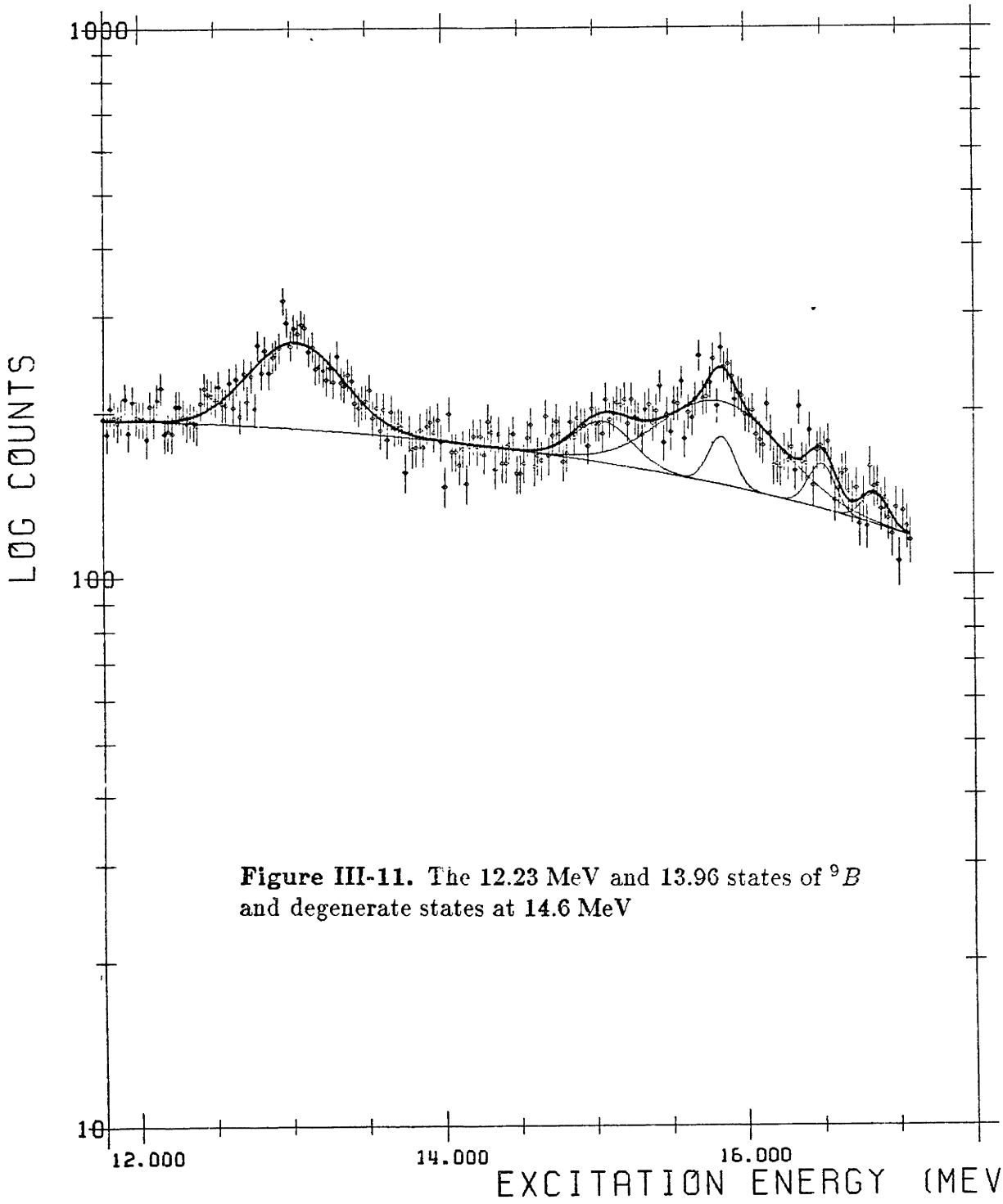

Figure III-11. The 12.23 MeV and 13.96 states of ^9B and degenerate states at 14.6 MeV

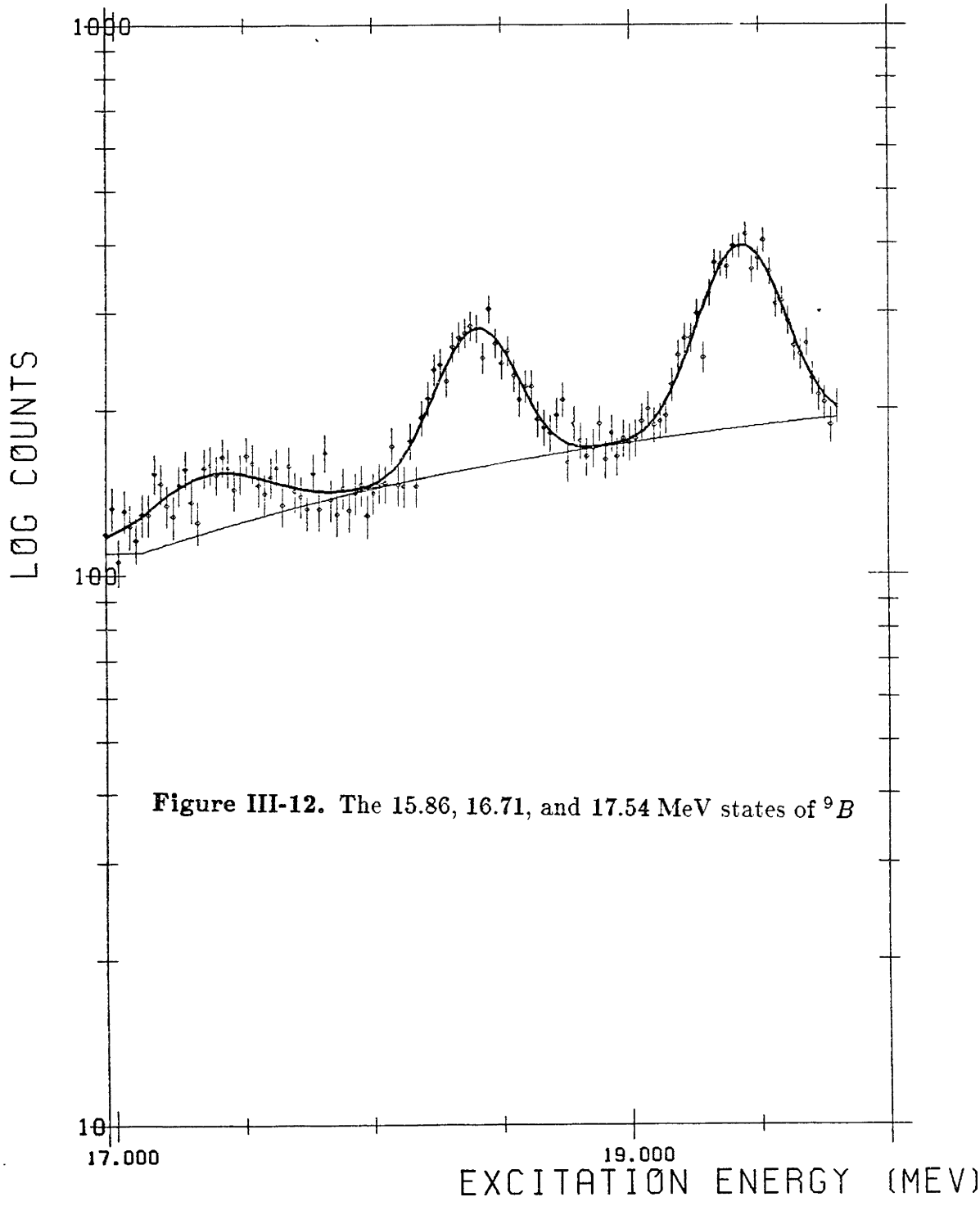

Figure III-12. The 15.86, 16.71, and 17.54 MeV states of ^9B

Table $III-1$. The states of ^9B seen in this measurement.

^9B states	
E_x (MeV)	FWHM (MeV)
0.00	
2.36	
2.71±0.1	0.71±0.1
2.75±0.3	3.13±0.2
4.3±0.2	1.6±0.2
7.0±0.1	2.0
11.63±0.2	
12.23±0.1	0.5±0.1
13.96±0.1	
14.60±0.1	
14.60±0.1	0.6±0.1
15.15±0.1	
15.44±0.1	
15.86±0.1	
16.71±0.1	
17.54±0.1	

Table $III-2$. The ^9B states in [AJZ79,LED78,SAJ60,BAI64,SLO67].

^9B states		
E_x (MeV±keV)	FWHM (KeV)	J^π
g.s	0.54±0.21	$\frac{3}{2}^-$
2.361±5	81±5	$\frac{5}{2}^-$
2.788±30	550±40	$(\frac{3}{2},\frac{5}{2})^+$
(4.1±100)		
(4.8±100)	1000±200	
6.97±60	2000±200	$\frac{7}{2}^-$
11.70±70	800±50	$(\frac{7}{2})^-$
12.06±60	800±200	
14.01±70	390±110	
14.6550±2.5	0.275±0.093	$\frac{3}{2}^-$
14.70±180	1350±200	$(\frac{5}{2})^-$
15.29±40		
15.58±40		
16.024±25	180±16	
17.076±4	22±5	
17.19±25	120±40	
17.637±10	71±8	
(18.6)±10	1000	

The Observed ^{17}F States

The states seen in this measurement of the $^{17}O(p,n)^{17}F$ reaction are listed in table $III-3$. As in table $III-1$, blank space in the width column means that the width of the state was not discernible with our experimental resolution. For comparision, table $III-4$ lists the states of ^{17}F within 8 MeV according to recent compilations [AJZ82,LED78]. The $^{17}O(p,n)^{17}F$ cross section and analyzing power measurements reported here are shown graphically in figures $III-34$ to $III-43$. These results are tabulated numerically in the appendix. The appendix also details the correspondence between the scattering angle in the center of mass frame and momentum transfer.

The next few sections explain the manner in which peak areas were derived from the spectra by line shape analysis using the code ALLFIT described in chapter II. In most cases the uncertainties quoted for cross sections are those determined by ALLFIT using the error matrix method described in [BEV69]. In a few cases special considerations were necessary in estimating uncertainties. These cases will be described below as they arise.

It should be emphasized that cross section uncertainties quoted do not include the uncertainty in the detector efficiencies. As discussed in chapter II, this uncertainty is estimated to be 10% and applies systematically to all cross section data.

The ground state of ^{17}F

The cross section for the $^{17}O(p,n)$ reaction leading to the ground state of ^{17}F is displayed in figure $III-34$. The spectrum and line fit at 0° is shown in figure $III-13$. The ground state of ^{17}F was somewhat obscured by the broad strength of Boron. Subtraction of ^{9}B spectra from ^{17}F spectra to eliminate this contamination revealed the ^{17}F ground state peak to be quite symmetric at all angles. Therefore, for the purpose of cross section measurement, all narrow ^{17}F peaks were constrained to be symmetric. This was done by constraining the parameters which control the exponential tails instead of allowing them freedom as was done in the case of the ground state of ^{9}B.

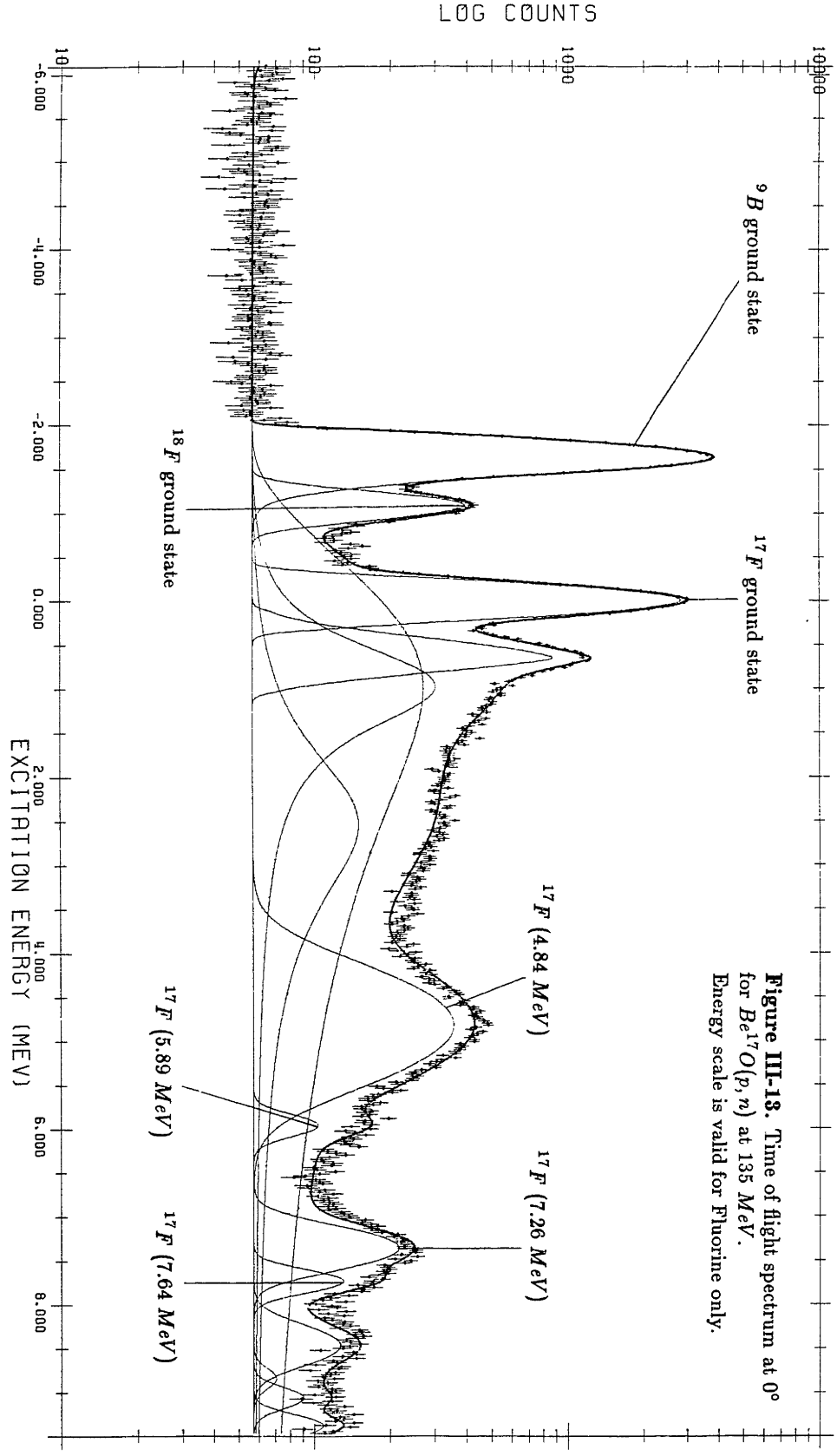

Figure III-13. Time of flight spectrum at 0° for $Be^{17}O(p,n)$ at 135 MeV. Energy scale is valid for Fluorine only.

Other narrow states of ^{17}F

At certain angles greater than 0° the $\frac{1}{2}^+$ state at 0.5 MeV was visible. For fitting, the excitation energy was fixed at 0.495 MeV and the lineshape width was constrained to equal that of the ground state. The cross section for exciting this state is shown in figure $III-35$.

At forward angles two weak states were seen at 5.89 MeV and 6.34 MeV. These positions were fixed and the widths constrained to equal that of the ground state. It is not possible to identify these states unambiguously with any previouly reported states given in [AJZ82] and listed in table $III-4$. These cross sections are portrayed in figures $III-37$ and $III-38$.

At 3° to 18° a narrow state was seen at about 9.3 MeV which can perhaps be identified with a previously reported $\frac{3}{2}^-$ state at 9.17 ± 0.060 MeV [AJZ82]. The cross section peaks at about 0.5 fm^{-1}, which is consistent with a $\frac{3}{2}^-$ state. The cross section is given in figure $III-41$.

At 3° to 15° a narrow state was seen at about 14.3 MeV. This is too close to other ^{17}F states to attempt an identification. Its cross section is shown in figure $III-42$.

The broad state at 4.84 MeV

There appeared one strong isolated state in ^{17}F at 4.84 MeV which is strongest at forward angles. It is labeled in the 0° spectrum and fit shown in figure $III-13$. A Lorentzian shape was at first assumed for this peak but this resulted in an overestimate of the measured cross section in the high excitation portion of the tail region of the Lorentzian. Subtraction of the Beryllium background from the $Be^{17}O$ spectrum revealed that indeed this state had no extended tail. It was not Lorentzian in shape. Nor could it be represented as a Breit-Wigner shape. A broad gaussian shape proved to represent this peak in a manner most consistent with the data. The cross section for exciting this state is given in figure $III-36$.

Two states at 7.26 and 7.64 MeV

Two states appeared at 7.26 and 7.64 MeV which could not be resolved unambiguously. These peaks are labeled in the 0° spectrum and the fit is shown in

figure $III - 13$. It proved possible to represent the state at 7.26 MeV adequately by either a Gaussian or a Breit-Wigner shape. Figure $III - 14$ shows a fit at 0° using a Breit-Wigner shape for this state. Cross sections reported for this state use results of the Gaussian representation. The Breit-Wigner representation is used to estimate the uncertainty in the cross section reported.

The state at 7.64 MeV suffers greatly as a result of this ambiguity. This is reflected in the uncertainties indicated for this state as well.

Numerous states above 8 MeV.

In figure $III - 13$ there appears reaction strength above 8 MeV which may in fact correspond to unresolved quasi-stationary states. It was not possible to resolve this strength unambiguously into separate states. The integrated cross section up to 14 MeV including this strength is given and discussed in a later section.

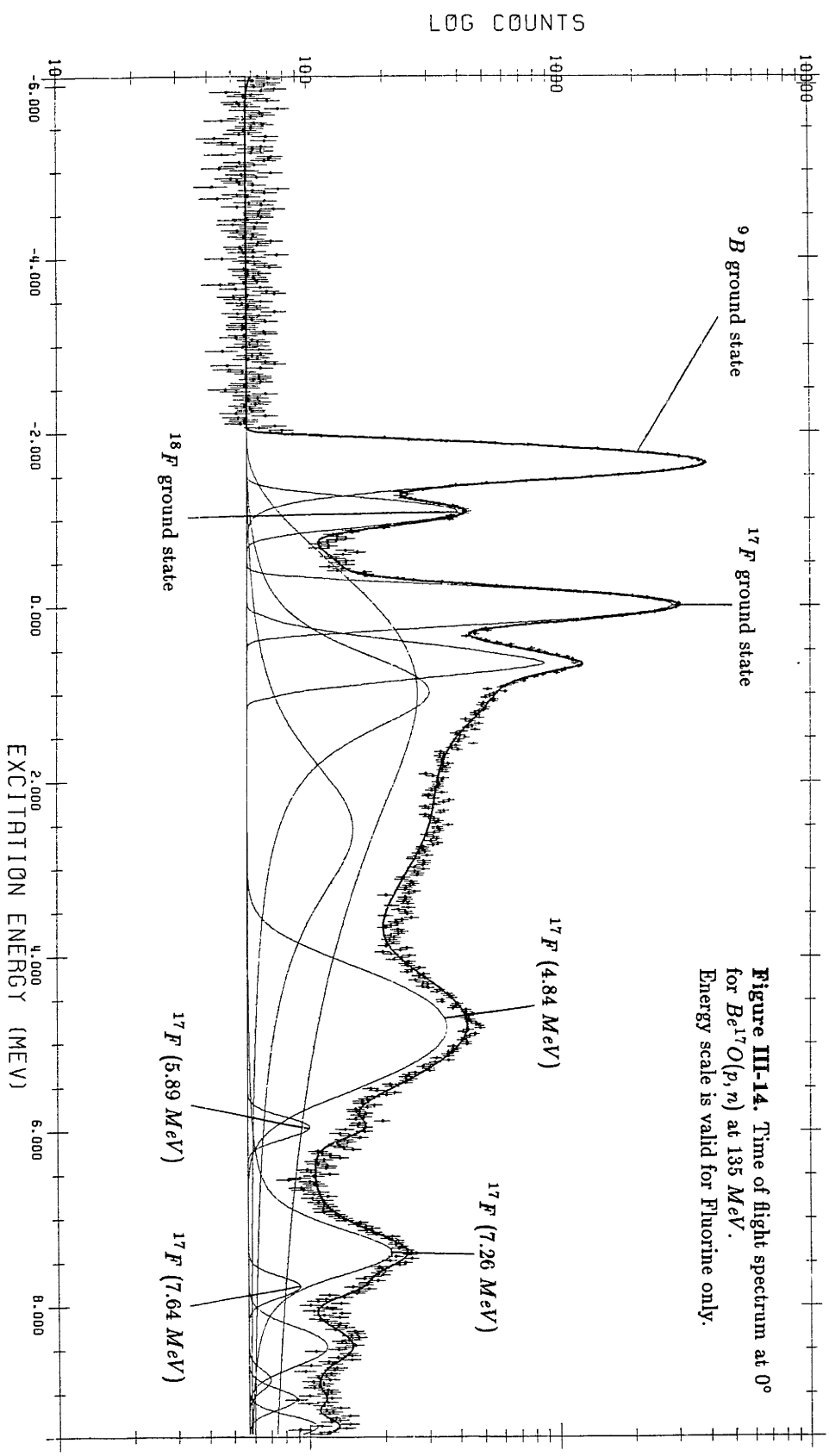

Figure III-14. Time of flight spectrum at 0° for $Be^{17}O(p,n)$ at 135 MeV. Energy scale is valid for Fluorine only.

At zero degrees it is expected that the stronger excited states are Gamow-Teller states, which is to say their excitation is accomplished almost entirely as a result of spin interactions. This is because of the relative dominance of the spin flip part of the isovector part of the strong force at this energy and the supression of orbital motion transfer at small momentum transfer.

In the case of ^{17}F there are $\frac{3}{2}^+$ states in the first few MeV which should be strongly excited by the spin interactions of the nuclear force. In particular, [AJZ79] lists a $\frac{3}{2}^+$ state at 5.1 MeV. We do not see any state at 5.1 MeV but a strong state is seen at 4.84 MeV. These results seem to indicate that the state at 5.1 MeV is probably not $\frac{3}{2}^+$ and that the state reported at 4.7 MeV in [AJZ79] should be regarded as a $\frac{3}{2}^+$ state.

Indeed at one time the spin-parity of the 4.7 MeV state was believed to be $\frac{3}{2}^+$ and that of the 5.1 MeV state was believed to be $\frac{1}{2}^+$ [AJZ59]. In 1954 a Zürich group scattered 5-7 MeV protons on ^{16}O and studied the cross section for elastic scattering as a function of energy. At such low energies the scattering process proceeds via a ^{17}F intermediate state. Interpreting their data using nuclear dispersion theory, they concluded that the ^{17}F system had a $\frac{3}{2}^-$ excited state at 4.5 MeV, a $\frac{3}{2}^+$ state at 4.6 MeV, a $\frac{1}{2}^+$ state at 5.15 MeV, and a $\frac{1}{2}^+$ excited state at 6.65 MeV. [SEM54].

These results were contradicted in 1962 by a study at the University of Wisconsin using the same experimental technique but with a slightly more extensive energy range (4.2-8.6 MeV protons) [SAL62a,SAL62b]. Another difference was that they also made use of a computer program to do a phase shift analysis whereas the Zürich group used a graphical method. The Wisconsin group made 15 spin-parity assignments in ^{17}F. Among these they concluded that there was a $\frac{3}{2}^-$ state at 4.7 MeV and a $\frac{3}{2}^+$ state at 5.1 MeV.

The present results are in agreement with the older Zürich results and the earlier compilation [AJZ59].

Table $III-3$. The states of ^{17}F seen in this measurement.

^{17}F states	
E_x (MeV)	FWHM (MeV)
0.00	
0.5±0.05	
4.84±0.1	1.8±0.05
5.89±0.2	
6.34±0.2	
7.26±0.2	
7.64±0.2	
9.3±0.1	
14.3±0.1	

Table $III-4$. The ^{17}F states in [AJZ82] with $E_x \leq 8MeV$.

^{17}F states		
E_x (MeV±keV)	FWHM (KeV)	J^π
g.s.	$\tau_{\frac{1}{2}} = 64.49 \pm 0.16 sec$	$\frac{5}{2}^+$
0.49533±0.10	$\tau_m = 412 \pm 9 psec$	$\frac{1}{2}^+$
3.104±3	19±1	$\frac{1}{2}^-$
3.857±4	1.5±0.2	$\frac{5}{2}^-$
4.696±10	225	$\frac{3}{2}^-$
5.103±10)	1530	$\frac{3}{2}^+$
5.817±10	180	$\frac{3}{2}^+$
6.036±10	30	$\frac{1}{2}^-$
6.556±10	200	$\frac{1}{2}^+$
7.356±10	10±2	$\frac{3}{2}^+$
7.448±7	$\leq$5	
7.454±7	7±2	
7.471±7	5±2	
7.479±10	795	$\frac{3}{2}^+$
7.546±10	30	$\frac{7}{2}^-$
7.75±20	179±3	$\frac{1}{2}^+$
7.95±15	10±3	
8.01±20	50±20	

Summary of states seen in this experiment

Table $III-5$ shows the probable identity of the ^9B states reported above. The assignments are based on a comparison of excitation energies with those compiled in [AJZ79] except in the case of the 4.3 MeV state. This state is identified with a state reported by several researchers to be at about 4.1 MeV [SAJ60,BAI64,SLO67]. This criterion afforded a fairly unambiguous identification for the ^9B states. Note that the three ^9B states between 15.0 and 15.9 MeV have excitation energies which deviate from accepted values systematically. The absolute values of the excitation energies are consistent with the estimated uncertainty of the excitation energy measured in this experiment. This corroborates the identification suggested here.

Table $III-6$ shows the probable identity of the ^{17}F states reported above. In some cases an unambiguous identification is impossible. The assignments are based on excitation energies and currently accepted spin-parity assignments in [AJZ82]. As discussed earlier, the strength of the 4.84 MeV state indicates and error in the currently accepted spin-parity of this state.

Table $III-5$. Comparison of the states of ^9B seen in this measurement with states seen by previous studies of this nucleus. The first column gives results of this experiment. The second column gives the closest excitation energy found in the literature. The third column gives the difference in excitation energy.

E_x (MeV) (p,n)	E_x (MeV) book	Δ (MeV)	remarks
0.0	0.0	0.	peaks at 0 fm^{-1}
2.36	2.361	0.	peaks at 0 fm^{-1}
2.71	2.788	−0.08	
2.75			
4.3	4.1	+0.02	
7.0	6.97	+0.03	peaks at 1.5 fm^{-1}
11.63	11.70	−0.07	
12.23	12.06	+0.17	
13.96	14.01	−0.04	
14.6	14.655	−0.06	peaks at 1. fm^{-1}
14.6	14.70	−0.10	
15.15	15.29	−0.14	
15.44	15.58	−0.14	
15.86	15.58	−0.14	
16.71	17.08	−0.37	peaks at 0.5 fm^{-1}
17.54	17.6	−0.06	peaks at 0.5 fm^{-1}

Table $III-6$. Comparison of the states of ^{17}F seen in this measurement with states seen by previous studies of this nucleus. The first column gives results of this experiment. The second column gives the excitation energy of this state found in the literature. The third column gives the difference in excitation energy.

E_x (MeV) (p,n)	E_x (MeV) book	Δ (MeV)	remarks
0.0	0.0	0.	peaks at 0 fm^{-1}
0.5	0.5	0.	peaks at 0.6 fm^{-1}
4.84	4.696	+0.14	peaks at 0 fm^{-1}
5.89	5.817	+0.07	
6.34	6.556	−0.22	
7.26	7.356	−0.10	peaks at 0 fm^{-1}
7.64			
9.3			peaks at 0.5 fm^{-1}
14.3			peaks at 0.5 fm^{-1}

As mentioned in the first section of this chapter, the (p,n) reaction at these energies provides a way to measure the Gamow-Teller matrix element of a given transition. In the case of $^{17}O(p,n)^{17}F$ leading to the ground state of ^{17}F, the ground states of both nuclei have angular momentum $\frac{5}{2}^+$ so that both spin-flip and nonspin-flip nuclear forces can effect this transition. This means that both Fermi and Gamow-Teller matrix elements contribute to the cross section, as was detailed in the first section.

According to the single particle picture of these nuclei, the nuclear spin-flip force can also excite one other single particle state, namely the $d_{\frac{3}{2}}$ state. This transition would not involve the Fermi, or nonspin-flip, part of the nuclear force at all. We may calculate this Gamow-Teller matrix element as in the analog ground state transition,

$$|M_F|^2 = |\langle \mathbf{1} \rangle|^2 = 0$$

$$|M_{GT}|^2 = \left(\frac{1}{2(2J_i+1)}\right) \sum_{\chi_i,\chi_f=\uparrow,\downarrow} \sum_{m_i=-\frac{5}{2}}^{\frac{5}{2}} \sum_{m_f=-\frac{3}{2}}^{\frac{3}{2}} |\langle \chi_f d_{\frac{3}{2}} m_f | \sigma_p \cdot \sigma_t | \chi_i d_{\frac{5}{2}} m_i \rangle|^2$$

$$= \frac{1}{12} \times \frac{96}{5} = \frac{8}{5}$$

where χ_i and χ_f represent spin projections of the projectile. σ_p and σ_t operate on the projectile and target nucleons respectively. The matrix elements and summations were done explicitly by constructing normalized angular momentum states, a simple albeit tedious method.

It is interesting to note that summing $|M_{GT}|^2$ over both possible Gamow-Teller transitions we obtain

$$\sum |M_{GT}|^2 = \frac{7}{5} + \frac{8}{5} = 3$$

which is also $|M_{GT}|^2$ for the beta decay of a free neutron. This result turns out to be independent of the single particle model employed here, as will be discussed in the next section.

The model independence of this result makes it of interest to determine how much of this Gamow-Teller matrix element is actually seen for the limited set of $J = \frac{5}{2}$ and $J = \frac{3}{2}$ states observed in this experiment. For this purpose we shall use the method of [GOOD80] described in the first section of this chapter. We shall use the value of $|M_{GT}|^2$ determined from the β-decay of ^{17}F (assuming $|M_F|^2 = 1$ to determine the nuclear volume integrals J_τ and $J_{\sigma\tau}$. Keeping the distortion factors constant, we maintain the ratio $\frac{J_{\sigma\tau}}{J_\tau}$ to the ratio given by [TAD81] and adjust these nuclear force volume integrals to get the experimentally determined differential cross section for $^{17}O(p,n)^{17}F_{g.s.}$ at 0°, 8.4 mb/sr. The values $J_\tau = 83 MeV\,fm^3$

and $J_{\sigma\tau} = 180 MeV fm^3$ maintain the ratio of [TAD81] and when employed in equation $III - 1$ that equation becomes

$$\begin{aligned}\sigma(\theta = 0°) &= \left(\frac{\mu}{\pi\hbar^2}\right)^2 \frac{k_f}{k_i}\left[N_\tau^D |J_\tau M_F|^2 + N_{\sigma\tau}^D |J_{\sigma\tau} M_{GT}|^2\right] \\ &= \left(\frac{994 MeV}{\pi(197 MeV fm)^2}\right)^2 \\ &\quad \times \left[0.353 \times (83 MeV fm^3)^2 + 0.463 \times (180 MeV fm^3)^2 \times 0.677\right] \\ &= 8.4 mb/sr\end{aligned}$$

It is seen that comparatively little change in the nuclear force integrals is required to reproduce the (p,n) results. We may now use the (p,n) measurement at 0° to estimate the Gamow-Teller strength evidenced at 0°.

The excitation function of $^{17}O(p,n)^{17}F$ at 0° is shown in figure $III - 15$. This was obtained by spectrum subtraction. A narrow peak is wider for the pure Beryllium target than for the same peak seen using the Beryllium Oxide target due to the difference in the target thicknesses. This caused anomalous peaks in subtracted spectrum which have been removed in figure $III - 15$. Also, a peak around $E_x = 14\ MeV$ corresponding to the ground state of ^{12}N has been removed. The ground state is known to be mixed Fermi and Gamow-Teller. We may obtain an upper limit to the possible Gamow-Teller strength within the first 14 MeV of excitation by assuming all strength other than the ground state to be fragmented $d_{\frac{3}{2}}$ strength, that is, pure Gamow-Teller strength. Neglecting the ground state, the total strength within the first 14 MeV is found to be 8.4 mb/sr. We then use the above nuclear force integrals and equation $III - 1$ to write

$$\begin{aligned}\sigma(\theta = 0°) &= \left(\frac{\mu}{\pi\hbar^2}\right)^2 \frac{k_f}{k_i}\left[N_\tau^D |J_\tau M_F|^2 + N_{\sigma\tau}^D |J_{\sigma\tau} M_{GT}|^2\right] \\ &= \left(\frac{994 MeV}{\pi(197 MeV fm)^2}\right)^2 \\ &\quad \times \left[0.353 \times (83 MeV fm^3)^2 \times 0 + 0.463 \times (180 MeV fm^3)^2 \times |M_{GT}|^2\right] \\ &= 8.4 mb/sr\end{aligned}$$

Solving this equation for $|M_{GT}|^2$ we get

$$|M_{GT}|^2 = 0.8$$

We add this to the Gamow-Teller strength for the ground state analog transition determined by nuclear β decay, namely 0.677, to get the total Gamow-Teller strength seen within the first 14 MeV of excitation,

$$\sum |M_{GT}|^2 = 0.677 + 0.8 = 1.5$$

Thus only one half of the expected value of 3 is seen within the first 14 MeV of excitation.

We may also use this method to obtain the total Gamow-Teller strength seen in the reaction $^9Be(p,n)^9B$ at 0°. In this case there is no β-decay information so that we must rely entirely on the (p,n) reaction. The excitation function of $^9Be(p,n)^9B$ at 0° is shown in figure $III-16$. The ground state is mixed Fermi and Gamow-Teller as in the case of ^{17}F. The narrow state at 2.36 MeV is believed to have an angular momentum of $\frac{5}{2}^-$ making it a pure Gamow-Teller state. Assuming the dominant broad state to be $p_{\frac{1}{2}}$ makes it also pure Gamow-Teller. We therefore sum all strength from 0.8 Mev to 18.3 MeV and obtain 16.9 mb/sr as an upper limit to the pure Gamow-Teller strength seen below about 18 MeV. For this reaction the reduced energy is $\mu = 930.5$ MeV. The distortion factors were calculated as in the case of ^{17}F. Using the nuclear volume integrals above we obtain for the ground state analog transition to ^9B,

$$\begin{aligned}
\sigma(\theta = 0°) &= \left(\frac{\mu}{\pi\hbar^2}\right)^2 \frac{k_f}{k_i} \left[N_\tau^D |J_\tau M_F|^2 + N_{\sigma\tau}^D |J_{\sigma\tau} M_{GT}|^2\right] \\
&= \left(\frac{931 MeV}{\pi (197 MeV\, fm)^2}\right)^2 \\
&\quad \times \left[0.426 \times (83 MeV\, fm^3)^2 \times |M_F|^2 + 0.567 \times (180 MeV\, fm^3)^2 \times |M_{GT}|^2\right] \\
&= 9.52 mb/sr
\end{aligned}$$

where the value 9.52 mb/sr is from this measurement. If we assume $|M_F|^2 = 1$, then the above equation may be solved for $|M_{GT}|^2$ to obtain

$$|M_{GT}|^2 = 0.7$$

Assuming the rest of the 0° spectrum to represent pure Gamow-Teller strength, we use equation $III-1$ to calculate the Gamow-Teller matrix element corresponding to 16.9 mb/sr,

$$\begin{aligned}
\sigma(\theta = 0°) &= \left(\frac{\mu}{\pi\hbar^2}\right)^2 \frac{k_f}{k_i} \left[N_\tau^D |J_\tau M_F|^2 + N_{\sigma\tau}^D |J_{\sigma\tau} M_{GT}|^2\right] \\
&= \left(\frac{931 MeV}{\pi (197 MeV\, fm)^2}\right)^2 \\
&\quad \times \left[0.426 \times (83 MeV\, fm^3)^2 \times 0 + 0.567 \times (180 MeV\, fm^3)^2 \times |M_{GT}|^2\right] \\
&= 16.9 mb/sr
\end{aligned}$$

where the value 16.9 mb/sr is the integrated cross section from 0.8 MeV to 18.3 MeV taken from figure $III-16$. The above equation may be solved for $|M_{GT}|^2$ to get

$$|M_{GT}|^2 = 1.6$$

We add this to the Gamow-Teller strength determined for the ground state analog transition to get the total Gamow-Teller strength seen within the first 18.3 MeV of excitation,

$$\sum |M_{GT}|^2 = 0.7 + 1.6 = 2.3$$

Thus we see possibly as much as 70% of the Gamow-Teller strength expected for the mass 9 system within the first 18.3 MeV.

It should be noted that the above results ignore the dependence of the cross section on momentum transfer. The error incurred can be roughly estimated by assuming a simple 0^{th} order spherical Bessel function dependence for the $l = 0$ part of the interaction. The greatest effect is for ^9B at the highest excitation energy. At 18 MeV of excitation the center of mass momentum transfer is about 0.21 fm^{-1}. Estimating the radius of ^9B to be 2.5 fm we obtain $|j_0(qR)|^2 = |j_0(0.53)|^2 = 0.91$. The correction for the whole spectrum is less than this extreme case.

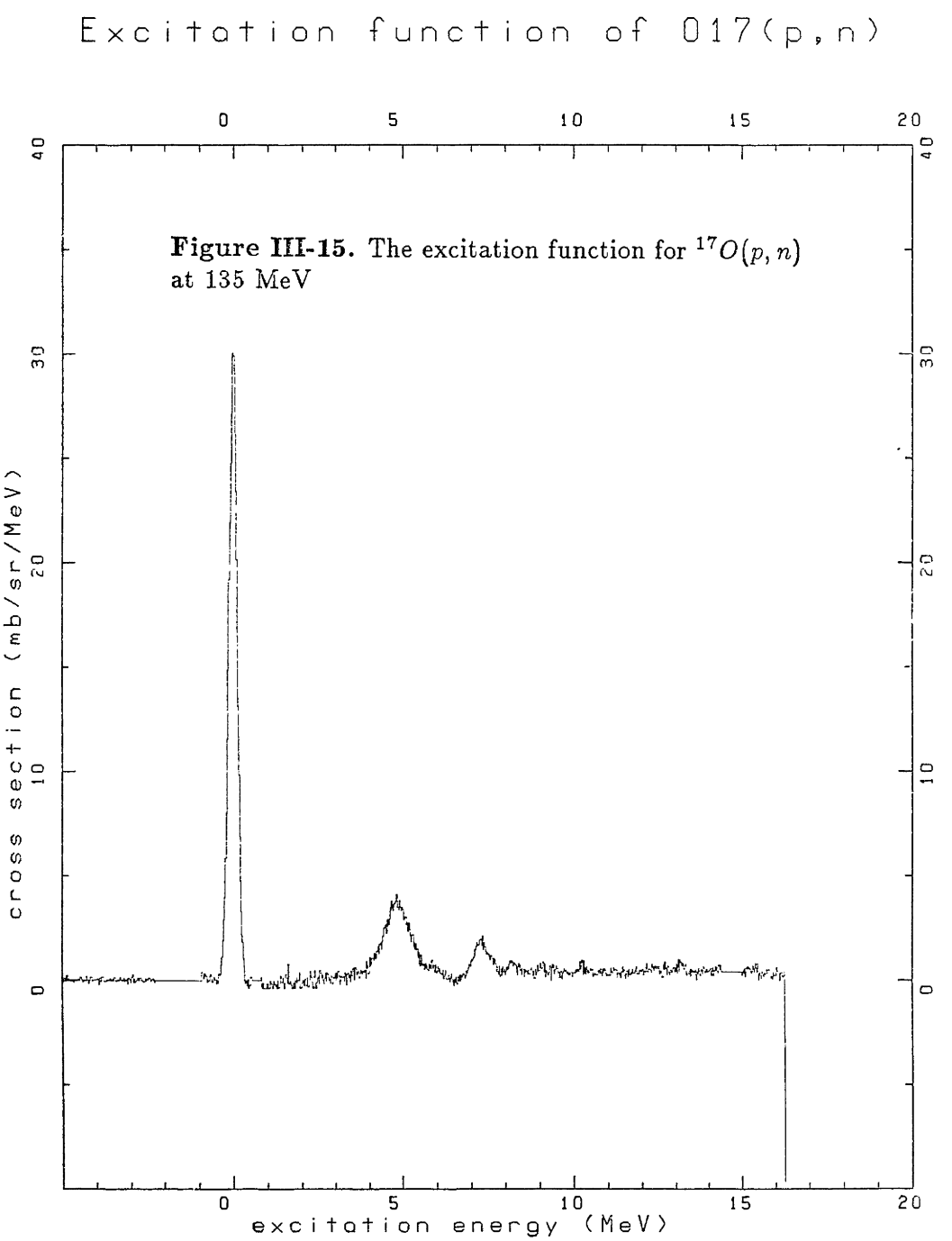

Figure III-15. The excitation function for $^{17}O(p,n)$ at 135 MeV

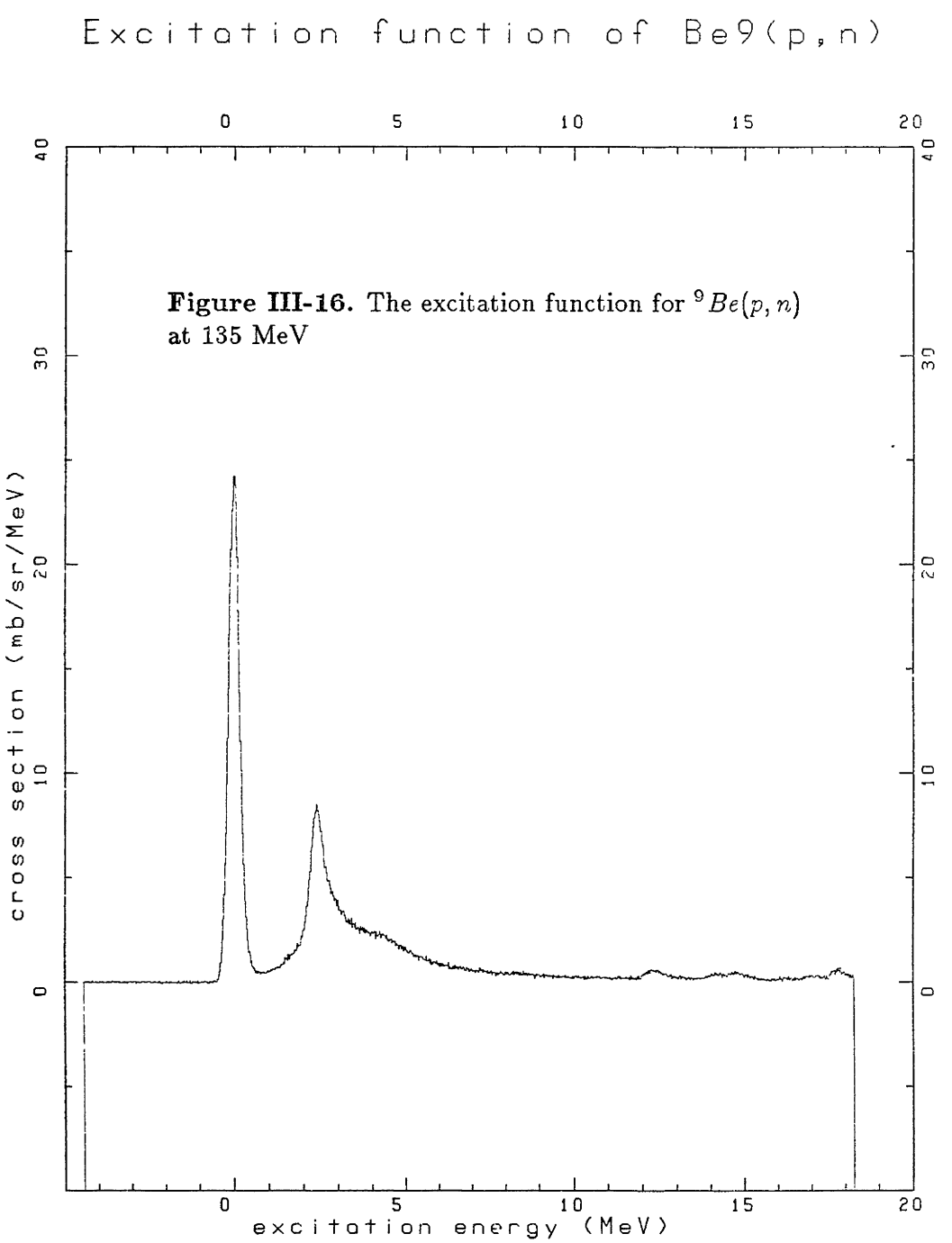

Figure III-16. The excitation function for $^{9}Be(p,n)$ at 135 MeV

The above considerations provide an example of the application of a general sum rule of the Gamow-Teller force which may be expressed as

$$\begin{aligned} S_{\beta-} - S_{\beta+} &= \sum_f |\langle f|\beta_-|i\rangle|^2 - \sum_f |\langle f|\beta_+|i\rangle|^2 \\ &= \sum_f |\langle f| \sum_{k=1}^{A} \sum_{\mu} \sigma_\mu(k) t_-(k)|i\rangle|^2 \\ &\quad - \sum_f |\langle f| \sum_{k=1}^{A} \sum_{\mu} \sigma_\mu(k) t_+(k)|i\rangle|^2 \\ &= 3(N-Z) \end{aligned} \qquad III-4$$

This equation expresses the condition that Gamow-Teller β decay, and any force which likewise induces isospin and spin transitions, shall act upon individual nucleons as in free space with due allowance for the consequences of energetics and the Pauli exclusion principle. This equation is otherwise model independent since its basis is simply the commutation relations for the spin and isospin degrees of freedom. If the nucleus is made of individual nucleons then this relation should obtain. To the extent that the Gamow-Teller matrix elements in equation $III-4$ can be measured, it is possible to use this relation as a test of the theory of the nucleus as a many-nucleon system.

It has been known for some time that most β decays in nature do not exhaust this sum rule. For example, the case of $^{17}F \rightarrow ^{17}O$ requires a Gamow-Teller matrix element whose square is only about half the value expected on the basis of assuming a $d_{\frac{5}{2}} \rightarrow d_{\frac{5}{2}}$ transition. It is possible that the ground states of these two nuclei are not well described by this simple model. In this case the β decay strength may represent only one of many terms of equation $III-4$, the others being perhaps energetically not allowed for β transitions. It is here that Goodman's observation regarding the (p,n) reaction at 0° is useful. The 0° (p,n) reaction at 100 to 200 MeV provides a way to measure the Gamow-Teller matrix element whose energetic limitations are far less severe than those of β decay.

Nonetheless, we have seen that the results reported here for the $^{17}O(p,n)^{17}F$ reaction do not reveal any obvious neglected Gamow-Teller strength for this case. The ground state analog transition only reconfirms the β decay results. Furthermore, the 0° spectrum does not contain enough strength within the first 14 MeV of excitation to account for the total strength expected from the sum rule. The $^9Be(p,n)^9B$ reaction shows a similar absence of Gamow-Teller strength in the first 18 MeV of excitation. Should core excitations allow β^+ decay, we would expect to measure more Gamow-Teller strength with the (p,n) reaction. We would not in any case expect less.

Sum rules such as equation $III-4$ are always of very general dynamical significance. Such an expression represents the strength of a force in terms which are independent of the particular motions of the system involved.

The Gamow-Teller sum rule may be compared to the Thomas-Kuhn sum rule for the oscillator strengths of optical dispersion,

$$\sum_{\text{absorption}} f_i \; - \sum_{\text{emission}} f_j \; = \; Z$$

This equation expresses the condition that at high frequencies the dispersion should reproduce the classical result of W. Thomas for X-ray scattering. This sum rule is a statement of the total electromagnetic force producing the dispersion and its simple form is the result of dynamic simplifications at X-ray frequencies. Similarly, for the (p,n) reaction at 135 MeV, the description of the 0° cross section has provided a fairly simple and direct measure of the isovector spin-spin part of the nuclear force. The deficiency of Gamow-Teller strength in spin-flip transitions could therefore very well indicate a general misunderstanding of the nature of the nucleus itself. This suspicion is corroborated by the fact that this violation of the $\langle \sigma\tau \rangle$ sum rule has been seen in a number of other nuclei.

The (p,n) reaction in this instance may be regarded as a device to count neutron excess in much the same way that X-ray scattering may be used to count the electrons of an atomic element. Any neutron of ^{17}O is a candidate for charge exchange (or a less likely knock-out) unless this transition be Pauli blocked by a core proton of like motion. It has been suggested that the lack of so called Gamow-Teller strength is owing to the lack of neutrons, *i.e.* that nucleon motion in the nucleus is comprised partly of Δ degrees of freedom[BOH81]. Others feel that the missing strength can be at least partially accounted for by considering transitions into the continuum. For example, Osterfeld [OST82] calculated the continuous parts of the $^{40}Ca(p,n)$ and $^{48}Ca(p,n)$ spectra at 160 MeV on the basis of a simple microscopic independent particle model for these nuclei. He concludes that most of the background subtracted in the experimental analysis of the $^{48}Ca(p,n)$ Gamow-Teller resonance is actually Gamow-Teller strength. Including this strength, however, still accounts for only about one half of the predicted strength. In the case of $^{90}Zr(p,n)$ at 200 MeV Bertsch and Hamamoto conclude, on the basis of a perturbative independent particle calculation, that roughly half of the Gamow-Teller strength is shifted to the region of 10 to 45 MeV of excitation in the product nucleus Niobium [BER82]. The Gamow-Teller peak is at 5.1 MeV. Thus it seems that a substantial amount of Gamow-Teller strength may lie at higher excitation energies. If we looked at even higher excitation energies we might find all the sum rule strength. Looking at higher excitation energies is complicated by the presence of higher angular momentum transfer contributions to the cross section.

Whatever the solution proves to be, the ubiquity of this phenomenon indicates that finding this missing Gamow-Teller strength will reveal a very general feature

of nuclear dynamics.

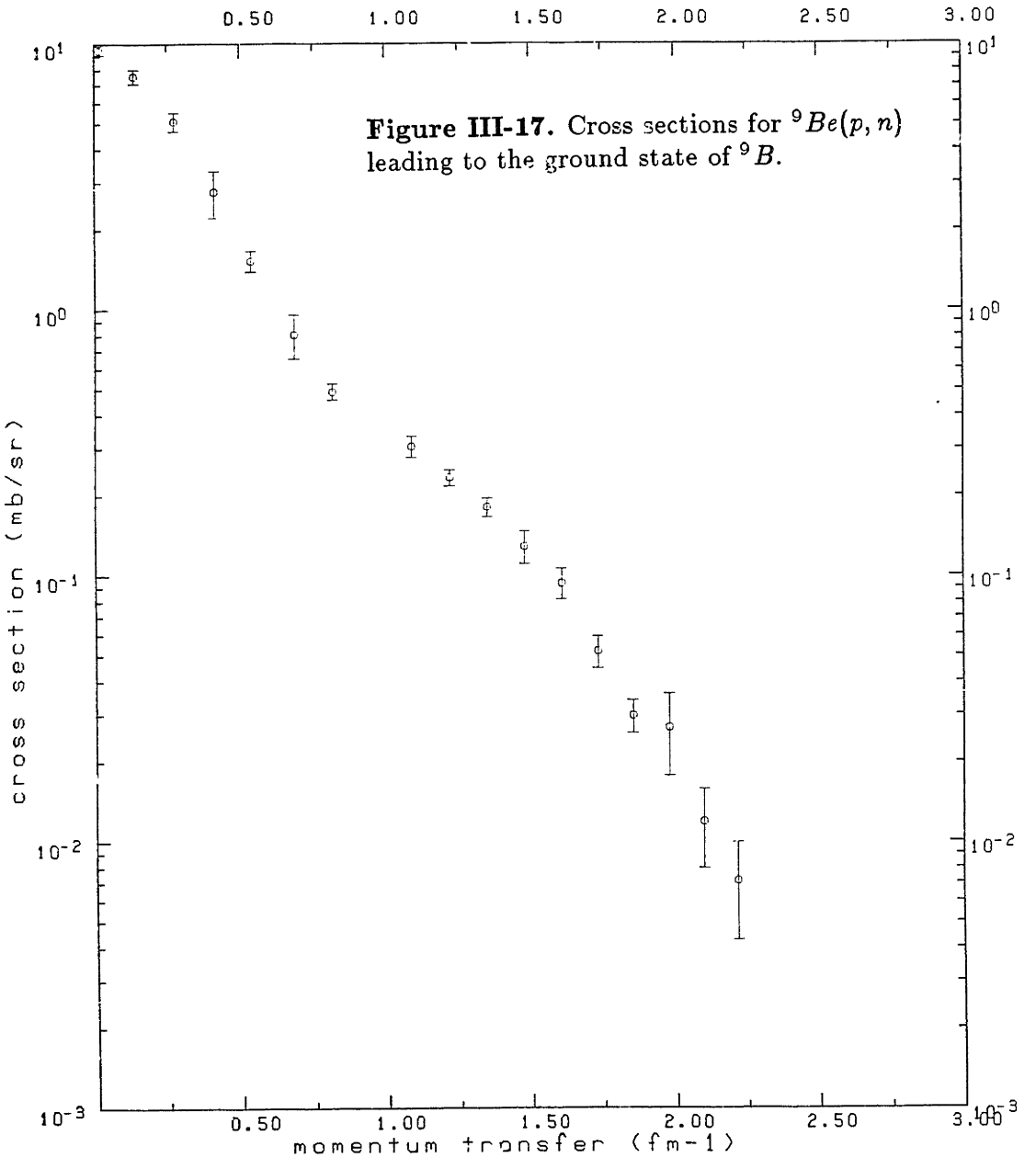

Figure III-17. Cross sections for $^9Be(p,n)$ leading to the ground state of ^9B.

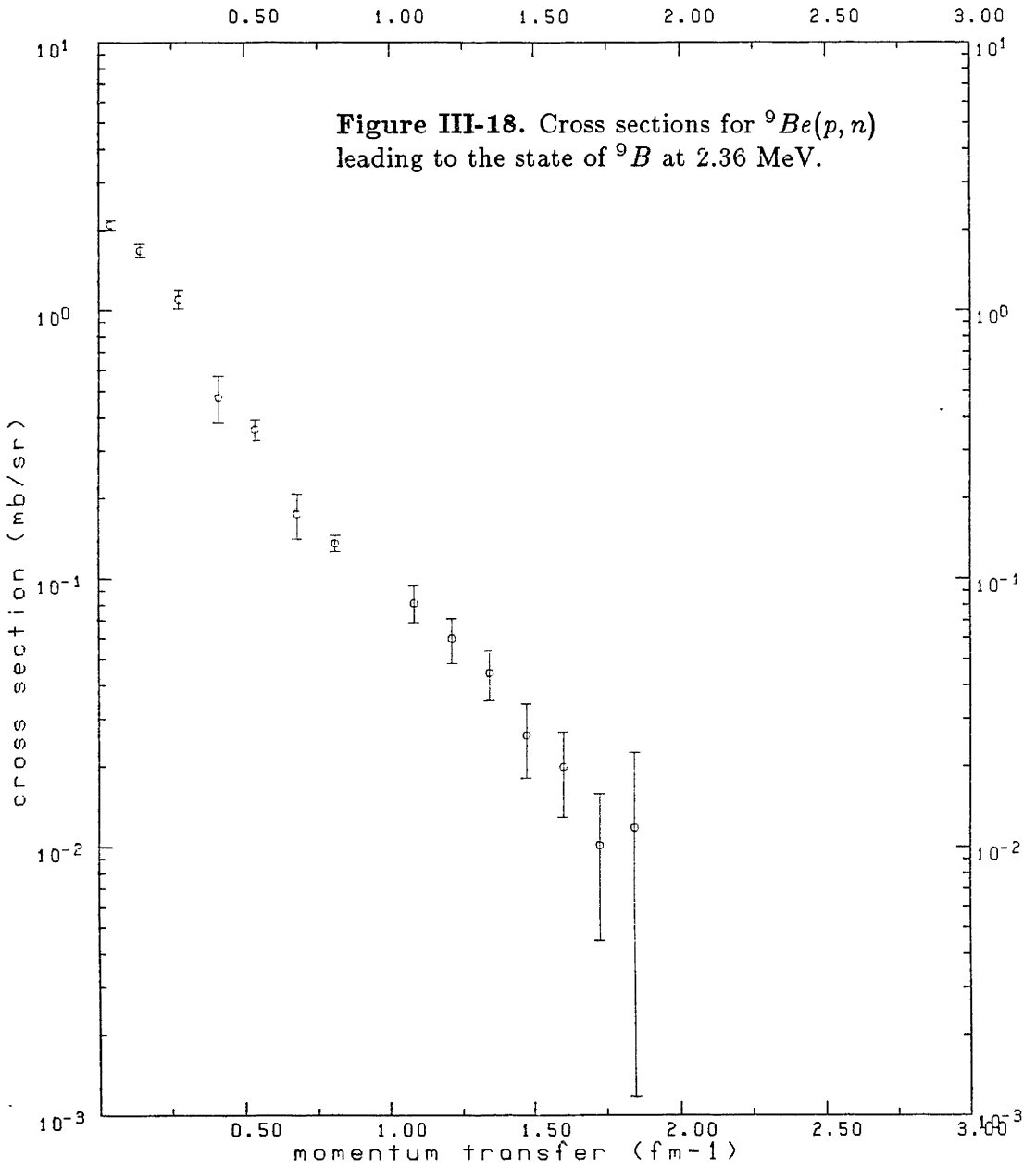

Figure III-18. Cross sections for $^9Be(p,n)$ leading to the state of ^9B at 2.36 MeV.

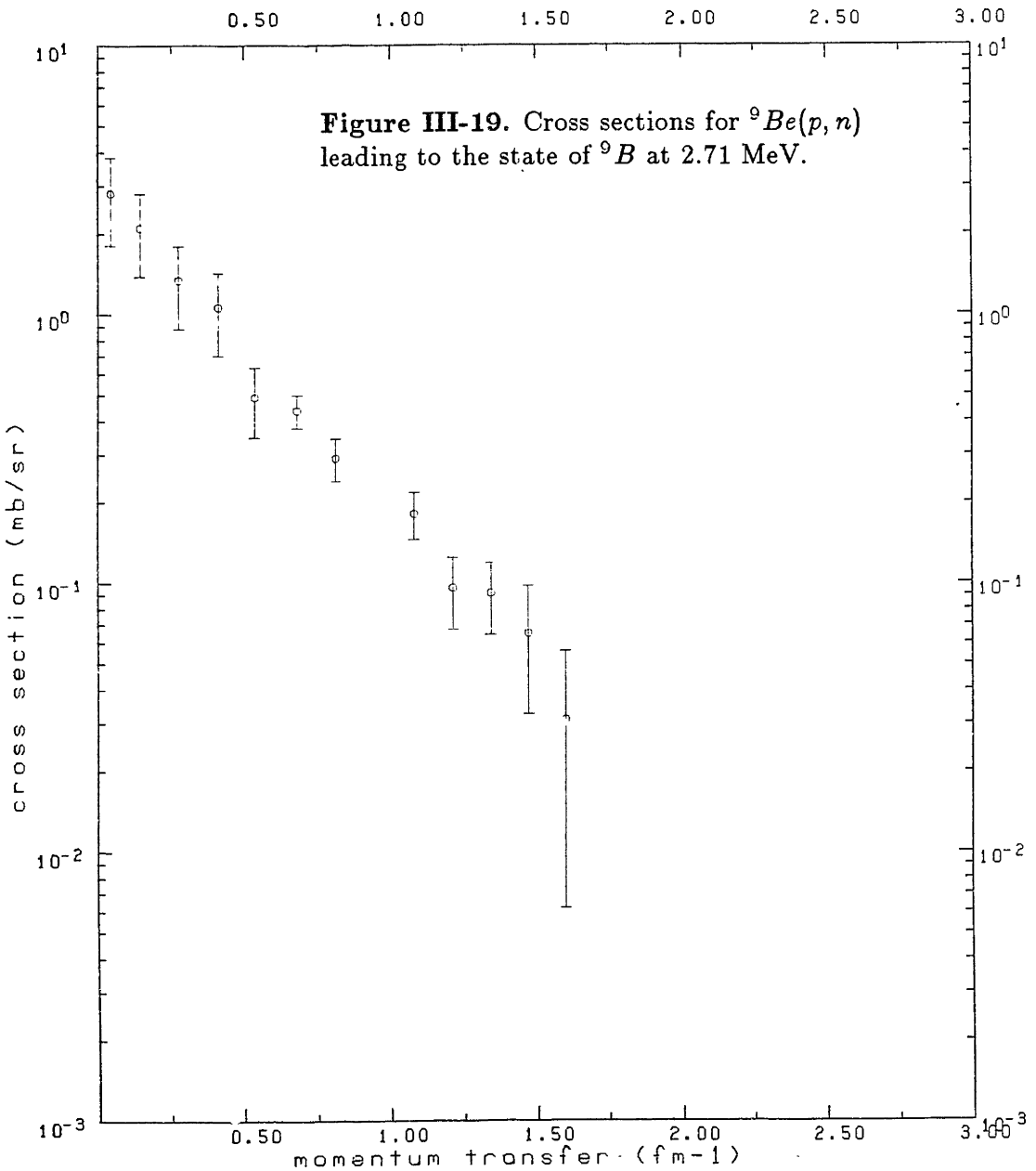

Figure III-19. Cross sections for $^9Be(p,n)$ leading to the state of ^9B at 2.71 MeV.

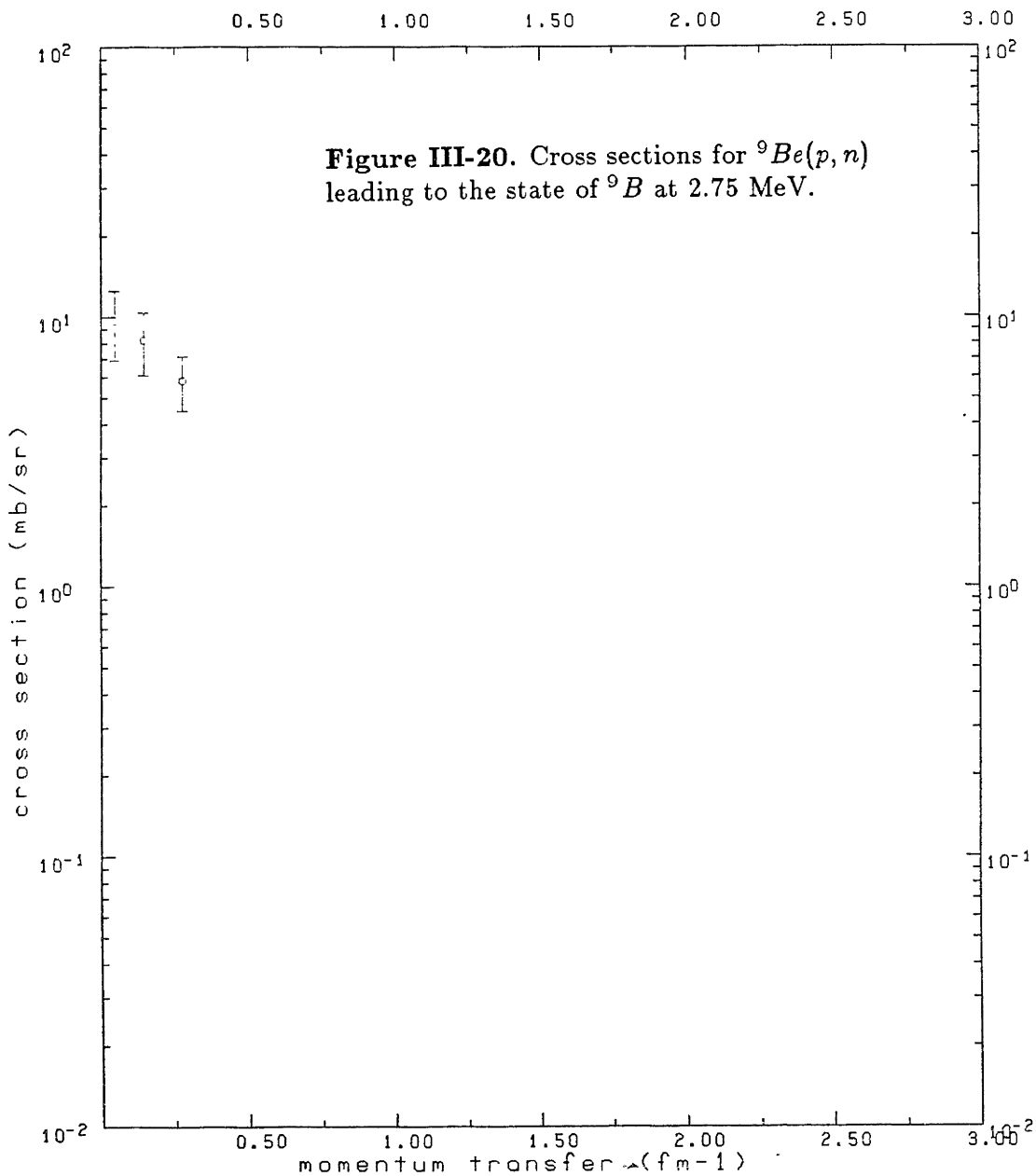

Figure III-20. Cross sections for $^9Be(p,n)$ leading to the state of ^9B at 2.75 MeV.

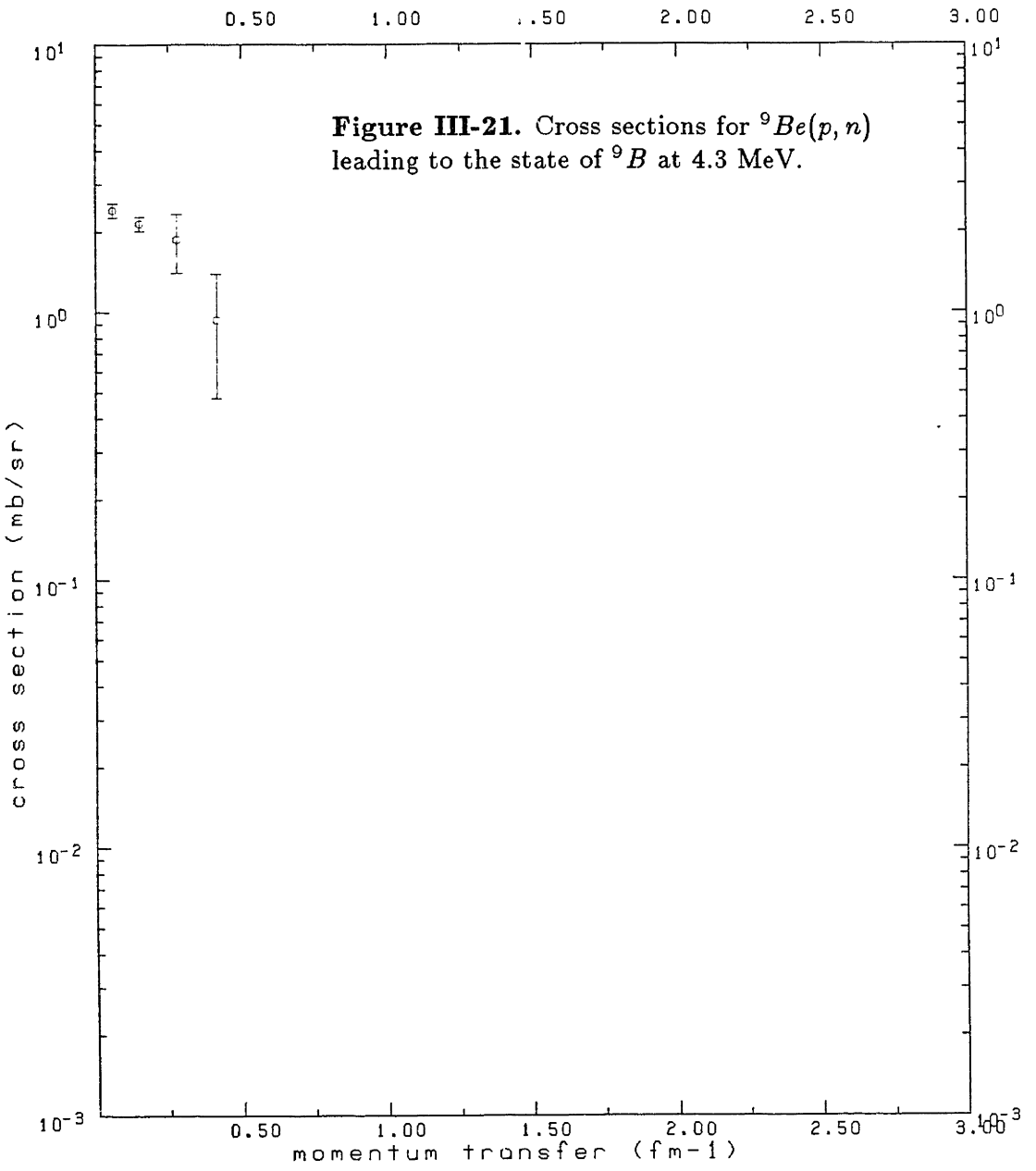

Figure III-21. Cross sections for $^9Be(p,n)$ leading to the state of ^9B at 4.3 MeV.

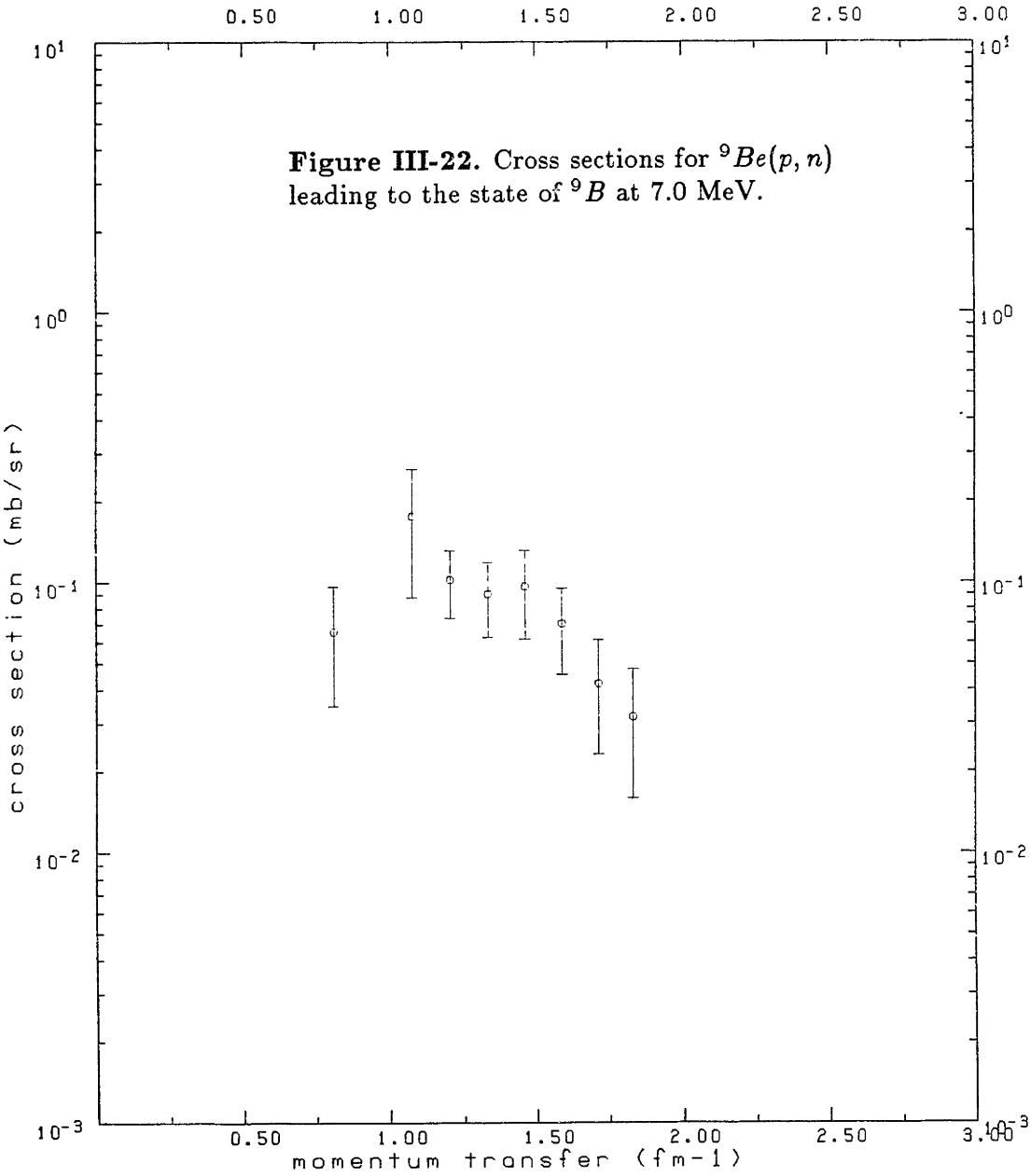

Figure III-22. Cross sections for $^9Be(p,n)$ leading to the state of ^9B at 7.0 MeV.

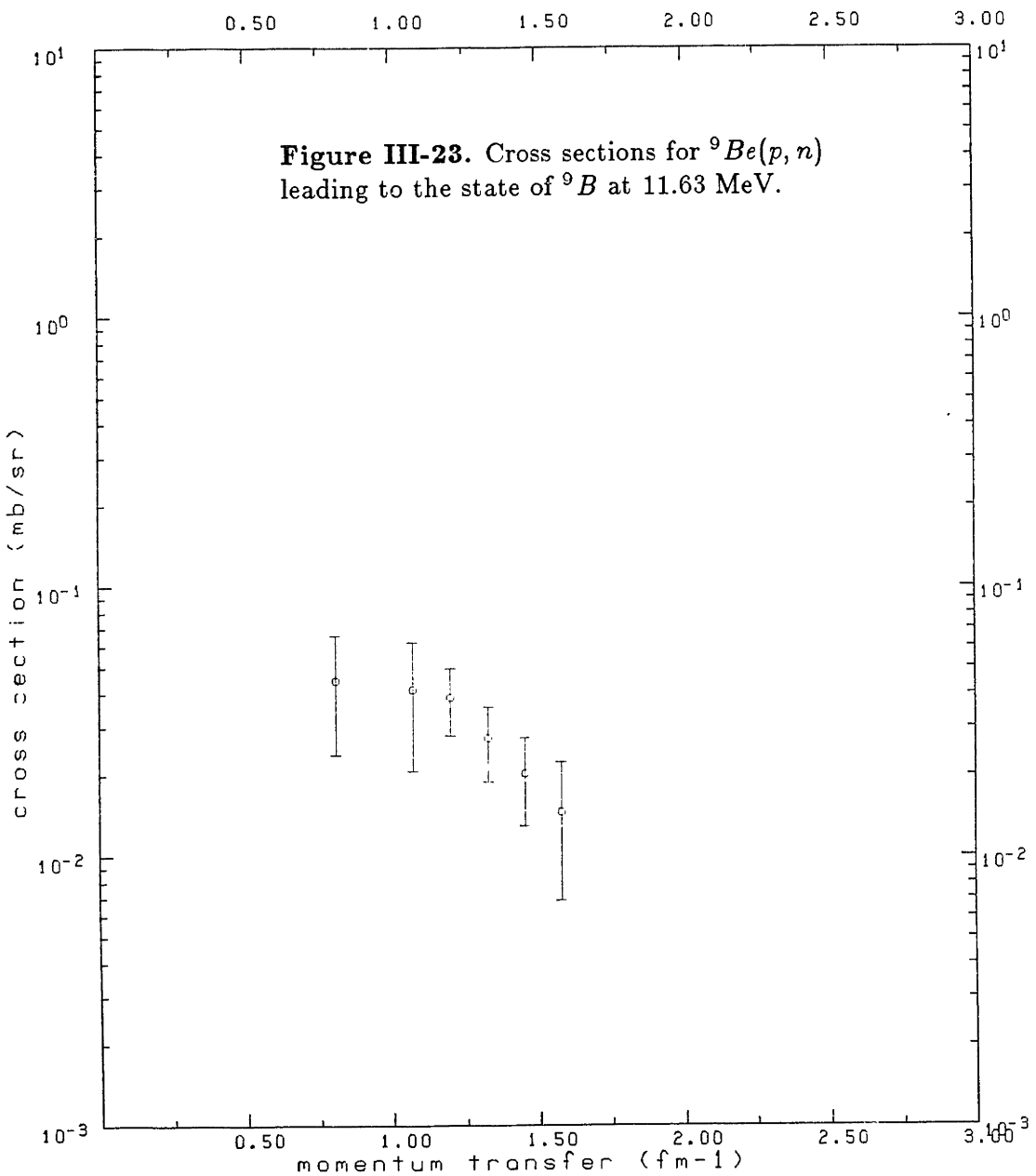

Figure III-23. Cross sections for $^9Be(p,n)$ leading to the state of ^9B at 11.63 MeV.

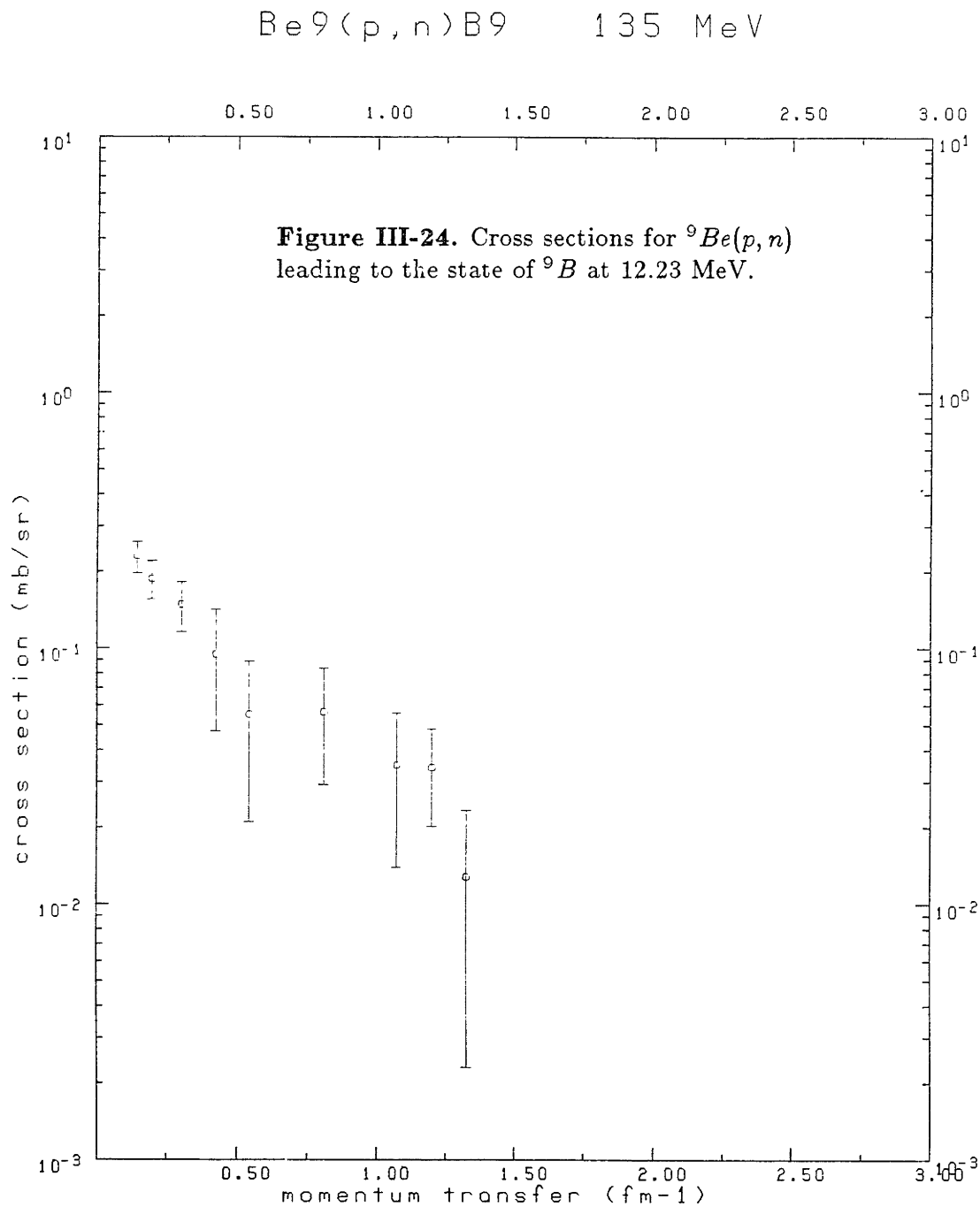

Figure III-24. Cross sections for $^9Be(p,n)$ leading to the state of ^9B at 12.23 MeV.

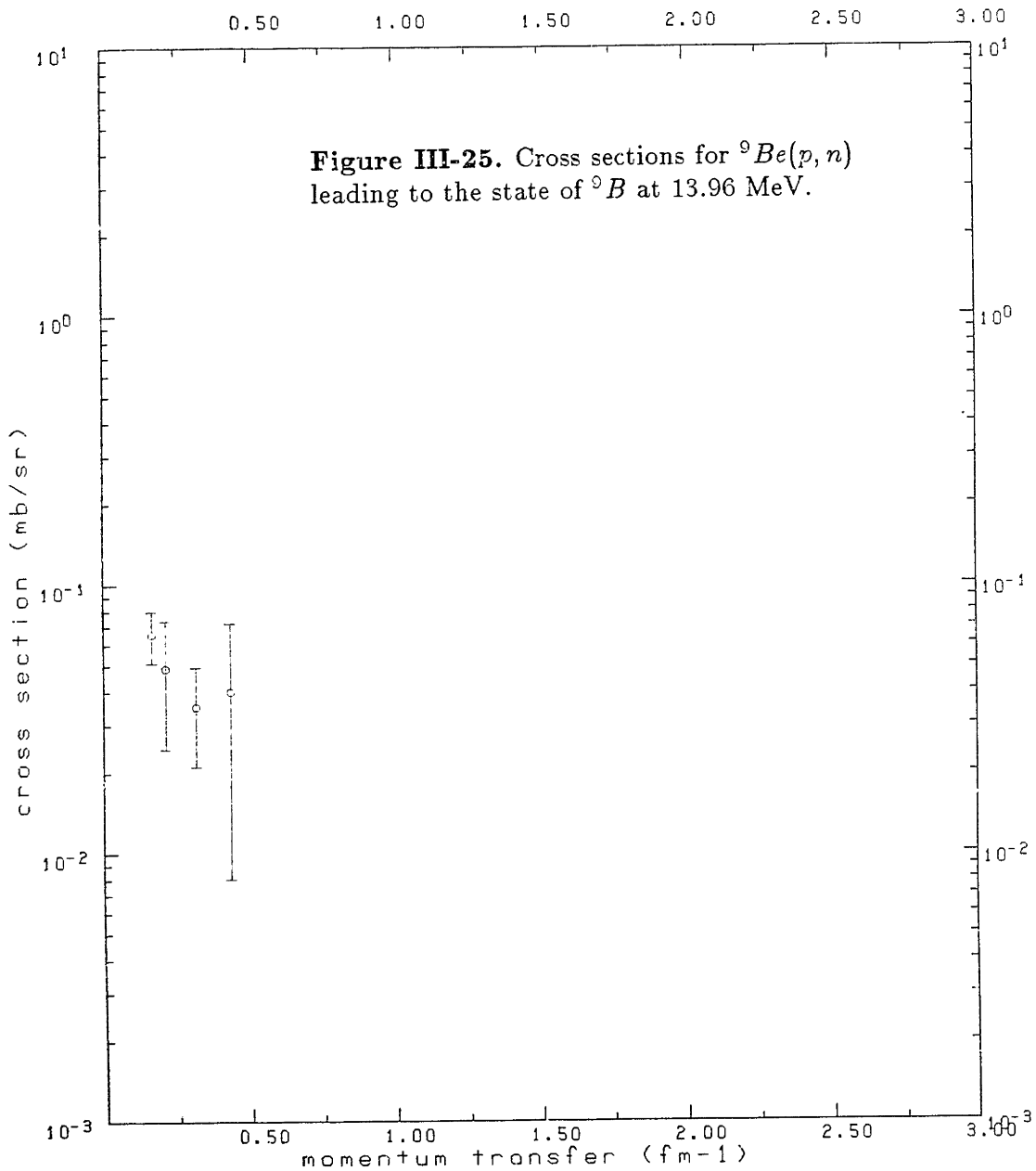

Figure III-25. Cross sections for $^9Be(p,n)$ leading to the state of ^9B at 13.96 MeV.

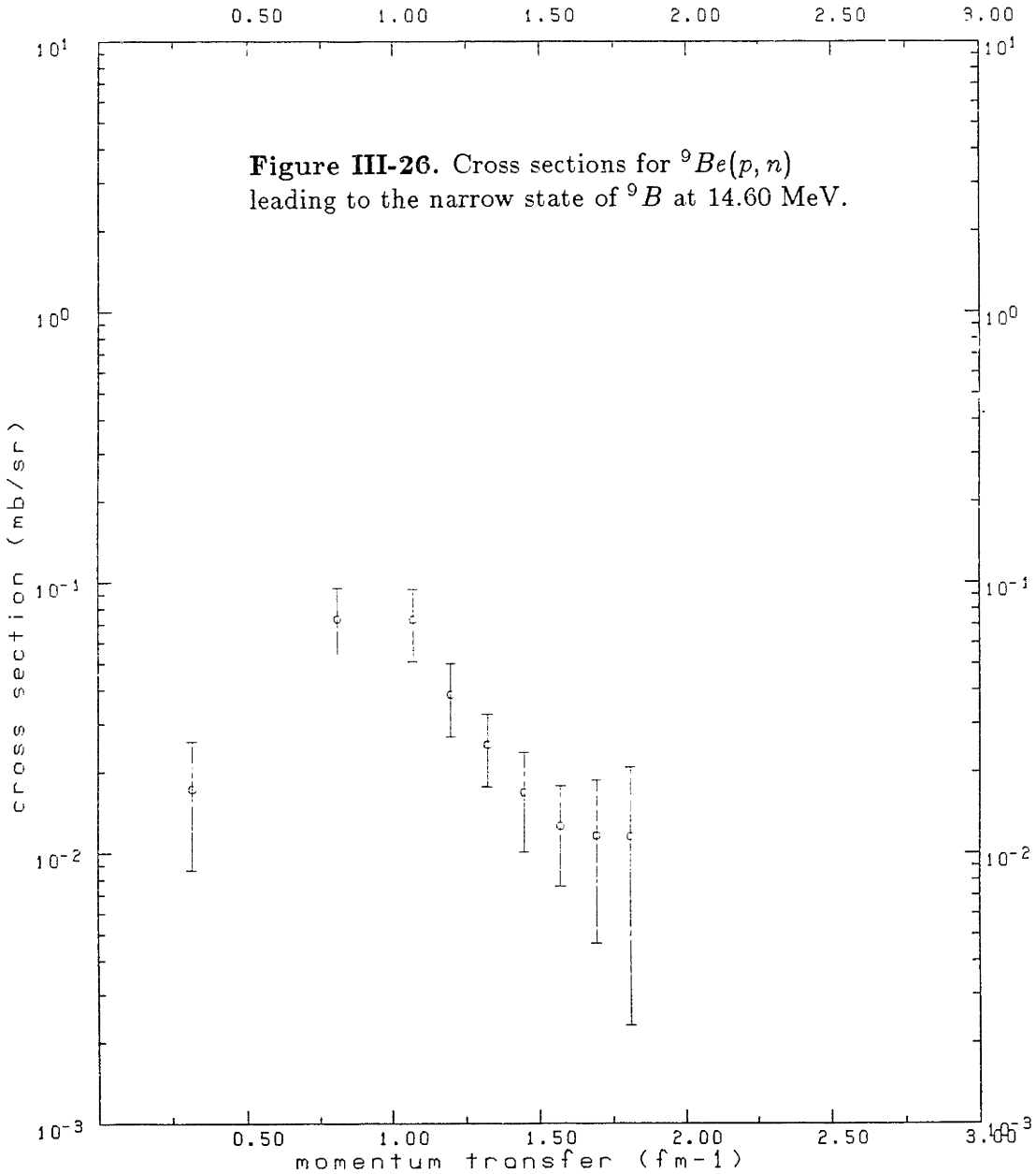

Figure III-26. Cross sections for $^9Be(p,n)$ leading to the narrow state of ^9B at 14.60 MeV.

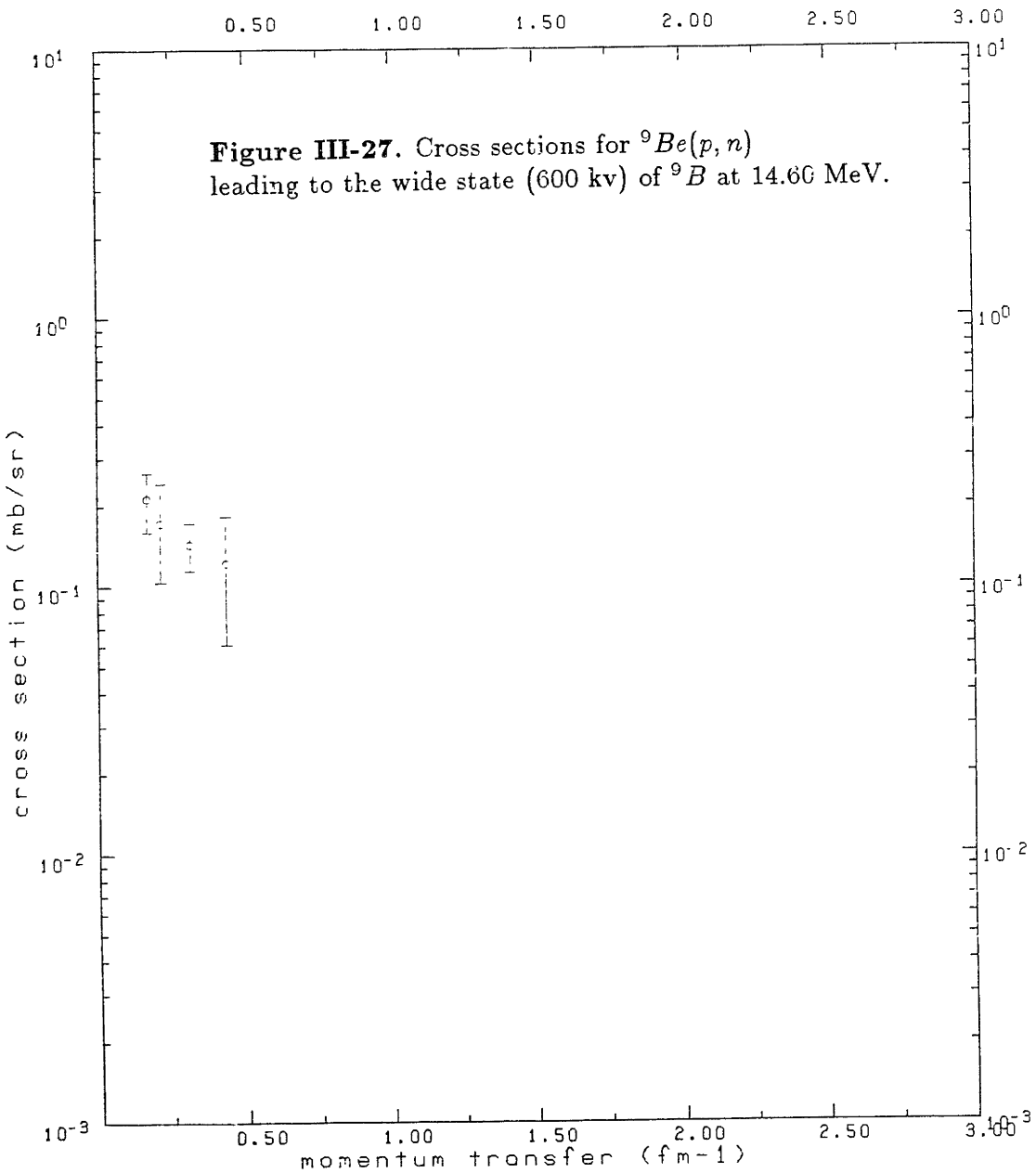

Figure III-27. Cross sections for $^9Be(p,n)$ leading to the wide state (600 kv) of ^9B at 14.60 MeV.

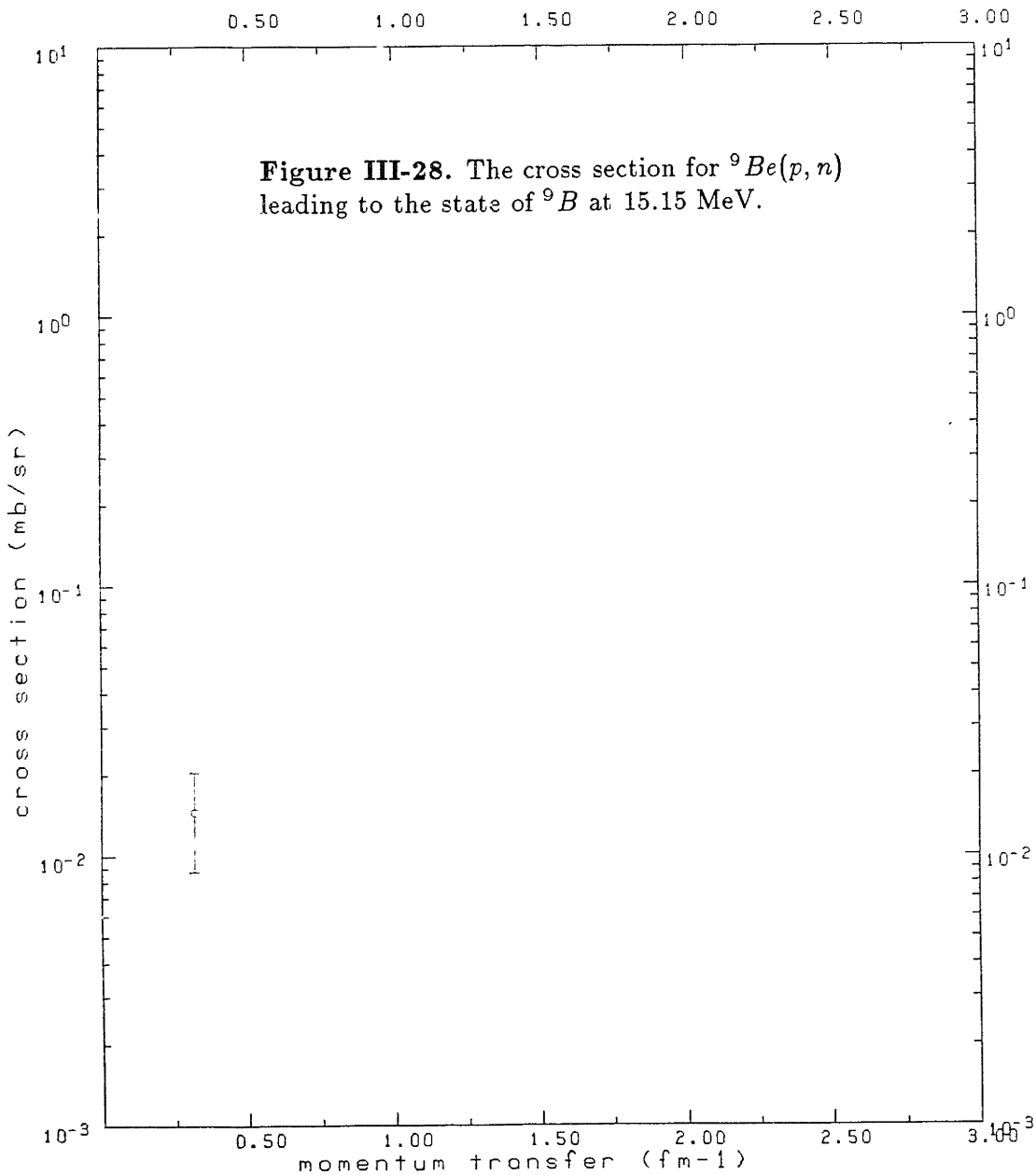

Figure III-28. The cross section for $^9Be(p,n)$ leading to the state of ^9B at 15.15 MeV.

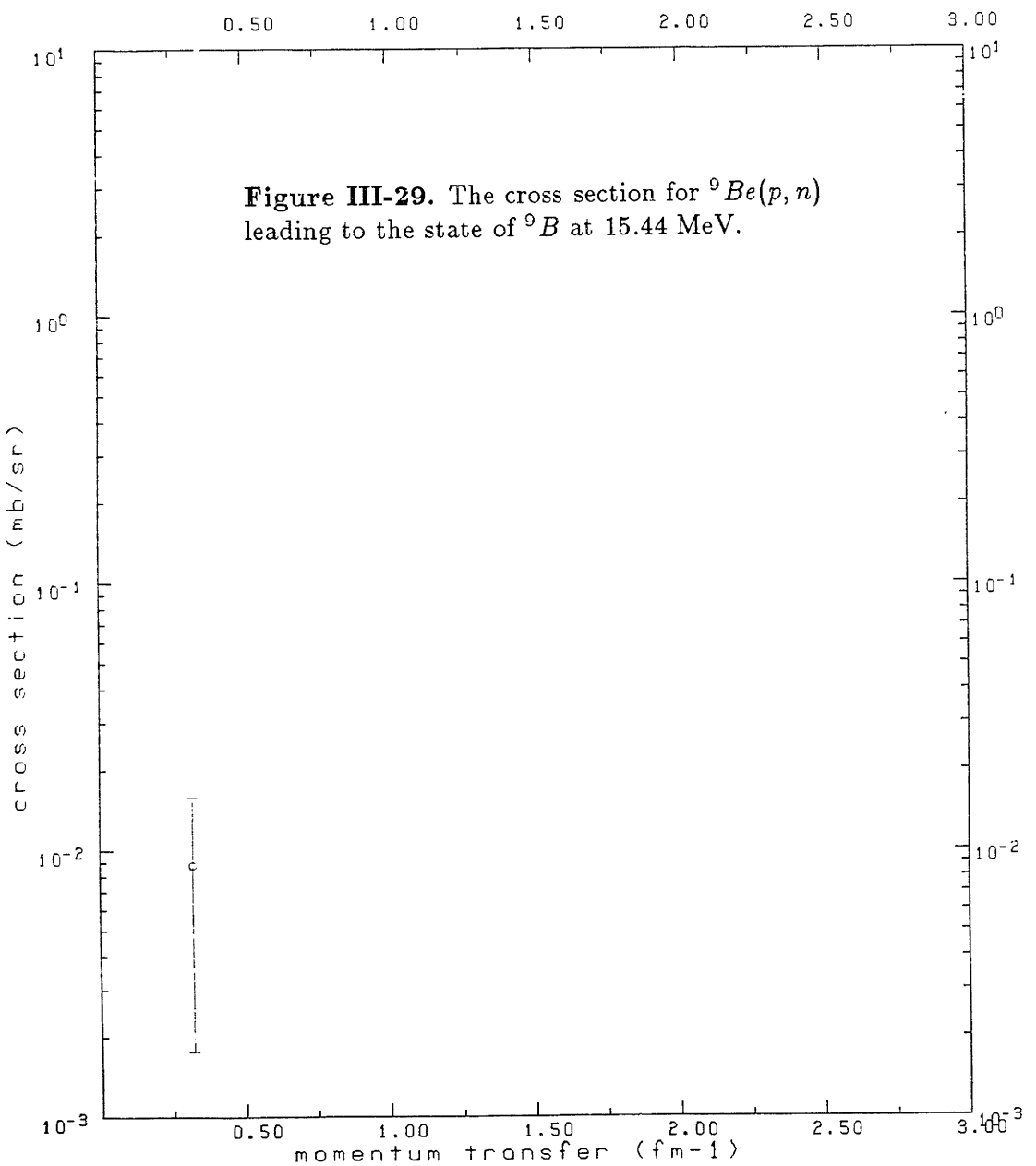

Figure III-29. The cross section for $^9Be(p,n)$ leading to the state of ^9B at 15.44 MeV.

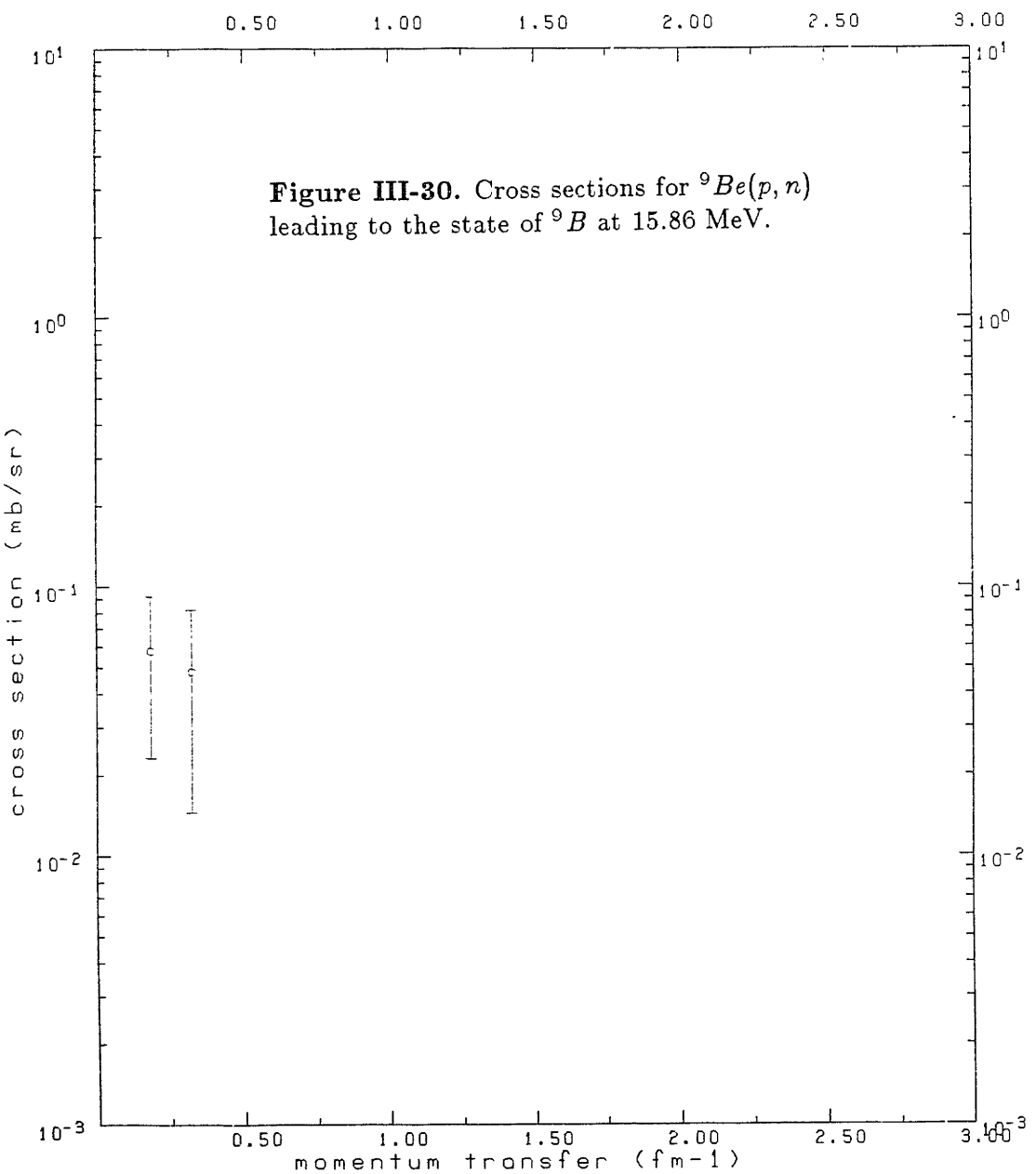

Figure III-30. Cross sections for $^9Be(p,n)$ leading to the state of ^9B at 15.86 MeV.

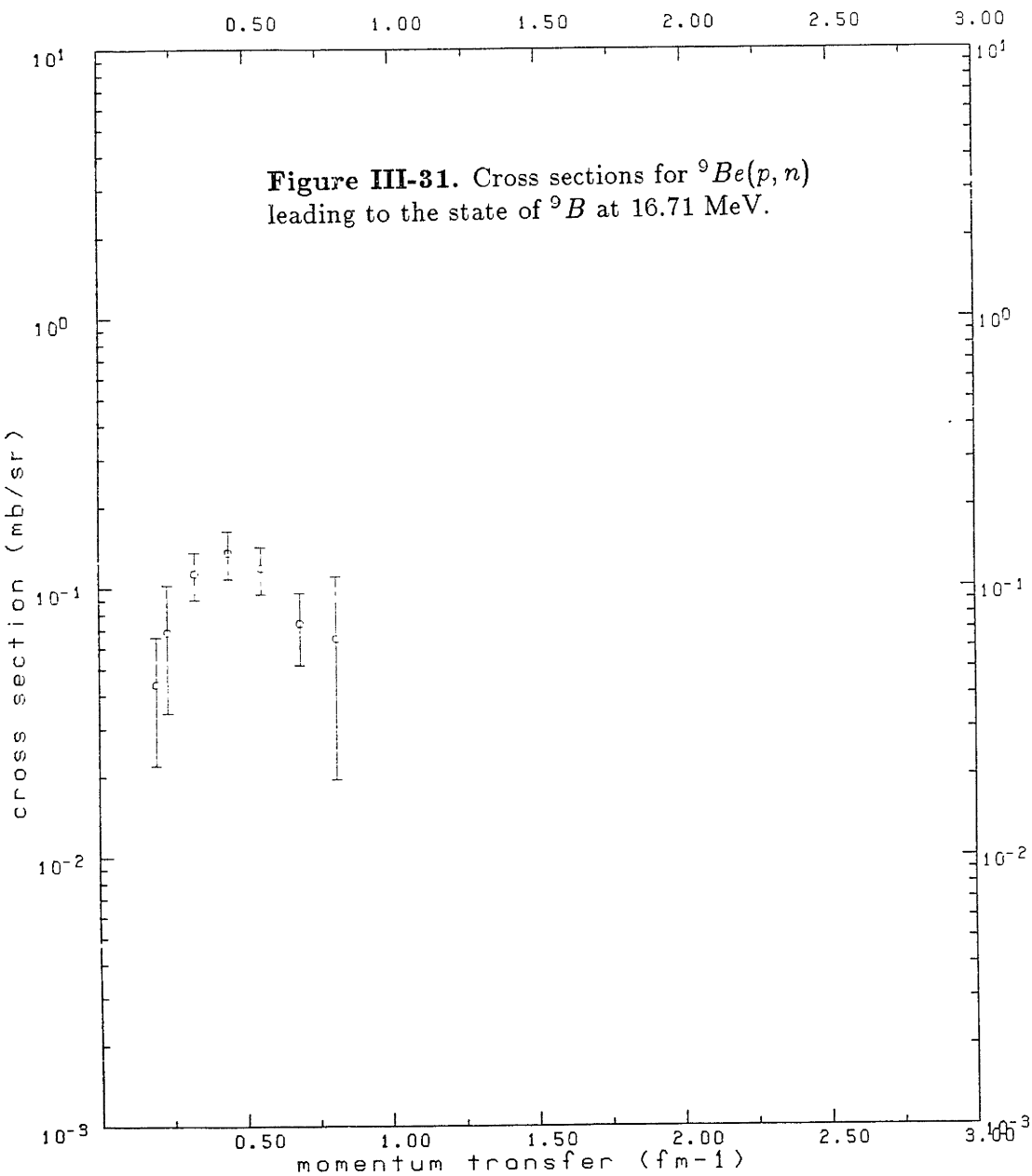

Figure III-31. Cross sections for $^9Be(p,n)$ leading to the state of ^9B at 16.71 MeV.

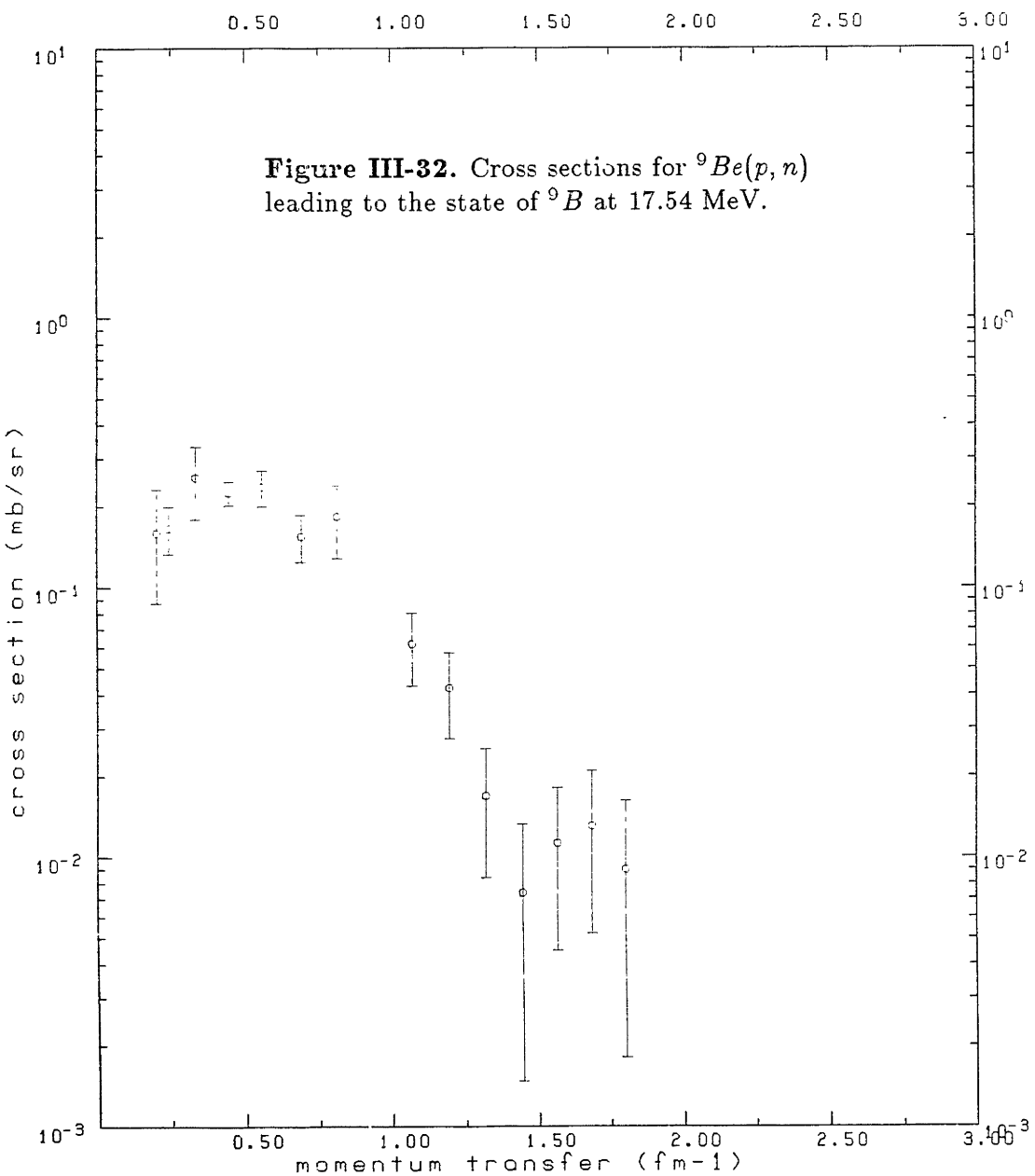

Figure III-32. Cross sections for $^9Be(p,n)$ leading to the state of ^9B at 17.54 MeV.

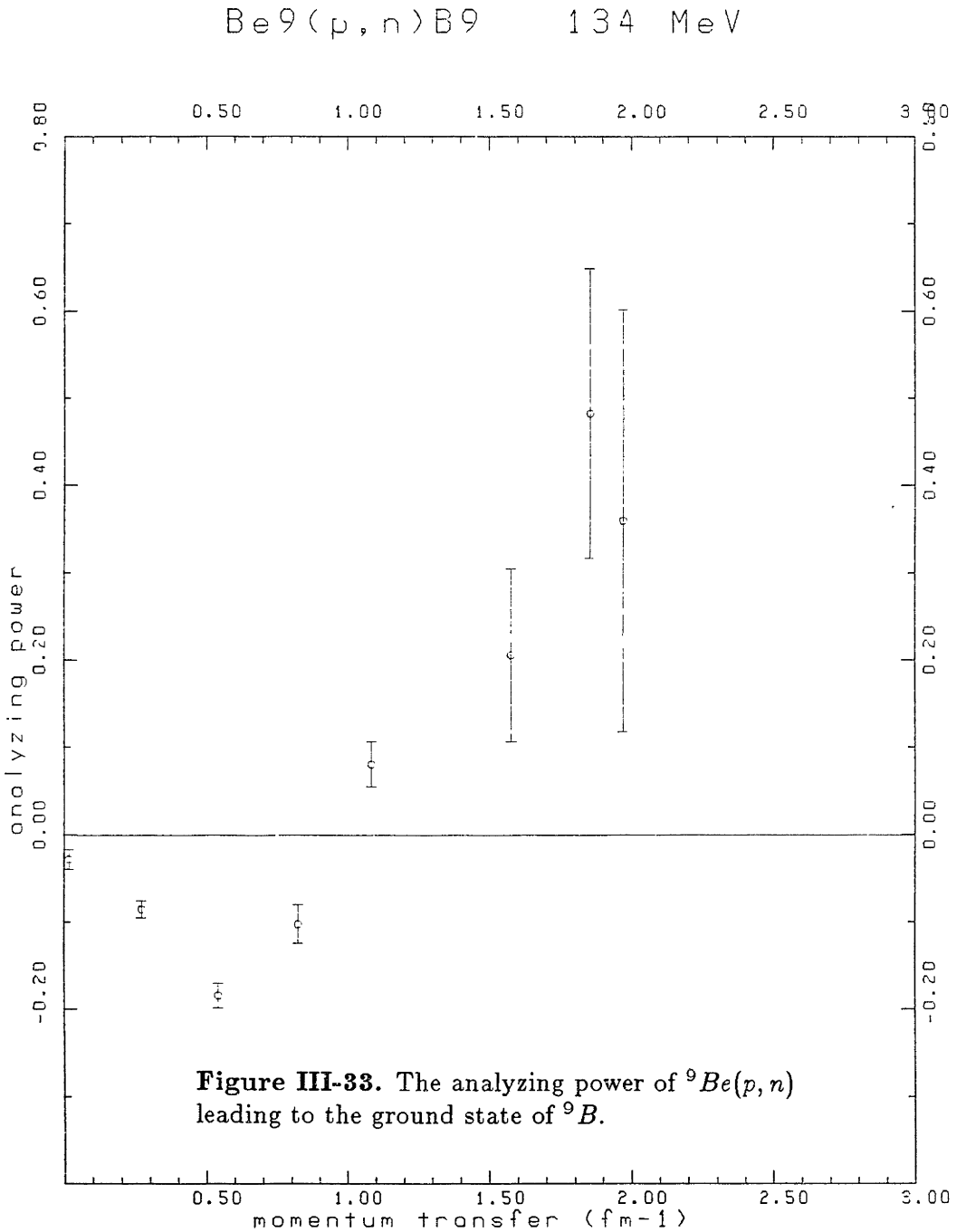

Figure III-33. The analyzing power of $^9Be(p,n)$ leading to the ground state of ^9B.

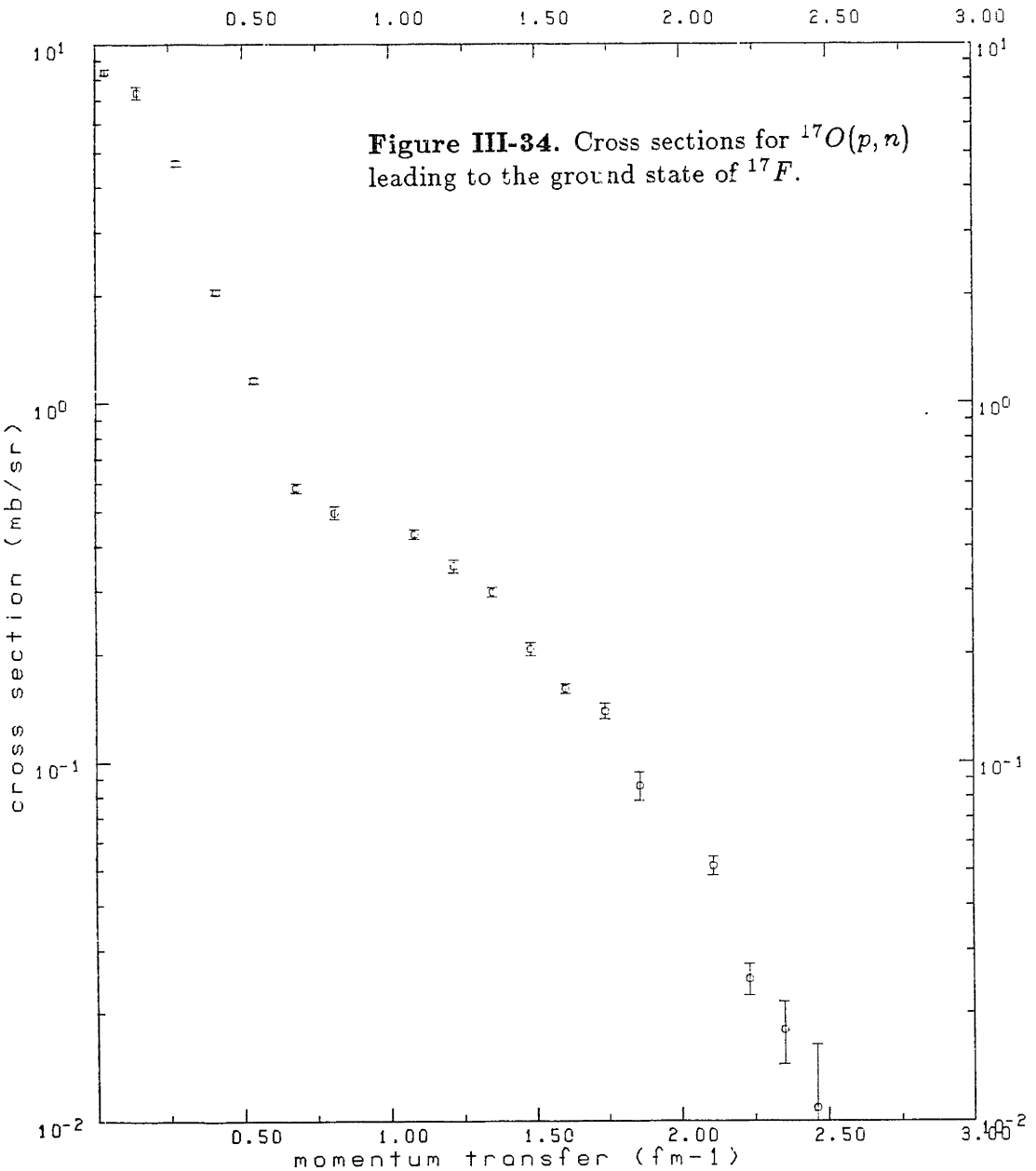

Figure III-34. Cross sections for $^{17}O(p,n)$ leading to the ground state of ^{17}F.

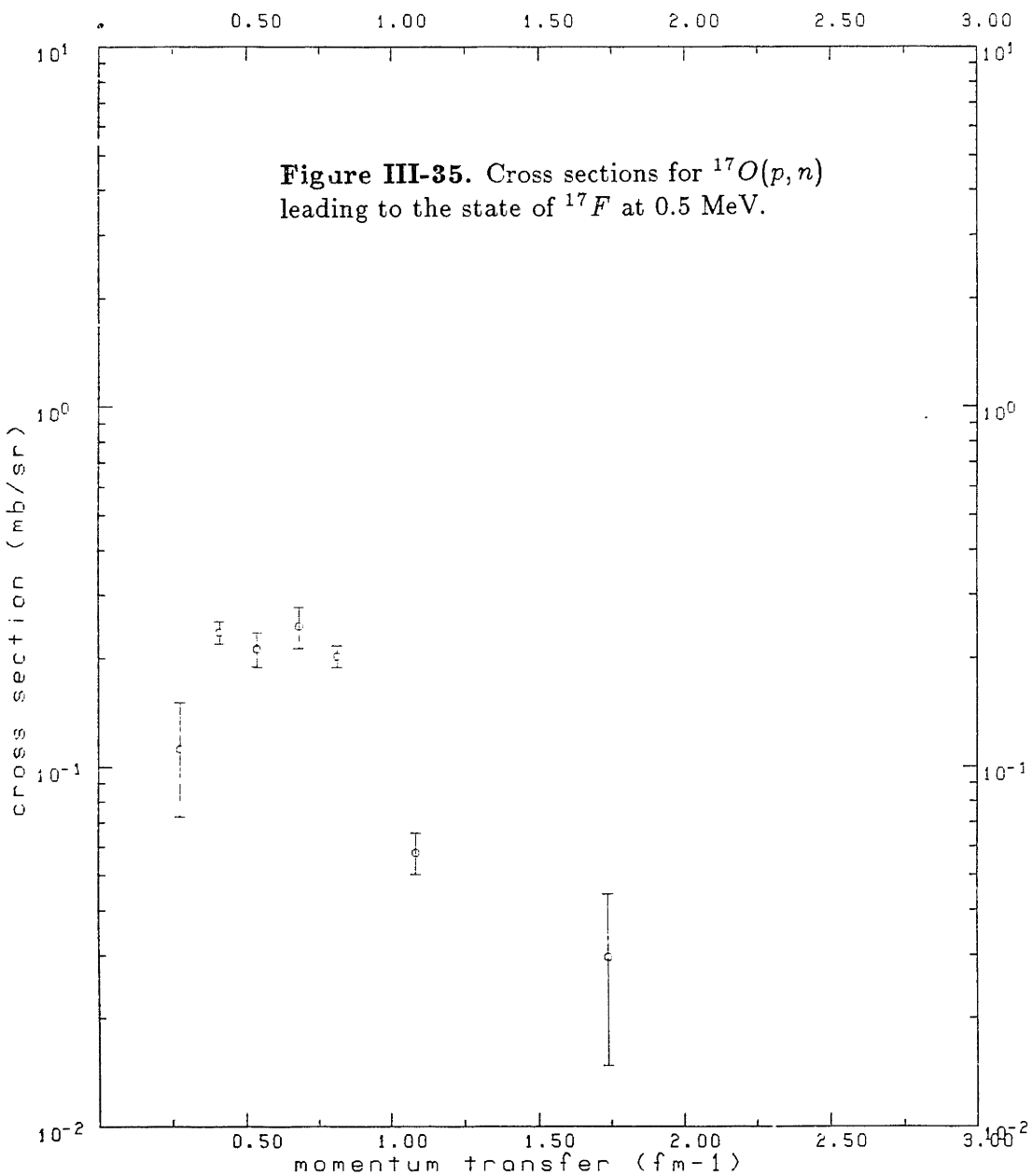

Figure III-35. Cross sections for $^{17}O(p,n)$ leading to the state of ^{17}F at 0.5 MeV.

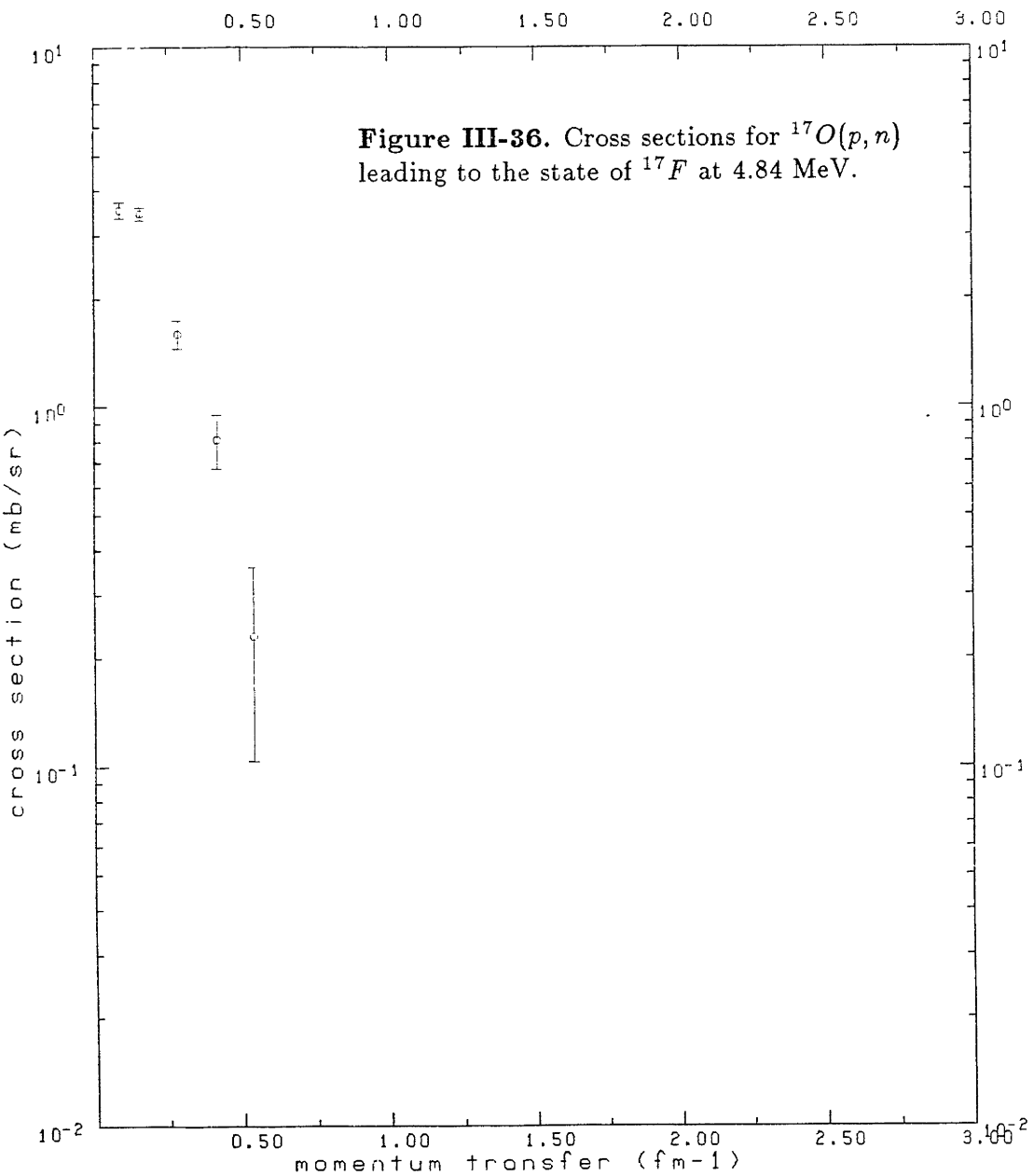

Figure III-36. Cross sections for $^{17}O(p,n)$ leading to the state of ^{17}F at 4.84 MeV.

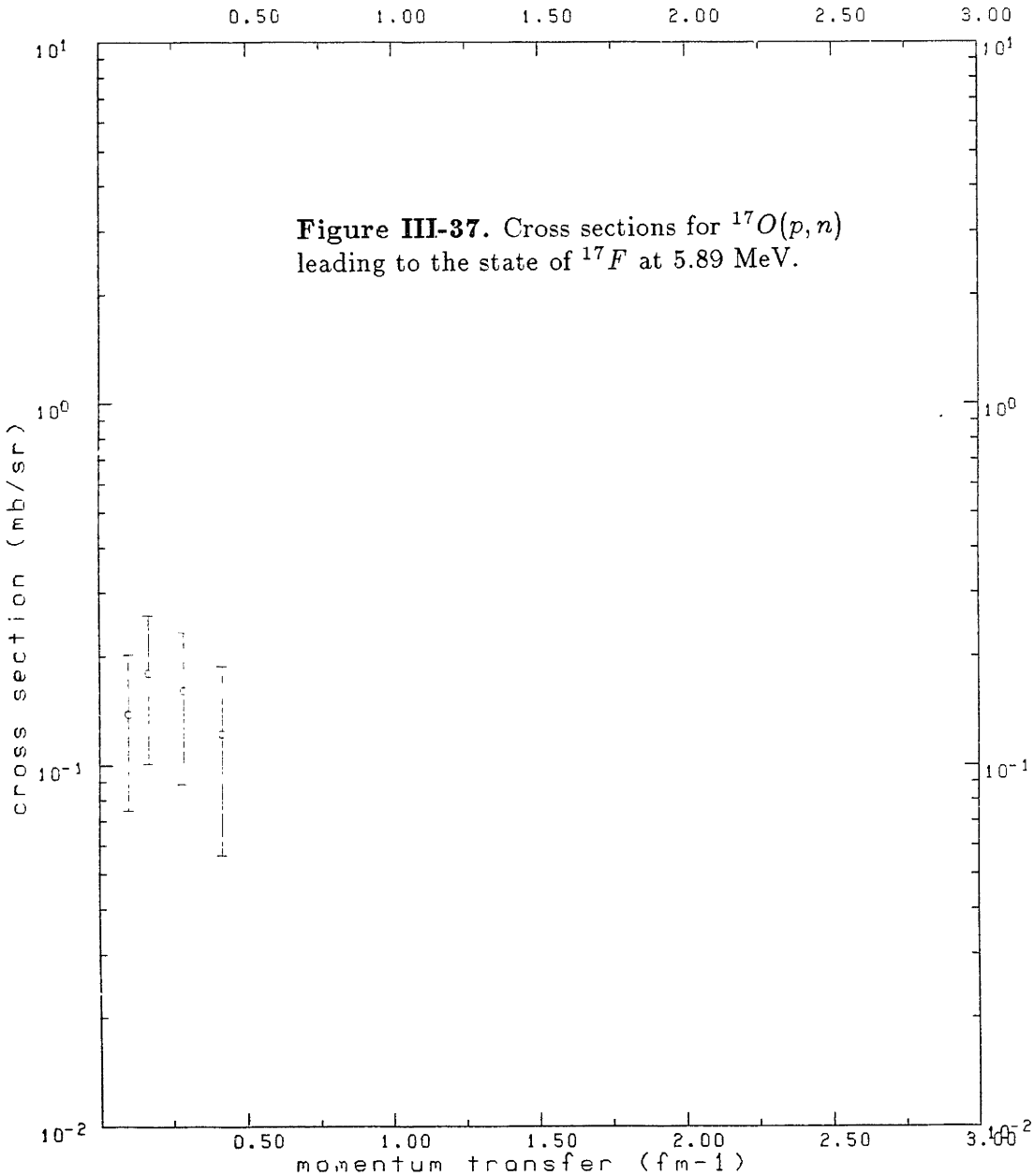

Figure III-37. Cross sections for $^{17}O(p,n)$ leading to the state of ^{17}F at 5.89 MeV.

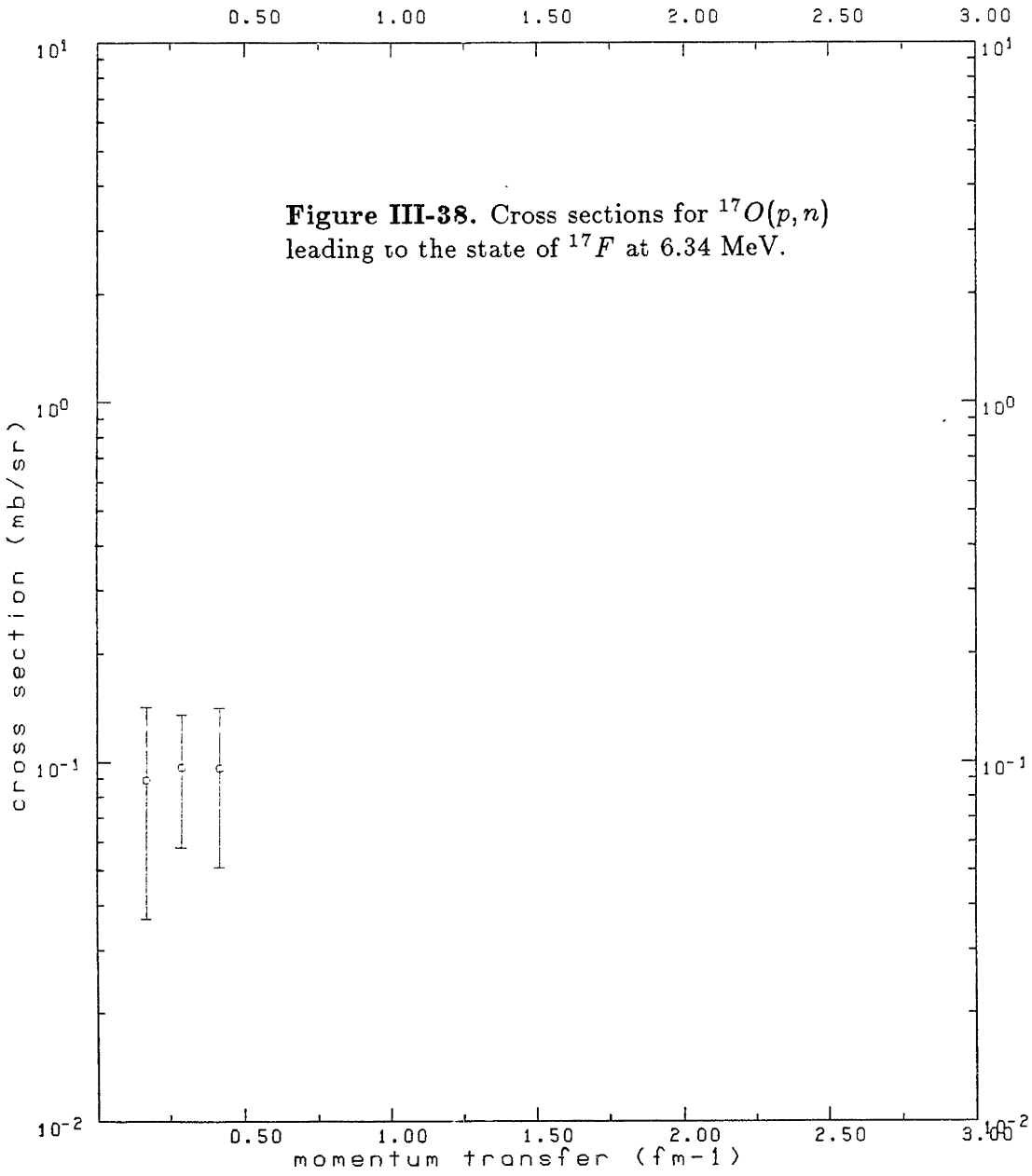

Figure III-38. Cross sections for $^{17}O(p,n)$ leading to the state of ^{17}F at 6.34 MeV.

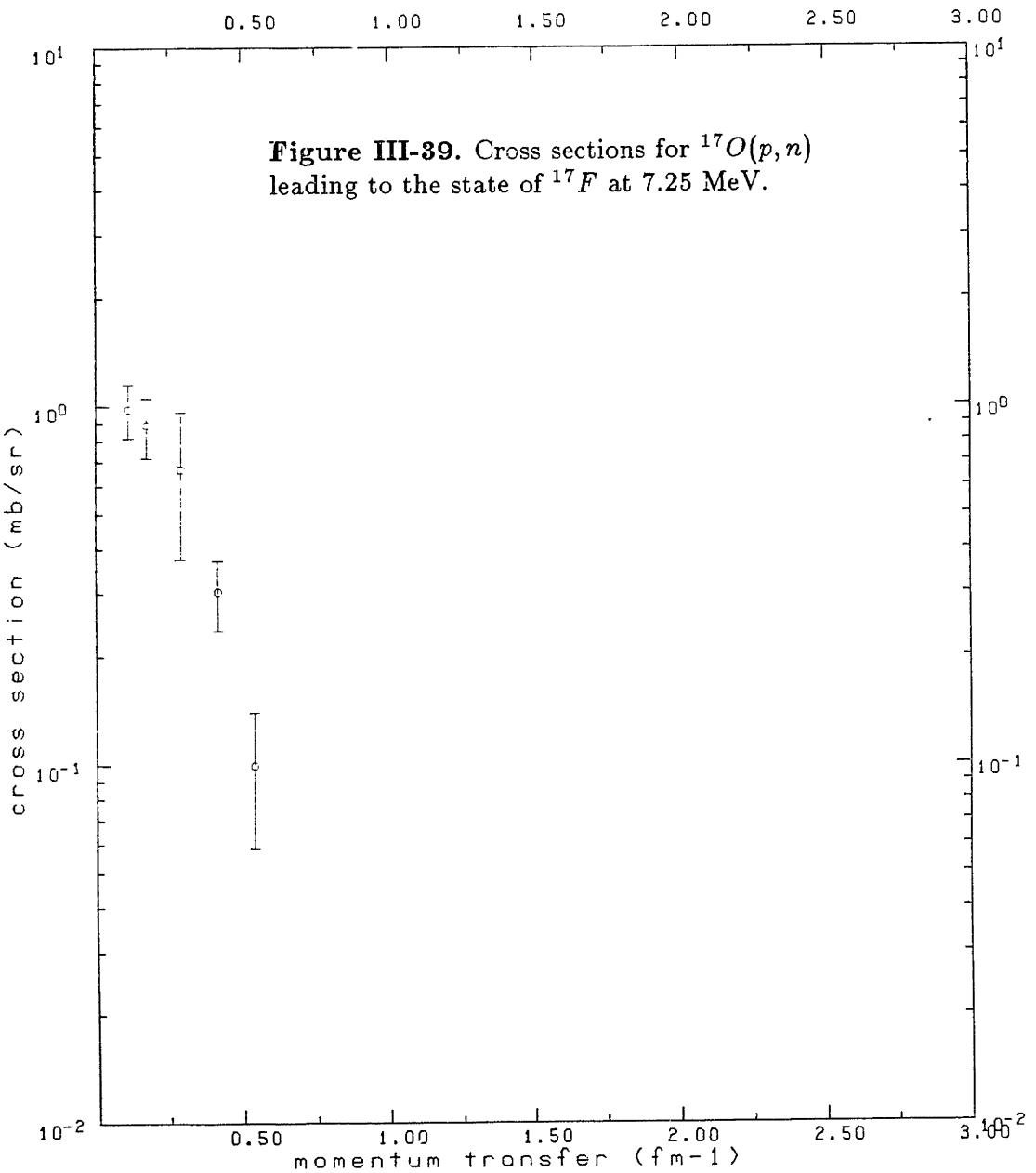

Figure III-39. Cross sections for $^{17}O(p,n)$ leading to the state of ^{17}F at 7.25 MeV.

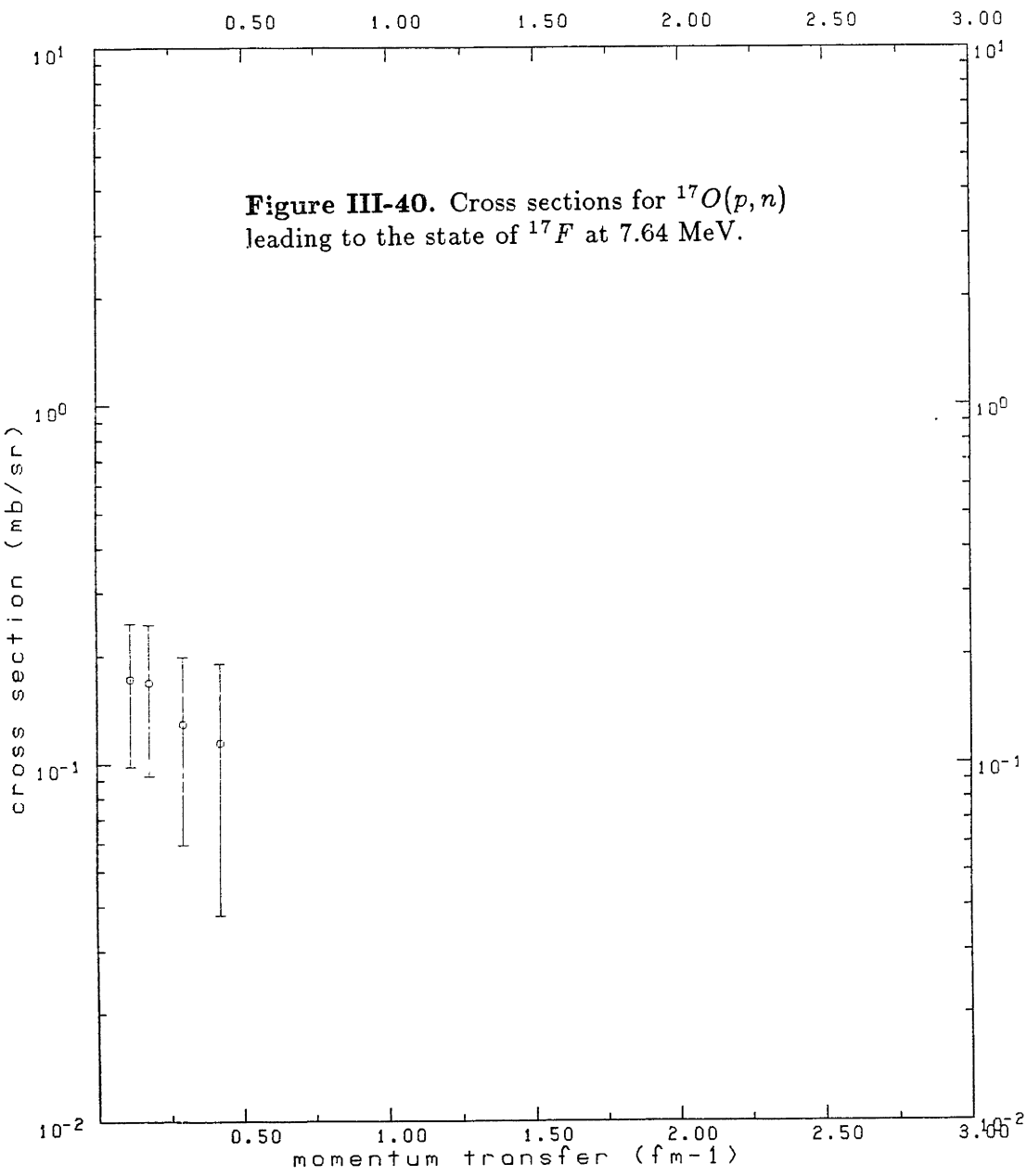

Figure III-40. Cross sections for $^{17}O(p,n)$ leading to the state of ^{17}F at 7.64 MeV.

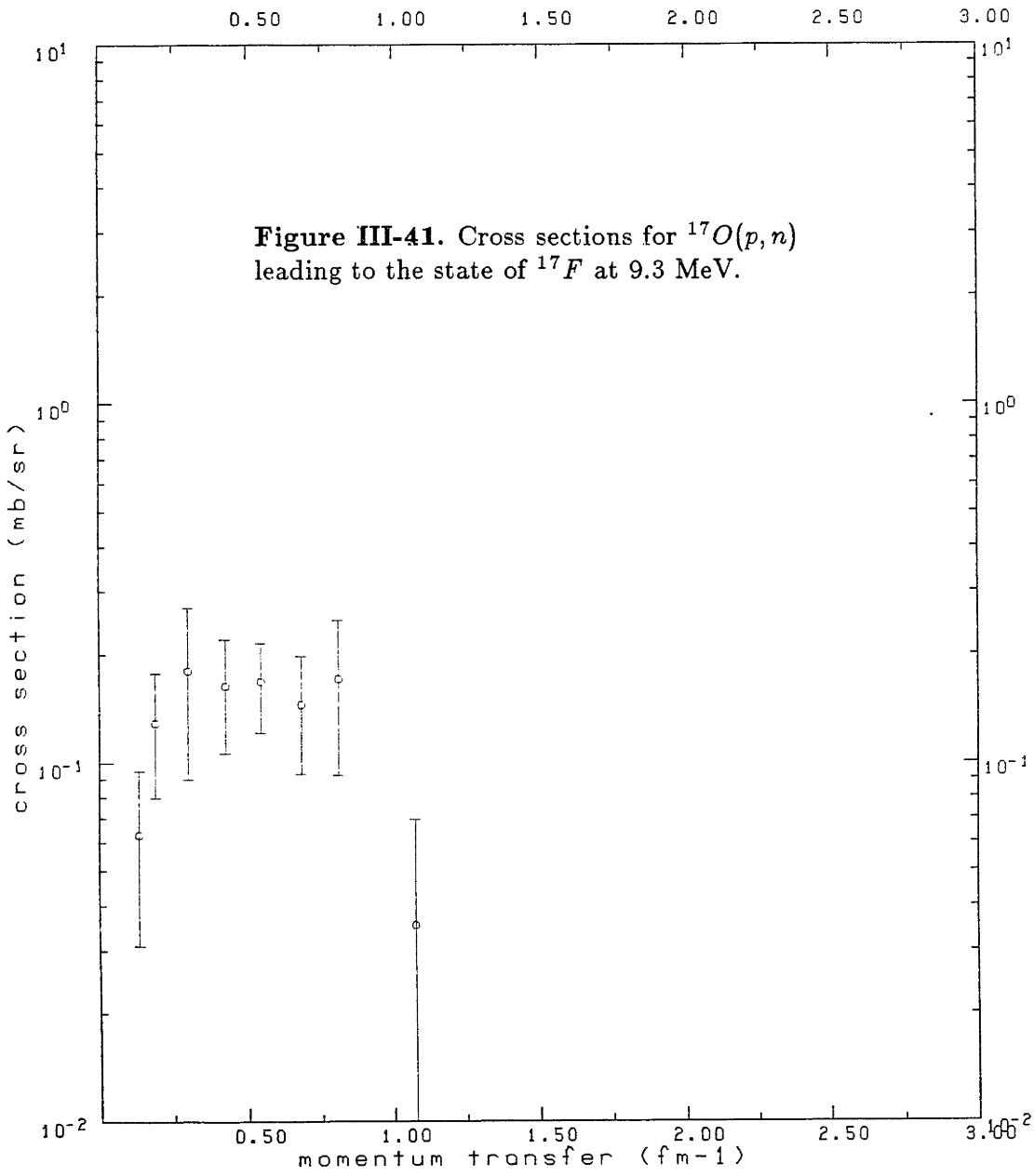

Figure III-41. Cross sections for $^{17}O(p,n)$ leading to the state of ^{17}F at 9.3 MeV.

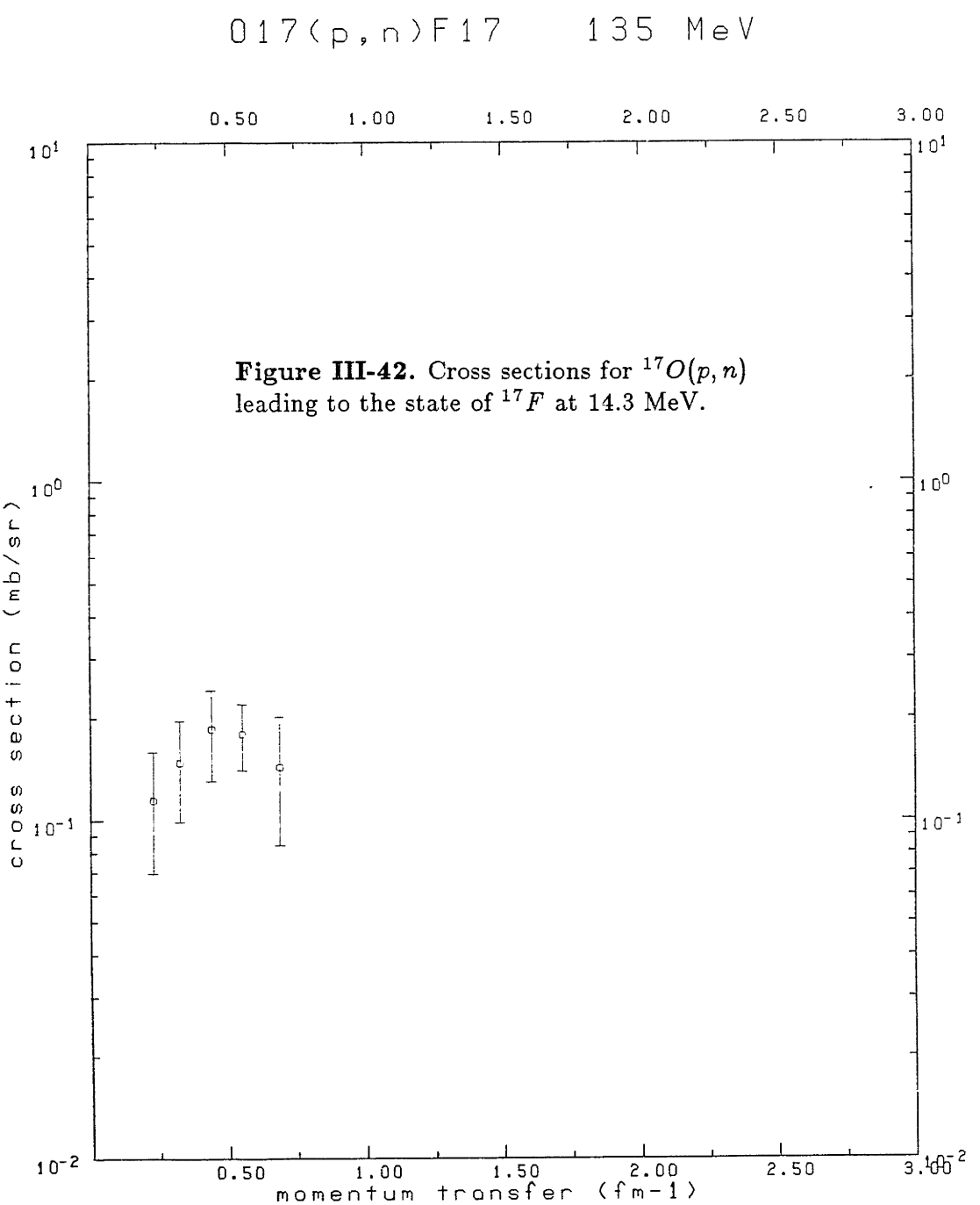

Figure III-42. Cross sections for $^{17}O(p,n)$ leading to the state of ^{17}F at 14.3 MeV.

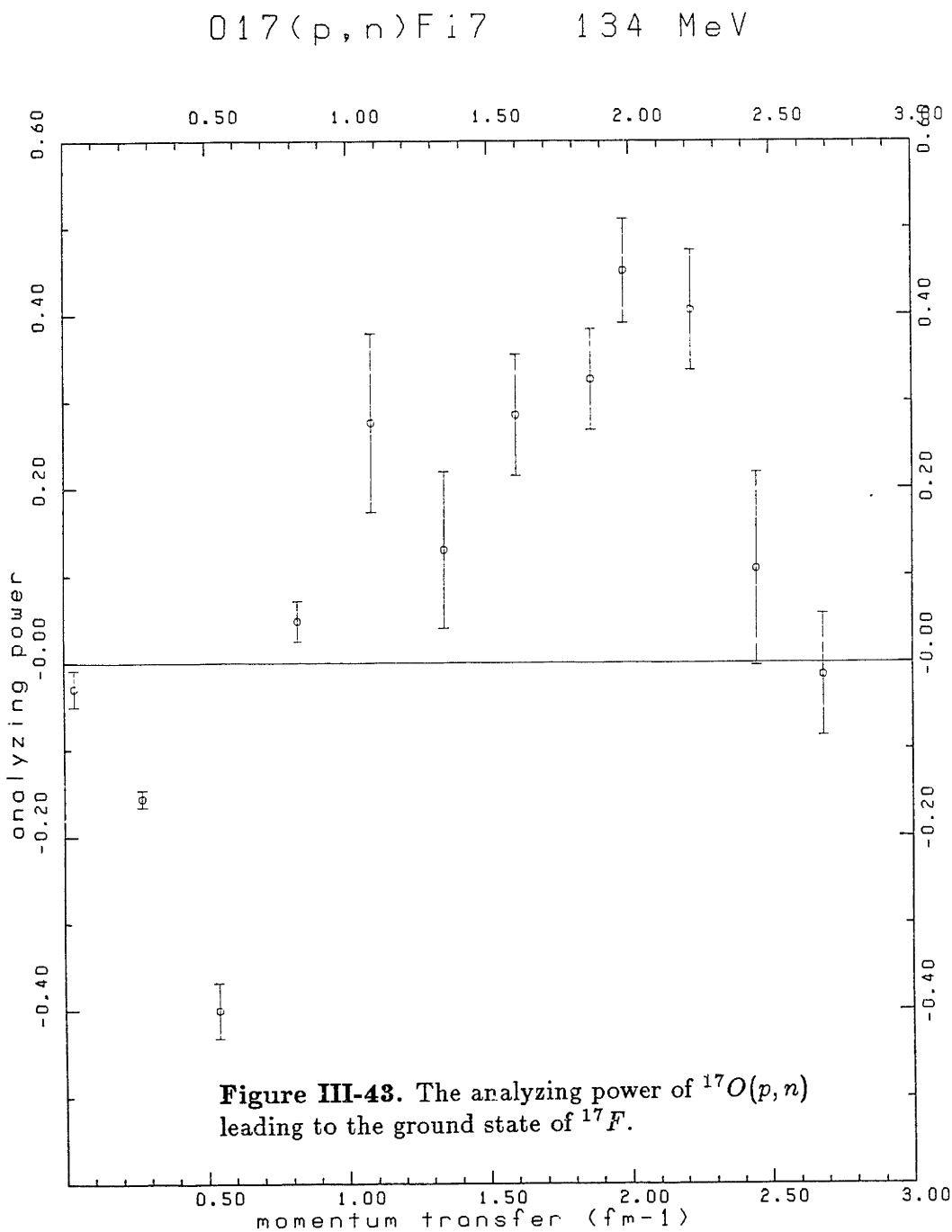

Figure III-43. The analyzing power of $^{17}O(p,n)$ leading to the ground state of ^{17}F.

$^9Be(p,n)$ to the ground state of ^9B

Petrovich *et al* [PET85] calculated the differential cross sections for $^9Be(p,n)$ transitions to the ground state and the 2.36 MeV state of ^9B at E_p = 135 MeV using the distorted wave impulse approximation (DWIA). The free nucleon-nucleon interaction of [LOV78] was used to calculate transition matrix elements. The mass 9 nuclei were described by the simple harmonic oscillator radial wave function parameterization of Cohen-Kurath [COH65]. These wave functions were derived from matrix elements of the two body interaction determined from fitting measured excitation energies and binding energies of various p shell nuclei. The resulting matrix elements were used to extract the wave functions of all excited states possible in this limited basis set. These wave functions were tested by calculating M1 transitions and *log ft* values of Gamow-Teller β-decay transitions and were found to give reasonable results. Figure $IV-1$ shows the fit using these wave functions to the square of the magnetic form factor of the ^9Be ground state. This form factor was measured by [RAN66] using elastic electron scattering from ^9Be. It should be noted that these results were not reported in terms of effective momentum transfer. That is, the effect of Coulomb acceleration of the electron is not accounted for. Including this effect would shift the low momentum tranfer data by about 4% to higher momentum transfer. The ground state of ^9Be has $J = \frac{3}{2}$ and the transverse form factor has contributions with J-transfer equal to 1 and 3, corresponding to M1 and M3 magnetic multipole scattering respectively. To achieve the fit shown, an oscillator constant $\alpha = 0.585\ fm^{-1}$ ($b = 1.71\ fm$) was needed and the J=1 and J=3 amplitudes were normalized by $N_1 = 0.933$ and $N_3 = 0.656$ corresponding to magnetic dipole and octupole moments of $\mu = -1.18\ nm$ and $\Omega = 4.08\ nm\ fm^2$, respectively. The experimentally determined magnetic dipole moment listed in [AJZ79] was used as a data point in the fitting procedure. The usual oscillator center of mass correction $exp[\frac{1}{A}(\frac{qb}{2})^2]$ has been applied to the single particle model form factor in the electron scattering calculations [DEF66]. The finite size of the nucleon was taken into consideration. The electron scattering formalism is described in [PET84].

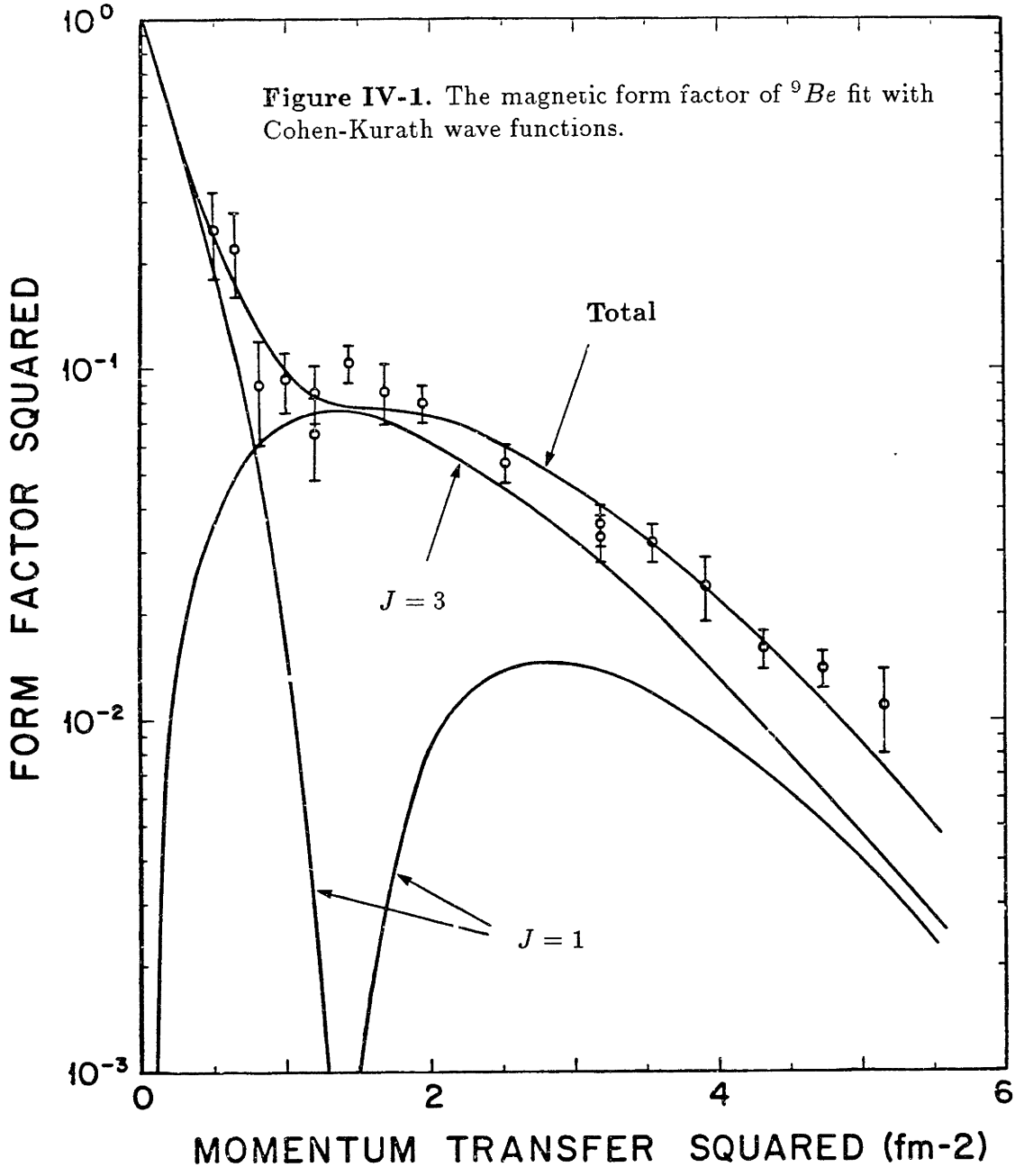

Figure IV-1. The magnetic form factor of ^9Be fit with Cohen-Kurath wave functions.

The (p,n) calculations were made with the code DWBA70 [SCH70]. Elastic scattering was described by an optical model of the form

$$U(r) = V_C(r) + Vf(r) + iWf'(r) + \frac{1}{r}\left[V_{SO}\frac{d}{dr}f_{SO}(r) + iW_{SO}\frac{d}{dr}f_{SO}(r)\right]\vec{l}\cdot\vec{\sigma}$$

The Coulomb force is parameterized in terms of a uniformly charged sphere of radius $R_C = r_C A^{\frac{1}{3}}$ and the corresponding potential is then

$$V_C = \begin{cases} \frac{\eta k}{R_C}(3 - r^2/{R_C}^2) & \text{for } r < R_C \\ \frac{2\eta k}{r} & \text{for } r > R_C \end{cases}$$

where η is the usual Coulomb parameter

$$\eta = \frac{zZe^2\mu}{k}$$

Here z and Z are the charges of the colliding particles, μ is the reduced energy of the collision in the center of mass, and k is the relative motion wave number in the center of mass.

The nuclear distortion is parameterized by complex Wood-Saxon potentials of strengths V and W and with radial shapes

$$f(r) = 1/(1+e^x), x = (r-R)/a, R = r_0 A^{\frac{1}{3}},$$
$$f'(r) = 1/(1+e^{x'}), x' = (r-R')/a', R' = r_0' A^{\frac{1}{3}},$$

The optical parameters used in these calculations were

$$\begin{aligned} V &= 16.2\ MeV & & \\ r_0 &= 1.20\ fm & V_{SO} &= 4.45 MeV \\ a &= 0.66\ fm & r_{SO} &= 0.90\ fm \\ W &= 11.1\ MeV & a_{SO} &= 0.50\ fm \\ r_0' &= 1.28\ fm & r_C &= 1.20\ fm \\ a' &= 0.63\ fm & & \end{aligned}$$

which come from the ^{12}C work of Comfort and Karp [COM80B], who obtained these numbers by fitting $^{12}C(p,p)$ elastic scattering cross sections and analyzing powers. To include the center of mass correction, which is not in the code DWBA70, the approximate coördinate space center of mass prescription

$$b \to b' = \left(\frac{A-1}{A}\right)^{\frac{1}{2}} b = 1.61\ fm (\alpha' = 0.621\ fm^{-1})$$

$$\sigma_L \to \sigma_L' = \left(\frac{A}{A-1}\right)^{L} \sigma_L = 1.00\ \sigma\ (J = 0,1)$$
$$= 1.27\ \sigma\ (J = 2,3)$$

was used in carrying out the calculations. J represents the total momentum transfer to the nucleus and the σ_L are cross sections for the different angular momentum transfers denoted by L.

The central and spin-orbit nature of the nucleon-nucleon interaction has been described by the t-matrix parameters of [LOV78] for $E_p = 135\ MeV$. These parameters were derived from the nucleon-nucleon phase shifts of [KER59]. Distorted Wave Impulse approximation calculations using these parameters were found in [LOV78] to provide a reasonable description of both the strength and shape of a strongly collective octupole excitation of ^{207}Pb ($E_x = 2.64\ MeV$) by proton scattering at 135 MeV. These parameters were also used by [LOV79] in distorted wave impulse approximation calculations of $^{12}C(\vec{p},p')$ at $E_p = 122\ MeV$. Cohen-Kurath wave functions were used to describe the nucleus of ^{12}C. Cross sections for excitation to both $T = 0$ and $T = 1$ excited states were calculated and compared to experiment. The calculation did very well for angles up to about $\theta_{CM} = 30 - 40°$ but decreased too rapidly thereafter.

The nucleon-nucleon interaction was given tensor properties using the potentials of [BER77]. These potentials were chosen to reproduce the simple harmonic oscillator matrix elements of [ELL68] which were derived from phase shift analyses of nucleon-nucleon scattering data.

The DWA results for the J-transfer 0, 1, 2, and 3 contributions to the cross section for the ground state transition in $^9Be(p,n)$ at $E_p = 135MeV$ are shown in figures $IV-2$ through $IV-5$. The J=2 and J=3 results include the 1.27 center of mass scale factor. For J=0 and J=1 the plane wave (PW) Born approximation results ($V = W = V_{SO} = W_{SO} = e^2 = 0$) are also shown. By comparing the DWBA and PWBA results one obtains

$$N_\tau^D = \frac{\sigma_{DW}\ (J=0)}{\sigma_{PW}\ (J=0)}|_{\theta=0°} = \frac{1.62\ mb}{3.80\ mb} = 0.426$$

$$N_{\sigma\tau}^D = \frac{\sigma_{DW}\ (J=0)}{\sigma_{PW}\ (J=0)}|_{\theta=0°} = \frac{8.56\ mb}{15.1\ mb} = 0.567$$

As explained in chapter III, these factors represent the effects of distortion in the absence of interference effects. (See equation $III-1$ and discussion). In addition, using

$$\sigma_{PW}(J=0)|_{\theta=0°} = \left(\frac{\mu}{\pi\hbar^2}\right)^2 |J_\tau|^2 |M_F|^2$$

$$\sigma_{PW}(J=1)|_{\theta=0°} = \left(\frac{\mu}{\pi\hbar^2}\right)^2 |J_{\sigma\tau}|^2 |M_{GT}|^2$$

one finds $|J_\tau| = 81.0\ MeV\ fm^3$ and $|J_{\sigma\tau}| = 153.3\ MeV\ fm^3$. These force volume integrals are smaller than those found in chapter III on the basis of the β decay of ^{17}F. The reduced energy used here is $\mu = 930.5MeV$ which is the reduced energy for a 135 MeV proton on ^9Be. The Fermi and Gamow-Teller matrix elements shall be taken to be $|M_F|^2 = 1$, and $|M_{GT}|^2 = 1.11$ corresponding to the Cohen-Kurath wave functions. Note that in computing N_τ^D and $N_{\sigma\tau}^D$ here the kinematic k_f/k_i

factor has not been separated out as in the work of Goodman *et al* [GOOD80] and in the representation found used in chapter III.

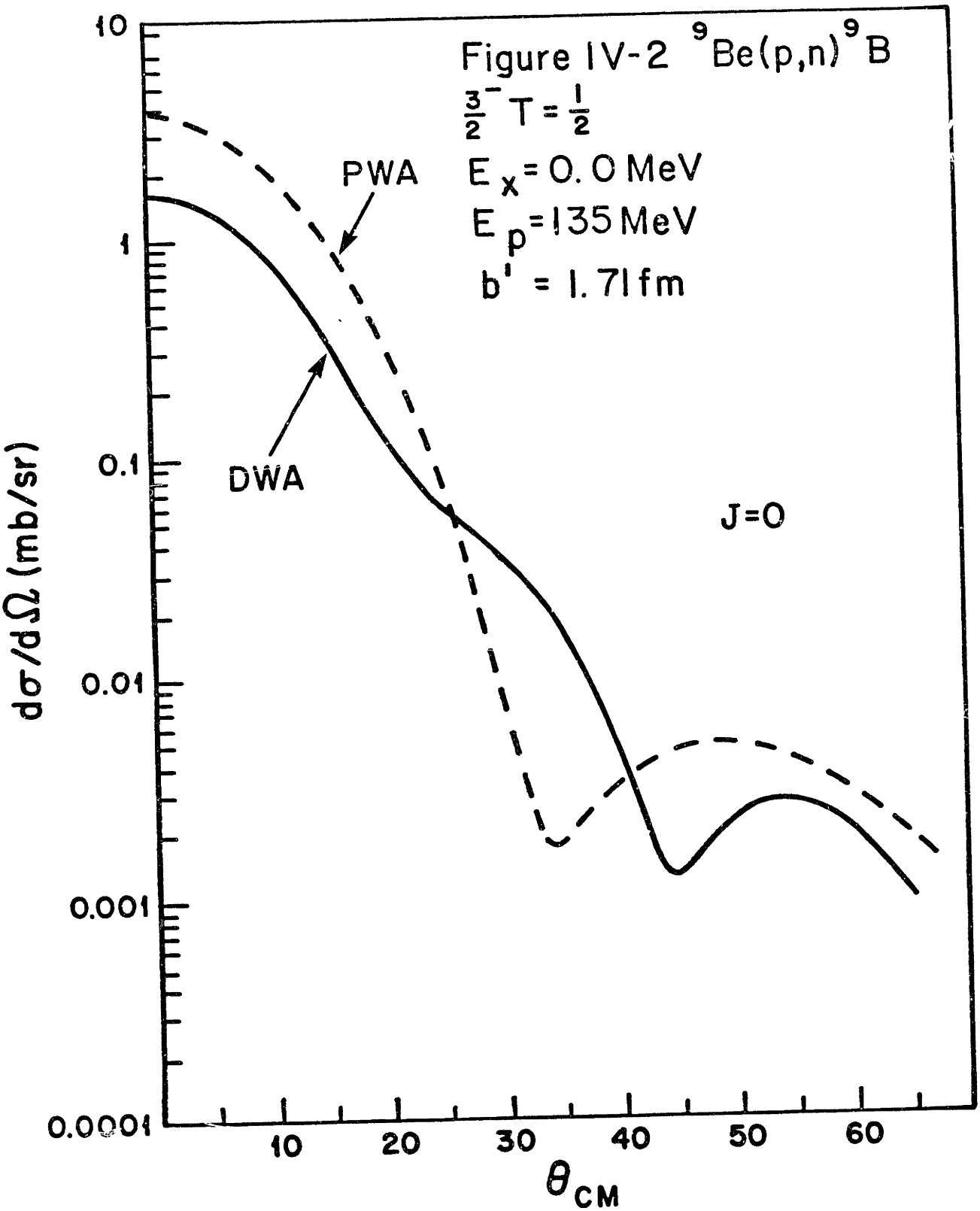
Figure IV-2 $^{9}Be(p,n)^{9}B$
$\frac{3}{2}^{-}$ T = $\frac{1}{2}$
E_x = 0.0 MeV
E_p = 135 MeV
b' = 1.71 fm
PWA
DWA
J=0
10
1
0.1
0.01
0.001
0.0001
dσ/dΩ (mb/sr)
10
20
30
40
50
60
θ_{CM}

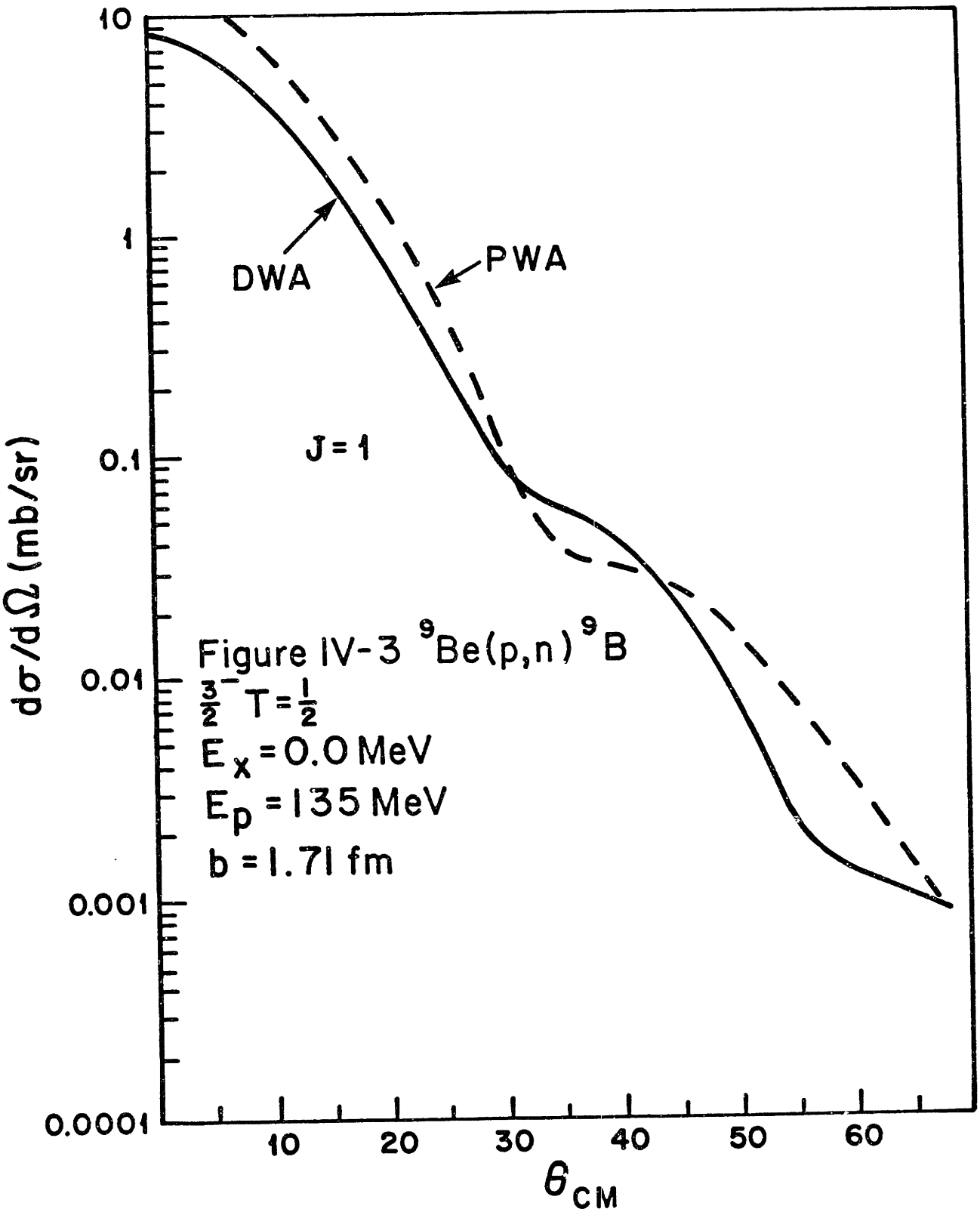
10
1
0.1
0.01
0.001
0.0001
dσ/dΩ (mb/sr)
DWA
PWA
J=1
Figure IV-3 $^{9}Be(p,n)^{9}B$
$\frac{3}{2}^{-}$ $T=\frac{1}{2}$
$E_x = 0.0$ MeV
$E_p = 135$ MeV
b = 1.71 fm
10
20
30
40
50
60
θ_{CM}

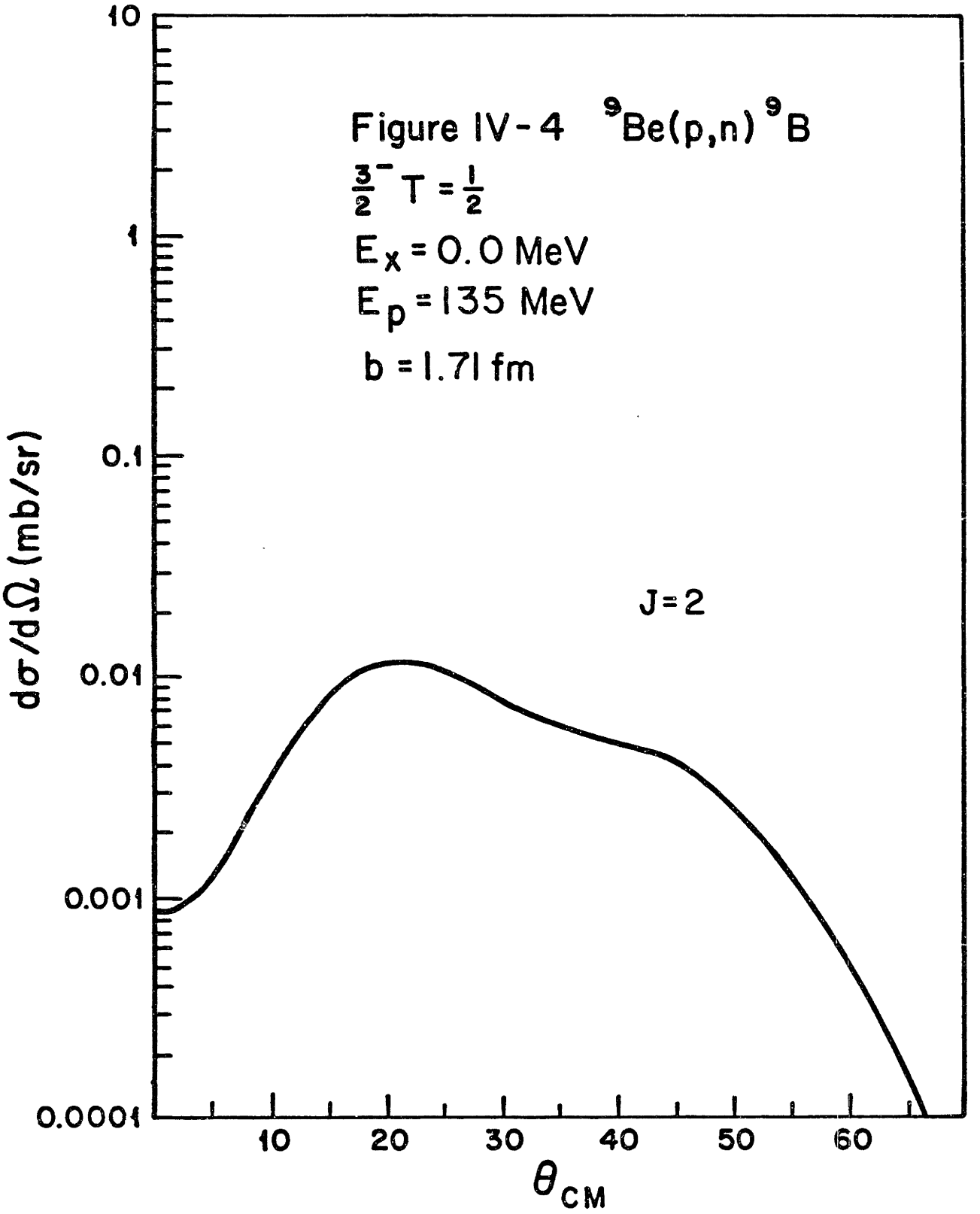
Figure IV-4 $^{9}Be(p,n)^{9}B$
$\frac{3}{2}^{-}$ T = $\frac{1}{2}$
E_x = 0.0 MeV
E_p = 135 MeV
b = 1.71 fm
J=2
dσ/dΩ (mb/sr)
10
1
0.1
0.01
0.001
0.0001
10
20
30
40
50
60
θ_{CM}

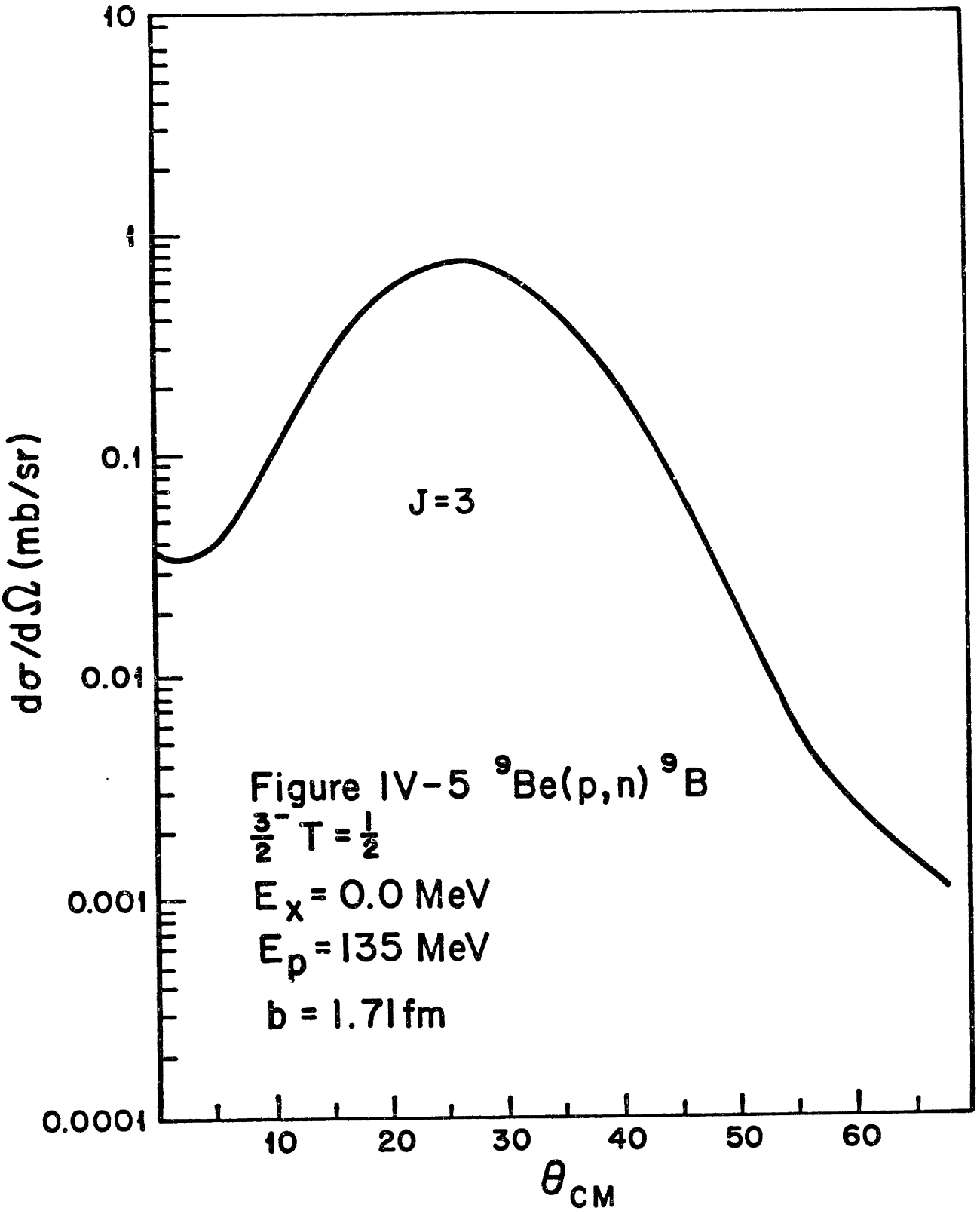

Figure IV-5 $^{9}Be(p,n)^{9}B$
$\frac{3}{2}^{-}$ $T=\frac{1}{2}$
$E_x = 0.0$ MeV
$E_p = 135$ MeV
b = 1.71 fm

To compare with the experimental data, the J=1 and J=3 contributions to the (p,n) cross section have been respectively normalized by $N_{\sigma 1} = N_1^2 = 0.870$ and $N_{\sigma 3} = N_3^2 = 0.430$ as required by the electron scattering data. The correction to the J=1 contribution corresponds to using $|M_{GT}|^2 = 0.966$. There is no β decay information on this matrix element. Force renormalization factors N_τ and $N_{\sigma\tau}$ are introduced which are fixed according to

$$\sigma_{exp}(\theta = 0°) = \left(\frac{\mu}{\pi\hbar^2}\right)^2 N_\tau N_\tau^D |J_\tau|^2 \left(|M_F|^2 + R^2 |M_{GT}|^2\right)$$

$$R^2 = \frac{N_{\sigma\tau} N_{\sigma\tau}^D |J_{\sigma\tau}|^2}{N_\tau N_\tau^D |J_\tau|^2} = \frac{N_{\sigma\tau}^D |J'_{\sigma\tau}|^2}{N_\tau^D |J'_\tau|^2}$$

The 0° differential cross section was measured in this work to be $\sigma_{exp}(\theta = 0°) = 9.5\ mb$. The ratio R is taken from the work of Taddeucci *et al* [TAD81] which finds this ratio to be mass independent and linear as a function of bombarding energy for target nuclei with $A = 7 - 42$ and bombarding energies in the range $50 - 200$ MeV. For 135 MeV they find $R^2 = 6.05$.

These constraints lead to $N_\tau = 0.840$ and $N_{\sigma\tau} = 1.07$ corresponding to the use of forces with $|J'_\tau| = 68.0\ MeV\ fm^3$ and $|J'_{\sigma\tau}| = 158.6\ MeV\ fm^3$. The latter is in rough agreement with the results of the work of Goodman *et al* and the more recent effort of Rapaport *et al* [RAP81] which quote $|J_{\sigma\tau}| = 168\ MeV\ fm^3$ for $E_p = 120\ MeV$ and $|J_{\sigma\tau}| = 174\ MeV\ fm^3$ for $E_p = 120 - 200\ MeV$. The nuclear force volume integrals $|J|$ refer to the nucleon-nucleon force. In this approximation all mass dependence is contained in the distortion factors N_τ^D and $N_{\sigma\tau}^D$. Finally the J=2 contribution to the cross section has been reduced by an additional factor of 2 to account for quadrupole enhancement effects which correlate protons and neutrons in the nucleus hence reducing isovector J=2 transition densities. The factor of 2 was found appropriate for mass seven systems as discussed by Petrovich *et al* [PET82].

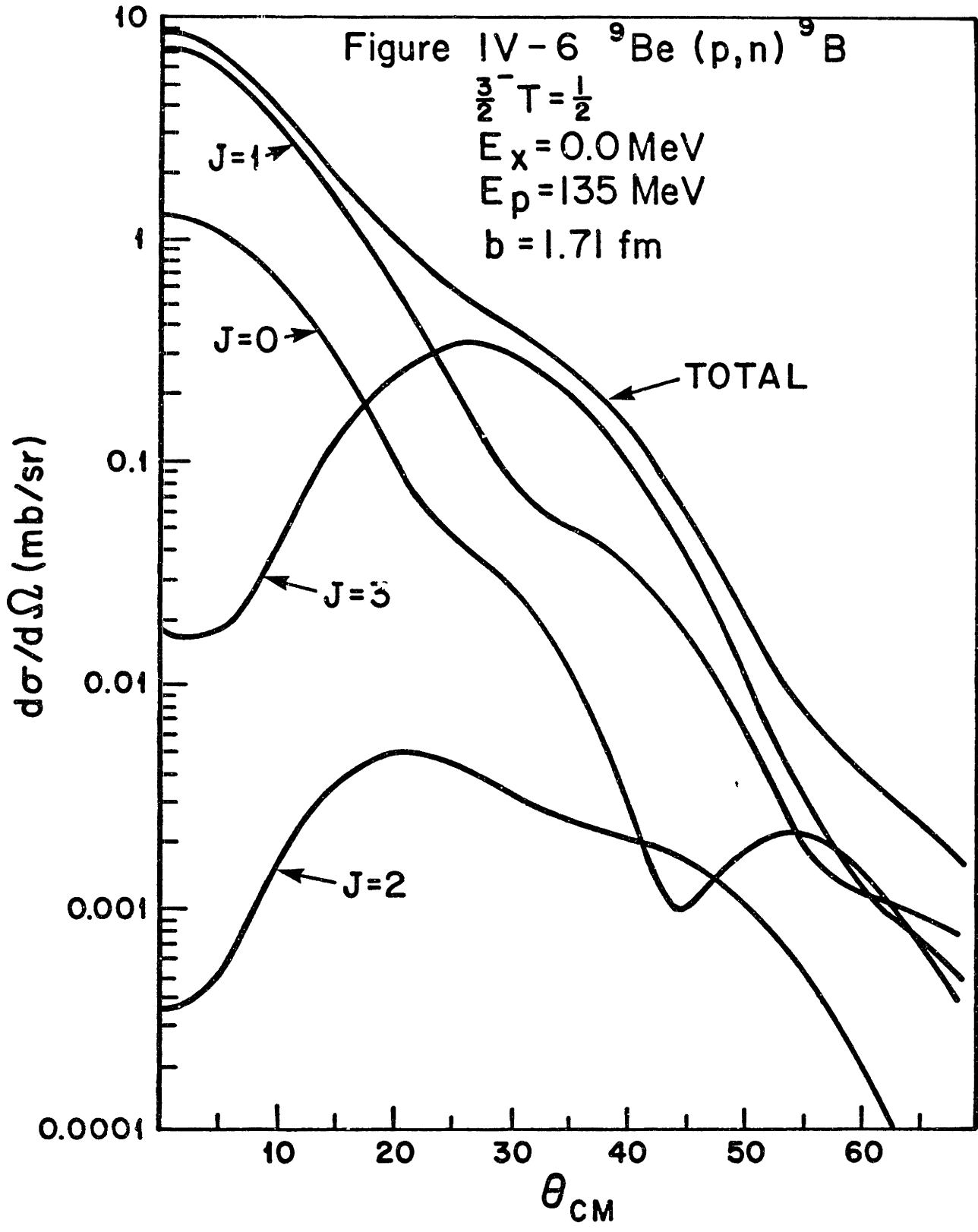
Figure IV-6 ^{9}Be (p,n) ^{9}B
$\frac{3}{2}^{-}$ T = $\frac{1}{2}$
E_x = 0.0 MeV
E_p = 135 MeV
b = 1.71 fm
J=1
J=0
TOTAL
J=3
J=2
10
1
0.1
0.01
0.001
0.0001
dσ/dΩ (mb/sr)
10
20
30
40
50
60
θ_{CM}

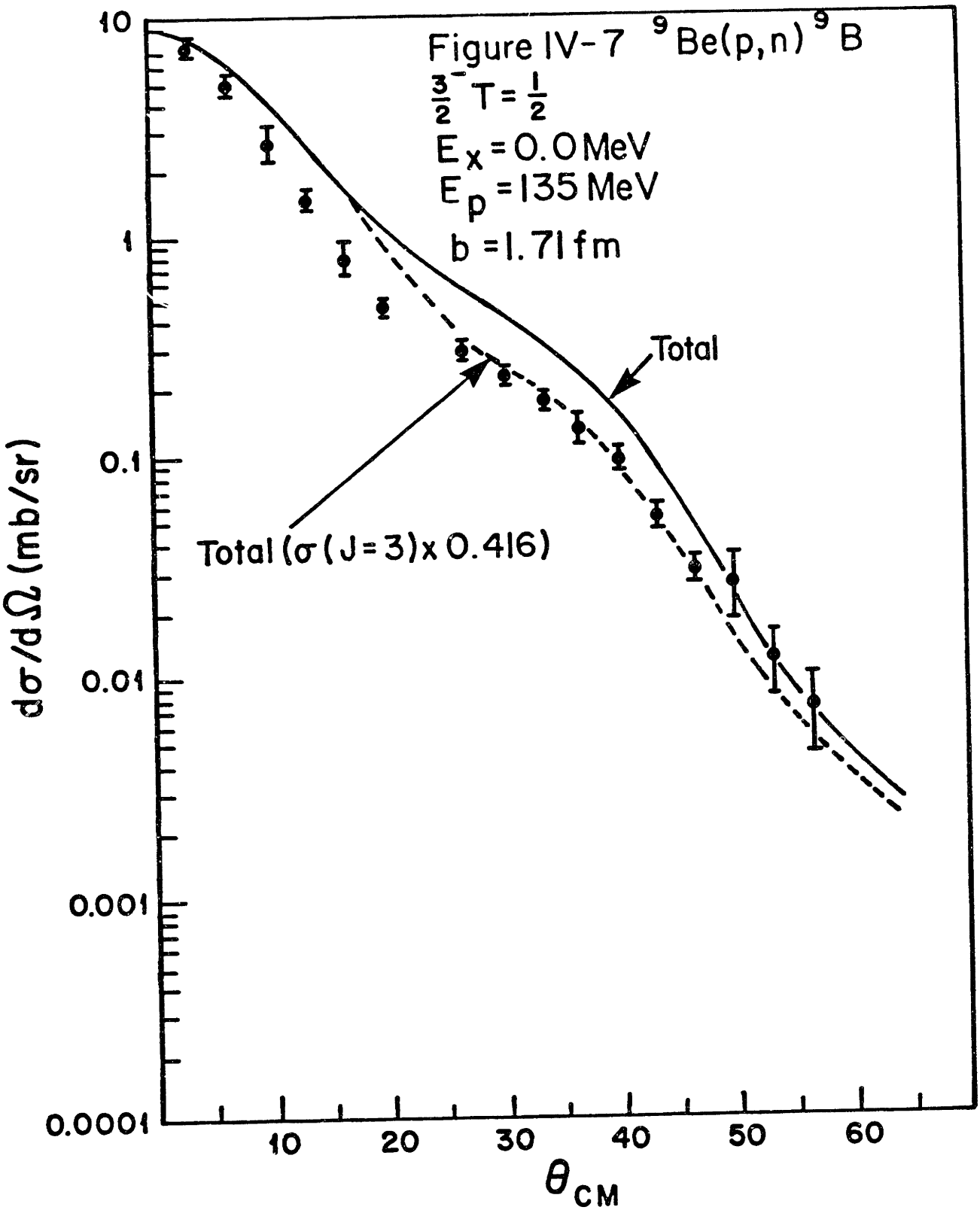
Figure IV-7 $^{9}Be(p,n)^{9}B$
$\frac{3}{2}^{-}$ T = $\frac{1}{2}$
E_x = 0.0 MeV
E_p = 135 MeV
b = 1.71 fm
Total
Total (σ (J=3) x 0.416)
dσ/dΩ (mb/sr)
10
1
0.1
0.01
0.001
0.0001
10
20
30
40
50
60
θ_{CM}

The complete structure of the calculated differential cross section for the ground state transition in $^9Be(p,n)$ at $E_p = 135\ MeV$ is shown in figure $IV-6$. The total calculated differential cross section is compared with the experimental data in figure $IV-7$. There is rough qualitative agreement between theory and experiment, but one should remember here that the agreement at 0° has been forced by the force renormalizations. The theoretical curve is clearly too high in the middle angle region. This deficiency can be remedied to some extent by reducing the J=3 contribution to the cross section by $N_{\sigma 3} = 0.417$ as indicated by the dashed curve in the figure. It should be emphasized that this multiplicative factor is over and above the factor $N_{\sigma 3} = N_3^2 = 0.430$ required by the electron scattering data so that the total multiplicative suppresion of the J=3 cross section is $0.430 \times 0.417 = 0.179$. Even with this reduction the theoretical result is too high in the region $\theta_{CM} \approx 10 - 25°$. This problem can only be remedied by using a larger oscillator constant b (that is a smaller α) corresponding to a larger nucleus. There are a number of arguments that can be advanced to explain the apparent inconsistency between the (e,e') results in figure $IV-1$ and the (p,n) results in figure $IV-7$. For example, the basis of Cohen-Kurath does not include the effects of core polarization. Also, the electron scattering force contains convective terms not present in the (p,n) reaction.

Rather than consider these without the benefit of a detailed nuclear model, it is instructive to examine the empirical modifications required to fit the (p,n) cross section.

To this end the (p,n) calculation was repeated with $b = 2.06\ fm$ ($\alpha = 0.486\ fm^{-1}$). Again the forces were normalized to obtain the experimentally determined differential cross section at 0° while maintaining the force ratio of [TAD81]. Some differences in parameters were obtained, *i.e.* $\sigma_{DW}(J=0) = 1.90\ mb$ and $\sigma_{DW}(J=1) = 9.0\ mb$ corresponding to $N_\tau^D = 0.500$ and $N_{\sigma\tau}^D = 0.597$ which leads to $N_\tau = 0.716$ and $N_{\sigma\tau} = 1.01$ corresponding to $|J'_\tau| = 62.8\ MeV\ fm^3$ and $|J'_{\sigma\tau}| = 154.1\ MeV\ fm^3$. The results for the (p,n) cross section are displayed in figures $IV-8$ through $IV-12$ with the total theoretical differential cross section compared with experiment in figure $IV-13$. Now by reducing the J=3 contribution to the cross section by an additional factor $\bar{N}_{\sigma 3} = 0.571$ one obtains a good fit to the data for $\theta_{CM} \approx 0 - 35°$, but the fit deteriorates for $\theta_{CM} > 35°$. In figure $IV-14$ is shown a result obtained by combining the J=0 and J=1 cross sections calculated with $b = 2.06\ fm$ and the J=2 and J=3 cross sections calculated with $b = 1.71\ fm$ and applying $\bar{N}_{\sigma 3} = 0.546$. This is quite good for θ_{CM} out to about 45°. There is no reason to believe that the p-shell wave functions with a single oscillator constant give the correct relative shapes of the J=0,1,2,and 3 transition densities. Therefore a variation of the shapes of the J=2 and J=3 parts relative to the J=0 and J=1 parts is not entirely unreasonable from a physical point of view. On the other hand, these efforts do not emerge from a consistent nuclear model. In addition, the number of free parameters is perhaps too great to lead to any fundamental understanding.

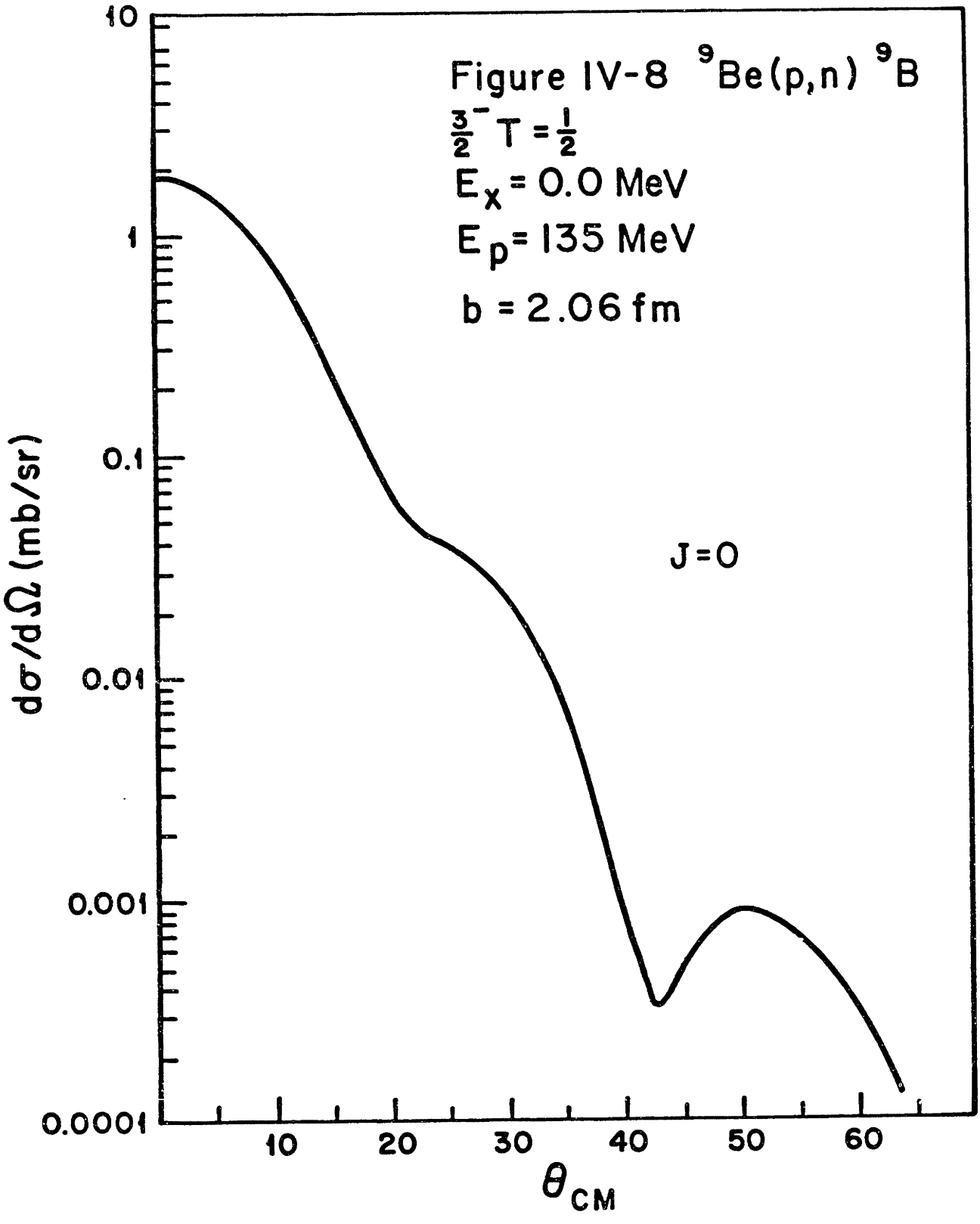
Figure IV-8 $^{9}Be(p,n)\ ^{9}B$
$\frac{3}{2}^{-}\ T=\frac{1}{2}$
E_x = 0.0 MeV
E_p = 135 MeV
b = 2.06 fm
J=0
$d\sigma/d\Omega$ (mb/sr)
10
1
0.1
0.01
0.001
0.0001
10
20
30
40
50
60
θ_{CM}

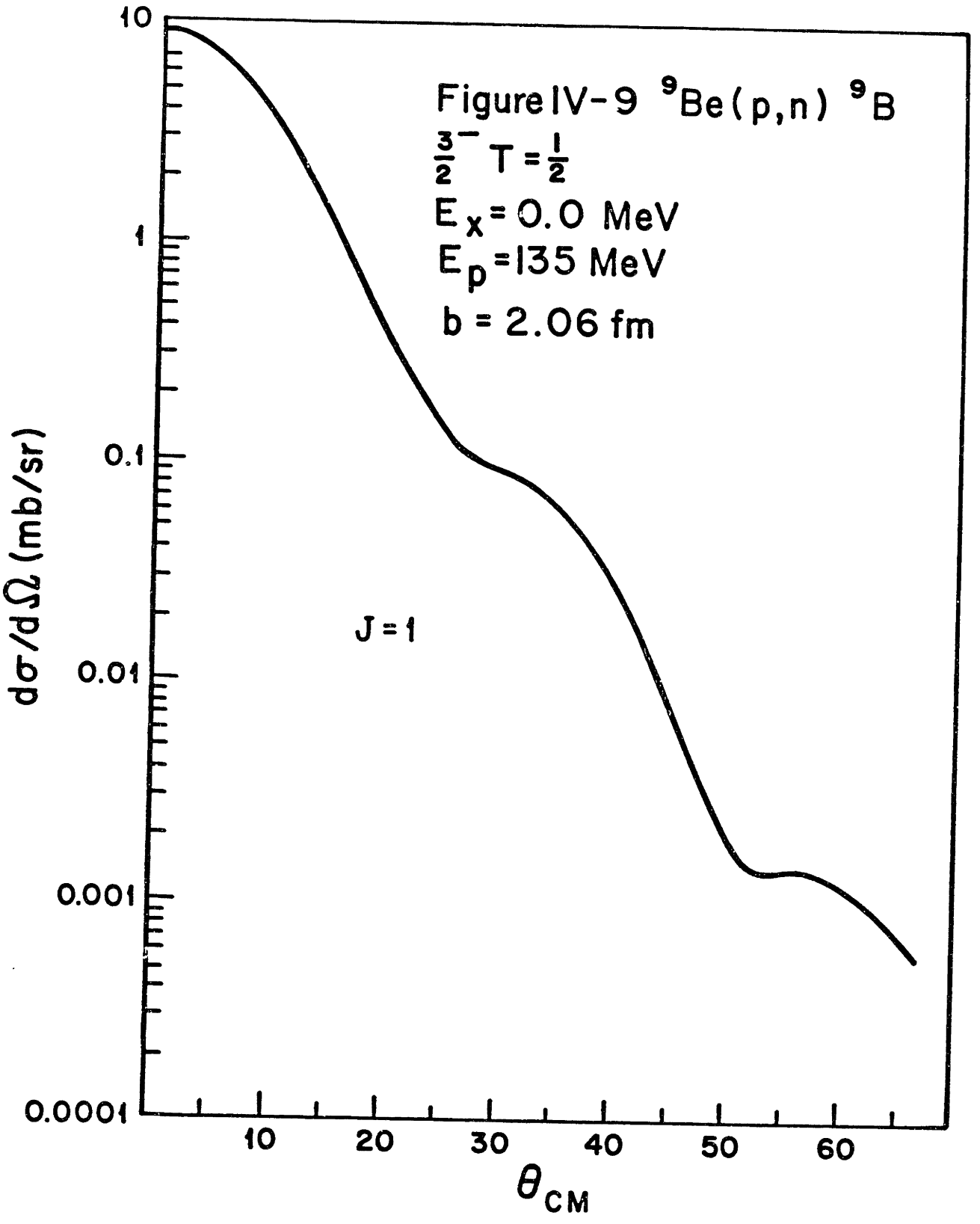
Figure IV-9 $^{9}Be(p,n)\ ^{9}B$
$\frac{3}{2}^{-}\ T=\frac{1}{2}$
$E_x = 0.0$ MeV
$E_p = 135$ MeV
b = 2.06 fm
J = 1
$d\sigma/d\Omega$ (mb/sr)
10
1
0.1
0.01
0.001
0.0001
10
20
30
40
50
60
θ_{CM}

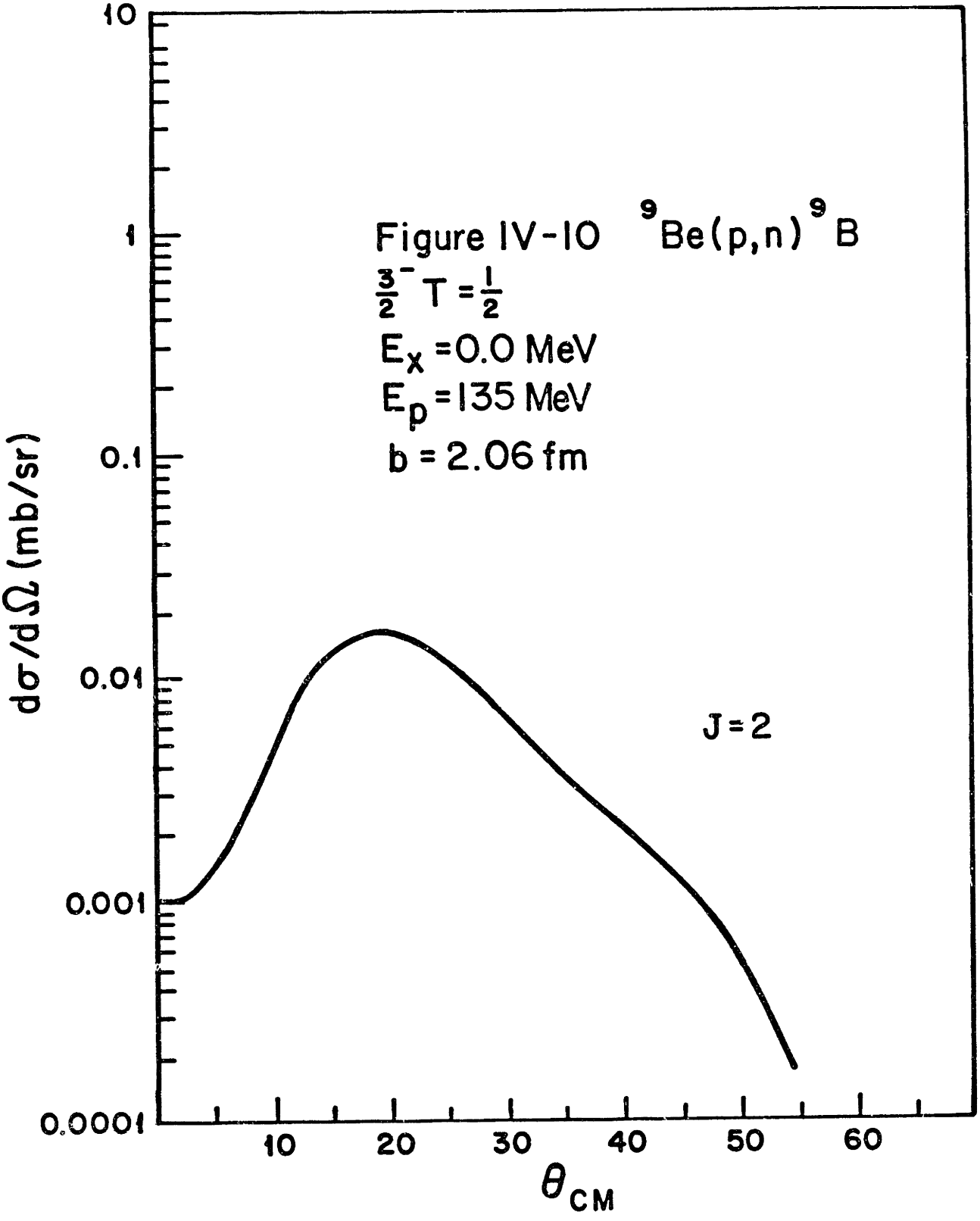
Figure IV-10 $^{9}Be(p,n)^{9}B$
$\frac{3}{2}^{-}$ T = $\frac{1}{2}$
E_x = 0.0 MeV
E_p = 135 MeV
b = 2.06 fm
J = 2
dσ/dΩ (mb/sr)
10
1
0.1
0.01
0.001
0.0001
10
20
30
40
50
60
θ_{CM}

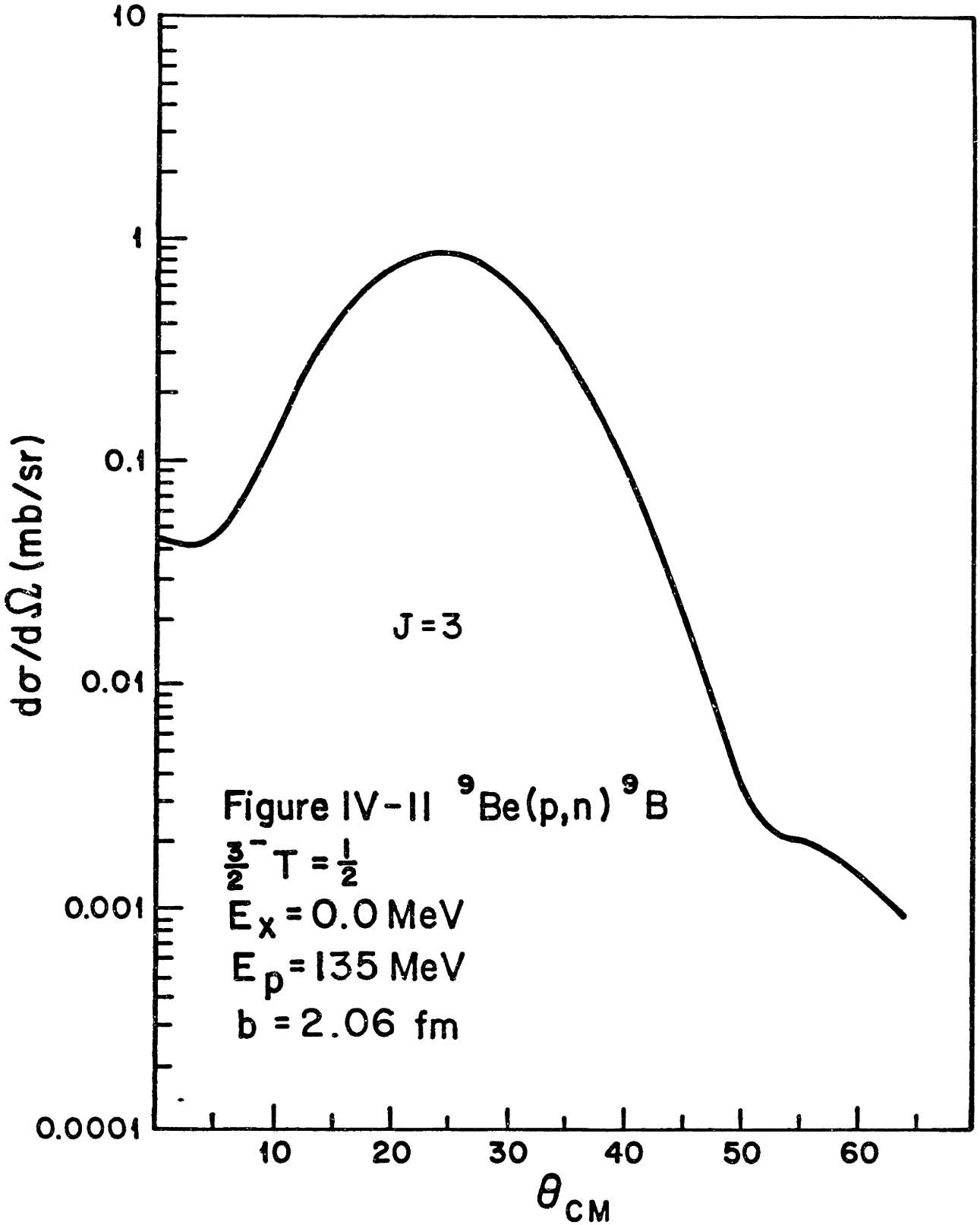
10
1
0.1
0.01
0.001
0.0001
dσ/dΩ (mb/sr)
J=3
Figure IV-11 $^{9}Be(p,n)^{9}B$
$\frac{3}{2}^{-}$ T = $\frac{1}{2}$
E_x = 0.0 MeV
E_p = 135 MeV
b = 2.06 fm
10
20
30
40
50
60
θ_{CM}

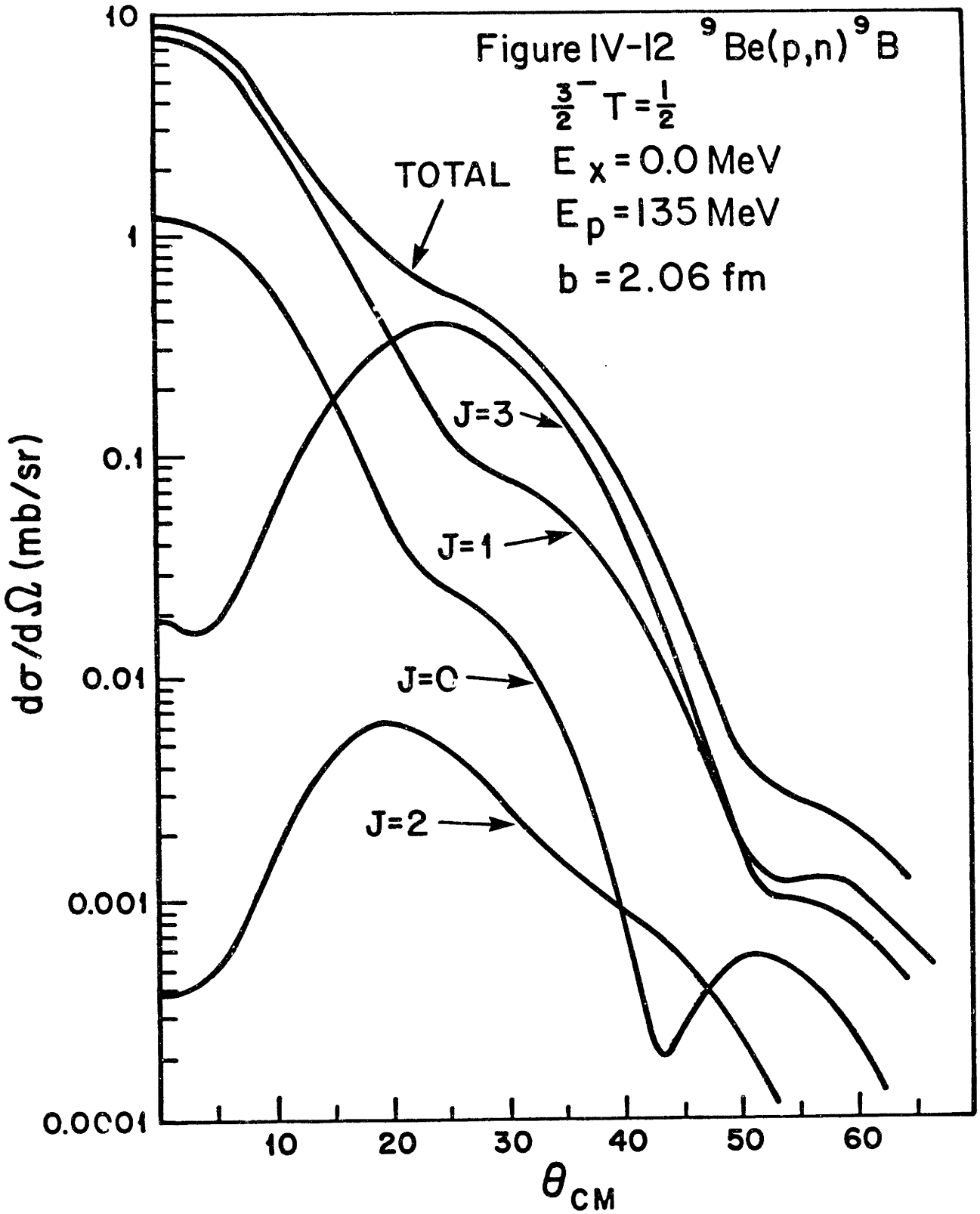
Figure IV-12 $^{9}Be(p,n)^{9}B$
$\frac{3}{2}^{-}$ $T=\frac{1}{2}$
$E_x = 0.0$ MeV
$E_p = 135$ MeV
$b = 2.06$ fm
TOTAL
J=3
J=1
J=0
J=2
$d\sigma/d\Omega$ (mb/sr)
10
1
0.1
0.01
0.001
0.0001
10
20
30
40
50
60
θ_{CM}

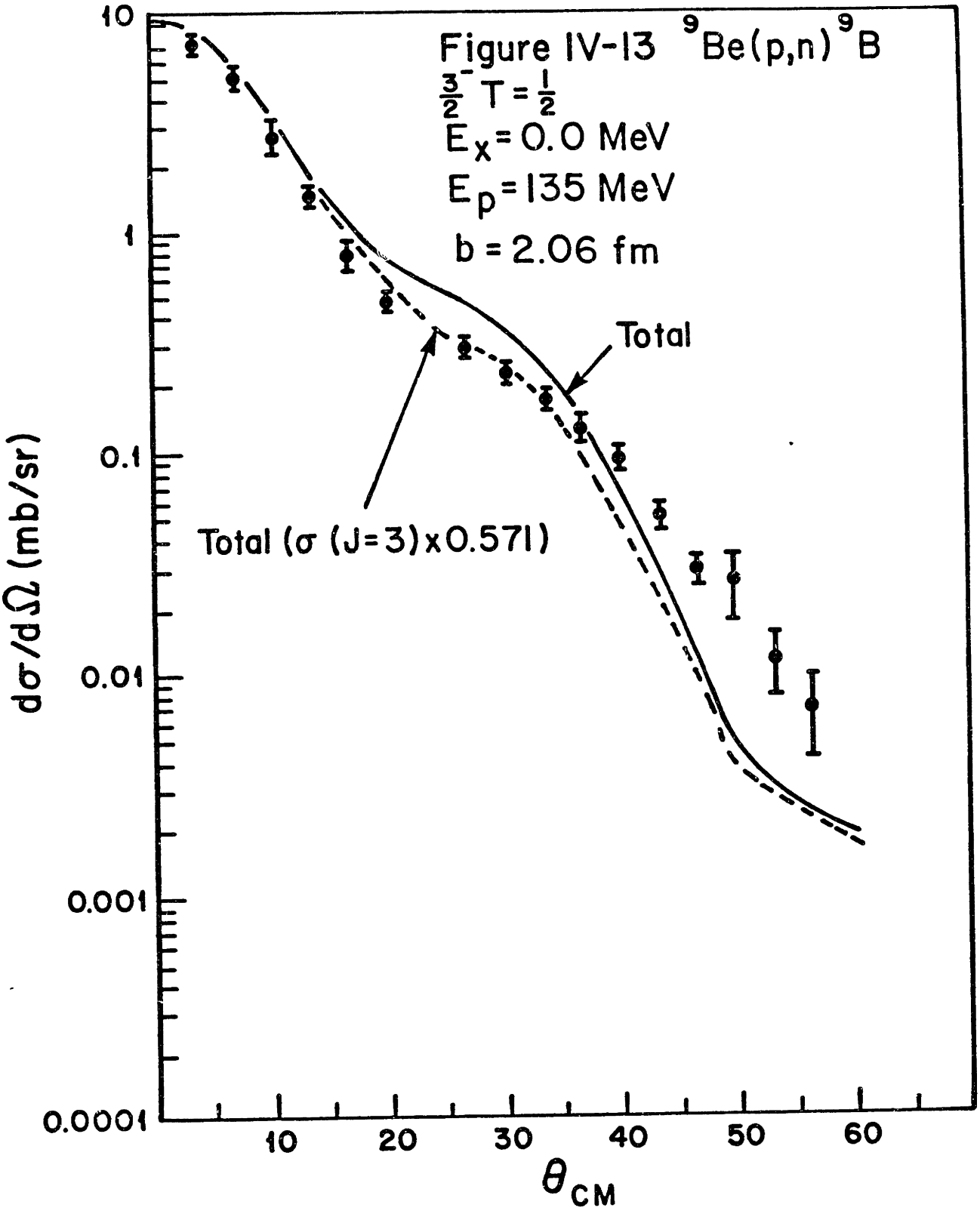
Figure IV-13 $^{9}Be(p,n)^{9}B$
$\frac{3}{2}^{-}$ $T=\frac{1}{2}$
E_x = 0.0 MeV
E_p = 135 MeV
b = 2.06 fm
Total
Total (σ (J=3)x0.571)
$d\sigma/d\Omega$ (mb/sr)
10
1
0.1
0.01
0.001
0.0001
10
20
30
40
50
60
θ_{CM}

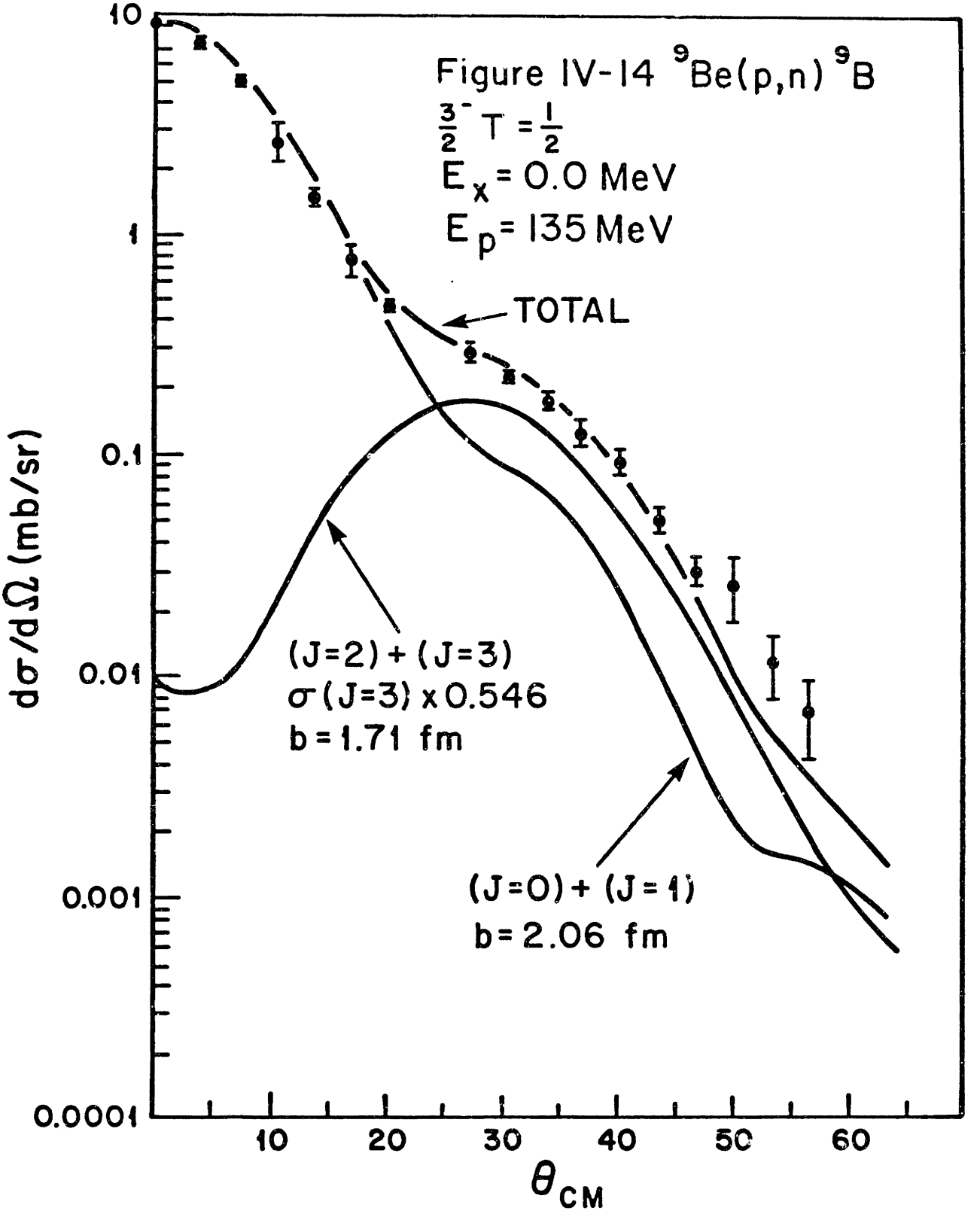
Figure IV-14 $^{9}Be(p,n)^{9}B$
$\frac{3}{2}^{-}$ $T=\frac{1}{2}$
E_x = 0.0 MeV
E_p = 135 MeV
TOTAL
(J=2) + (J=3)
σ(J=3) x 0.546
b = 1.71 fm
(J=0) + (J=1)
b = 2.06 fm
dσ/dΩ (mb/sr)
10
1
0.1
0.01
0.001
0.0001
10
20
30
40
50
60
θ_{CM}

$^9Be(p,n)$ *to the excited state at 2.36 MeV*

The cross section for the transition to the $(J^\pi, T) = (\frac{5}{2}^-, \frac{1}{2})$ $(E_x = 2.361 MeV)$ level in $^9Be(p,n)^9B$ at $E_p = 135 MeV$ has been calculated from the Cohen-Kurath wave functions using $b = 2.06\ fm$ for J=1 and $b = 1.71\ fm$ for J=2 and 3 as for the ground state calculation shown in figure $IV-14$. The J=1-3 contributions are shown separately in figures $IV-15$ through $IV-17$ and the complete cross section is shown with the data in figure $IV-18$. For the latter the factors $N_\tau = 0.716$, $N_{\sigma\tau} = 1.01$, $N_1{}^2 = N_{\sigma 1} = 0.871$, $N_{\sigma 2} = 0.119$, and $N_{\sigma 3} = 0.143$ have been used. The first two values come from the ground state result while the last three values were selected to fit the data. $N_{\sigma 2}$ is poorly determined. The Cohen-Kurath wave functions give $|M_{GT}|^2 = 0.25$ and the use of $N_{\sigma 1} = 0.871$ corresponds to assuming $|M_{GT}|^2 = 0.22$. The J=3 contribution to the cross section for the $\frac{5}{2}^-$ level is somewhat smaller (relative to J=1) than in the case of the $\frac{3}{2}^-$ ground state transition.

$^9Be(p,n)$ *using a different force normalization.*

In the next section, the Gamow-Teller matrix elements experimentally determined from the β-decay of ^{17}F to the ground state of ^{17}O will be used to normalize the nucleon-nucleon forces using the results of [TAD81] and the (p,n) differential cross section at 0° determined by this experiment. The force normalization which results ($N_\tau = 1.31$ and $N_{\sigma\tau} = 1.43$) differs from the one obtained above using the Gamow-Teller matrix element calculated from the Cohen-Kurath wave functions of the mass 9 system. If the calculations had been done assuming the $^{17}O(p,n)$ force normalization, then for the ground state transition $\sigma_{DW}(J=0)|_{\theta=0°} = 2.49\ mb/sr$ and $\sigma_{DW}(J=1)|_{\theta=0°} = 6.81\ mb/sr$ corresponding to $|M_{GT}|^2 = 0.587$. $\bar{N}_{\sigma 3}$ would have to be taken to be 0.386. The resulting fit to the ground state cross section is shown in figure $IV-19$. For the transition to the $\frac{5}{2}^-$ level the curves in figure $IV-18$ would be unchanged but $N_{\sigma 1}$,$N_{\sigma 2}$, and $N_{\sigma 3}$ would be 0.615, 0.065, and 0.101 corresponding to $|M_{GT}|^2 = 0.15$. The J=1, J=2, and J=3 contributions using this force normalization are shown separately in figures $IV-20$ through $IV-22$ and the complete cross section is shown with the data in figure $IV-23$. In using these numbers for ^9Be, one implicitly assumes that a good choice of optical parameters to characterize the relative differences between the mass 9 and mass 17 systems has been made. This is as yet untested in these calculations.

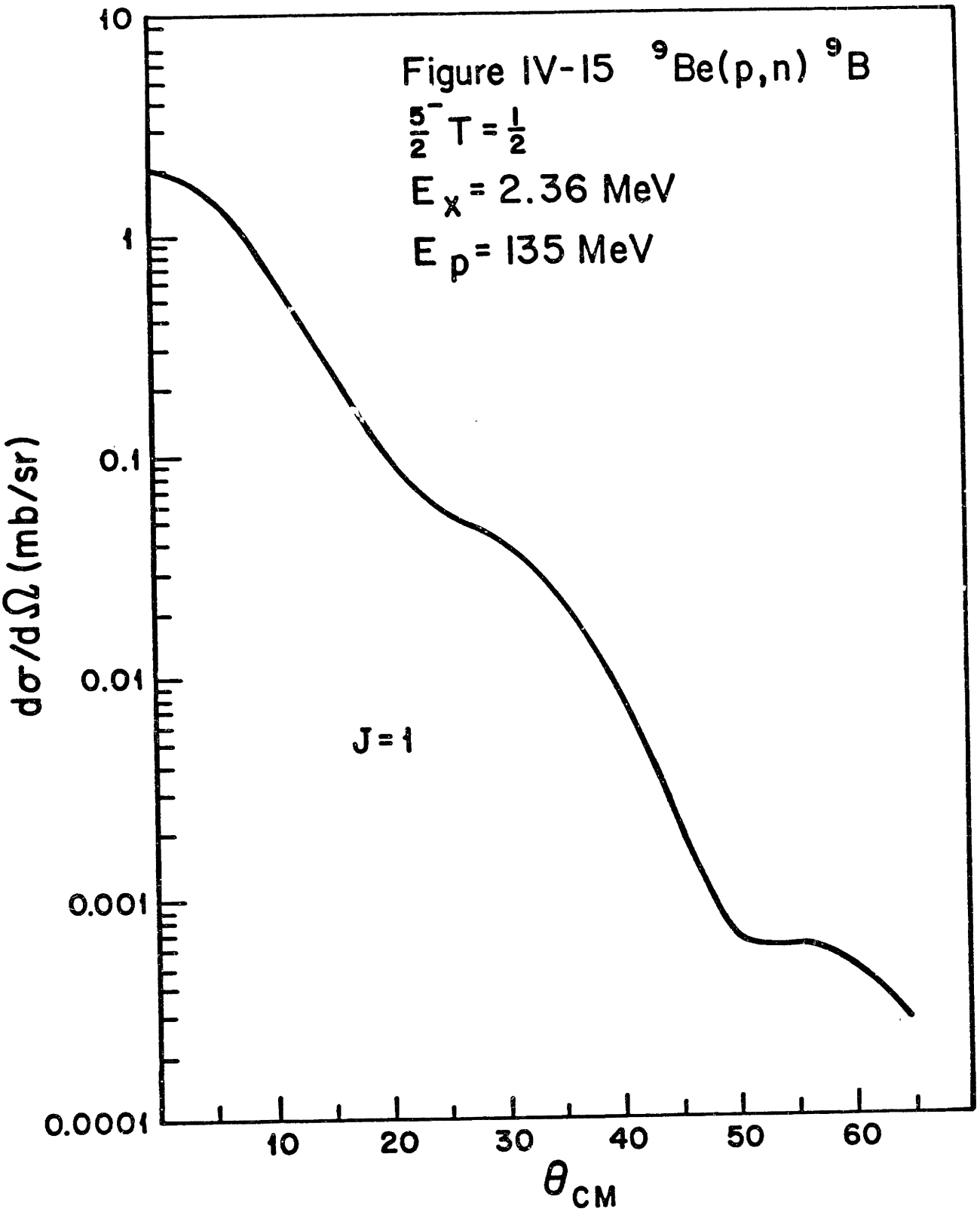
Figure IV-15 $^{9}Be(p,n)\ ^{9}B$
$\frac{5}{2}^{-}\ T=\frac{1}{2}$
$E_x = 2.36$ MeV
$E_p = 135$ MeV
J=1
$d\sigma/d\Omega$ (mb/sr)
10
1
0.1
0.01
0.001
0.0001
10
20
30
40
50
60
θ_{CM}

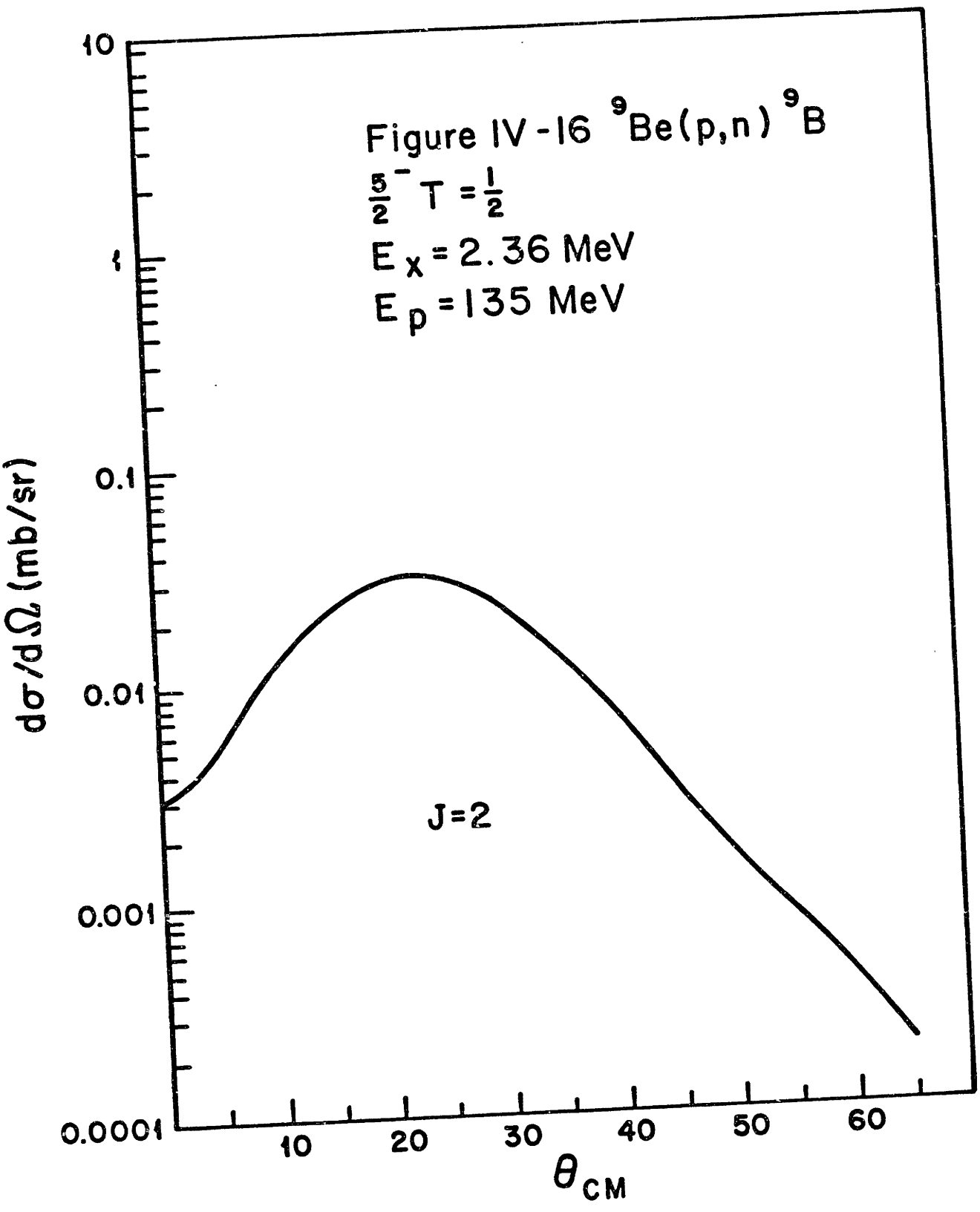
Figure IV-16 $^{9}Be(p,n)^{9}B$
$\frac{5}{2}^{-}$ $T=\frac{1}{2}$
$E_x = 2.36$ MeV
$E_p = 135$ MeV
J=2
$d\sigma/d\Omega$ (mb/sr)
10
1
0.1
0.01
0.001
0.0001
10
20
30
40
50
60
θ_{CM}

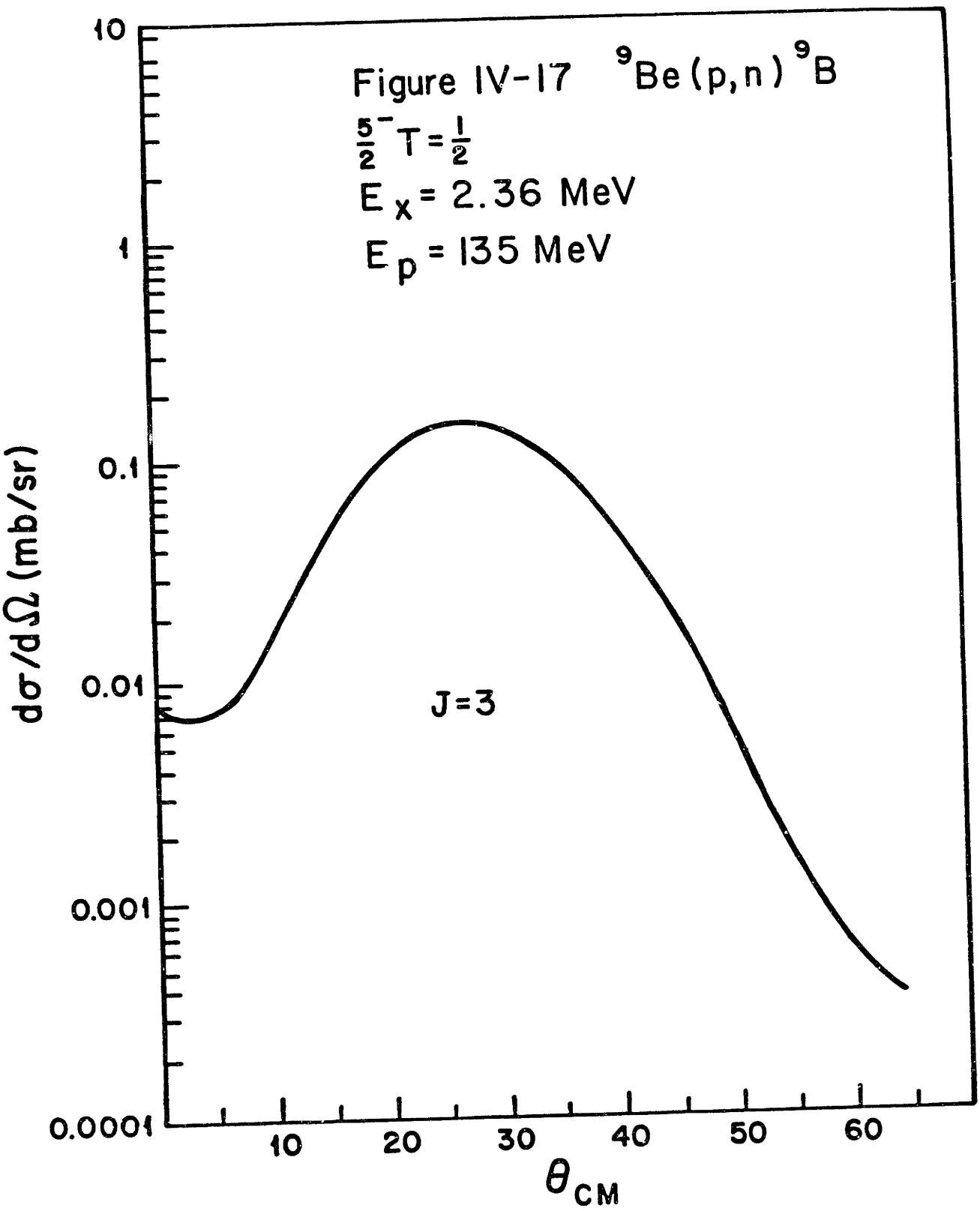
Figure IV-17 $^{9}Be(p,n)^{9}B$
$\frac{5}{2}^{-}$ $T=\frac{1}{2}$
$E_x = 2.36$ MeV
$E_p = 135$ MeV
J=3
$d\sigma/d\Omega$ (mb/sr)
10
1
0.1
0.01
0.001
0.0001
10
20
30
40
50
60
θ_{CM}

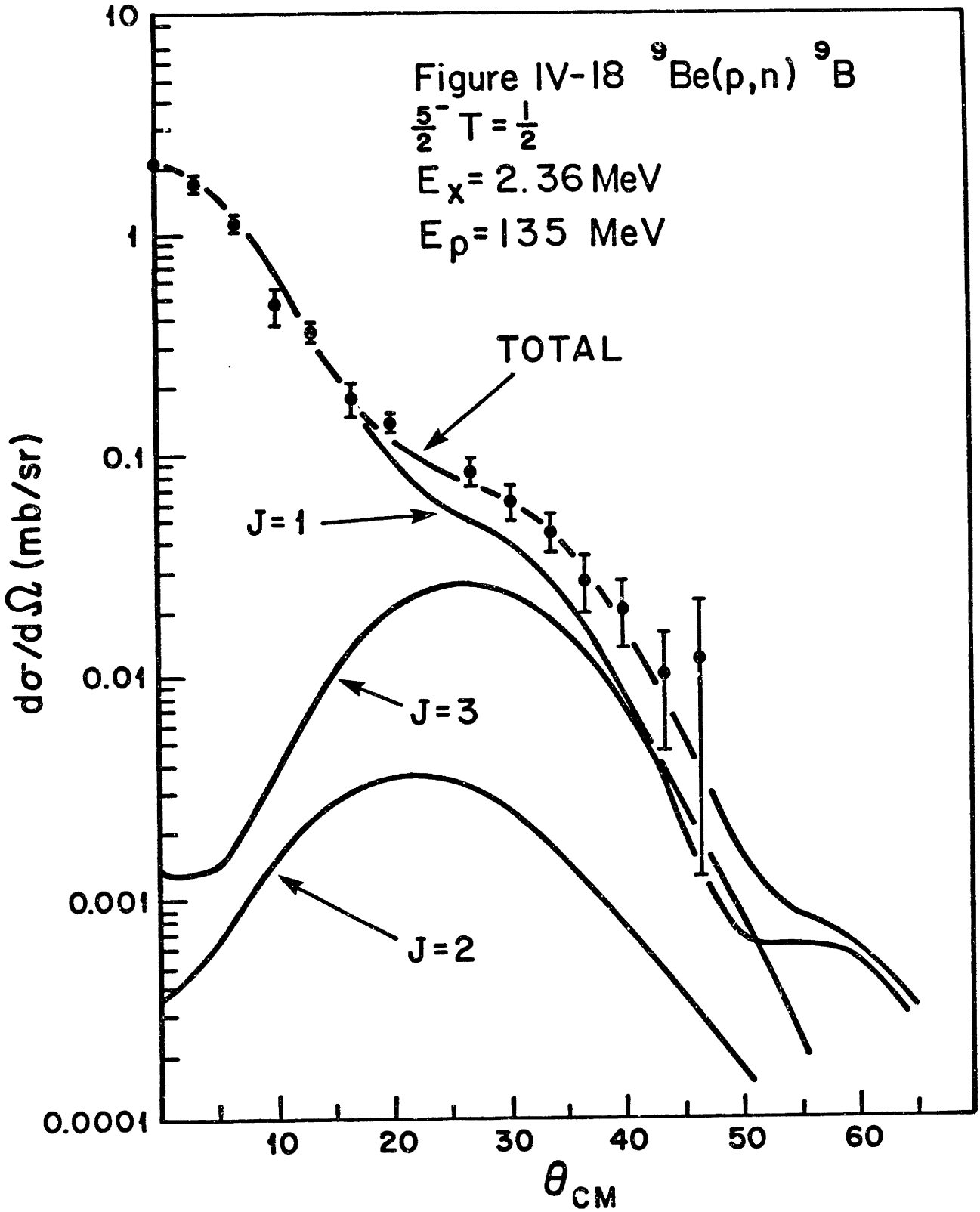
Figure IV-18 ^{9}Be(p,n) ^{9}B
$\frac{5}{2}^{-}$ T = $\frac{1}{2}$
E_x = 2.36 MeV
E_p = 135 MeV
TOTAL
J=1
J=3
J=2
dσ/dΩ (mb/sr)
10
1
0.1
0.01
0.001
0.0001
10
20
30
40
50
60
θ_{CM}

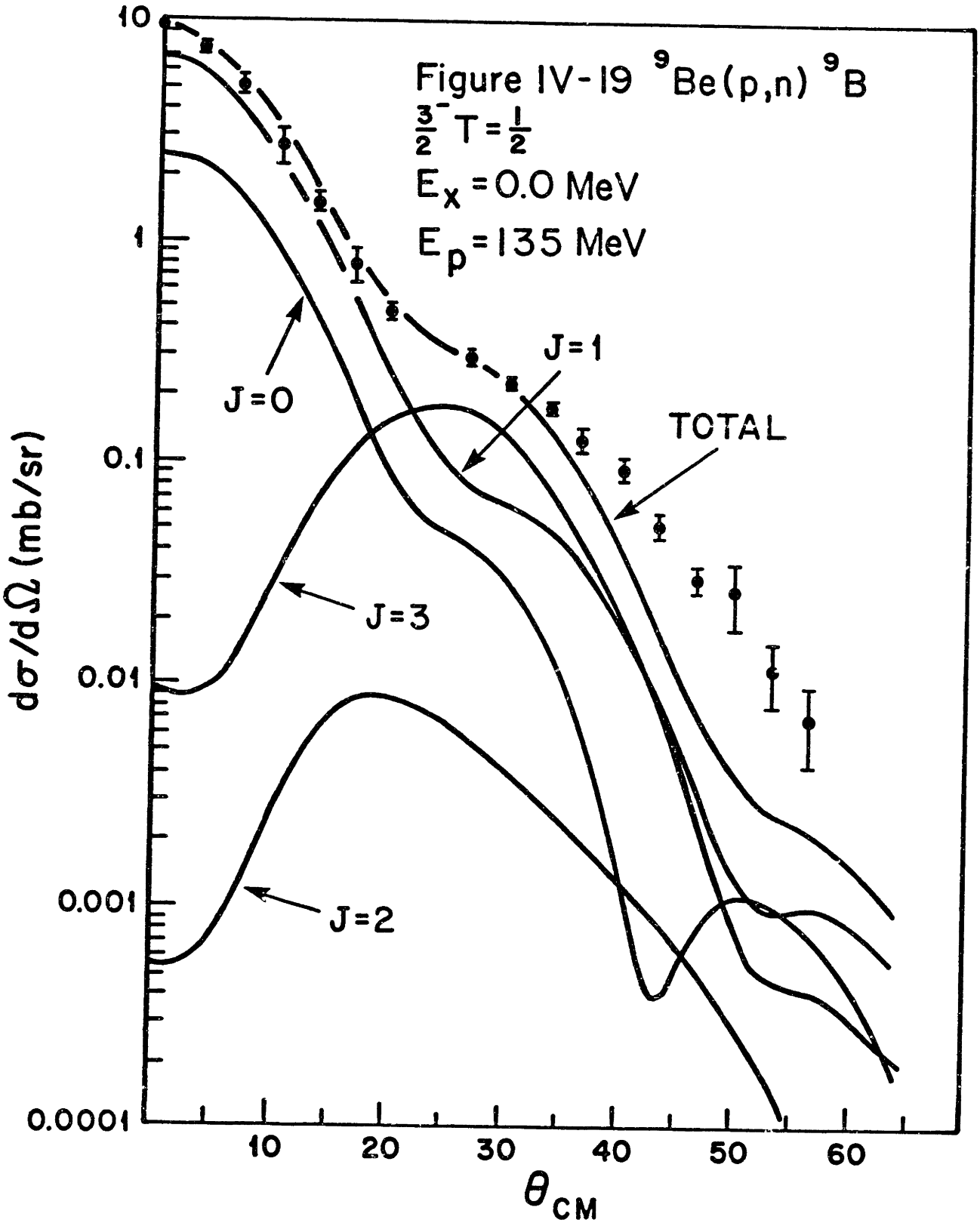
Figure IV-19 $^{9}Be(p,n)\,^{9}B$
$\frac{3}{2}^{-}\ T=\frac{1}{2}$
$E_x = 0.0$ MeV
$E_p = 135$ MeV
J=0
J=1
J=2
J=3
TOTAL
$d\sigma/d\Omega$ (mb/sr)
θ_{CM}
10
1
0.1
0.01
0.001
0.0001
10
20
30
40
50
60

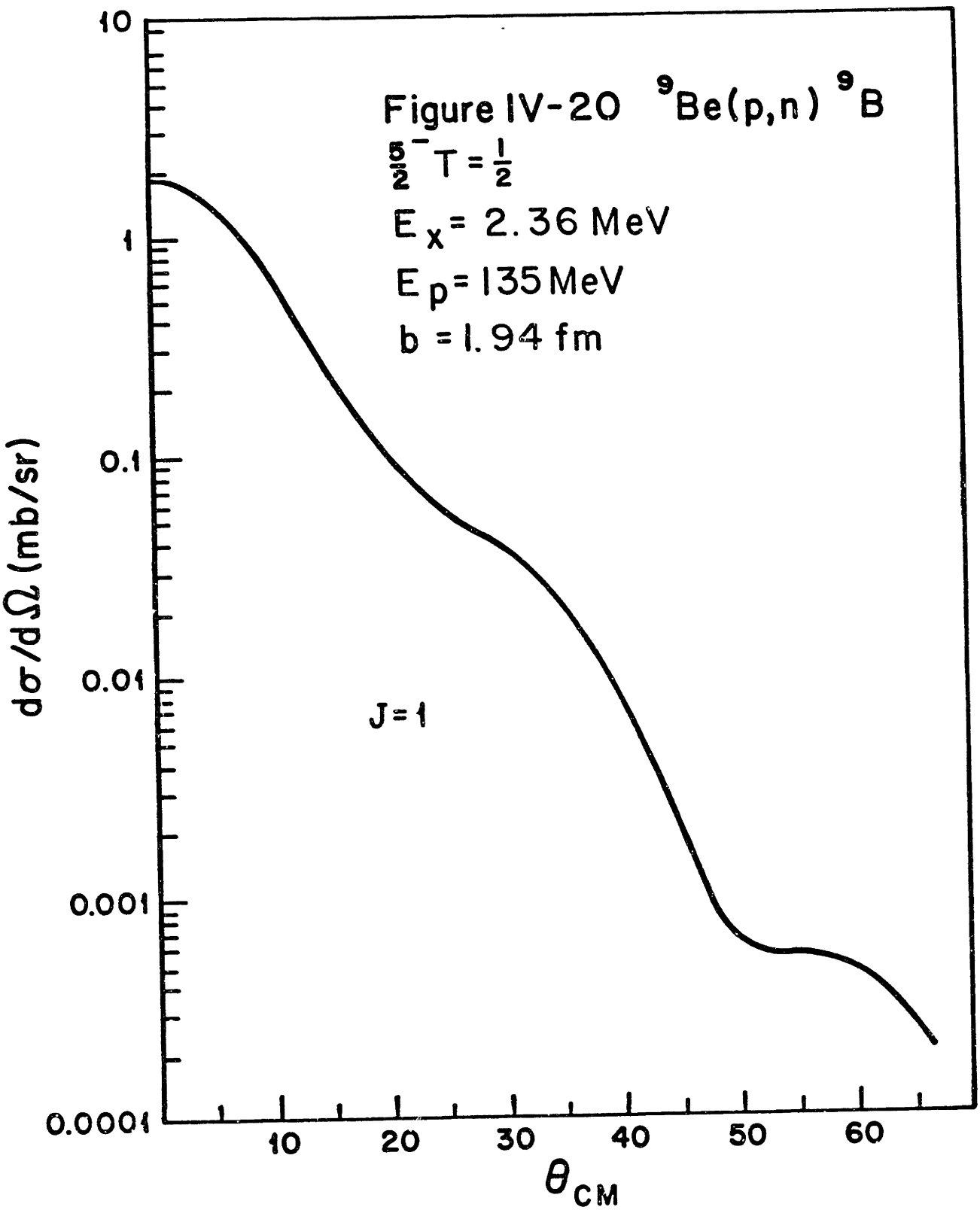
Figure IV-20 $^{9}Be(p,n)^{9}B$
$\frac{5}{2}^{-}$ T = $\frac{1}{2}$
E_x = 2.36 MeV
E_p = 135 MeV
b = 1.94 fm
J = 1
dσ/dΩ (mb/sr)
10
1
0.1
0.01
0.001
0.0001
10
20
30
40
50
60
θ_{CM}

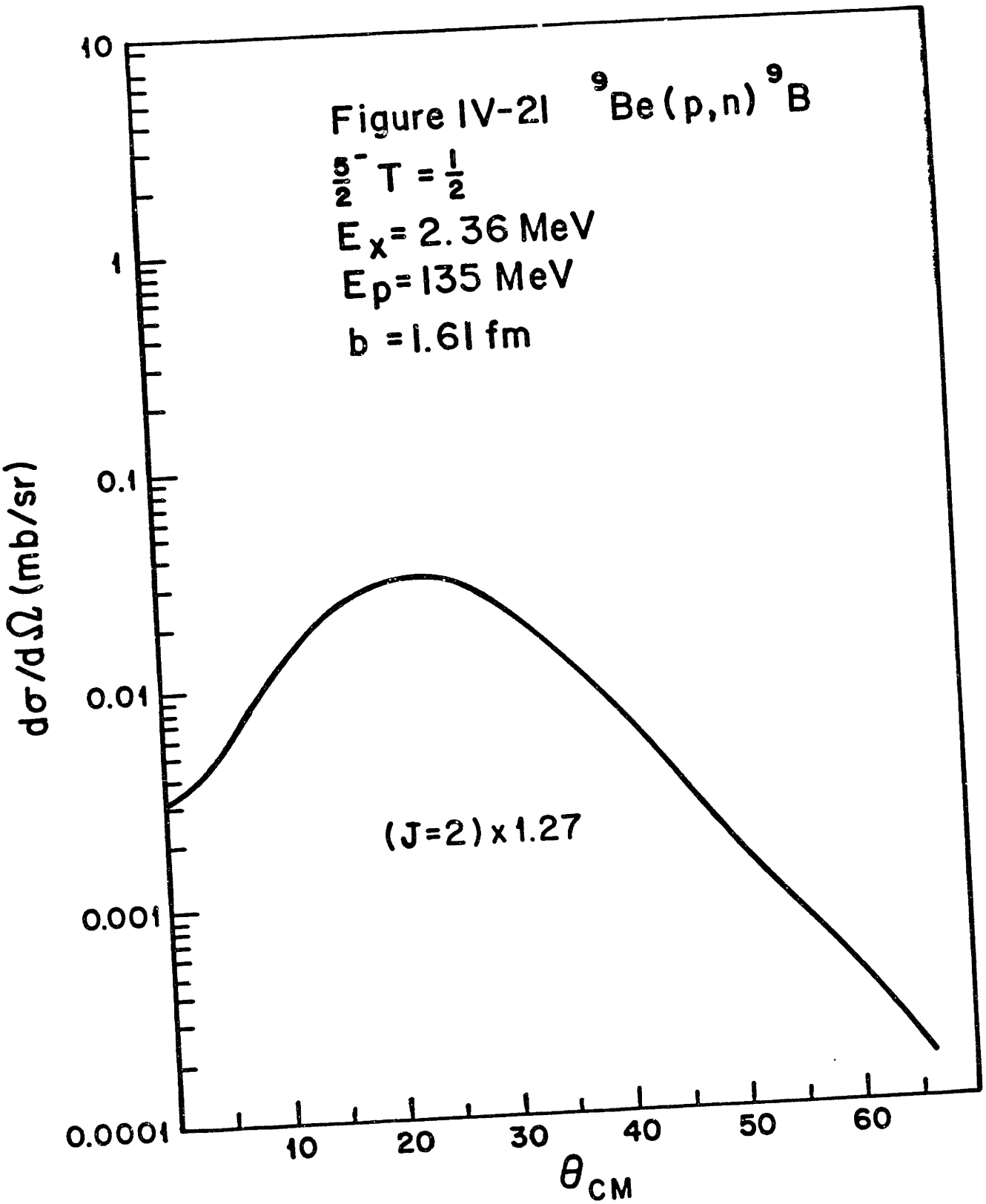
Figure IV-21 $^{9}Be(p,n)^{9}B$
$\frac{5}{2}^{-}$ T = $\frac{1}{2}$
E_x = 2.36 MeV
E_p = 135 MeV
b = 1.61 fm
(J=2) x 1.27
dσ/dΩ (mb/sr)
10
1
0.1
0.01
0.001
0.0001
10
20
30
40
50
60
θ_{CM}

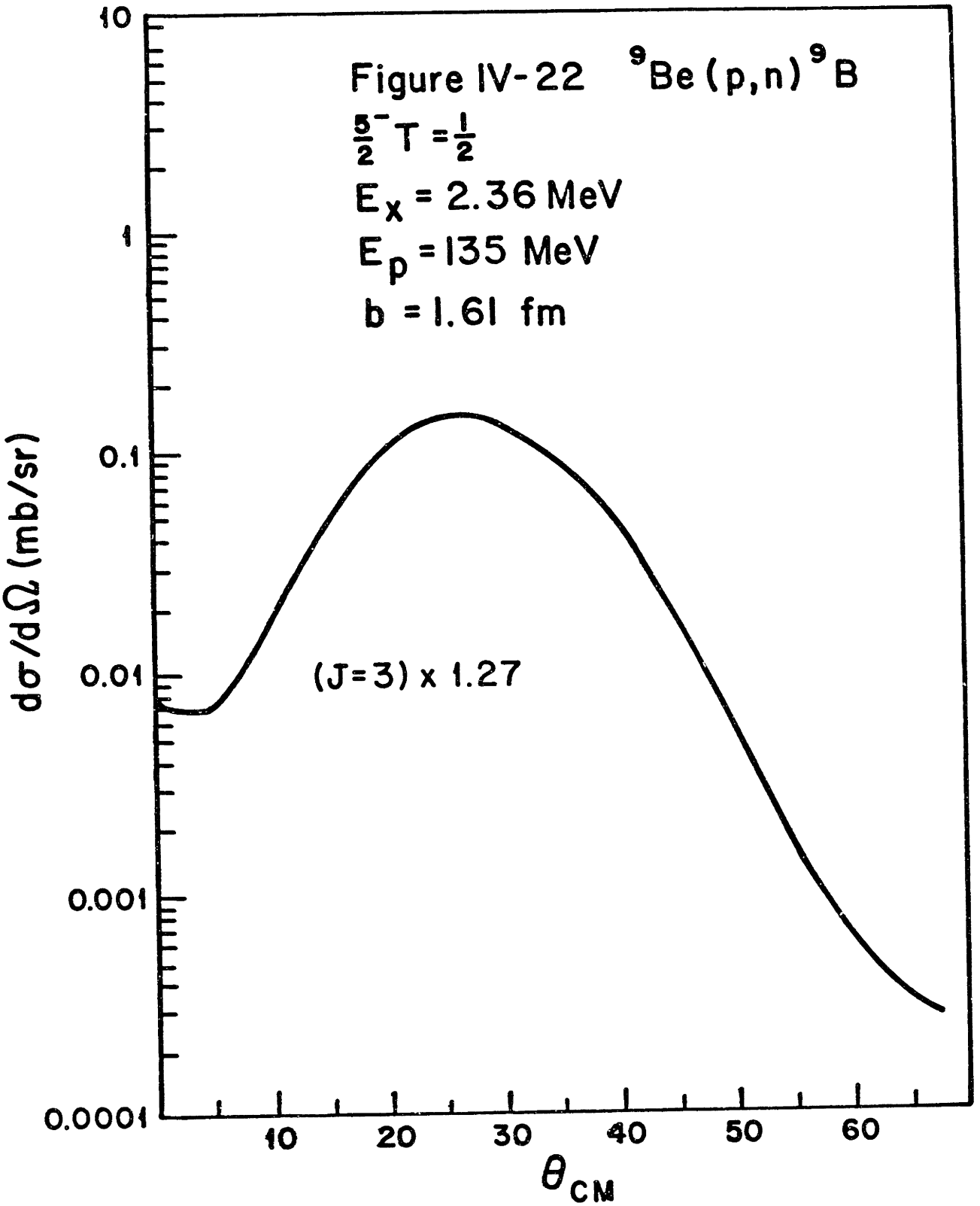
Figure IV-22 $^{9}Be(p,n)^{9}B$
$\frac{5}{2}^{-}$ T = $\frac{1}{2}$
E_x = 2.36 MeV
E_p = 135 MeV
b = 1.61 fm
(J=3) x 1.27
dσ/dΩ (mb/sr)
10
1
0.1
0.01
0.001
0.0001
10
20
30
40
50
60
θ_{CM}

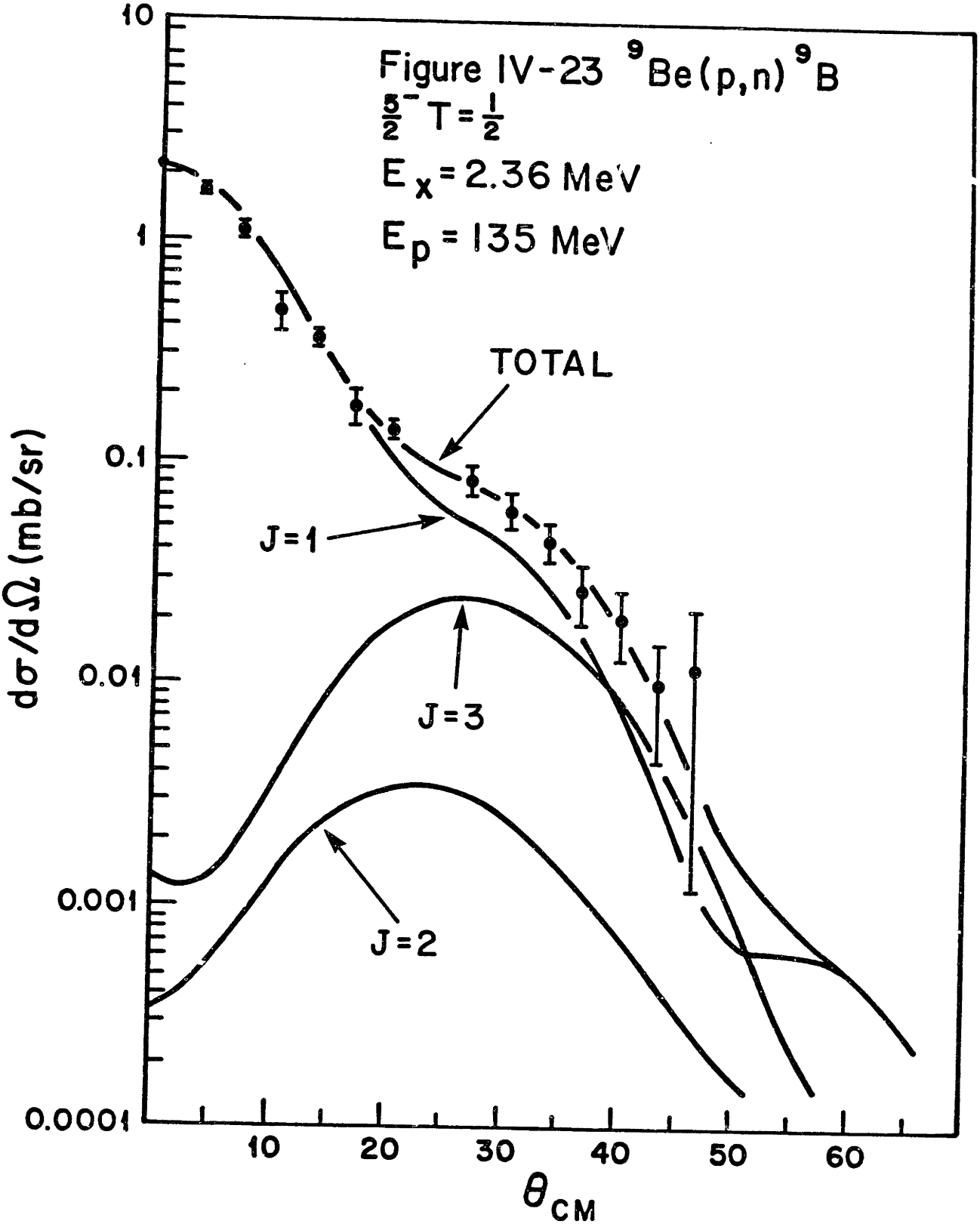
Figure IV-23 $^{9}Be(p,n)^{9}B$
$\frac{5}{2}^{-}$ T=$\frac{1}{2}$
E_x = 2.36 MeV
E_p = 135 MeV
TOTAL
J=1
J=3
J=2
dσ/dΩ (mb/sr)
10
1
0.1
0.01
0.001
0.0001
10
20
30
40
50
60
θ_{CM}

For our data at $E_p = 135\ MeV$, Petrovich *et al* [PET85] calculated the differential cross sections for the $(J^\pi,T) = (\frac{5}{2}^+,\frac{1}{2})$ $(E_x = 0.0MeV)$, $(J^\pi,T) = (\frac{1}{2}^+,\frac{1}{2})$ $(E_x = 0.5MeV)$, and the $(J^\pi,T) = (\frac{3}{2}^+,\frac{1}{2})$ $(E_x = 4.8MeV)$ levels in $^{17}O(p,n)^{17}F$. They used the DWIA and single particle wave functions from the simple harmonic oscillator model. The calculation assumes the ground state to be pure $d_{\frac{5}{2}}$ and neglects the effects of core polarization. Figure $IV-24$ shows a comparison to the transverse electron scattering form factor for the ground state of ^{17}O obtained using simple harmonic oscillator wave functions with a slightly different oscillator parameter. The figure is from the thesis of Hynes [HYN78] and and is also reported in [HYN79]. Curve 1 indicates the individual multipole contributions for $b = 1.8\ fm$. The theoretical curve 2 assumes $b = 1.8\ fm$ $(\alpha = 0.556\ fm^{-1}\ )$ with the usual finite nucleon size and center of mass corrections included. Curve 1 indicates the individual multipole contributions for this case. Curve 3 indicates the fit obtained assuming $b = 1.7\ fm$ $(\alpha = 0.588\ fm^{-1}\ )$. The ground state has a spin of $\frac{5}{2}$ and the transverse form factor has J=1, 3, and 5 contributions, corresponding to M1, M3, and M5 multipoles. No renormalization of the single particle results has been made although it is clear that a reduction of the J=3 contribution is needed to produce a good fit to the data. The single particle wave functions give $\mu = -1.91$ nuclear magnetons for ^{17}O which agrees well with the experimental value of $\mu = -1.894$ nuclear magnetons.

[HIC82] was able to fit the magnetic scattering form factor in an *ad hoc* fashion by multiplying the single particle M3 amplitude by 0.59±0.06 corresponding to a cross section reduction of $0.59^2 = 0.35$ and using wave functions for a Wood-Saxon potential 53 MeV deep, a spin-orbit strength of 6 MeV, and a diffuseness of 0.55 fm. The radius was a free parameter and was determined to be 1.24±0.06. The M5 moment was also free to be quenched but this was not required, the best fit giving 1.03±0.11. The fit obtained by [HIC82] is reproduced in figure $IV-25$.

Figure IV-24. The magnetic form factor of ^{17}O.
Reproduced from [HYN78]. See text for curves.

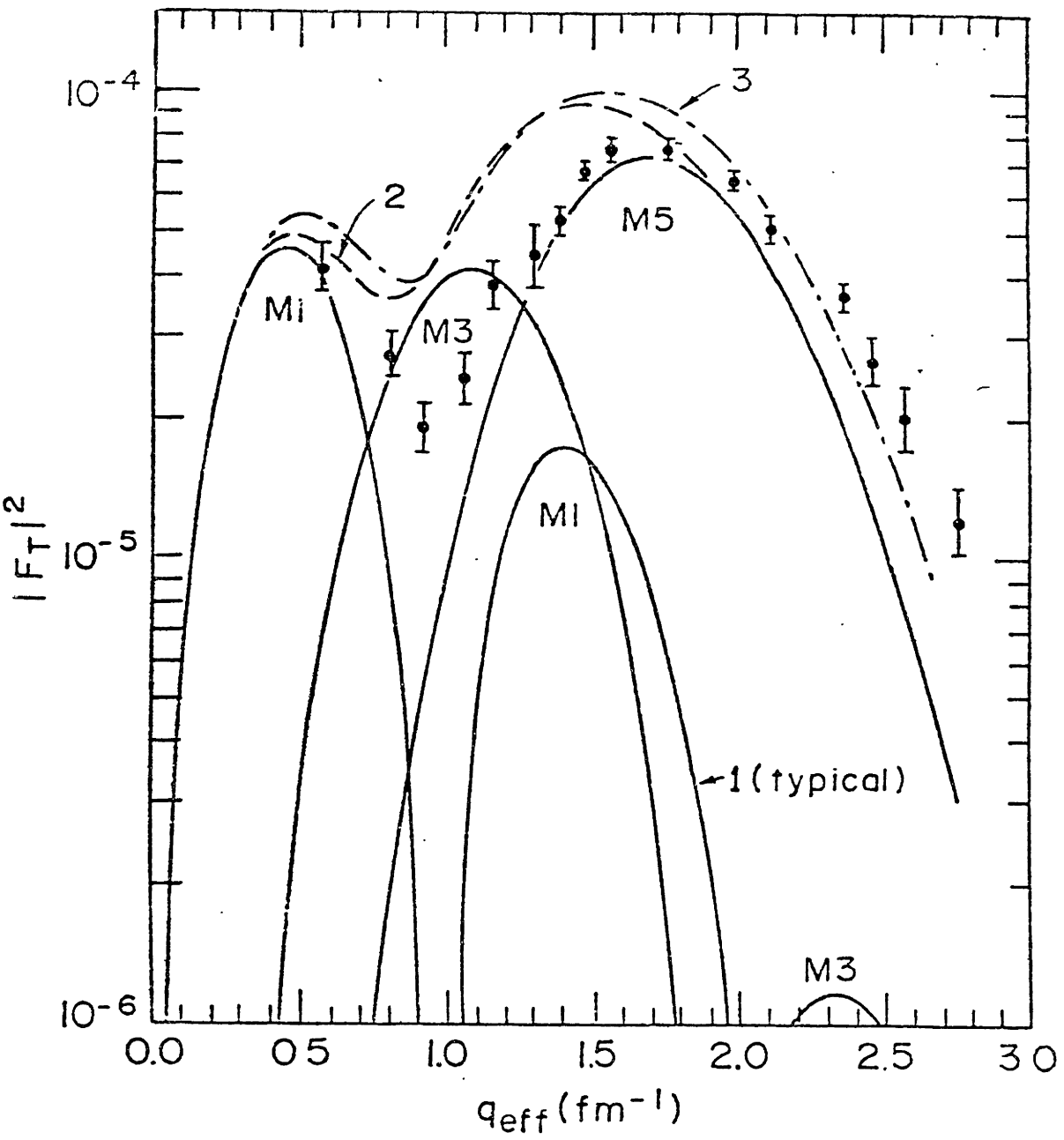

Figure IV-25. A Wood-Saxon fit of the magnetic form factor of ^{17}O. Taken from [HIC82].

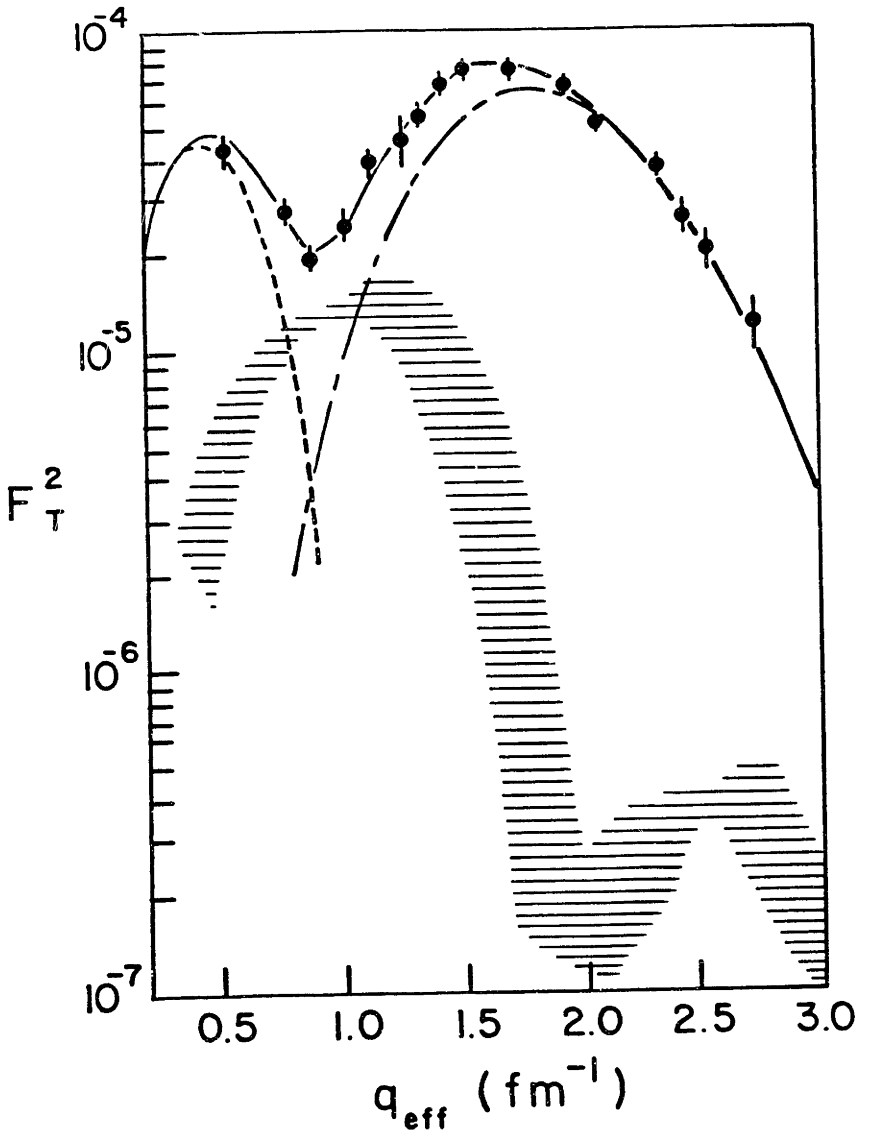

The (p,n) calculations were again made with the code DWBA70 using $b' = 1.75\ fm$ ($\alpha' = 0.573\ fm^{-1}$) to describe the $d_{\frac{5}{2}}$ neutron. The center of mass correction consisted of the cross section renormalization factors of 1.00, 1.13, and 1.27 for J=0,1, J=2,3, and J=4,5, respectively. The (p,n) interaction is the same as used in the ^9Be calculations. The optical parameters are

$$\begin{aligned} V &= 15.3\ MeV & V_{SO} &= 3.90 MeV \\ r_0 &= 1.35\ fm & W_{SO} &= -0.25 MeV \\ a &= 0.63\ fm & r_{SO} &= 0.96\ fm \\ W &= 11.26\ MeV & a_{SO} &= 0.49\ fm \\ r_0' &= 1.33\ fm & r_C &= 1.28\ fm \\ a' &= 0.59\ fm \end{aligned}$$

which were taken from the thesis of Kelly [KEL81]. The DWA results for the J=0,1,2,3,4, and 5 contributions to the cross section for the ground state transition in $^{17}O(p,n)^{17}F$ at $E_p = 135 MeV$ are shown in figures $IV-26$ through $IV-31$. For J=0 and 1 the Born approximation results are also shown. By comparing the DWBA and PWBA results, one obtains $N_\tau^D = 0.353$ and $N_{\sigma\tau}^D = 0.463$. The PWBA results also yield $|J_\tau| = 73.5\ MeV\ fm^3$ and $|J_{\sigma\tau}| = 151.3\ MeV\ fm^3$ using $\mu = 994.1\ MeV$, $|M_F|^2 = 1$, and $|M_{GT}|^2 = 1.4$. The force constants J_τ and $J_{\sigma\tau}$ are slightly lower than the values obtained for $^9Be(p,n)$ which is expected because of the slightly higher center of mass energy for $^{17}O(p,n)$. To normalize the J=0 and J=1 contributions to the experimental data, the force normalization factors N_τ and $N_{\sigma\tau}$ are again introduced and, as in the case of ^9Be, are fixed according to

$$\sigma_{exp}(\theta = 0°) = \left(\frac{\mu}{\pi\hbar^2}\right)^2 N_\tau N_{\sigma\tau} |J_\tau|^2 \left(|M_F|^2 + R^2 |M_{GT}|^2\right)$$

$$R^2 = \frac{N_{\sigma\tau} N_{\sigma\tau}^D |J_{\sigma\tau}|^2}{N_\tau N_\tau^D |J_\tau|^2} = \frac{N_{\sigma\tau}^D |J'_{\sigma\tau}|^2}{N_\tau^D |J'_\tau|^2}$$

The differential cross section measured in this experiment is $\sigma_{exp}(\theta = 0°) = 8.0\ mb$. As for ^9Be, $R^2 = 6.05$ may be used since this ratio was determined by [TAD82] to be mass independent. The Gamow-Teller matrix element is taken to be $|M_{GT}|^2 = 0.643$. This number follows from the experimental $\log ft = 3.488$ for the β-decay of ^{17}F [AJZ82] and using

$$|M_F|^2 + 1.57 |M_{GT}|^2 = 6180/ft$$

Using these numbers, it follows from the above two equations involving R and $\sigma_{exp}(\theta = 0°)$ that $N_\tau = 1.31$ and $N_{\sigma\tau} = 1.43$ corresponding to $|J'_\tau| = 84.1\ MeV\ fm^3$ and $|J'_{\sigma\tau}| = 180.9\ MeV\ fm^3$ which are somewhat higher than the values assumed for ^9Be. As noted in the previous section, this inconsistency can be removed by reinterpreting the ^9Be results in terms of smaller $|M_{GT}|^2$. Note that the experimental $|M_{GT}|^2$ for ^{17}F implies the use of a renormalization factor $N_{\sigma 1} = 0.459$

for the $^{17}O(p,n)$ results. Figure $IV-32$ shows the complete structure of the calculated differential cross section for the ground state transition in $^{17}O(p,n)^{17}F$ at $E_p = 135\ MeV$ compared with the experimental data. The J=3 and J=5 contributions have been normalized by $N_{\sigma 3} = 0.107$ and $N_{\sigma 5} = 0.346$ to fit the data. Note that $N_{\sigma 3}/N_{\sigma 1} = 0.232$ while $N_{\sigma 5}/N_{\sigma 1} = 0.754$ indicating that the data prefer less J=5 quenching than J=3 as is true of the electron scattering data in figures $IV-25.$ and $IV-26.$

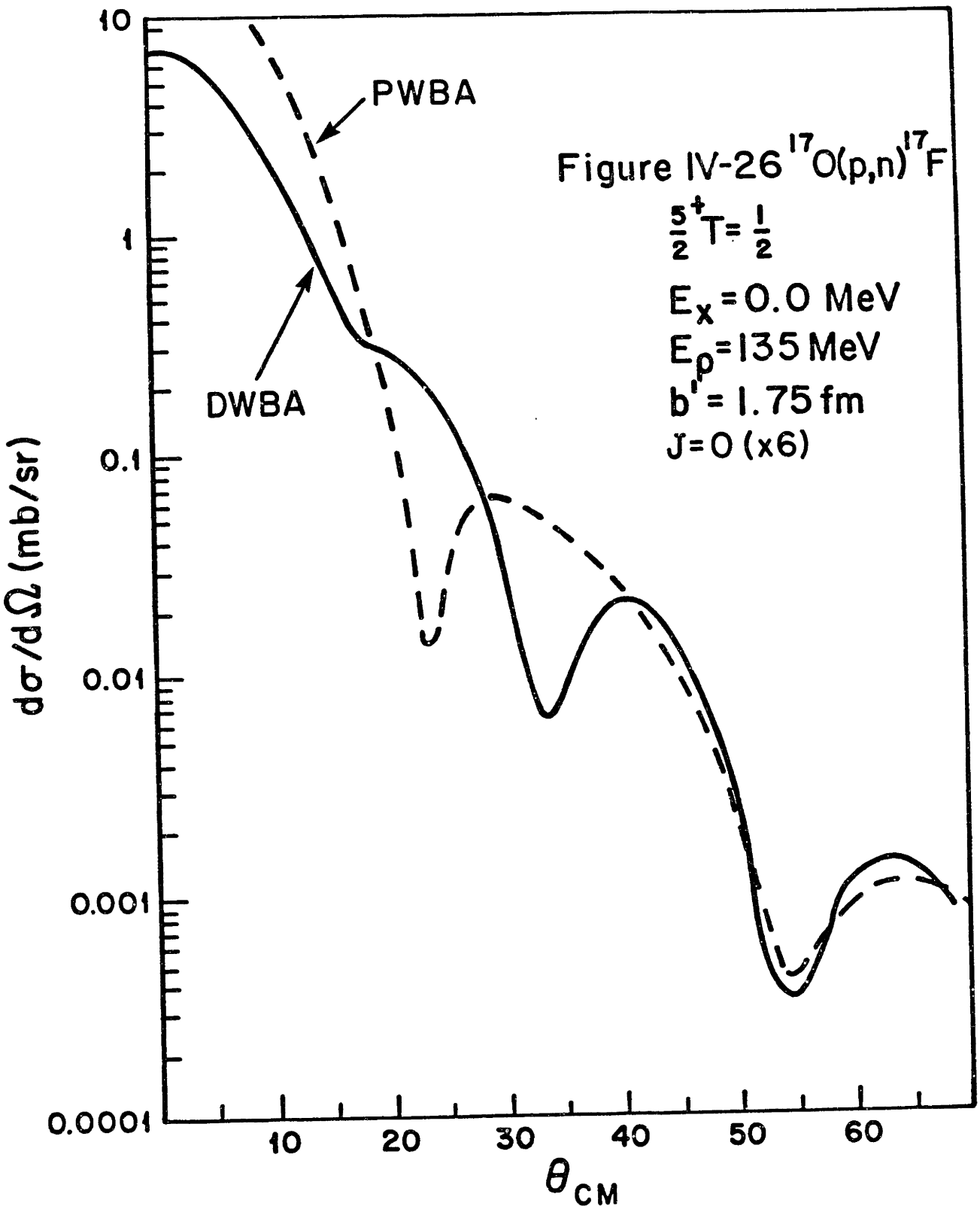
Figure IV-26 $^{17}O(p,n)^{17}F$
$\frac{5}{2}^+ T = \frac{1}{2}$
$E_x = 0.0$ MeV
$E_p = 135$ MeV
$b' = 1.75$ fm
$J = 0$ (x6)
PWBA
DWBA
$d\sigma/d\Omega$ (mb/sr)
10
1
0.1
0.01
0.001
0.0001
10
20
30
40
50
60
θ_{CM}

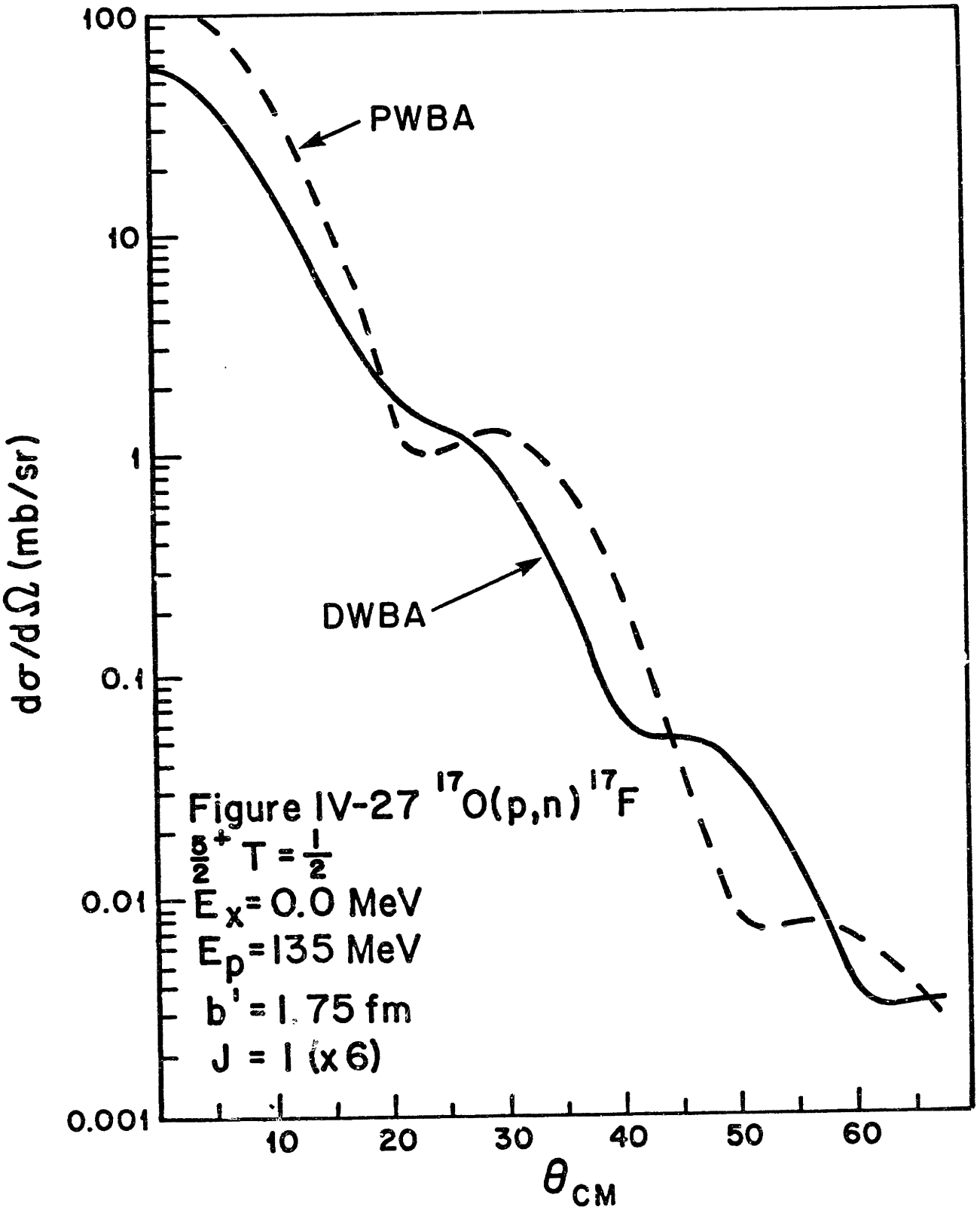
100
10
1
0.1
0.01
0.001
dσ/dΩ (mb/sr)
PWBA
DWBA
10
20
30
40
50
60
θCM
Figure IV-27 17O(p,n)17F
5/2+ T = 1/2
Ex = 0.0 MeV
Ep = 135 MeV
b' = 1.75 fm
J = 1 (x6)

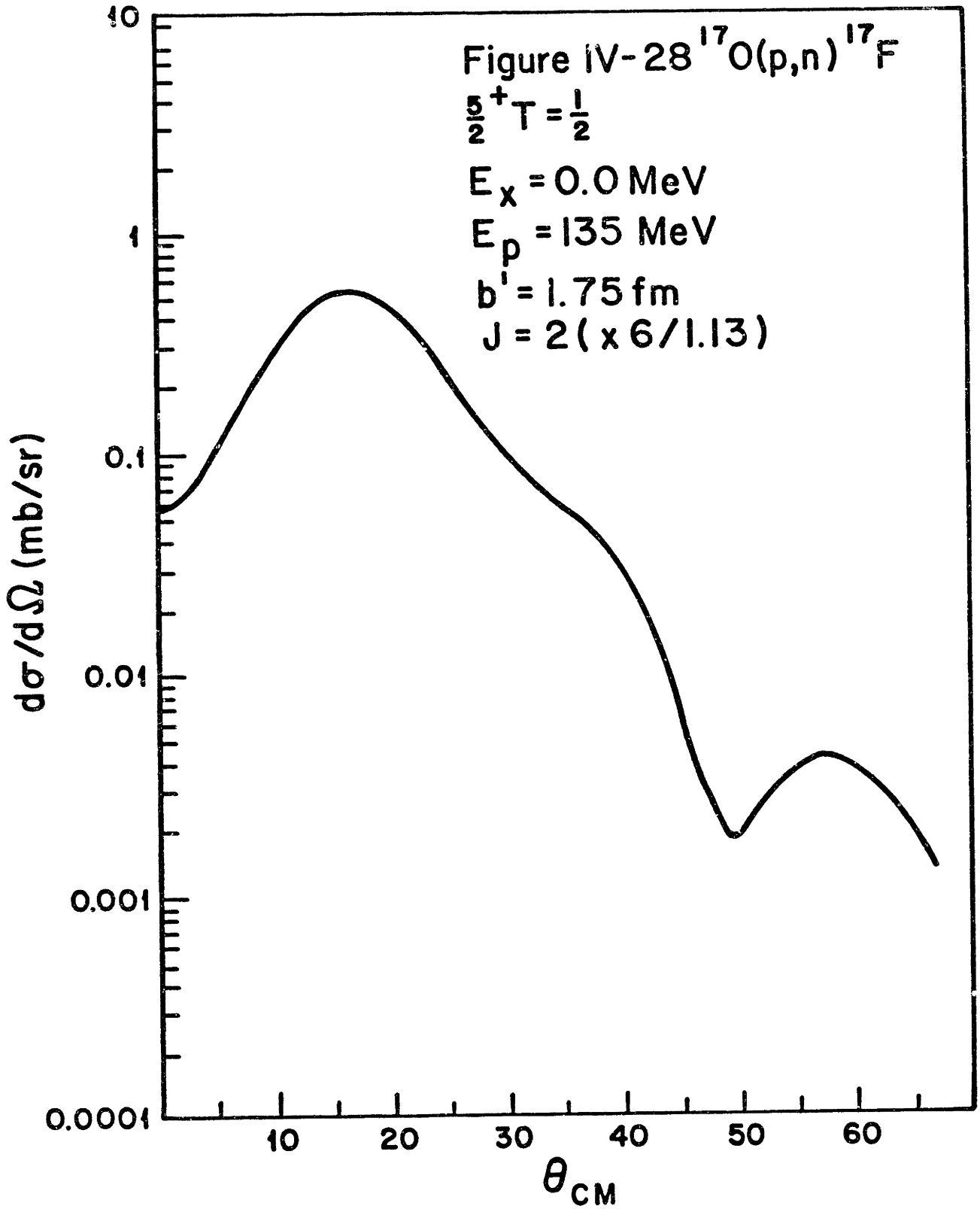
Figure IV-28 $^{17}O(p,n)^{17}F$
$\frac{5}{2}^+ T = \frac{1}{2}$
$E_x = 0.0$ MeV
$E_p = 135$ MeV
$b' = 1.75$ fm
$J = 2 (\times 6/1.13)$
$d\sigma/d\Omega$ (mb/sr)
10
1
0.1
0.01
0.001
0.0001
10
20
30
40
50
60
θ_{CM}

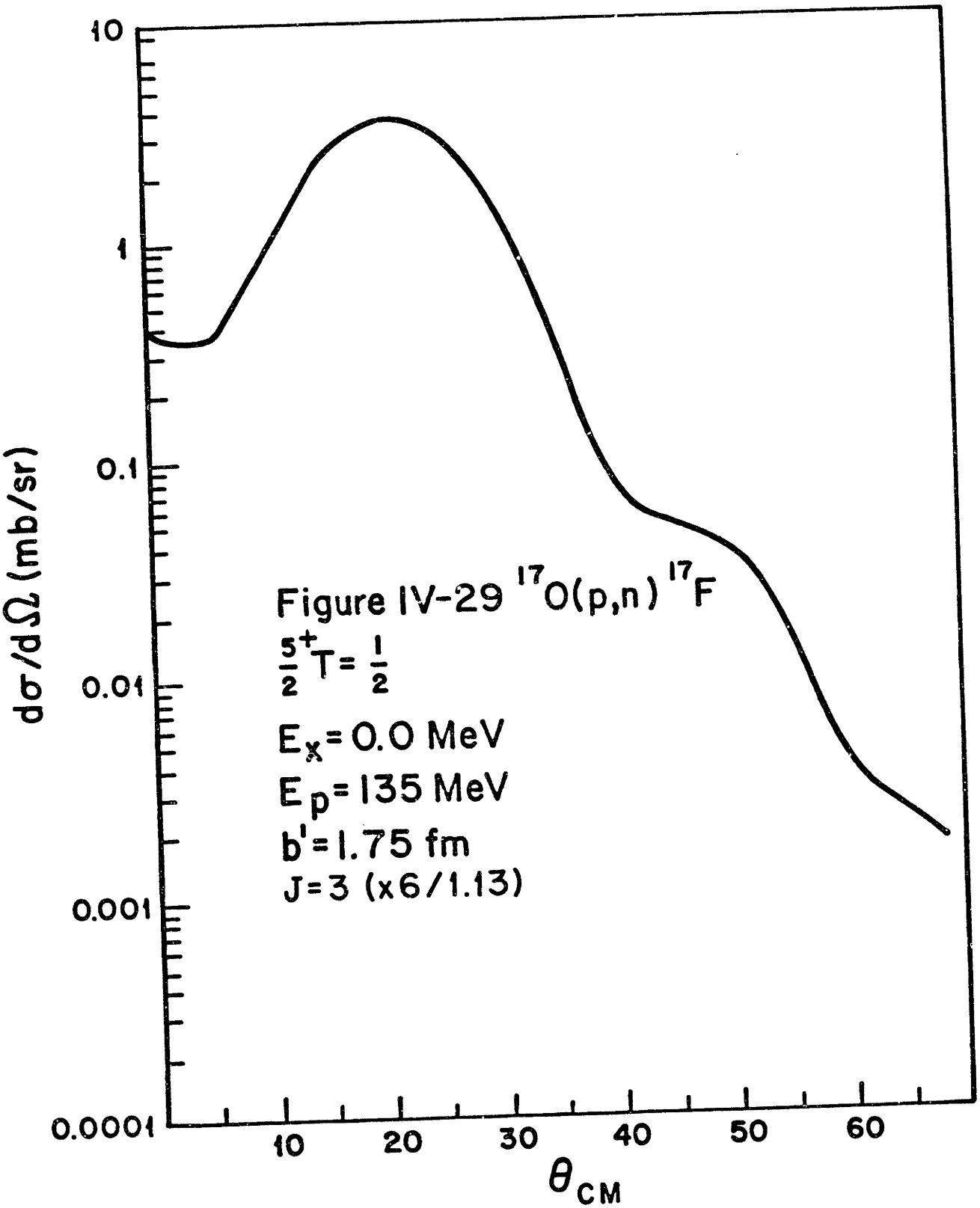
10
1
0.1
0.01
0.001
0.0001
dσ/dΩ (mb/sr)
10
20
30
40
50
60
θCM
Figure IV-29 17O(p,n) 17F
5/2+ T= 1/2
Ex= 0.0 MeV
Ep= 135 MeV
b'= 1.75 fm
J=3 (x6/1.13)

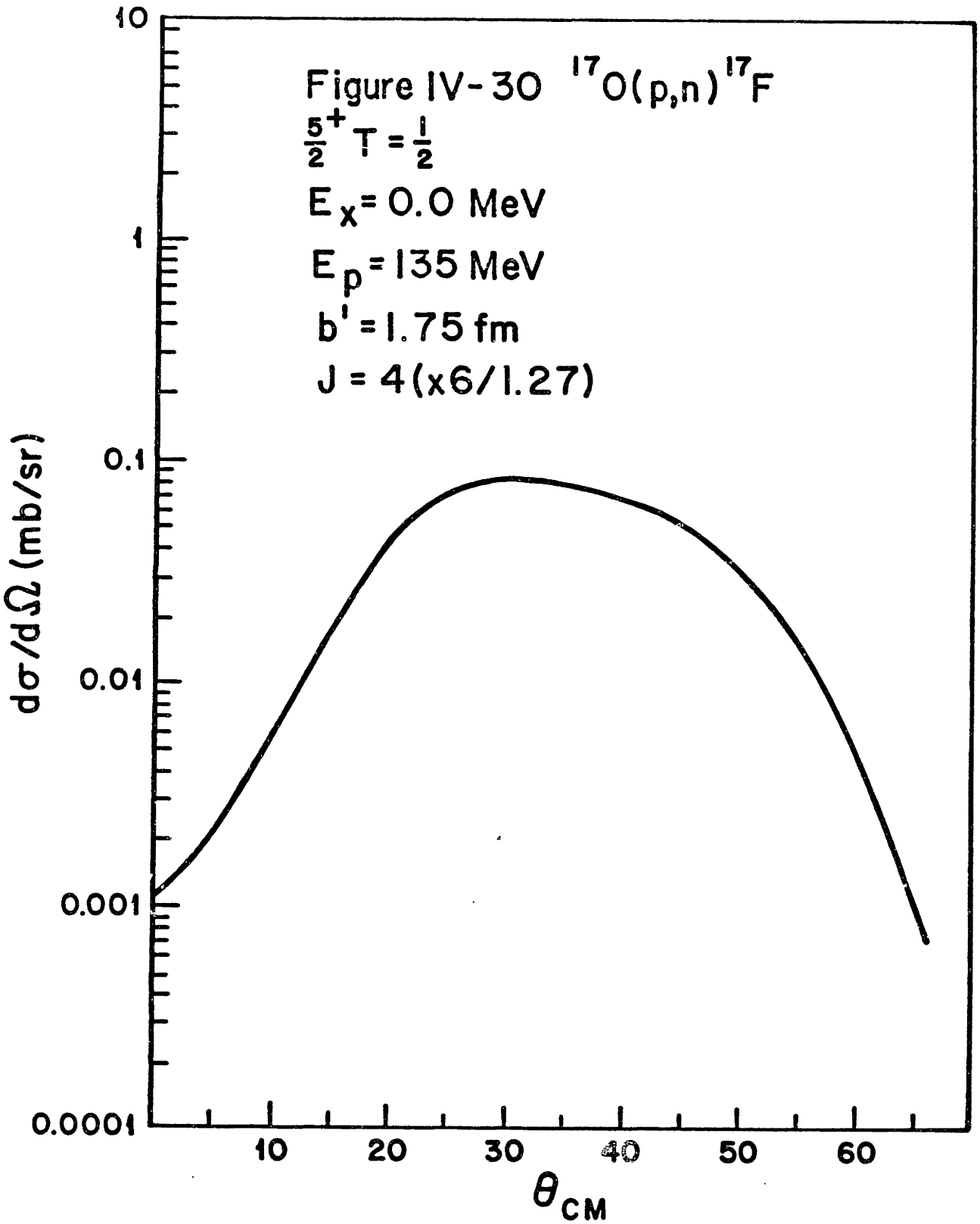
Figure IV-30 $^{17}O(p,n)^{17}F$
$\frac{5}{2}^+ T = \frac{1}{2}$
E_x = 0.0 MeV
E_p = 135 MeV
b' = 1.75 fm
J = 4 (x6/1.27)
10
1
0.1
0.01
0.001
0.0001
$d\sigma/d\Omega$ (mb/sr)
10
20
30
40
50
60
θ_{CM}

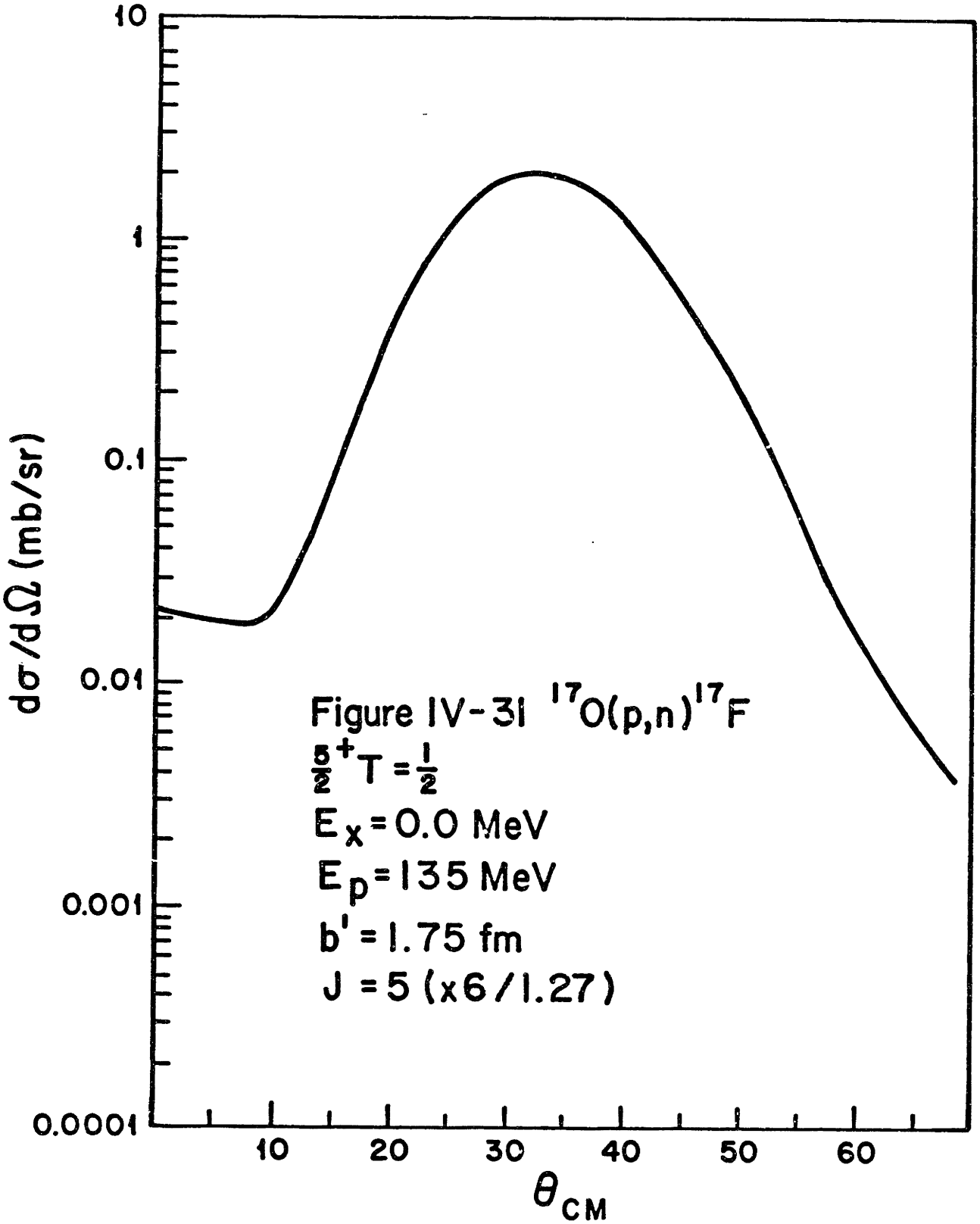
10
1
0.1
0.01
0.001
0.0001
dσ/dΩ (mb/sr)
10
20
30
40
50
60
θCM
Figure IV-31 17O(p,n)17F
5/2+ T = 1/2
Ex = 0.0 MeV
Ep = 135 MeV
b' = 1.75 fm
J = 5 (x6/1.27)

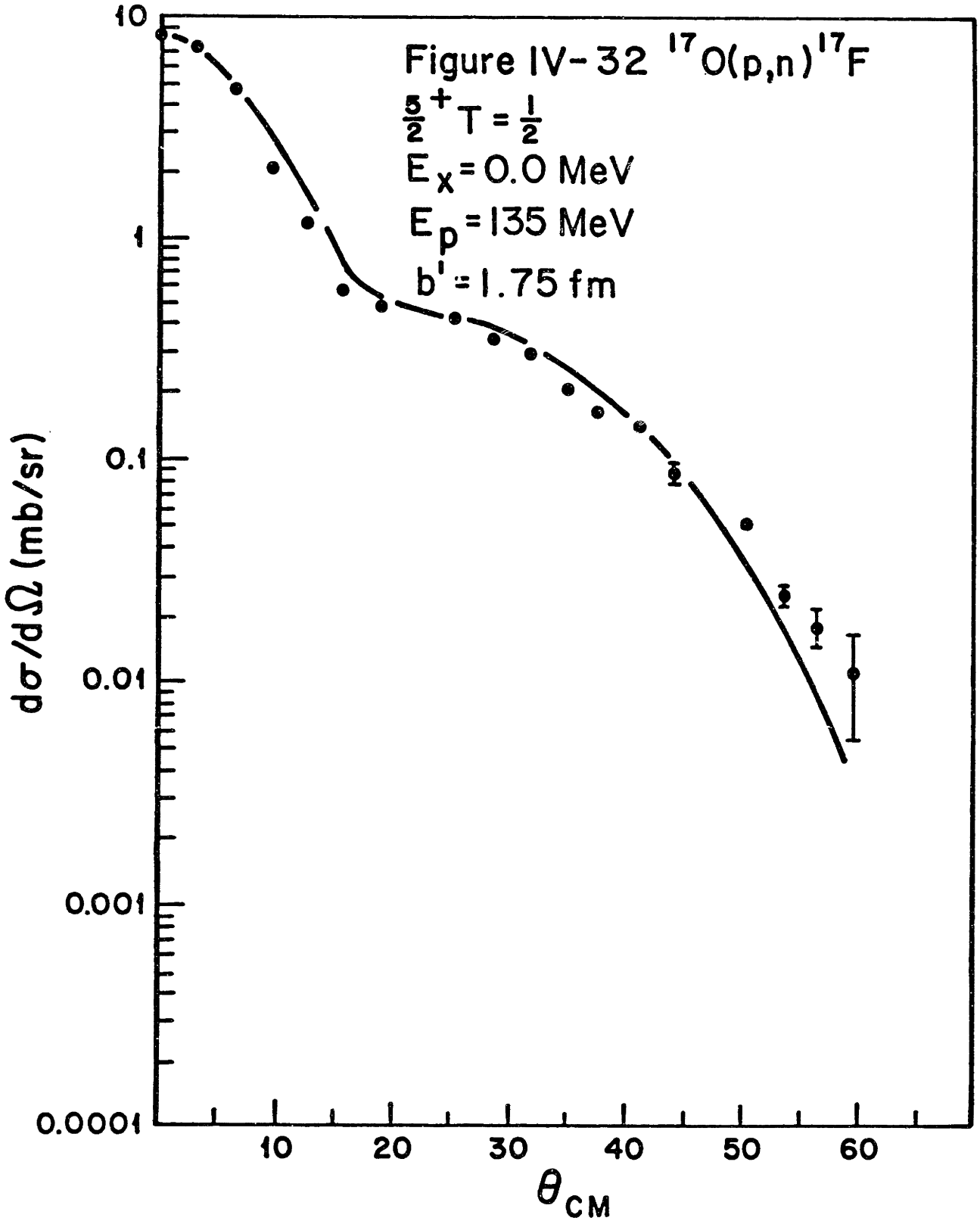
Figure IV-32 $^{17}O(p,n)^{17}F$
$\frac{5}{2}^+ T = \frac{1}{2}$
$E_x = 0.0$ MeV
$E_p = 135$ MeV
$b' = 1.75$ fm
$d\sigma/d\Omega$ (mb/sr)
10
1
0.1
0.01
0.001
0.0001
10
20
30
40
50
60
θ_{CM}

$^{17}O(p,n)$ *to the excited state at 4.8 MeV*

The theoretical results for the J=1-4 contributions to the $\frac{5}{2}^+ \rightarrow \frac{3}{2}^+$ ($E_x = 4.8MeV$) transition in $^{17}O(p,n)^{17}F$ at $E_p = 135\ MeV$ are shown in figures $IV-33$ through $IV-36$. Again pure single particle wave functions have been assumed. The J=1 contribution is shown normalized to the data in figure $IV-37$ using $N_{\sigma\tau} = 1.43$ from the ground state transition and $N_{\sigma 1} = 0.223$ which corresponds to a reduction in the model $|M_{GT}|^2$ from the single particle value of 1.6 to 0.357. The data does not extend to far enough angles to allow any statement about the J=2-4 contributions to the cross section. Possible $\frac{3}{2}^+$ strength is also observed experimentally in discrete states up to about $E_x = 14.5$ MeV with a total cross section equal to 1.6 mb/sr as compared to 3.5 mb/sr at 0° for the 4.8 MeV excitation. Scaling suggests that these additional $\frac{3}{2}^+$ levels contain $\sum |M_{GT}|^2 = 0.160$.

$^{17}O(p,n)$ *to the excited state at 0.5 MeV*

The cross section was also calculated for the $\frac{5}{2}^+ \rightarrow \frac{1}{2}^+ (E_x = 0.5Mev)$ transition in $^{17}O(p,n)^{17}F$ at $E_p = 135\ MeV$ assuming single particle wave functions. This transitions has J=2 and J=3 and thus contains no Gamow-Teller strength. The J=2 and J=3 contributions are shown separately in figures $IV-38$ and $IV-39$. These two curves are shown normalized to the data in figure $IV-40$. The normalization factors are $N_{\sigma 2} = 0.932$ and $N_{\sigma 3} = 0.328$. The data would appear to favor the J=2 shape although the cross section for this transition is quite likely sensitive to other features of the calculations such as the bound state radial functions since the final orbit has a node.

Analyzing powers

The analyzing powers for the analog ground state transitions were calculated using the same calculation parameters which produced the cross sections in figures $IV-14$ and $IV-23$. The calculated analyzing powers were found to be very sensitive to the normalization factors which multiplied the incoherent J-transfer cross sections. It is likely that the analyzing powers are sensitive to the optical potential as has been found for the case of $^{12}C(p,p')$ at 155 MeV [SHE70]. The calculation is seen to agree with experiment out to about 55° (2.3 fm^{-1}). This

is consistent with the cross section results and indicates that the distortion effects have been handled with some accuracy.

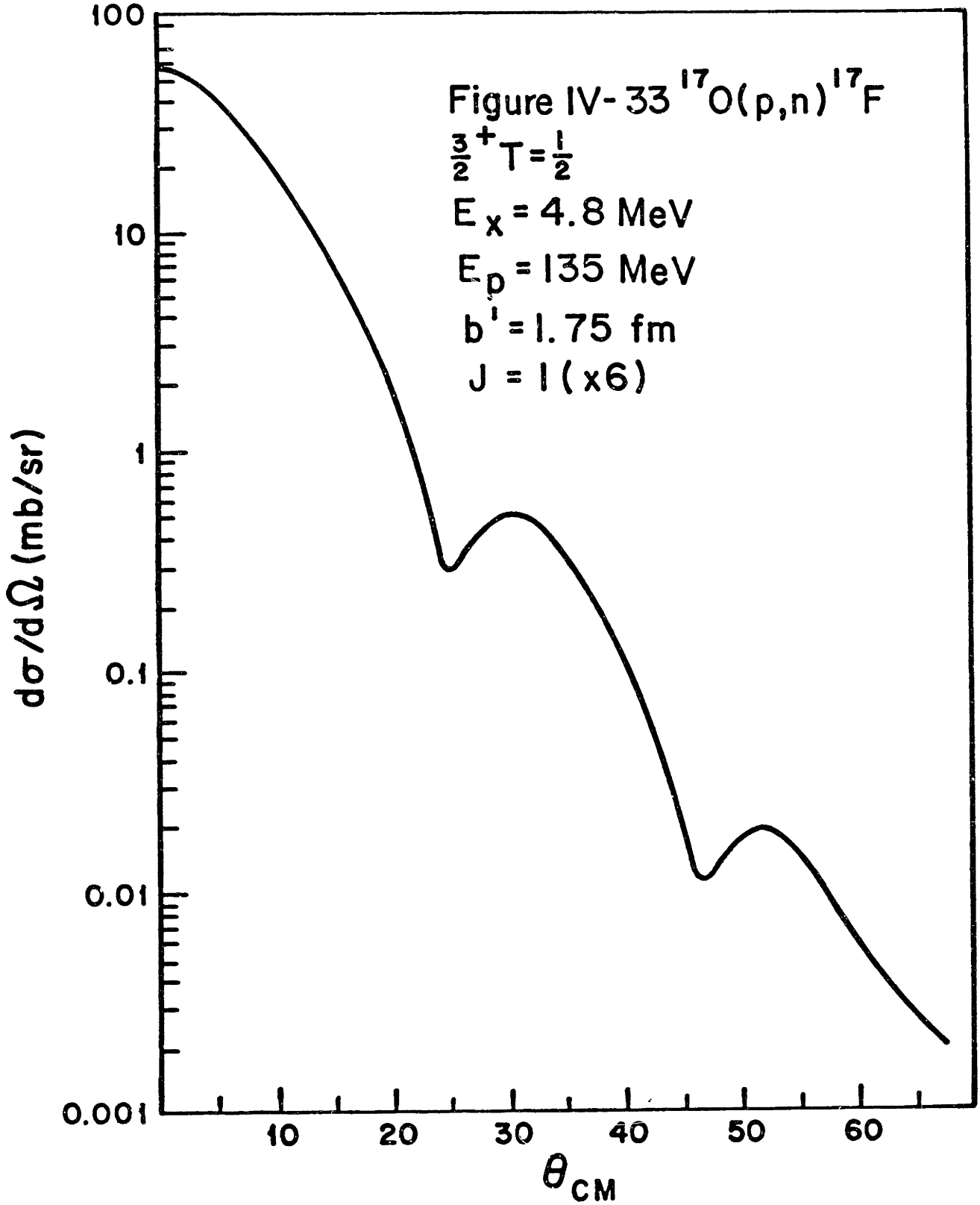
Figure IV-33 $^{17}O(p,n)^{17}F$
$\frac{3}{2}^+ T=\frac{1}{2}$
$E_x = 4.8$ MeV
$E_p = 135$ MeV
$b' = 1.75$ fm
$J = 1 (x6)$
100
10
1
0.1
0.01
0.001
$d\sigma/d\Omega$ (mb/sr)
10
20
30
40
50
60
θ_{CM}

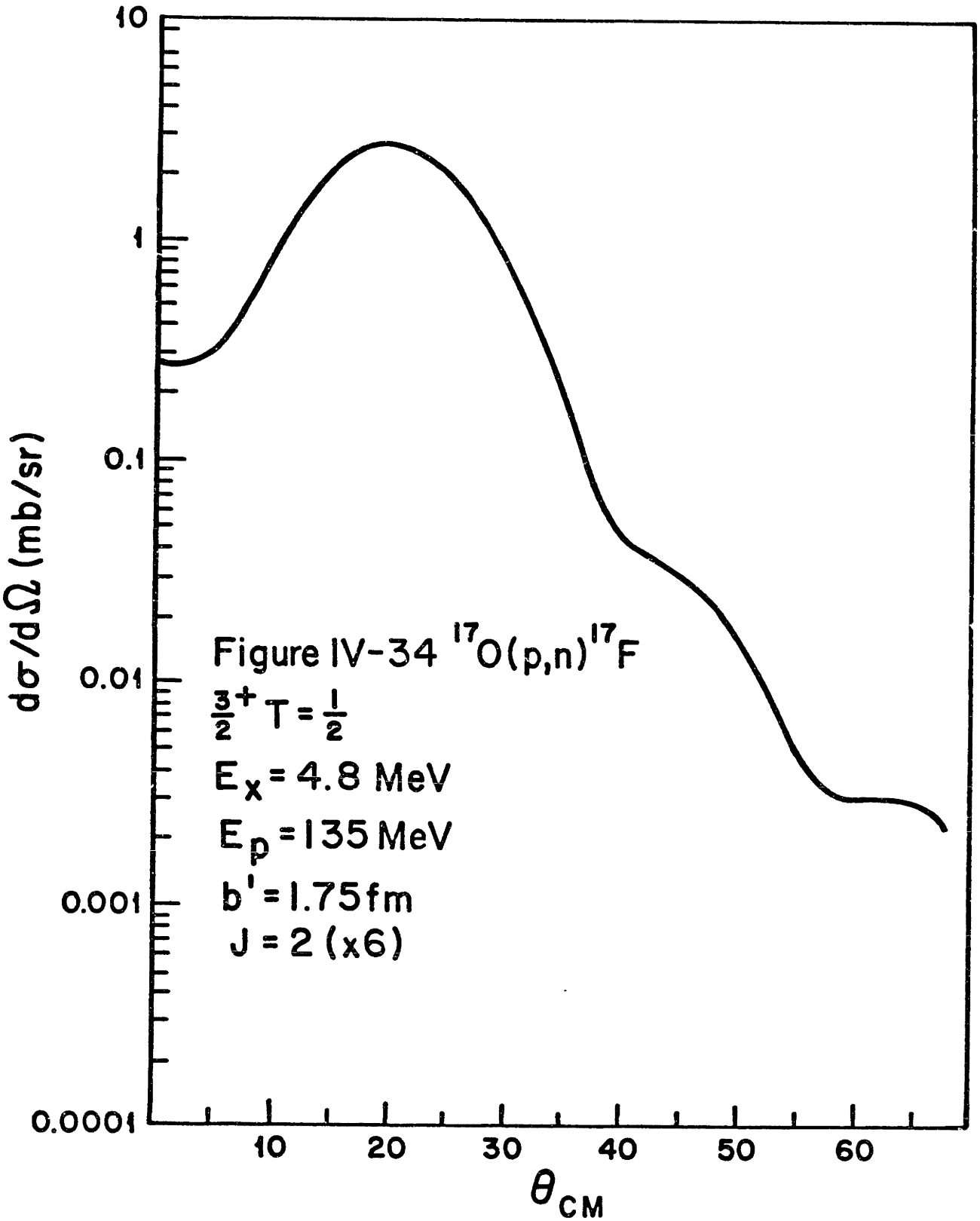
10
1
0.1
0.01
0.001
0.0001
dσ/dΩ (mb/sr)
10
20
30
40
50
60
θCM
Figure IV-34 17O(p,n)17F
3/2+ T = 1/2
Ex = 4.8 MeV
Ep = 135 MeV
b' = 1.75 fm
J = 2 (x6)

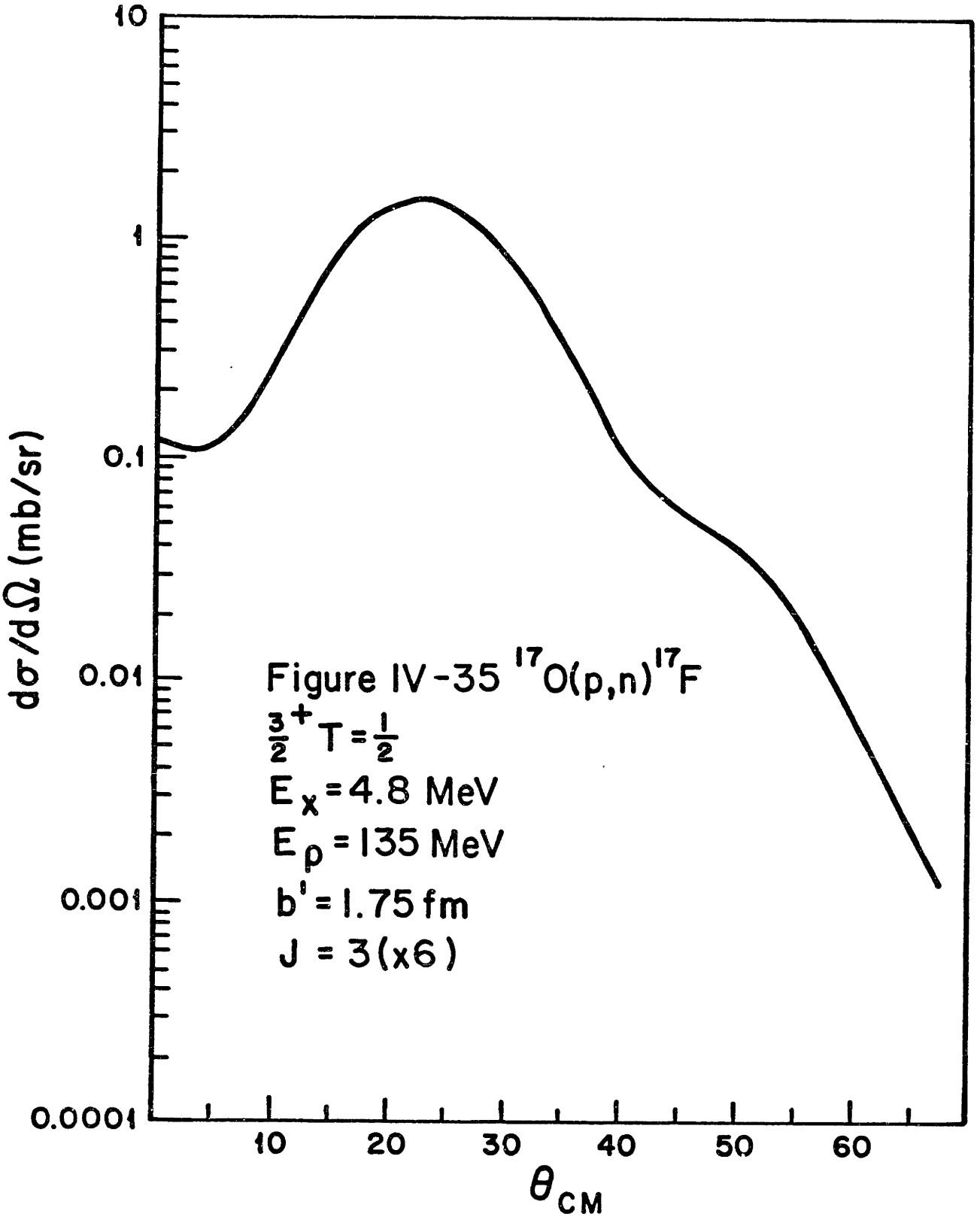
10
1
0.1
0.01
0.001
0.0001
dσ/dΩ (mb/sr)
10
20
30
40
50
60
θCM
Figure IV-35 17O(p,n)17F
3/2+ T=1/2
Ex=4.8 MeV
Ep=135 MeV
b'=1.75 fm
J = 3(x6)

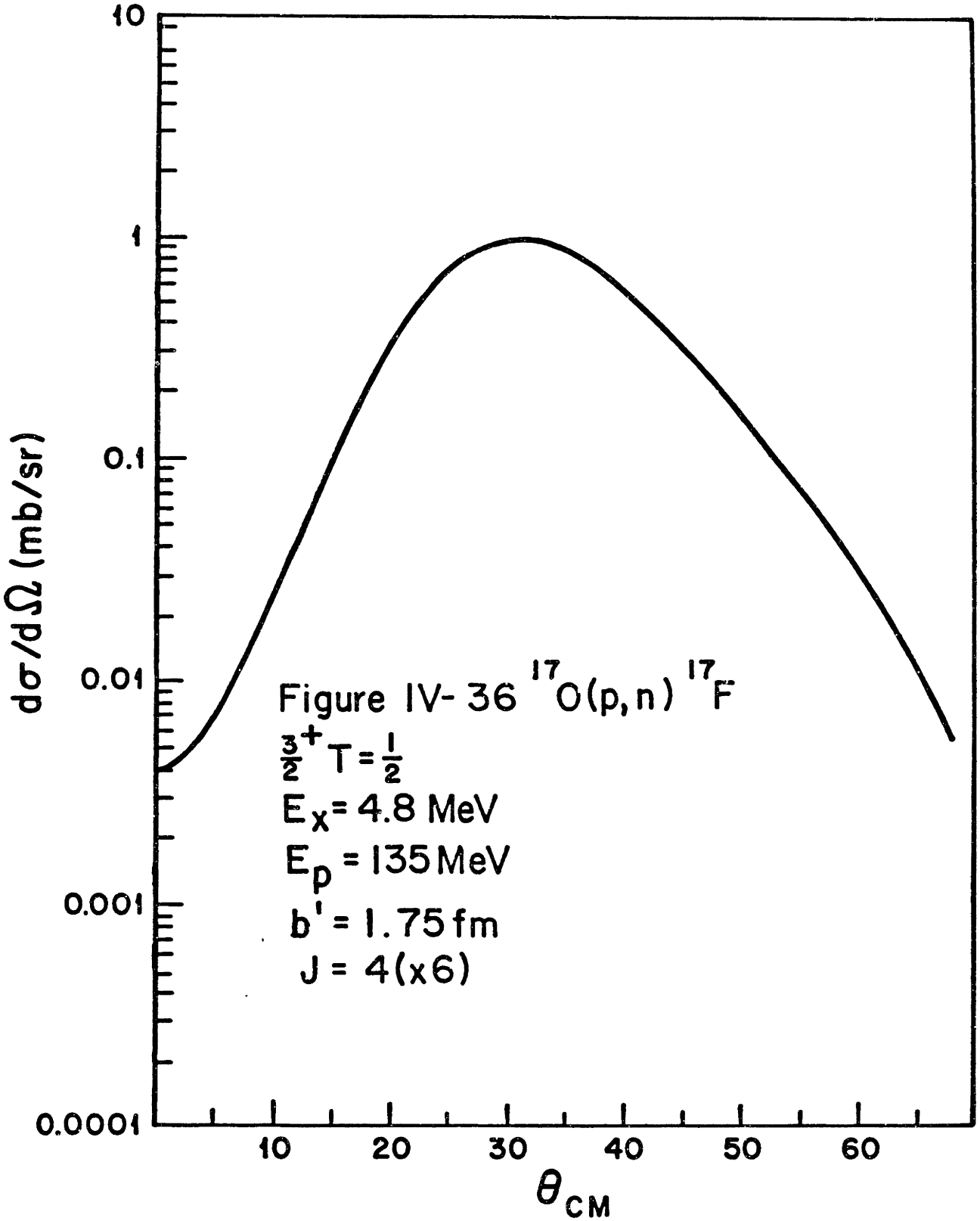
10
1
0.1
0.01
0.001
0.0001
dσ/dΩ (mb/sr)
10
20
30
40
50
60
θCM
Figure IV-36 17O(p,n) 17F
3/2+ T=1/2
Ex= 4.8 MeV
Ep = 135 MeV
b' = 1.75 fm
J = 4(x6)

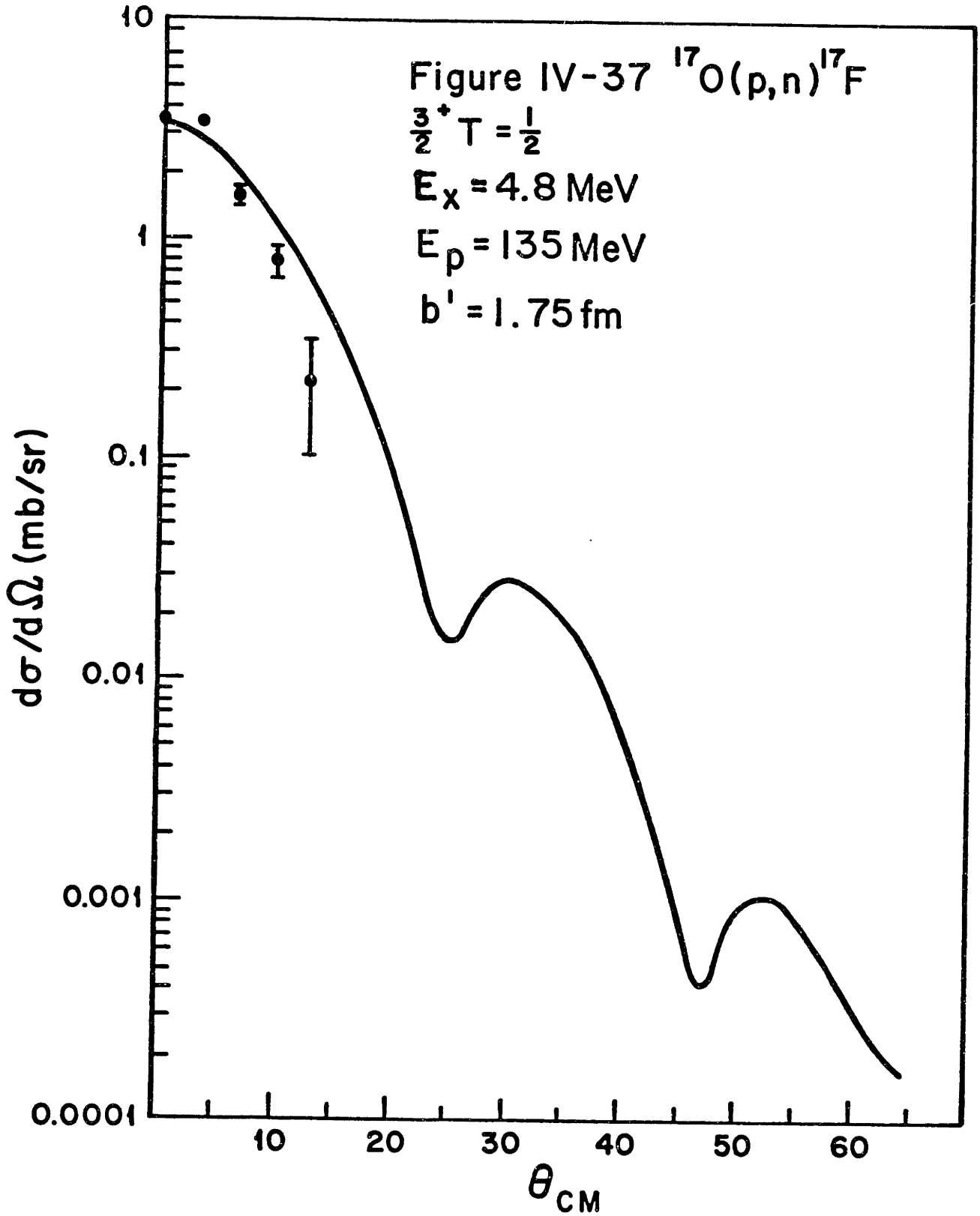
Figure IV-37 $^{17}O(p,n)^{17}F$
$\frac{3}{2}^+ T = \frac{1}{2}$
$E_x = 4.8$ MeV
$E_p = 135$ MeV
$b' = 1.75$ fm
$d\sigma/d\Omega$ (mb/sr)
10
1
0.1
0.01
0.001
0.0001
10
20
30
40
50
60
θ_{CM}

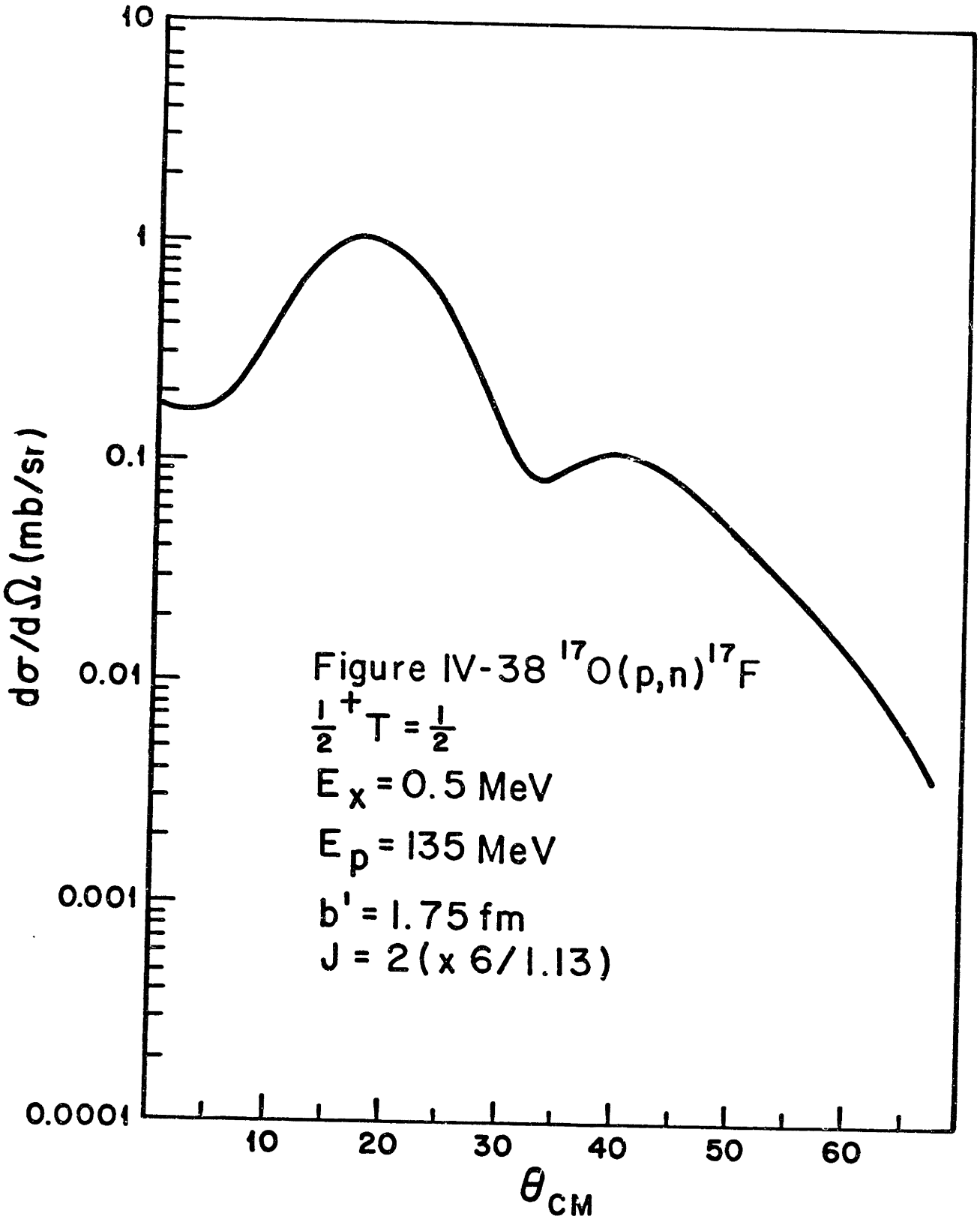
10
1
0.1
0.01
0.001
0.0001
dσ/dΩ (mb/sr)
10
20
30
40
50
60
θCM
Figure IV-38 17O(p,n)17F
1/2+ T = 1/2
Ex = 0.5 MeV
Ep = 135 MeV
b' = 1.75 fm
J = 2 (x 6/1.13)

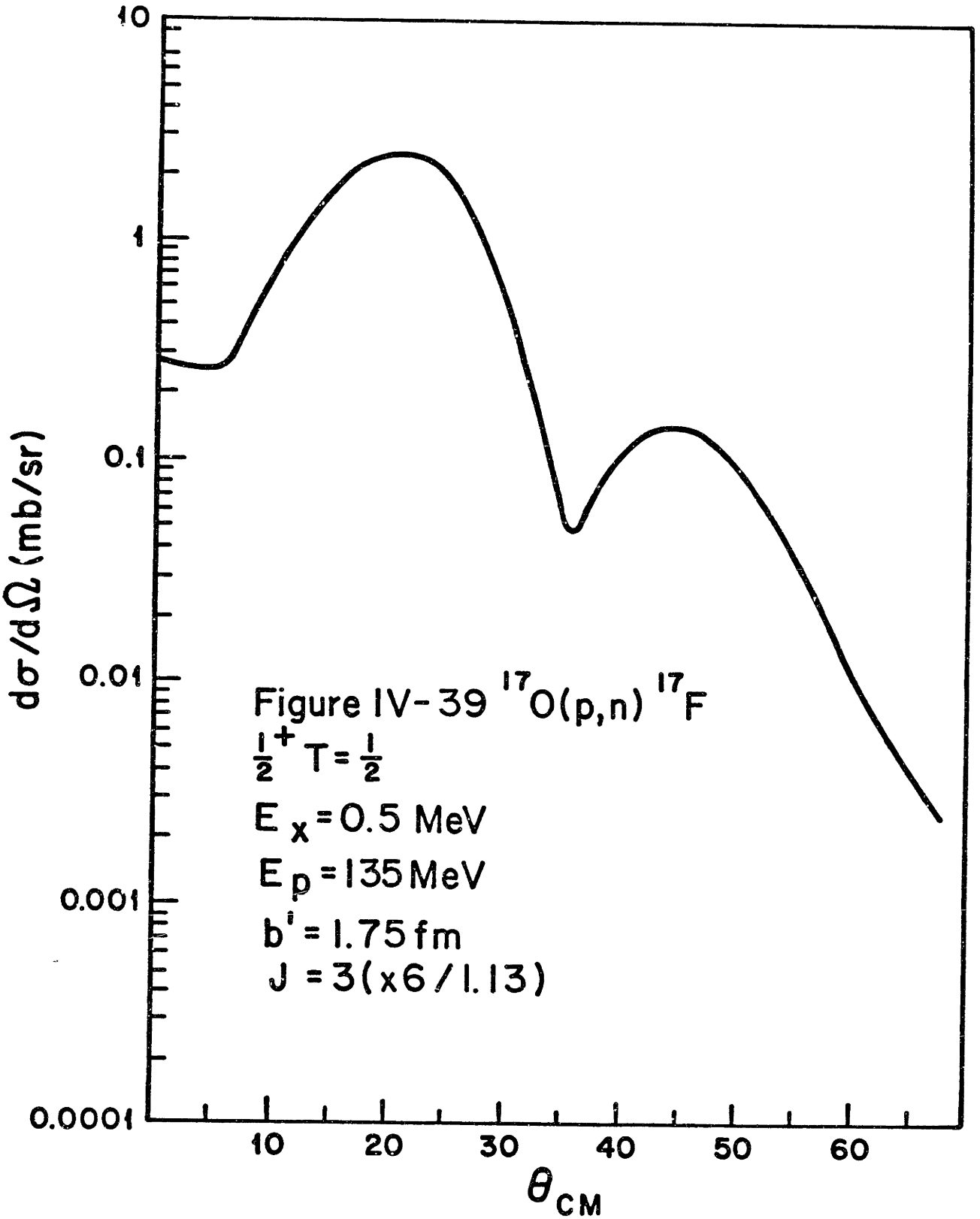
10
1
0.1
0.01
0.001
0.0001
dσ/dΩ (mb/sr)
10
20
30
40
50
60
θCM
Figure IV-39 17O(p,n) 17F
1/2+ T=1/2
Ex=0.5 MeV
Ep=135 MeV
b'=1.75 fm
J=3(x6/1.13)

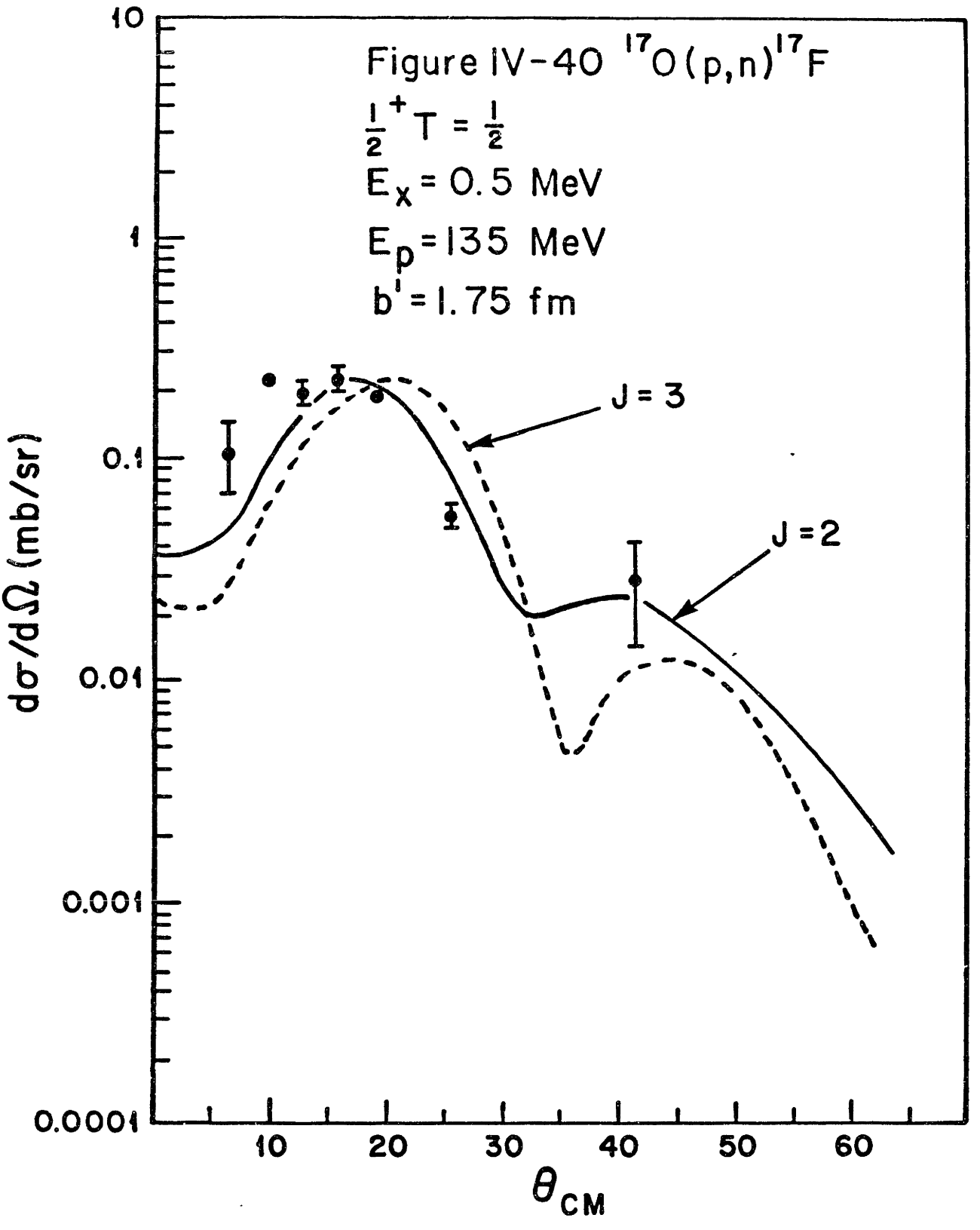
Figure IV-40 $^{17}O(p,n)^{17}F$
$\frac{1}{2}^+ T = \frac{1}{2}$
$E_x = 0.5$ MeV
$E_p = 135$ MeV
$b' = 1.75$ fm
J = 3
J = 2
$d\sigma/d\Omega$ (mb/sr)
θ_{CM}
10
1
0.1
0.01
0.001
0.0001
10
20
30
40
50
60

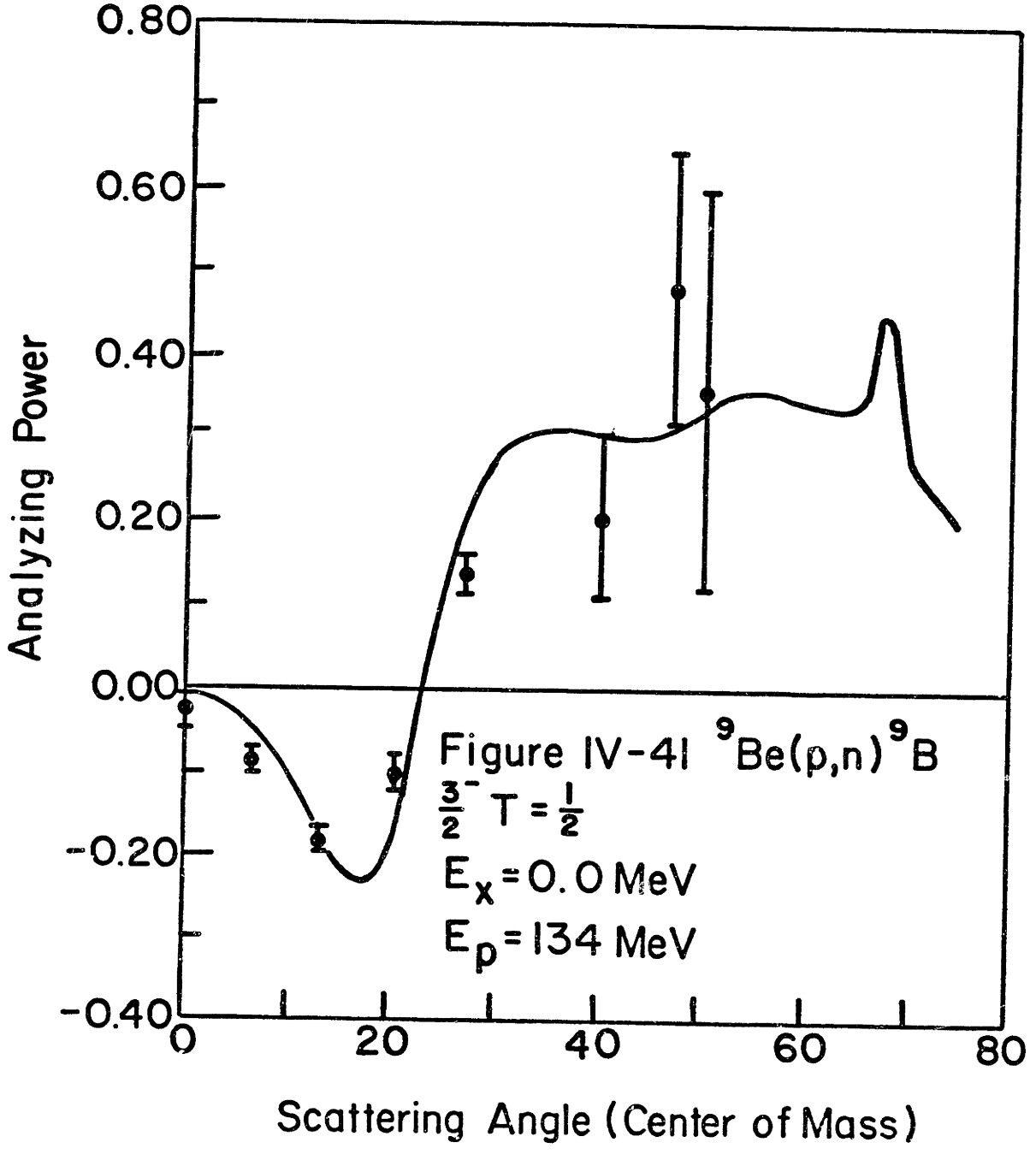
0.80
0.60
0.40
0.20
0.00
-0.20
-0.40
Analyzing Power
0
20
40
60
80
Scattering Angle (Center of Mass)
Figure IV-41 $^{9}Be(p,n)^{9}B$
$\frac{3}{2}^{-}$ $T=\frac{1}{2}$
$E_x = 0.0$ MeV
$E_p = 134$ MeV

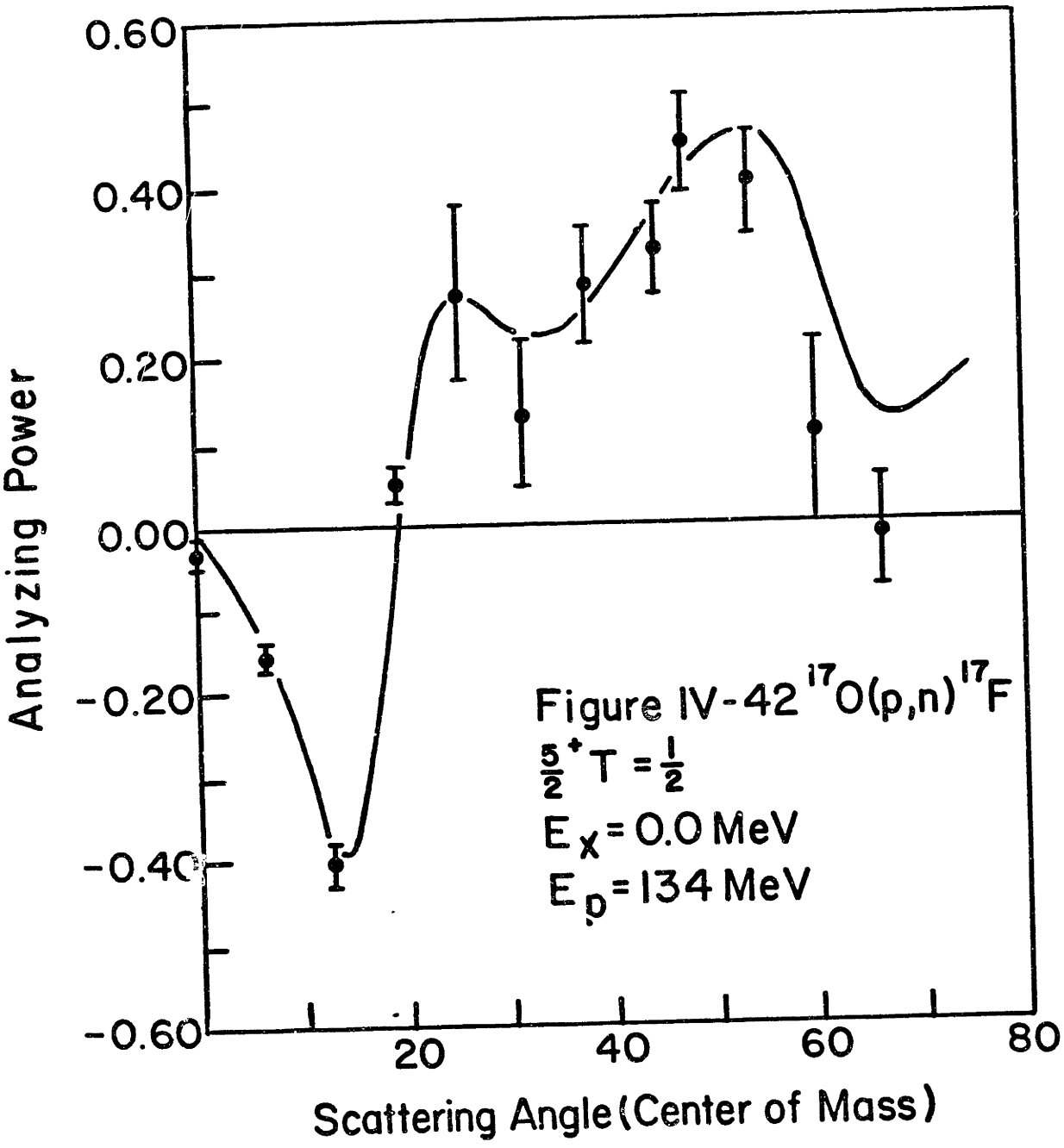
0.60
0.40
0.20
0.00
-0.20
-0.40
-0.60
Analyzing Power
20
40
60
80
Scattering Angle (Center of Mass)
Figure IV-42 $^{17}O(p,n)^{17}F$
$\frac{5}{2}^+ T = \frac{1}{2}$
$E_x = 0.0$ MeV
$E_p = 134$ MeV

We have seen single particle wave functions, which adequately describe electron scattering, fail to reproduce the momentum transfer dependence of the (p,n) results reported herein. The Cohen-Kurath description of the mass 9 system with its M1 and M3 components independently normalized proved adequate to describe elastic magnetic electron scattering out to 2 fm^{-1}, but these normalized wave functions were not capable of accounting for the analog ground state transition in the (p,n) reaction in a consistent fashion. Only by adopting two different oscillator parameters and three normalization coefficients does it prove possible to fit the $^9Be(p,n)^9B_{gs}$ cross section out to 2 fm^{-1} in the context of simple harmonic oscillator wave functions. That the Cohen-Kurath wave functions require independent M1 and M3 renormalization means that there are contributions to the nucleon currents not included in he model. Thus the wave functions, although providing appropriate magnetic dipole moments, energy levels, and M1 transitions at zero momentum transfer, are not complete enough to describe the nonzero momentum components in the ^9Be nucleus. On this basis one might view the (p,n) results as providing a wealth of new information concerning ^9Be. The magnetization that can be described by simply renormalizing the J=1 and J=3 multipoles cannot be used to parameterize the (p,n) process within the Cohen-Kurath scheme. This means that there may be other important spin-flip components in the wavefunctions for these transitions. To extract this new information, we need confidence in the reaction theory and a systematic test in this regard is important, including the recently discovered importance of density dependence in the nucleon-nucleon interaction [KEL81,TELL82]. These results indicate a deficiency in the Cohen-Kurath description of ^9Be. This is apparent in both the (e,e') and (p,n) data. Both data sets require normalization of the Cohen-Kurath results though different normalizations are required in the two cases. The Cohen-Kurath description includes only p states so that one is perhaps led to consider further calculations within a more complete basis.

The analysis of the $^{17}O(p,n)^{17}F_{g.s.}$ cross sections revealed a similar sensitivity. In this case the magnetization of ^{17}O is also not understood but an *ad hoc* renormalization of the M3 form factor has been shown [HIC82] to fit the magnetic form factor out to 2.7 fm^{-1}. Even with additional renormalization, over and above the normalization required by (e,e') data, the (p,n) data cannot be described beyond 2 fm^{-1} in the context of a simple harmonic oscillator basis. It is impossible without further analysis to know whether the difficulties in fitting these data are due to nuclear structure effects or an inaccurate description of the reaction process. There are many reasons to suspect the accuracy of the DWIA. One of these is the knowledge that density dependent interactions are of importance to elastic distortions. One other is that the shape of the calculated J=0 DWBA cross section is quite different from the PWBA cross section as is shown in figure $IV-3$. The distortion evidently causes the cross section to decrease less rapidly with increasing momentum transfer in comparison to the PWBA. If this effect is incorrectly caculated, it

could necessitate the adoption of different values of the oscillator parameter b, much as was necessary in the ^9Be calculation above. On the other hand, core polarization has been ignored in these calculations. The inclusion of core excitations may be expected to influence results of both (e,e') and (p,n)calculations but not in the same manner because of the importance of currents in (e,e') which are not present in the (p,n) reaction.

A more detailed theoretical analysis of these data is warranted in view of the possible sensitivity of this reaction to the structure of the mass 17 system. Such an analysis might provide evidence of core excitations influencing the structure of the mass 17 system and help distinguish between the convective and spin-flip terms in electron scattering [PET80].

The $^{17}O(p,n)$ measurements reported here have also provided additional information regarding the suppression of Gamow-Teller strength. The ground state analog transition was already known to be suppressed from the measured half life for the β-decay of ^{17}F to the ground state of ^{17}O. This is confirmed by the (p,n) results reported here. In addition, we have seen that the Gamow-Teller transition $\frac{5}{2}^+ \rightarrow \frac{3}{2}^+$ in $^{17}O(p,n)^{17}F$ is weaker than expected, even after allowing for the ground state suppression. The single particle value of $|\mathcal{M}_{GT}|^2$ for the $\frac{5}{2}^+ \rightarrow \frac{3}{2}^+$ transition is 1.6. The total strength observed in this experiment summing over the discrete low lying excited states was $|\mathcal{M}_{GT}|^2 = 0.517$. The suppresion of the Gamow-Teller strength of the ground state analog transition (0.677 as compared to the single particle value of 1.4) would suggest that for the $\frac{5}{2}^+ \rightarrow \frac{3}{2}^+$ transitions we should see $|\mathcal{M}_{GT}|^2 = \frac{0.677}{1.4} \times 1.6 = 0.774$. This is about 50% greater than actually seen in this experiment, implying perhaps that more strength is located at higher excitations. Finally we may recall that for both $^9Be(p,n)$ and $^{17}O(p,n)$ the integrated Gamow Teller strengths reported in chapter III are about half the sum rule strength. In the case of $^9Be(p,n)$ the integration was up to 18 MeV and for $^{17}O(p,n)$ the integration was up to 16 MeV. Thus a deficiency of Gamow Teller strength has been seen in both specific transitions and in the integrated strength. It is possible that the rest of the strength lies at higher excitations. The Gamow Teller strength was in the case of $^{17}O(p,n)$ integrated out to an excitation energy of 16 MeV. At these energies the excitation strength was about 0.2–0.3 mb/sr/MeV. If this strength continued unabated beyond 15 MeV the sum rule would be satisfied at about 40 MeV of excitation. Also, with increasing excitation energies, the momentum transfer increases and this decreases the cross sections corresponding to a given strength at zero momentum transfer. A correction for this effect implies that the Gamow-Teller sum rule would be satisfied by an integration to less than 40 MeV of excitation. We may estimate this effect by assuming the L=0 strength to behave as a zero order Bessel function. At 40 MeV the momentum transfer for either of these nuclei is about 0.5 fm^{-1}. In the case of ^{17}F we might suppose $R = 2.8fm^{-1}$. This gives $|j_0(qR)|^2 = |j_0(1.3)|^2 = 0.6$. It is unfortunately not possible to carry out such a sum experimentally according to the method of [GOOD80] since their method requires a small momentum transfer in order to ensure a simple interpretation of the (p,n) cross section in terms of Gamow-Teller strength. Nevertheless, one

may say that these deficiencies in Gamow-Teller strength are in agreement with results reported by others [TELL79,TELL82] regarding several other nuclei and may indicate a very general inadequacy of current descriptions of nuclei.

In chapter III we have presented cross section measurements for many states of ^9B and several states of ^{17}F. Tables III-5 and III-6 summarize the states seen in this measurement and attempt to identify these states with states seen in other works. In many cases it is difficult to make definite identifications with states seen in previous works due to the ± 0.1 MeV uncertainty in the energy scale. Two statements may be made unequivocally.

We have seen in ^9B a broad collection of strength centered at about 2.8 MeV. The strength of this state and its excitation energy suggest that it may be the $p_{\frac{1}{2}}$ state which has for many years been expected to exist but has not been seen with any other reaction.

There is a strong spin-flip excitation of ^{17}F at 4.8 MeV. The currently assigned spin-parity assignment of $\frac{3}{2}^-$ for this state is in error. The spin-parity of this state is almost certainly $\frac{3}{2}^+$.

There is also strong evidence for a state in ^9B at 2.71 MeV whose (p,n) cross section is greatest at zero momentum transfer and decreases monotonically with increasing momentum transfer. This is difficult to understand if we identify this state with the $\frac{5}{2}^+$ state which has been previously seen in this nucleus at about this excitation energy. A $\frac{5}{2}^+$ state is also expected by comparison with ^9Be, the analog nucleus. Perhaps the unbound nature of the ^9B system could produce an angular distribution suggestive of zero momentum transfer.

Altogether these data provide a rich source of information for those interested in the spectroscopy and structure of ^9B and ^{17}F. Should a consistent theoretical description of these data be achieved it may be expected to greatly enhance our understanding of these nuclei.

Appendix

This appendix is a tabulation of all cross sections and analyzing powers measured in this experiment. The numbers in parentheses indicate the uncertainties in the measurements. For cross sections these uncertainties are expressed as percentages. For analyzing powers the number in parenthesis refers to uncertainty in the last few digits of the measurement. For example, $A_y = +0.173(60)$ means $A_y = +0.173 \pm 0.060$.

The uncertainties tabulated *do not* include the uncertainty due to detector efficiency. This is estimated to be about 10 % and applies systematically to all cross section data.

Table $A-1$. $^{9}Be(p,n)^{9}B \quad E_p = 135.18 MeV$.

$^{9}Be(p,n)^{9}B \quad E_x = 0.0\ MeV$		
$\theta_{\text{C.M.}}$	q(fm^{-1})	$d\sigma/d\omega$ (mb/sr)
0.00	0.018	9.52(4)
3.38	0.139	7.56(6)
6.76	0.276	5.12(8)
10.14	0.414	2.78(20)
13.29	0.541	1.54(9)
16.89	0.687	0.809(19)
20.14	0.818	0.493(7)
26.96	1.090	0.307(9)
30.31	1.222	0.234(7)
33.64	1.353	0.182(8)
36.96	1.482	0.129(14)
40.28	1.610	0.0941(13)
43.58	1.735	0.0521(14)
46.76	1.855	0.0299(14)
50.14	1.981	0.0270(34)
53.40	2.101	0.0119(33)
56.64	2.218	0.00716(40)

Table $A-2$. $^{9}Be(p,n)^{9}B \quad E_p = 135.18 MeV$.

$^{9}Be(p,n)^{9}B \quad E_x = 2.36\ MeV$		
$\theta_{\text{C.M.}}$	q(fm^{-1})	$d\sigma/d\omega$ (mb/sr)
0.00	0.042	2.09(4)
3.39	0.144	1.68(6)
6.77	0.278	1.10(8)
10.15	0.414	0.477(20)
13.30	0.540	0.362(9)
16.90	0.685	0.175(19)
20.16	0.815	0.136(7)
26.99	1.086	0.0813(16)
30.33	1.217	0.0598(19)
33.67	1.347	0.0447(21)
37.00	1.476	0.0262(31)
40.31	1.603	0.0199(35)
43.62	1.728	0.0102(56)
46.80	1.847	0.0118(90)

Table $A-3$. $^{9}Be(p,n)^{9}B \quad E_p = 135.18 MeV$.

$^{9}Be(p,n)^{9}B \quad E_x = 2.71\ MeV$		
$\theta_{\text{C.M.}}$	q(fm^{-1})	$d\sigma/d\omega$ (mb/sr)
0.00	0.045	2.83(36)
3.39	0.145	2.10(34)
6.77	0.278	1.34(34)
10.15	0.414	1.066(34)
13.31	0.540	0.492(29)
16.90	0.684	0.439(14)
20.16	0.815	0.292(18)
26.99	1.086	0.181(20)
30.34	1.217	0.0959(29)
33.67	1.347	0.0916(29)
37.00	1.475	0.0651(50)
40.32	1.602	0.0311(80)

Table $A-4$. $^{9}Be(p,n)^{9}B \quad E_p = 135.18 MeV$.

$^{9}Be(p,n)^{9}B \quad E_x = 2.75\ MeV$		
$\theta_{\text{C.M.}}$	q(fm^{-1})	$d\sigma/d\omega$ (mb/sr)
0.00	0.048	9.73(29)
3.39	0.145	8.24(26)
6.77	0.278	5.84(23)

Table $A-5$. $^{9}Be(p,n)^{9}B \quad E_p = 135.18 MeV$.

$^{9}Be(p,n)^{9}B \quad E_x = 4.3\ MeV$		
$\theta_{\text{C.M.}}$	q(fm^{-1})	$d\sigma/d\omega$ (mb/sr)
0.00	0.061	2.41(6)
3.39	0.150	2.15(6)
6.77	0.280	1.87(25)
10.16	0.415	0.939(49)

Table $A-6$. $^{9}Be(p,n)^{9}B \quad E_p = 135.18 MeV$.

$^{9}Be(p,n)^{9}B \quad E_x = 7.0\ MeV$		
$\theta_{\text{C.M.}}$	q(fm^{-1})	$d\sigma/d\omega$ (mb/sr)
20.24	0.812	0.0441(47)
27.09	1.075	0.0406(50)
30.45	1.203	0.0382(28)
33.80	1.330	0.0269(31)
37.14	1.456	0.0198(36)
40.39	1.591	0.0704(35)
43.70	1.714	0.0422(45)
46.88	1.832	0.0319(50)

Table $A-7$. $^9Be(p,n)^9B \quad E_p = 135.18 MeV$.

$^9Be(p,n)^9B \quad E_x = 11.6\ MeV$		
$\theta_{\text{C.M.}}$	q(fm^{-1})	$d\sigma/d\omega$ (mb/sr)
20.24	0.812	0.0450(47)
27.09	1.075	0.0417(50)
30.45	1.203	0.0390(28)
33.80	1.330	0.0275(31)
37.14	1.456	0.0203(36)
40.47	1.580	0.0146(52)

Table $A-8$. $^9Be(p,n)^9B \quad E_p = 135.18 MeV$.

$^9Be(p,n)^9B \quad E_x = 12.2\ MeV$		
$\theta_{\text{C.M.}}$	q(fm^{-1})	$d\sigma/d\omega$ (mb/sr)
0.00	0.146	0.230(14)
3.38	0.199	0.188(17)
6.80	0.306	0.149(22)
10.19	0.429	0.0950(50)
13.36	0.548	0.0552(62)
20.24	0.812	0.0566(48)
27.10	1.075	0.0350(59)
30.46	1.203	0.0342(41)
33.81	1.329	0.0128(82)

Table $A-9$. $^9Be(p,n)^9B \quad E_p = 135.18 MeV$.

$^9Be(p,n)^9B \quad E_x = 14.0\ MeV$		
$\theta_{\text{C.M.}}$	q(fm^{-1})	$d\sigma/d\omega$ (mb/sr)
0.00	0.165	0.0657(22)
3.40	0.212	0.0490(50)
6.80	0.315	0.0353(40)
10.20	0.435	0.040(80)

Table $A-10$. $^9Be(p,n)^9B \quad E_p = 135.18 MeV$.

$^9Be(p,n)^9B \quad E_x = 14.6\ MeV$		
$\theta_{\text{C.M.}}$	q(fm^{-1})	$d\sigma/d\omega$ (mb/sr)
6.81	0.318	0.0173(50)
20.27	0.813	0.0734(29)
27.13	1.073	0.0728(29)
30.49	1.200	0.0385(29)
33.85	1.326	0.0251(29)
37.19	1.451	0.0168(40)
40.52	1.574	0.0126(40)
43.84	1.695	0.0116(59)
47.03	1.811	0.00116(80)

Table $A-11$. $^9Be(p,n)^9B \quad E_p = 135.18 MeV$.

$^9Be(p,n)^9B \quad E_x = 14.6\ MeV \quad \Gamma = 0.6\ MeV$		
$\theta_{\text{C.M.}}$	q(fm^{-1})	$d\sigma/d\omega$ (mb/sr)
0.00	0.171	0.213(25)
3.40	0.218	0.173(40)
6.81	0.318	0.144(20)
10.21	0.437	0.122(50)

Table $A-12.$ $^9Be(p,n)^9B \quad E_p = 135.18 MeV.$

$^9Be(p,n)^9B \quad E_x = 15.2\ MeV$		
$\theta_{\text{C.M.}}$	q(fm^{-1})	$d\sigma/d\omega$ (mb/sr)
6.81	0.321	0.0146(40)

Table $A-13.$ $^9Be(p,n)^9B \quad E_p = 135.18 MeV.$

$^9Be(p,n)^9B \quad E_x = 15.4\ MeV$		
$\theta_{\text{C.M.}}$	q(fm^{-1})	$d\sigma/d\omega$ (mb/sr)
6.81	0.323	0.00882(80)

Table $A-14.$ $^9Be(p,n)^9B \quad E_p = 135.18 MeV.$

$^9Be(p,n)^9B \quad E_x = 15.9\ MeV$		
$\theta_{\text{C.M.}}$	q(fm^{-1})	$d\sigma/d\omega$ (mb/sr)
0.00	0.185	0.0578(59)
6.81	0.325	0.0485(70)

Table $A-15.$ $^9Be(p,n)^9B \quad E_p = 135.18 MeV.$

$^9Be(p,n)^9B \quad E_x = 16.7\ MeV$		
$\theta_{\text{C.M.}}$	q(fm^{-1})	$d\sigma/d\omega$ (mb/sr)
0.00	0.194	0.0441(50)
3.41	0.236	0.0688(50)
6.81	0.330	0.113(20)
10.22	0.445	0.136(20)
13.39	0.559	0.119(20)
17.01	0.692	0.0740(295)
20.29	0.815	0.0651(70)

Table $A-16.$ $^9Be(p,n)^9B \quad E_p = 135.18 MeV.$

$^9Be(p,n)^9B \quad E_x = 17.5\ MeV$		
$\theta_{\text{C.M.}}$	q(fm^{-1})	$d\sigma/d\omega$ (mb/sr)
0.00	0.203	0.160(45)
3.41	0.244	0.166(20)
6.82	0.335	0.256(29)
10.22	0.448	0.225(10)
13.39	0.561	0.235(15)
17.02	0.694	0.155(20)
20.30	0.816	0.183(29)
27.17	1.073	0.0617(29)
30.54	1.198	0.0423(35)
33.89	1.323	0.0168(50)
37.24	1.446	0.00738(80)
40.58	1.568	0.0113(59)
43.90	1.688	0.0130(59)
47.10	1.803	0.00903(80)

Table $A-17$. $^{9}Be(p,n)^{9}B \quad E_p = 133.56 MeV$.

$^{9}Be(p,n)^{9}B \quad E_x = 0.0\ MeV$		
$\theta_{\text{C.M.}}$	q(fm^{-1})	analyzing power
0.00	0.018	$-0.028(36)$
6.76	0.274	$-0.124(6)$
13.29	0.545	$-0.184(8)$
20.14	0.828	$-0.112(18)$
27.07	1.087	$+0.081(26)$
40.28	1.597	$+0.193(42)$
46.76	1.857	$+0.487(31)$
50.14	1.972	$+0.241(81)$

Table $A-18.$ $^{17}O(p,n)^{17}F$ $\quad E_p = 135.18\ MeV$

$^{17}O(p,n)^{17}F$ $\quad E_x = 0.0\ MeV$		
$\theta_{\text{C.M.}}$	q(fm^{-1})	$d\sigma/d\omega$ (mb/sr)
0.00	0.035	8.39(2)
3.20	0.142	7.37(4)
6.41	0.277	4.67(2)
9.61	0.413	2.04(2)
12.60	0.541	1.16(2)
16.01	0.686	0.582(3)
19.10	0.816	0.496(4)
25.59	1.089	0.431(4)
28.77	1.222	0.352(4)
31.95	1.354	0.298(3)
35.12	1.484	0.207(4)
38.08	1.604	0.161(3)
41.45	1.740	0.139(5)
44.50	1.862	0.0862(9)
50.89	2.113	0.0516(6)
54.03	2.233	0.0249(10)
57.15	2.351	0.0180(20)
60.06	2.461	0.0109(50)

Table $A-19.$ $^{17}O(p,n)^{17}F$ $\quad E_p = 135.18\ MeV$

$^{17}O(p,n)^{17}F$ $\quad E_x = 0.5\ MeV$		
$\theta_{\text{C.M.}}$	q(fm^{-1})	$d\sigma/d\omega$ (mb/sr)
6.41	0.277	0.112(35)
9.61	0.413	0.237(7)
12.60	0.540	0.212(11)
16.01	0.685	0.246(13)
19.10	0.816	0.203(7)
25.59	1.088	0.0578(13)
41.46	1.740	0.0296(50)

Table $A-20.$ $^{17}O(p,n)^{17}F \qquad E_p = 135.18\ MeV$

$^{17}O(p,n)^{17}F \qquad E_x = 4.8\ MeV \quad \Gamma = 1.8\ MeV$		
$\theta_{\text{C.M.}}$	q(fm^{-1})	$d\sigma/d\omega$ (mb/sr)
0.00	0.089	3.54(5)
3.21	0.161	3.45(4)
6.42	0.285	1.59(9)
9.62	0.417	0.811(17)
12.60	0.542	0.231(55)

Table $A-21.$ $^{17}O(p,n)^{17}F \qquad E_p = 135.18\ MeV$

$^{17}O(p,n)^{17}F \qquad E_x = 5.9\ MeV$		
$\theta_{\text{C.M.}}$	q(fm^{-1})	$d\sigma/d\omega$ (mb/sr)
0.00	0.100	0.139(45)
3.21	0.168	0.181(44)
6.42	0.288	0.161(45)
9.62	0.419	0.123(53)

T ble $A-22.$ $^{17}O(p,n)^{17}F \qquad E_p = 135.18\ MeV$

$^{17}O(p,n)^{17}F \qquad E_x = 6.3\ MeV$		
$\theta_{\text{C.M.}}$	q(fm^{-1})	$d\sigma/d\omega$ (mb/sr)
3.21	0.170	0.0893(58)
6.42	0.290	0.0968(40)
9.62	0.419	0.0964(47)

Table $A-23$. $^{17}O(p,n)^{17}F \qquad E_p = 135.18\ MeV$

$^{17}O(p,n)^{17}F \qquad E_x = 7.3\ MeV$		
$\theta_{\text{C.M.}}$	q(fm^{-1})	$d\sigma/d\omega$ (mb/sr)
0.00	0.111	0.986(17)
3.21	0.176	0.887(19)
6.42	0.293	0.668(44)
9.63	0.421	0.304(22)
12.62	0.543	0.0993(41)

Table $A-24$. $^{17}O(p,n)^{17}F \qquad E_p = 135.18\ MeV$

$^{17}O(p,n)^{17}F \qquad E_x = 7.6\ MeV$		
$\theta_{\text{C.M.}}$	q(fm^{-1})	$d\sigma/d\omega$ (mb/sr)
0.00	0.114	0.173(43)
3.21	0.178	0.169(45)
6.42	0.294	0.130(53)
9.63	0.422	0.114(66)

Table $A-25$. $^{17}O(p,n)^{17}F \qquad E_p = 135.18\ MeV$

$^{17}O(p,n)^{17}F \qquad E_x = 9.3\ MeV \quad \Gamma = 1.8\ MeV$		
$\theta_{\text{C.M.}}$	q(fm^{-1})	$d\sigma/d\omega$ (mb/sr)
0.00	0.134	0.0631(51)
3.21	0.190	0.129(38)
6.42	0.301	0.180(50)
9.63	0.426	0.164(35)
12.63	0.546	0.169(28)
16.04	0.685	0.146(36)
19.04	0.812	0.171(45)
25.64	1.077	0.0352(97)

Table $A-26$. $^{17}O(p,n)^{17}F \qquad E_p = 135.18\ MeV$

$^{17}O(p,n)^{17}F \qquad E_x = 14.3\ MeV \quad \Gamma = 1.8\ MeV$		
$\theta_{\text{C.M.}}$	q(fm^{-1})	$d\sigma/d\omega$ (mb/sr)
3.22	0.230	0.115(39)
6.43	0.327	0.148(33)
9.64	0.442	0.186(29)
12.64	0.556	0.180(22)
16.06	0.691	0.143(41)

Table $A-27$. $^{17}O(p,n)^{17}F \qquad E_p = 133.56\ MeV$

$^{17}O(p,n)^{17}F \qquad E_x = 0.0\ MeV$		
$\theta_{\text{C.M.}}$	q(fm^{-1})	analyzing power
0.00	0.036	−0.029(21)
6.41	0.275	−0.156(10)
12.60	0.544	−0.400(32)
19.10	0.827	+0.048(23)
25.59	1.087	+0.276(103)
31.95	1.345	+0.130(90)
38.08	1.600	+0.285(70)
44.50	1.865	+0.326(58)
47.75	1.982	+0.451(60)
54.03	2.219	+0.406(69)
60.06	2.451	+0.108(111)
66.72	2.687	−0.014(70)

Bibliography

[AJZ59] F. Ajzenberg-Selove and T. Lauritsen
Energy Levels of Light Nuclei. VI,
Nuclear Physics **11** (1959) pp.232-233.

[AJZ71] F. Ajzenberg-Selove Energy Levels of Light Nuclei $A = 16 - 17$,
Nuclear Physics **A166** (1971) pp.87,91.

[AJZ79] F. Ajzenberg-Selove Energy Levels of Light Nuclei $A = 5 - 10$.,
Nuclear Physics **A320** (1979) pp.1-224.

[AJZ82] F. Ajzenberg-Selove Energy Levels of Light Nuclei $A = 16 - 17$.,
Nuclear Physics **A375** (192) pp.1-168.

[AND69] J.D. Anderson, S.D. Bloom, Calvin Wong, W.F. Hornyak,
and V.A. Madsen
Effective Two-Body Force Inferred from the (p,n) Reaction on
^{17}O, ^{18}O, ^{27}Al, and Other Light Nuclei,
Physical Review **177** no. 4 (1969) pp. 1416-1435.

[AND79] B.D. Anderson, R.A. Cecil, and R. Madey, in
The (p,n) Reaction and the Nucleon-Nucleon Force,
ed. C.D. Goodman et al,
Plenum Press, New York and London, (1979) pp. 333-342.

[AND80] B.D. Anderson, J.N. Knudson, R. Madey, and C.C. Foster,
A Comparison of $^{12}C(p,n)^{12}N$ and $^{12}C(p,p')^{12}C$
to Analog States as a Test of Monte-Carlo Calculated Efficiencies
for Large-Volume Neutron Counters,
Nucl. Inst. Meth. **169** (1980) pp. 153-159.

[AUE84] N. Auerbach, A. Klein Structure of isovector spin excitations in nuclei,
Physical Review C **30** no. 3 (1984) pp. 1032-1043.

[BAI64] J.K. Bair, C.M. Jones, and H.B. Willard
NEUTRONS FROM THE PROTON BOMBARDMENT of
Li^6, Li^7, Be^9, B^{11}, and O^{18},
Nuclear Physics **53** (1964) pp. 209-218.

[BER77] G. Bertsch, J. Borysowicz, H. McManus, and W.G. Love,
INTERACTIONS FOR INELASTIC SCATTERING DERIVED FROM
REALISTIC POTENTIALS,
Nuclear Physics **A284** (1977) pp. 399-419.

[BER82] G.F. Bertsch, I. Hamamoto Gamow-Teller strength at high excitations, Physical Review C **26** no. 3 (1982) pp. 1323-1326.

[BEV69] Philip R. Bevington, Data Reduction and Error Analysis for the Physical Sciences, (McGraw-Hill 1969)

[BLA79] John M. Blatt and Victor F. Weisskopf, Theoretical Nuclear Physics, (Springer-Verlag, 1979)

[BLO59] S.D. Bloom, N.K. Glendenning, S.A. Moszkowski, The Proton-Neutron Interaction and the (p,n) Reaction in Mirror Nuclei, Phys. Rev. Letters **3** no. 2 (1959) pp. 98-99.

[BLU65] R.A. Blue and W. Haeberli Polarization of Protons Elastically Scattered by Oxygen, Physical Review **137** no. 2B (1965) pp. B284-B293.

[BOH81] A. Bohr, B.R. Mottelson On the Role of the Δ Resonance in the Effective Spin-Dependent Moments of Nuclei, Physics Letters **100B** (1981) pp. 10-12.

[BORN26] Max Born, Zur Quantenmechanik der Stoßvorgänge. Zeitschrift für Physik **37** (1926) pp. 861-867. Quantenmechanik der Stoßvorgänge. Zeitschrift für Physik **38** (1926) pp. 803-827.

[BRE36] G. Breit and E. Wigner Capture of Slow Neutrons, Physical Review **49** (1936) pp. 519-531.

[BRI77] F.A. Brieva and J.R. Rook NUCLEON-NUCLEUS OPTICAL MODEL POTENTIAL (I). Nuclear matter approach, Nuclear Physics **A291** (1977) pp. 299-316. NUCLEON-NUCLEUS OPTICAL MODEL POTENTIAL, (II). Finite nuclei, Nuclear Physics **A291** (1977) pp. 317-341.

[BRI78] F.A Brieva and J.R. Rook MICROSCOPIC DESCRIPTION OF NUCLEON-NUCLEUS ELASTIC SCATTERING, Nuclear Physics **A307** (1978) pp. 493-514.

[BRO66] G.E. Brown, A.M. Green Even Parity States of ^{16}O and ^{17}O.,
Nuclear Physics **75** (1966) pp.401-417.

[BRO81] G.E. Brown, J. Speth, and J. Wambach,
Energy Dependence of the Coupling Potentials in (p,n) Reactions
Phys. Rev. Letters **46** no. 16 (1981) pp. 1057-1061.

[CEC79] R.A. Cecil, B.D. Anderson, and R. Madey,
Improved Predictions of Neutron Detection Efficiency
for Hydrocarbon Scintillators from 1 MeV to about 300 MeV
Nucl. Inst. Meth. **161** (1979) pp. 339-447.

[CER84] ISOLDE looks forward
CERN COURIER,
ed. B. Southworth, G. Fraser, H. Felder, (November 1984) p. 381.

[CHU80] W.H. Chung,Y.M. Shin The Positive Parity States in ^{17}O and ^{17}F.,
Il Nuovo Cimento **60A** (1980) pp. 27-40.

[CLE65] A.B. Clegg
High Energy Nuclear Reactions ,
(Oxford University Press, London, 1965)

[COH65] S. Cohen and D. Kurath
EFFECTIVE INTERACTIONS FOR THE $1p$ SHELL ,
Nuclear Physics **73** (1965) pp.1-24.

[COH67] S. Cohen and D. Kurath
SPECTROSCOPIC FACTORS FOR THE $1p$ SHELL ,
Nuclear Physics **A101** (1967) pp.1-16.

[COM80] J.R. Comfort, Sam M. Austin, P.T. Debevec, G.L. Moake, R.W. Finlay, and W.G. Love
Inelastic excitation of ^{12}C and ^{14}N by 122 MeV protons
and implications for the effective nucleon-nucleon interaction,
Physical Review C **21** no. 6 (1980) pp. 2147-2161.

[COM80B] J.R. Comfort and B.C. Karp Scattering and reaction
dynamics for the $^{12}C + p$ system ,
Physical Review C **21** no. 6 (1980) pp. 2162-2176.
Erratum: Physical Review C **22** (1980) p. 1809.

[DEB79] P.T. Debevec, G.L. Moake, P.A. Quin
Measurement of the Detection Efficiency for 130 MeV Neutrons of a Cylindrical NE213 Cell by the Associated Particle Method,
Nucl. Inst. Meth. **166** (1979) pp. 467-471.

[DEF66] T. de Forest and J.D. Walecka ,Electron Scattering and Nuclear Structure ,
Advances in Physics **15** (1966) pp. 1-109.

[DEL76] A. Del Guerra
A Compilation of n-p and n-C Cross Sections and their use in a Monte Carlo Program to Calculate the Neutron Detection Efficiency in Plastic Scintillator in the Energy Range 1-300 MeV,
Nucl. Inst. Meth. **135** (1976) pp. 337-352.

[DEVLIN] Dan Devlin. Private communication.

[DUG63] J.L. Duggan, P.D. Miller, and R.F. Gabbard
A Study of the Reactions $Be^9(He^3,n)C^{11}$, $Li^7(He^3,n)B^9$, and $C^{13}(He^3,n)O^{15}$.
Nuclear Physics **46** (1963) pp. 336-352.

[ELL68] J.P. Elliot, A.D. Jackson, H.A. Mavromatis, E.A. Sanderson, and B. Singh
MATRIX ELEMENTS OF THE NUCLEON-NUCLEON POTENTIAL FOR USE IN NUCLEAR-STRUCTURE CALCULATIONS ,
Nuclear Physics **A121** (1968) pp. 241-278.

[FER50] Enrico Fermi
Nuclear Physics ,
(The University of Chicago Press, 1950)

[FES54] H. Feshbach, C.E. Porter, V.F. Weisskopf Model for Nuclear Reactions with Neutrons,
Physical Review **96** (1954) pp. 448-464.

[GAA80] C. Gaarde, J.S. Larson, M.N. Harakeh, S.Y. van der Werf, M. Igarashi, and A. Müller-Arnke,
The $^{48}Ca(^3He,t)^{48}Sc$ reaction at 66 and 70 MeV Reaction Mechanism and Gamow-Teller Strength ,
Nuclear Physics **A334** (1980) pp. 248-268.

[GER79] H.V. von Geramb, F.A. Brieva, J.R. Rook, in
Microscopic Optical Potentials,
ed. H.V. von Geramb, (Springer-Verlag, Berlin, 1979) p. 104.

[GOOD79] C. D. Goodman *et al.*,A Facility for Studying Neutron
Energy Spectra at Intermediate Energies
IEEE Trans. Nucl. Sci., NS-26, 2248 (1979)

[GOOD80] C.D. Goodman, C.A. Goulding, M.B. Greenfield, J. Rapaport,
D.E. Bainum, C.C. Foster, W.G. Love, and F. Petrovich
Gamow-Teller Matrix Elements from 0°(p,n) Cross Sections,
Phys. Rev. Letters **44** no. 26 (1980) pp. 1755-1759.

[GOU79] C.A. Goulding, M.B. Greenfield, C.C. Foster, T.E. Ward, J. Rapaport,
D.E. Bainum, and C.D. Goodman,
Comparison of the $^{12}C(p,n)^{12}N$ and $^{12}C(p,p')^{12}C$ Reactions
at $E_p = 62$ and 120 MeV,
Nuclear Physics **A331** (1979) pp.29-38.

[GUL70] K. Gul, B.H. Armitage, and B.W. Hooton
The $^{18}O(^3He,n)^{20}Ne$ and $^7Li(^3He,n)^9B$ Reactions.,
Nuclear Physics **A153** (1970) pp.390-400.

[HAE67] W. Haeberli,Sources of Polarized Ions,
Ann. Rev. Nucl. Phys. **17** (1967) p. 373-421.

[HAR62] R.W. Harris, G.C. Phillips, and C. Miller Jones
Phase Shift Analysis of the Elastic Scattering,
of Protons from Oxygen,
Nuclear Physics **38** (1962) pp. 259-280.

[HIC82] R.S. Hicks,
Magnetic electron scattering and the radius
of the $1d_{5/2}$ orbit in ^{17}O ,
Physical Review C **25** no. 2 (1982) pp. 695-699.

[HOL78] R.J. Holt, H.E. Jackson, R.M. Laszewski, J.E. Monahan,
and J.R. Specht
Effects of channel and perturbative radiative transitions
in the interaction $^{17}O(\gamma,n_0)^{16}O$ reaction ,
Physical Review C **18** (1978) pp. 1962-1972.

[HOP51] J.I. Hopkins,
Electron Energy Studies with the Anthracene Scintillator,
Rev. Sci. Inst. **22** (1951) p. 29.

[HYD84] C. Hyde-Wright,Particle-Hole Structure in ^{16}O.
M.I.T. Ph.D. Thesis. Unpublished (1984)

[HYN78] M.V. Hynes,Elastic Magnetic Electron Scattering from ^{17}O,
M.I.T. Ph.D. Thesis. Unpublished (1978) pp. 55-60.

[HYN79] M.V. Hynes, H. Miska, B. Norum, W. Bertozzi, S. Kowalski,
F.N. Rad, C.P. Sargent, T. Sasanuma, W. Turchinetz, and B.L. Berman
Electron Scattering from the Ground-State
Magnetization Distribution of ^{17}O,
Phys. Rev. Letters **42** (1979) pp. 1444-1448.

[IUCF78] Technical and Scientific Progress Report,
February 1, 1978 to December 31, 1978

[IUCF79] Technical and Scientific Progress Report,
January 1, 1979 to December 31, 1979

[JOH59] Arne Johansson, Gunnar Tibell, and Peter Hillman
Polarization of High Energy Protons,
in Elastic and Inelastic Scattering ,
Nuclear Physics **11** (1959) pp.540-553.

[JOH79] R.G. Johnson, B.L. Berman, K.G. McNeill, J.G. Woodworth,
and J.W. Jury
Photoneutron reaction in ^{17}O : Ground-state differential
cross section at 98° ,
Physical Review C **20** (1980) pp. 27-37.

[KAM57] R.A. Kamper, K.R. Lea, and C.D. Lustig,
Hyperfine Structure and Nuclear Electric Quadrupole Moment of ^{17}O,
Proc. Phys. Soc. **70 B** (1957) pp. 897-899.

[KEL81] J.J. Kelly,Density Dependence in the Two-Nucleon
Effective Interaction near 150 MeV,
M.I.T. Ph.D. Thesis. Unpublished (1981).

[KER59] A.K. Kerman, H. McManus, and R.M. Thaler,
The Scattering of Fast Nucleons from Nuclei ,
Annals of Physics **8** (1959) pp. 551-635.

[KNO72] H.H. Knox and T.G. Miller,
A Technique for Determining Bias Settings for Organic Scintillators,
Nucl. Inst. Meth. **101** (1972) p. 519.

[KUR64] R.J. Kurz, LRL report UCRL-11339 (March 1964).

[LAU51a] R.A. Laubenstein, M.J.W. Laubenstein, L.J. Koester, and R.C. Mobley
The Elastic Scattering and Capture of Protons by Oxygen
Physical Review **84** no. 1 (1951) p. 12-18.

[LAU51b] R.A. Laubenstein and M.J.W. Laubenstein
Assignment of Angular Momenta to the Energy Levels of ^{17}F
Physical Review **84** no. 1 (1951) p. 18-28.

[LED78]Table of Isotopes, 7^{th} Edition,
ed C.Michael Lederer, Virginia S . Shirley (John Wiley & Sons Inc. 1978)

[LEE80] T.-S. H. Lee and D. Kurath Inelastic pion scattering for $1p$ shell targets ,
Physical Review C **21** no. 1 (1980) pp. 293-305.

[LOV78] W.G. Love, Alan Scott, F. Todd Baker, W.P. Jones, and J.D. Wiggins Jr.
A TEST OF THE DWIA AT 135 MeV USING
THE $^{207}Pb(p,p')$ REACTION
Physics Letters **73B** (1978) pp. 277-280.

[LOV79] W.G. Love, in
The (p,n) Reaction and the Nucleon-Nucleon Force,
ed. C.D. Goodman et al,
Plenum Press, New York and London, (1979) pp. 23-55.

[LOV81] W.G. Love and M. Franey Effective nucleon-nucleon
interaction for scattering at intermediate energies,
Physical Review C **24** (1981) pp. 1073-1094.

[MAD78] R. Madey, F.M. Waterman, A.R. Baldwin, J. Knudson,
,J.D. Carlson, and J. Rapaport,
The Response of NE-228A, NE-228, NE-224, and NE-102
Scintillators to Protons from 2.43 to 19.55 MeV,
Nucl. Inst. Meth. **151** (1978) pp. 445-450.

[MAV69] H.A. Mavromatis and B. Singh Calculation of the Quadrupole Moments
and B(E2) Values of ^{17}O and ^{17}F with the Sussex Matrix Elements,
Nuclear Physics **A139** (1966) p. 451.

[MCN74] M.W. McNaughton, F.P. Brady, W.B. Broste, A.L. Sagle, and S.W. Johnson,
An Investigation of the Neutron Detection Efficiency of a Plastic
Scintillator Detector with the Energy Range 6 to 41 MeV,
Nucl. Inst. Meth. **116** (1974) p. 25.

[MCN75] M.W. McNaughton, N.S.P. King, F.P. Brady, and J.L. Ullman, Improved Predictions of Neutron Detection Efficiency Resulting from New Measurements of $^{12}C(n,p)$ and $^{12}C(n,d)$ Reactions at 56 MeV, Nucl. Inst. Meth. **129** (1975) pp. 241-245.

[MEA66] Measday *et al.*,Neutron Total Cross Sections in the Energy Range 80 to 150 MeV, Nuclear Physics **85** (1966) pp.129-141.

[MEA66A] Measday,Monokinetic Neutron Beam in the Range of 50 to 150 MeV, Nucl. Inst. Meth. **40** (1966) p. 213.

[MOA80] G.L. Moake and P.T. Debevec Determination of the optical potential for elastic proton scattering on ^{6}Li,^{12}C, and ^{14}N at 144 MeV, Physical Review C **21** no. 1 (1980) pp. 21-27.

[OST82] F. Osterfeld Microscopic background calculations for (p,n) reactions at intermediate energies, Physical Review C **26** no. 2 (1982) pp. 762-765.

[PET80] F. Petrovich, W.G. Love, R.J. McCarthy Separation of current and spin contributions to isovector M1 excitations by means of the (e,e') and (p,n) reactions, Physical Review C **21** no. 5 (1980) pp. 1718-1723.

[PET82] F. Petrovich, R.H. Howell, C.H. Poppe, S.M. Austin, and G.M. Crawley, NUCLEON SCATTERING FROM LIGHT NUCLEI (I). The targets ^{6}Li and ^{7}Li, Nuclear Physics **A383** (1982) pp. 355-391.

[PET84] F. PETROVICH, R. J. PHILPOTT, A. W. CARPENTER, and J. A. CARR, SPIN DEPENDENCE IN THE NUCLEUS-NUCLEUS OPTICAL POTENTIAL, Nuclear Physics **A425** (1984) pp. 609-652.

[PET85] F. Petrovich ,J. A. Carr, and A. W. Carpenter. Private communication.

[RAP81] J. Rapaport, T. Taddeucci, C. Gaarde, C.D. Goodman, C.C. Foster, and C.A. Goulding, $^{12}C(p,n)^{12}N$ reaction at 120, 160, and 200 MeV, Physical Review C **24** no. 2 (1981) pp. 335-341.

[SAJ60] Yoshio Saji
Energy Spectrum and Angular Distributions of Neutrons from the Reaction $Be^9(p,n)B^9$ at 8 to 14 MeV of Proton Energies,
Journal of the Physical Society of Japan **15** no. 3 (1960) pp. 367-371.

[SAL62A] S.R. Salisbury, G. Hardie, L. Oppliger, and R. Dangle
Proton-Oxygen Differential Scattering Cross Sections. II
Physical Review **126** no. 6 (1962) pp. 2143-2147.

[SAL62B] S.R. Salisbury and H.T. Richards
F^{17} Level Parameters
Physical Review **126** no. 6 (1962) pp. 2147-2158.

[SAT64] G.R. Satchler, The Distorted-Waves Theory of Direct Nuclear Reactions with Spin-Orbit Effects,
Nuclear Physics **55** (1964) pp. 1-33.

[SAT67] G.R. Satchler, Some Studies of the Effective Interaction from the Inelastic Scattering of Nucleons,
Nuclear Physics **A95** (1967) pp. 1-37.

[SCH70] R. Schaeffer and J. Raynal, computer code DWBA70, unpublished.

[SCH77] S.D. Schery, L.E. Young, R.R. Doering,
S.M. Austin, and R.K. Bhowmik,
ACTIVATION AND ANGULAR DISTRIBUION MEASUREMENTS OF $^7Li(p,n)^7Be(0.0 + 0.429$ MeV) FOR $E_p = 25$-45 MeV:
A TECHNIQUE FOR ABSOLUTE
NEUTRON YIELD DETERMINATION,
Nucl. Inst. Meth. **147** (1976) pp. 399-404.

[SEM54] M. Sempert, H. Schneider, und M. Wilson,
Elastische Streuung von Protonen an O^{16} zwischen 3 und 7 MeV
Helvetica Physica Acta **27** (1954) pp. 313-336.

[SHE70] H. Sherif and J.S. Blair,
SPIN-DEPENDENT EFFECTS IN THE INELASTIC SCATTERING OF HIGH-ENERGY PROTONS,
Nuclear Physics **140** (1970) pp. 33-48.

[SLO67] R.J. Slobodrian, H. Bichsel, S.J.C. McKee, and W.F. Tivol
High-Resolution Fast-Neutron Spectroscopy of the Reaction $^9Be(p,n)^9B$ at 20 MeV,
Phys. Rev. Letters **19** no. 10 (1967) pp. 595-597.

[SPE60] R.R. Spencer, G.C. Philips, and T.E. Young
Energy Levels of Be^9 and B^9
Nuclear Physics **21** (1960) pp. 310-326.

[STAN71] N.R. Stanton, A Monte-Carlo program for
calculating neutron detection efficiencies
in plastic scintillators
Ohio State University preprint COO-1545-92, February 1971.

[TAD81] T.N. Taddeucci, J. Rapaport, D.E. Bainum, C.D. Goodman, C.C. Foster,
C. Gaarde, J. Larsen, C.A. Goulding, D.J. Horen,
T. Masterson, and E. Sugarbaker
Energy dependence of the ratio of isovector effective
interaction strengths $|J_{\sigma\tau}/J_\tau|$
from $0°(p,n)$ cross sections
Physical Review C **25** no. 2 (1981) pp. 1094-1097.

[TAY53] A.E. Taylor and E. Wood,Neutron Total Cross Sections
between 30 and 153 MeV,
Philosophical Magazine **44** (1953) pp. 95-101.

[TELL79] C.D. Goodman, S.M. Austin, S.D. Bloom, J. Rapaport, and G.R. Satchler, editors
The (p,n) Reaction and the Nucleon-Nucleon Force,
(Plenum Press, New York and London, (1980)

[TELL82] F. Petrovich, G.E. Brown, G.T. Garvey, C.D. Goodman,
R.A. Lindgren, and W.G. Love, editors
Spin Excitations in Nuclei ,
(Plenum Press, New York and London, (1980)

[TOB61] W. Tobocman
Theory of Direct Nuclear Reactions ,
(Oxford University Press, London, 1961)

[VOS56] R.G.P. Voss and R. Wilson,
Neutron inelastic cross sections between 55 and 140 MeV
Proc. Royal Soc. London **236** (1956) pp. 41-51.

[WAT74] J.W. Watson and R.G. Graves,
Finite-Size Effects in Neutron Detectors
Nucl. Inst. Meth. **117** (1974) p. 541-549.

[WAT76] J.W. Watson, C.A. Miller, and F.J. Wilson ,A Beam Burst Width Monitoring and Phase Stabilization System for Cyclotrons, Nucl. Inst. Meth. **133** (1976) p. 339-401.

[WAT83] J.W. Watson, B.D. Anderson, A.R. Baldwin, C. Lebo, B. Flanders, W. Pairsuwan, R. Madey, and C.C. Foster, A Comparison of Methods for Determining Neutron Detector Efficiencies at Medium Energies. Nucl. Inst. Meth. **215** (1983) pp. 413-421.

[WIL66] D.H. Wilkinson, J.T. Sample, and D.E. Alburger Decay of the 2.36- and 2.71-MeV States of B^9, Physical Review **146** no. 3 (1966) pp. 662-670.

[WON67] C. Wong, J.D. Anderson, J. McClure, B. Pohl, V.A. Madsen, and F. Schmittroth The $C^{14}(p,n)N^{14}$ Reaction and the Two-Body Force Physical Review **160** no. 4 (1967) pp. 769-774.

[ZYL56] C.P. van Zyl, R.G.P. Voss, and R. Wilson, The Elastic Scattering of 136 MeV Neutrons by Nuclei, Philosophical Magazine **1** (1956) pp. 1003-1027.

Acknowledgements

The multitude of people who have rendered valuable assistance towards the completion of this project is virtually uncountable so that these brief paragraphs must be regarded as indicative rather than exhaustive.

Bill Bertozzi is due many thanks for his guidance, criticism, and discussions during the preparation of this manuscript. His family must also surely be commended for their patience regarding his frequent absence from the dinner table.

Special thanks are due to our collaborators, the neutron experts at Kent State University. It was these gentlemen who actually accomplished the bulk of work necessary in the execution of these experiments and the M.I.T. group assisted whenever possible. This K.S.U. task force consisted of Bryon Anderson, Richard Madey, John Watson, and numerous graduate students.

The calculations presented in the last chapter of this work were done by the theoretical group at the Florida State University at Tallahassee consisting of Fred Petrovich, Art Carpenter, and Jim Carr. I wish to thank these gentlemen not only for these calculations but also for useful discussions.

Ruby Sherr provided timely criticism of particular aspects of the data analysis. Also, Gary Love is to be thanked for valuable theoretical commentary.

Warm thanks are certainly due Nasser Kalantar-Nayestanaki and Charles Hyde-Wright for proof reading this thesis in tedious detail. Various other members of our group at M.I.T. have been of assistance in the successful completion of these experiments.

It is a pleasure to acknowledge the patient assistance of Chuck Foster, our collaborator at the Indiana University Cyclotron Facility. He and many other members of the IUCF staff were invaluable.

For completeness, these acknowledgements should contain reference to many other individuals. Such an undertaking exceeds the limitations of my memory and I must therefore beg the pardon of those who may have been omitted.